

**ADVANCED NANOSTRUCTURED ELECTRODES  
FOR  
SOLAR FUEL CONVERSION**

by

**Salim Caliskan**

B.S, Middle East Technical University, Turkey, 2008

M.S, Middle East Technical University, Turkey, 2010

Submitted to the Graduate Faculty of  
Swanson School of Engineering in partial fulfillment  
of the requirements for the degree of  
Doctor of Philosophy

University of Pittsburgh

2018

UNIVERSITY OF PITTSBURGH  
SWANSON SCHOOL OF ENGINEERING

This dissertation was presented

by

Salim Caliskan

It was defended on

March 27, 2018

and approved by

**Ian Nettleship**, PhD, Associate Professor, Department of Mechanical Engineering and  
Materials Science, University of Pittsburgh

**Youngjae Chun**, PhD, Associate Professor, Department of Industrial Engineering,  
University of Pittsburgh

**Marcus Chmielus**, PhD, Assistant Professor, Department of Mechanical Engineering  
and Materials Science, University of Pittsburgh

**Dissertation Director: Jung-Kun Lee**, PhD, Associate Professor, Department of  
Mechanical Engineering and Materials Science, University of Pittsburgh

Copyright © by Salim Caliskan

2018

# **ADVANCED NANOSTRUCTURED ELECTRODES FOR SOLAR ENERGY CONVERSION**

Salim Caliskan, PhD

University of Pittsburgh, 2018

Photoelectrochemical (PEC) water splitting and electrochemical hydrogen evolution reaction (HER) appear to be key technological components of a hydrogen-based economy which may secure sustainable energy future. Nevertheless, several limitations of PEC cell and HER electrode materials is still present. Modification of semiconductor materials bearing narrow band gap for visible spectrum, high solar to hydrogen conversion efficiency and high stability for efficient PEC cell is required for futures commercially applicable energy conversion systems. Besides, development of cost effective non-noble metal electrocatalysts with remarkable electrocatalytic efficiency for HER to overcome the limitations of high cost noble platinum (Pt)-group materials, is necessary en route to profitable and efficient water splitting devices.

Thereupon, firstly we employed plasmonic nanoparticles combined with semiconductor to confine light absorption locally in active layer of semiconductor. These nanophotonic structures can generate surface plasmon resonances (SPR) which will act light antennas and localize electromagnetic radiation energy near the active surface layer. Accordingly, core@shell and core@shell@shell nanoparticles were implemented to modify PEC performance of BiVO<sub>4</sub> photoanode. In this regard, the heterostructure offered improved light absorption, higher catalytic efficiency and efficient separation and transport of photogenerated charge carriers leading to improved PEC cell efficiency.

Furthermore, metal chalcogenide sensitized SnO<sub>2</sub> nanowire based heteronanostructured systems tested as an active photoanode material for PEC cell. Highly conductive SnO<sub>2</sub> nanowire arrays has been fabricated and different sensitization methods has been used on these photoelectrodes. The novel photoelectrode exhibits panchromatic light absorption capability, low thermalization loss, and improved photogenerated charge carrier transport behavior, providing improved photocurrent density PEC cell system.

Lastly, Mo<sub>2</sub>C and Mo<sub>2</sub>C-GO electrocatalysts have been fabricated using in situ growth, microwave assisted, facile preparation method. Electrocatalytic activities were studied as a cathode for HER. Mo<sub>2</sub>C-GO nanocomposites provide enhanced electronic conductivity, reduced particle size, more electrocatalytic active sites, improved structural stability. Hence, molybdenum-based electrocatalysts are promising non-noble, cost-effective, conductive, catalytically active alternatives to noble Pt group electrocatalysts.

Overall, this dissertation study provides a detailed study to shed light into the rational design of advanced nanostructured PEC photoanodes and HER catalysts, and systematic study of synthesis, characterization, photoelectrochemical and electrochemical activities of the resultant photoanodes and cathodes.

## TABLE OF CONTENTS

<b>LIST OF TABLES .....</b>	<b>X</b>
<b>LIST OF FIGURES .....</b>	<b>XI</b>
<b>1.0 INTRODUCTION.....</b>	<b>1</b>
<b>1.1 MOTIVATION.....</b>	<b>1</b>
<b>1.2 RENEWABLE ENERGY SOURCES .....</b>	<b>3</b>
<b>1.3 SOLAR ENERGY .....</b>	<b>4</b>
<b>1.4 HYDROGEN ECONOMY .....</b>	<b>6</b>
<b>1.5 CLASSIFICATION OF WATER SPLITTING SYSTEMS .....</b>	<b>7</b>
<b>1.6 THESIS OUTLINE .....</b>	<b>9</b>
<b>2.0 BACKGROUND AND THEORY .....</b>	<b>10</b>
<b>2.1 PHOTOELECTROCHEMICAL CELL (PEC).....</b>	<b>10</b>
<b>2.2 HYDROGEN EVOLUTION REACTION (HER).....</b>	<b>45</b>

<b>3.0</b>	<b>EXPERIMENTAL METHODS .....</b>	<b>61</b>
	<b>3.1 SAMPLE PREPARATION .....</b>	<b>61</b>
	<b>3.2 PHYSICAL CHARACTERIZATION .....</b>	<b>69</b>
	<b>3.3 PHOTOELECTROCHEMICAL CHARACTERIZATION .....</b>	<b>70</b>
	<b>3.4 ELECTROCHEMICAL CHARACTERIZATION .....</b>	<b>73</b>
<b>4.0</b>	<b>CONCENTRATED LIGHT ABSORPTION AND ITS EFFECT ON PHOTOELECTROCHEMICAL REACTION IN PLASMONIC NANOPARTICLES DECORATED BiVO<sub>4</sub> PHOTOANODES .....</b>	<b>76</b>
	<b>4.1 OBJECTIVES.....</b>	<b>76</b>
	<b>4.2 RESULTS AND DISCUSSION.....</b>	<b>80</b>
	<b>4.2.1 Microstructure and Crystal structure of BiVO<sub>4</sub> Film and Plasmonic Nanoparticles.....</b>	<b>80</b>
	<b>4.2.2 Optical Property of BiVO<sub>4</sub> Films and Core-Shell Plasmonic Particles .....</b>	<b>84</b>
	<b>4.2.3 Effect of Plasmonic Nanoparticles on Photoelectrochemical Performance of BiVO<sub>4</sub> Film .....</b>	<b>91</b>
	<b>4.2.4 Discussion on the Effect of Confined Light Absorption on Overall PEC Performance.....</b>	<b>100</b>

<b>5.0</b>	<b>PANCHROMATIC PHOTOELECTROCHEMICAL CELLS USING VERTICAL ALIGNMENT OF CDS AND CDSE ON SNO<sub>2</sub> NANOWIRES</b>	
	.....	<b>104</b>
<b>5.1</b>	<b>OBJECTIVES.....</b>	<b>104</b>
<b>5.2</b>	<b>RESULTS AND DISCUSSION.....</b>	<b>107</b>
	<b>5.2.1 Microstructure and Crystal Structure of SnO<sub>2</sub> Nanowires Before and After CdS and CdSe Coating Along the Radial Direction</b>	
	.....	<b>107</b>
	<b>5.2.2 Sequential Coating of CdS and CdSe Along the Longitudinal Direction of Nanowires .....</b>	<b>114</b>
	<b>5.2.3 Optical Properties of CdS and/or CdSe Coated SnO<sub>2</sub> Nanowires</b>	
	.....	<b>119</b>
	<b>5.2.4 Photoelectrochemical (PEC) Performance of Differently Sensitized SnO<sub>2</sub> Nanowires.....</b>	<b>121</b>
<b>6.0</b>	<b>MO<sub>2</sub>C AND MO<sub>2</sub>C-GO NANOCOMPOSITE FOR HIGH PERFORMANCE HYDROGEN EVOLUTION REACTION.....</b>	<b>135</b>
<b>6.1</b>	<b>OBJECTIVES.....</b>	<b>135</b>
<b>6.2</b>	<b>RESULTS AND DISCUSSION.....</b>	<b>136</b>

6.2.1	Molybdenum Carbide (Mo <sub>2</sub> C) Nanoparticles as Electrocatalyst	136
6.2.2	Molybdenum Carbide (Mo <sub>2</sub> C)-Graphene Oxide (GO) Nanocomposite as Electrocatalyst.....	152
7.0	CONCLUDING REMARKS AND FUTURE WORK.....	167
	REFERENCES.....	172

## LIST OF TABLES

<b>Table 1</b> Energy band parameters of most commonly used materials for sensitization .....	43
<b>Table 2</b> Summary of four phases of molybdenum carbide. ....	56
<b>Table 3</b> Several synthetic methods for the $\text{Mo}_x\text{C}_y$ composites. ....	58
<b>Table 4</b> Comparison of the PEC activity of metal chalcogenide sensitized metal oxide semiconductor photoelectrodes reported recently for PEC water splitting .....	127

## LIST OF FIGURES

<b>Figure 1</b> World Energy Source Distribution in 2015. ....	2
<b>Figure 2</b> Available yearly renewable energy sources and yearly global energy consumption .....	4
<b>Figure 3</b> Solar photovoltaics global capacity, by country/region, 2005-2015 .....	5
<b>Figure 4</b> Schematic presentation of “how hydrogen economy works “ .....	7
<b>Figure 5</b> Classification scheme for water splitting systems .....	8
<b>Figure 6</b> Energy conversion strategies from solar irradiation.....	11
<b>Figure 7</b> Schematic on a water splitting diagram of a PEC cell consisting of the photoanode and the counter electrode.....	12
<b>Figure 8</b> Energy diagrams of photoelectrochemical water splitting using a) a photocathode, and b) a photoanode and cathode in a tandem cell configuration.....	13
<b>Figure 9</b> Energy level diagram of the semiconductor/liquid/metal system (a) before contact and (b) after contact.....	14
<b>Figure 10</b> Photon flux in the solar spectrum (AM1.5).....	16
<b>Figure 11</b> Band edge positions of various semiconductors in contact with the aqueous electrolyte at pH=0 with respect to NHE and the vacuum level. For comparison water oxidation and reduction potentials are also depicted. (Adopted from literature ).....	17
<b>Figure 12</b> Donor/acceptor level band gap modification formed by metal ion doping .....	19

<b>Figure 13</b> Schematic illustration of the bandgap alignment between a wide bandgap semiconductor and a narrow bandgap sensitizer material. Sensitizer material enhances light absorption and enables easier electron transfer to the wide band gap semiconductor material.....	20
<b>Figure 14</b> (A) Scheme and (B) SEM images of different morphology of ZnO nanostructures coated on TCO substrate. (i) nanoparticles, (ii) disordered nanorods, (iii) array of nanorods, (iv) array of nanotubes, (v) array of nanoforests, (vi) array of bilayer nanostructures. (Adopted from literature " " ).....	21
<b>Figure 15</b> A typical photoelectrochemically cell made of photoanode (semiconductor metal oxide material coated on transparent conductive oxide (TCO)), cathode (Pt), and aqueous electrolyte .....	23
<b>Figure 16</b> Crystal structure of TiO <sub>2</sub> (rutile) unit cell .....	24
<b>Figure 17</b> Crystal structures of different BiVO <sub>4</sub> polymorphs: (a) tetragonal scheelite and (b) tetragonal zircon, (c) monoclinic scheelite BiVO <sub>4</sub> .....	25
<b>Figure 18</b> The scheme of the BiVO <sub>4</sub> tetragonal and monoclinic band structures.....	26
<b>Figure 19</b> Unit cell and coordination polyhedral of SnO <sub>2</sub> : (a) Octahedral coordination of tin cations; (b) Triangle around the oxygen anions.....	28
<b>Figure 20</b> Schematic illustration of the pulse layer deposition (PLD) system used for thin films depositions. ....	32
<b>Figure 21</b> Schematics of steps of Chemical Vapor Deposition (CVD) .....	33

**Figure 22** Schematic of ALD process. (a) Functionalized substrate surface. (b) Pulse of precursor A and reaction at the surface. (c) Excess precursor and reaction by-products are purged with inert gas carrier. (d) Pules of precursor B and reaction at the surface. (e) Excess precursor and reaction by products are purged with inert carrier gas. (f) Sequential steps in order to have desired material thickness and film quality. (Adopted from literature ) ..... 34

**Figure 23** Illustration of how electrochemical deposition works in a 3-electrode system..... 37

**Figure 24** Solar spectrum absorbed in a 2 mm thick Si. (Adopted from literature )..... 38

**Figure 25** Schematic diagrams illustrating (a) a surface plasmon polariton (SPP), and (b) a localized surface plasmon resonance (LSPR). ..... 40

**Figure 26** Schematics for several energy transfer mechanisms in a plasmonic solar water splitting system. N-type semiconductor nanostructure in contact with (a) pure metal nanoparticle, and (b) metal core – insulator shell nanoparticle. (adapted from literature ) ..... 41

**Figure 27** Schematic illustration of multicomponent heteronanostructures formed by (a) sequential and (b) simultaneous deposition of narrow band gap materials with different light absorbing regions: green (495-570nm), yellow (570-590 nm), red (620-750 nm). ..... 44

**Figure 28** Schematic illustration of a catalytic process. A and B react on surface of catalyst and product P is formed, and the cyclod is regenerated with separation of catalyst. .... 46

**Figure 29** Cyclic voltammogram for pure water and H<sub>2</sub>SO<sub>4</sub> on Pt micro-disk electrodes. A scanning rate is 80 mV/s. A DHE/PEM system is used as a reference electrode. (Adopted and edited from literature) ..... 51

**Figure 30** Volcano plot for the most active HER catalysts (Adopted from literature) ..... 52

<b>Figure 31</b> X-ray diffraction (XRD) patterns for a $\alpha$ -MoC <sub>1-x</sub> (JCPDS 01-089-2868), b) $\eta$ -MoC (JCPDS 01-089-4305), c) $\lambda$ -MoC (JCPDS 00045-1015), and d) $\beta$ -Mo <sub>2</sub> C (JCPDS 00-011-0608), where insets show the corresponding crystal structure. (Adopted from literature ).....	55
<b>Figure 32</b> Phase diagram for MoC (Adopted from literature) .....	57
<b>Figure 33</b> Schematic illustration of various graphene-based electrodes for electrocatalytic water splitting.....	60
<b>Figure 34</b> Schematic illustration of the preparation of plasmonic nanoparticles decorated BiVO <sub>4</sub> thin films (a) preparation of plasmonic nanoparticles, (b) fabrication of BiVO <sub>4</sub> thin films, (c) decoration of BiVO <sub>4</sub> thin films with plasmonic nanoparticles, .....	63
<b>Figure 35</b> Illustration of VLS growth method for SnO <sub>2</sub> nanowires.....	64
<b>Figure 36</b> Fabrication process for polystyrene coating and removal on SnO <sub>2</sub> nanowires and electrodeposition of CdS and CdSe layers on SnO <sub>2</sub> nanowires.....	66
<b>Figure 37</b> Schematic illustration of microwave assisted synthesis of Molybdenum Carbide (Mo <sub>2</sub> C) and Molybdenum Carbide-Graphene Oxide (Mo <sub>2</sub> C-GO) nanocomposite synthesis..	68
<b>Figure 38</b> Typical thin film semiconductor photoelectrode (a) and assembled cell (b) for PEC measurements.....	72
<b>Figure 39</b> Schematics of the experimental setup to measure is Incident Photon to Current Efficiency (IPCE) of a photoanode.....	73
<b>Figure 40</b> Electrode setup used for all electrochemical measurements. WE (working electrode, CE (counter electrode), RE (reference electrode) .....	75

**Figure 41** Characterization of the BiVO<sub>4</sub> sample; scanning electron microscopy (SEM) morphology of bare as-synthesized BiVO<sub>4</sub> thin films, (a) top view (b) cross sectional view and (c) X-ray diffraction (XRD) of the samples..... 81

**Figure 42** Characterization of core shell nanoparticles: (a) schematic representation of core shell particles evolution starting from SiO<sub>2</sub> particles to SiO<sub>2</sub>@Ag@SiO<sub>2</sub>, (b) a size distribution of SiO<sub>2</sub>, Ag@SiO<sub>2</sub> and SiO<sub>2</sub>@Ag@SiO<sub>2</sub> particles, (c) SEM image of SiO<sub>2</sub>@Ag@SiO<sub>2</sub> particles. .... 82

**Figure 43** Transmission electron microscopy (TEM) images of (a) SiO<sub>2</sub> spheres, (b) SiO<sub>2</sub>@Au seeds, (c) SiO<sub>2</sub>@Ag core shell particles, and (d) SiO<sub>2</sub>@Ag@SiO<sub>2</sub> core shell shell particles. .... 83

**Figure 44** Characterization of the core shell particles coated BiVO<sub>4</sub> samples; Scanning electron microscopy (SEM) morphology of core shell particles coated BiVO<sub>4</sub> thin films, (a) top view (b) cross sectional view and (c) X-ray diffraction (XRD) of the samples, BiVO<sub>4</sub>:BVO, sAg:SiO<sub>2</sub>@Ag..... 84

**Figure 45** Experimental measured and theoretically calculated extinction spectra of 800 nm thick BiVO<sub>4</sub> films on FTO/glass substrate (the calculation was performed using FTDT simulation). .... 85

**Figure 46** UV-vis absorbance spectra of experimental (a) and theoretical data calculated by FTDT simulations of 110 nm core shell particles in aqueous solution..... 86

**Figure 47** UV-visible extinction (left) and transmittance spectra (right) of bare and plasmonic particle coated BiVO<sub>4</sub> thin film. BVO: BiVO<sub>4</sub>, sAg: SiO<sub>2</sub>@Ag, sAgs: SiO<sub>2</sub>@Ag@SiO<sub>2</sub> ..... 87

**Figure 48** Calculated light absorption of bare and plasmonic particle coated BiVO<sub>4</sub> films using FDTD simulation results (light is illuminated from the top surface) ; (a) Absorption spectra of bare and plasmonic particle (SiO<sub>2</sub>@Ag and SiO<sub>2</sub>@Ag@SiO<sub>2</sub>) coated BiVO<sub>4</sub> film, (b) absorption contour plot (b-1: bare BiVO<sub>4</sub> film, b-2: SiO<sub>2</sub>@Ag coated BiVO<sub>4</sub> film, b-3: SiO<sub>2</sub>@Ag@SiO<sub>2</sub> coated BiVO<sub>4</sub> film)..... 90

**Figure 49** J-V curves of bare and plasmonic nanoparticle coated BiVO<sub>4</sub> thin films at AM 1.5 condition (light is illuminated from the electrolyte – BiVO<sub>4</sub> interface or the electrolyte – plasmonic particle/BiVO<sub>4</sub> interface). BVO: BiVO<sub>4</sub>, sAg: SiO<sub>2</sub>@Ag, sAgs: SiO<sub>2</sub>@Ag@SiO<sub>2</sub>..... 91

**Figure 50** Incident photon to current conversion efficiency (IPCE) measured at 1.0 V vs RHE of the bare BiVO<sub>4</sub>: BVO, SiO<sub>2</sub>@Ag/BiVO<sub>4</sub> (sAg) and SiO<sub>2</sub>@Ag@SiO<sub>2</sub> /BiVO<sub>4</sub> (sAgs). ..... 93

**Figure 51** A schematic explanation of separation and catalysis on photoanodes and equations to calculate J<sub>ph</sub>, J<sub>abs</sub>, η<sub>separation</sub> and η<sub>catalysis</sub>. ..... 95

**Figure 52** Separation (a) and catalysis (b) efficiencies of bare BiVO<sub>4</sub>, SiO<sub>2</sub>@Ag@SiO<sub>2</sub> and SiO<sub>2</sub>@Ag plasmonic particles decorated BiVO<sub>4</sub> thin films. .... 96

**Figure 53** Amperometric i-t measurements for BiVO<sub>4</sub> and core shell particles decorated BiVO<sub>4</sub>. BiVO<sub>4</sub> (BVO), BiVO<sub>4</sub>\_SiO<sub>2</sub>@Ag (BVO\_sAg) and BiVO<sub>4</sub>\_SiO<sub>2</sub>@Ag@SiO<sub>2</sub> (BVO\_sAgs)..... 99

**Figure 54** Amperometric i-t measurements for BiVO<sub>4</sub> and core shell shell particles decorated BiVO<sub>4</sub>. BiVO<sub>4</sub>: BVO, SiO<sub>2</sub>@Ag (sAg) and SiO<sub>2</sub>@Ag@SiO<sub>2</sub> (sAgs)..... 100

**Figure 55** Light trapping by plasmonic nanoparticles from metal nanoparticles on the top surface of the semiconductor thin film (BiVO<sub>4</sub>)..... 101

<b>Figure 56</b> FDTD calculated simulation results for plasmonics effect at a contour plot of absorption at different wavelengths (a) $\lambda=400$ nm, (b) $\lambda=465$ nm, and (c) $\lambda=600$ nm.....	103
<b>Figure 57</b> Cross-sectional SEM images of SnO <sub>2</sub> nanowires that were grown on the Au coated FTO for 1 hr (a) and 30 minutes (b); insets of plan-view images.....	108
<b>Figure 58</b> X-ray Diffraction (XRD) patterns of 1hr long grown SnO <sub>2</sub> nanowires. ....	109
<b>Figure 59</b> Cross-sectional SEM images of SnO <sub>2</sub> nanowires (a) and Sb-doped SnO <sub>2</sub> nanowires (both were grown for 1 hr); insets of plan-view images. ....	110
<b>Figure 60</b> EDAX results for as grown SnO <sub>2</sub> and Sb-SnO <sub>2</sub> nanowires .....	111
<b>Figure 61</b> SEM image of (a) bare SnO <sub>2</sub> nanowires, (b) CdS coated SnO <sub>2</sub> nanowires, (c) CdSe coated SnO <sub>2</sub> nanowires, and (d) SnO <sub>2</sub> nanowires sequentially coated with CdS and CdSe.....	112
<b>Figure 62</b> EDAX results for CdS, CdSe and CdS/CdSe coated on SnO <sub>2</sub> nanowires.....	113
<b>Figure 63</b> Cross-sectional SEM image of (a) bare SnO <sub>2</sub> nanowires, (b-d) SnO <sub>2</sub> nanowires spin-coated with polystyrene for 30 sec; (b) at 2000 rpm, (c) at 3000 rpm, (d) at 4000 rpm. ....	115
<b>Figure 64</b> Schematic representation of polystyrene treatment of SnO <sub>2</sub> nanowires for sequential deposition of CdS and CdSe layers .....	115
<b>Figure 65</b> Cross-sectional SEM images of the polystyrene coated SnO <sub>2</sub> nanowire arrays (insets show the plan-view images): (a) after spin-coating of the polystyrene layer, (b)-(d) after soaking the polystyrene layer in ethyl acetate solution for (b) 10 sec, (c) 30 sec, (d) 60 sec.....	116
<b>Figure 66</b> Cross-sectional SEM images of CdSe/CdS/SnO <sub>2</sub> nanowires which were sequentially coated with CdS and CdSe along the longitudinal direction of the nanowires. ....	118

<b>Figure 67</b> EDX analysis results of the top and bottom parts of the coating layer which was sequentially deposited along the longitudinal direction of the nanowires.....	119
<b>Figure 68</b> Diffuse transmittance spectrum of bare SnO <sub>2</sub> , CdS/SnO <sub>2</sub> , CdSe/SnO <sub>2</sub> , CdS/CdSe/SnO <sub>2</sub> nanowires (sequential coating along the radial direction of the nanowire, and PS: sequential coating along the longitudinal direction of the nanowire).....	120
<b>Figure 69</b> Photos of (a) SnO <sub>2</sub> nanowires, (b) CdS/SnO <sub>2</sub> , (c) CdSe/SnO <sub>2</sub> and (d) CdSe/ CdS/SnO <sub>2</sub> heteronanostructures. ....	121
<b>Figure 70</b> Linear sweep voltammograms of pure SnO <sub>2</sub> nanowires, CdS coated SnO <sub>2</sub> nanowires and CdSe coated SnO <sub>2</sub> nanowires at a scan rate of 100 mVs <sup>-1</sup> at applied potentials from -0.9 to +0.3 V vs. Ag/AgCl under illuminated (AM1.5G) conditions.....	123
<b>Figure 71</b> Linear sweep voltammograms of photoanodes fabricated from CdSe/CdS/SnO <sub>2</sub> NWs (with, PS, and without PS) at a scan rate of 100 mVs <sup>-1</sup> at applied potentials from -0.9 to +0.3 V vs. Ag/AgCl, under illuminated (AM1.5G) conditions.....	124
<b>Figure 72</b> Schematic illustration of band alignment and charge transfer at CdS/CdSe coated SnO <sub>2</sub> nanowires during the photoreaction. ....	126
<b>Figure 73</b> IPCE spectra of CdS/SnO <sub>2</sub> nanowires, CdSe/SnO <sub>2</sub> nanowires and CdSe/CdS/SnO <sub>2</sub> nanowires (sequential coating along the radial or longitudinal direction) at 1.0 V vs. RHE.....	129
<b>Figure 74</b> Conductivity of SnO <sub>2</sub> nanowire as a function of Sb doping content.....	130
<b>Figure 75</b> Linear sweep voltammograms of photoanodes fabricated from CdSe/CdS/Sb-SnO <sub>2</sub> NWs (with and without polystyrene treatment), at a scan rate of 100 mVs <sup>-1</sup> at applied potentials from -0.9 to +0.3 V vs. Ag/AgCl, under a light intensity of 100 mWcm <sup>-2</sup> . ....	131

<b>Figure 76</b> Measured IPCE spectra of CdSe/CdS/Sb-SnO <sub>2</sub> and CdSe/CdS/Sb-SnO <sub>2</sub> (PS) samples, from 300-800 nm at a potential of 1.0 V vs. RHE.....	132
<b>Figure 77</b> The photocurrent responses (amperometric i-t curves, light on-off mode) of SnO <sub>2</sub> CdS/CdSe (without polystyrene treatment) samples, chopped and continues light mode, at an applied potential of 1.0 V versus RHE .....	133
<b>Figure 78</b> The photocurrent responses (amperometric i-t curves, light on-off mode) of Sb-SnO <sub>2</sub> CdS/CdSe (without polystyrene treatment) samples, chopped and continues light mode, at an applied potential of 1.0 V versus RHE .....	134
<b>Figure 79</b> X-Ray Diffraction (XRD) patterns for Mo <sub>2</sub> C nanoparticles with different amount of urea content (R). .....	137
<b>Figure 80</b> SEM images of as-synthesized particles and thermally annealed particles (a) as synthesized after the microwave reaction, (b) annealed at 400 °C (b) annealed at 600 °C and (d) annealed at 800 °C (R of the precursor = 7). .....	138
<b>Figure 81</b> Raman spectra of Mo <sub>2</sub> C synthesized by the microwave reaction and the sol-gel method (after the chemical reaction, products were thermally annealed at 800 °C). .....	140
<b>Figure 82</b> Raman spectra of Mo <sub>2</sub> C nanoparticles from the microwave reaction at different R: as-received nanoparticles were annealed at 600 °C or 800 °C. ....	141
<b>Figure 83</b> XPS (a) survey spectrum, (b) Mo 3d spectrum and (c) C 1s spectrum of Mo <sub>2</sub> C with different urea content (R=5, 7, 9).....	142
<b>Figure 84</b> I-V curves of Mo <sub>2</sub> C synthesized at different R (=5, 7, 9). .....	144
<b>Figure 85</b> Linear sweep voltammetry (LSV) curves for Mo <sub>2</sub> C nanoparticles with different amount of urea content (R), the electrolyte was 0.5 M H <sub>2</sub> SO <sub>4</sub> , the was scan rate 20 mVs <sup>-1</sup> , the geometric area of the electrode was 1.0 cm <sup>2</sup> . .....	147

<b>Figure 86</b> Tafel plot; for Mo <sub>2</sub> C nanoparticles with different amount of urea content (R), the electrolyte was 0.5 M H <sub>2</sub> SO <sub>4</sub> , the was scan rate 20 mVs <sup>-1</sup> , the geometric area of the electrode was 1.0 cm <sup>2</sup> .	149
<b>Figure 87</b> EIS spectra (Nyquist Plots) of Mo <sub>2</sub> C nanoparticles of different R (R = 5, 7, 9) under external biasof 0, 50, 100,150, and 200mV (electrolyte: 0.5 M H <sub>2</sub> SO <sub>4</sub> , a frequency range of 100 mHz to 100 kHz.	150
<b>Figure 88</b> EIS spectra (BodePlots) of Mo <sub>2</sub> C nanoparticles of different R (R = 5, 7, 9) under external biasof 0, 50, 100,150, and 200mV (electrolyte: 0.5 M H <sub>2</sub> SO <sub>4</sub> , a frequency range of 100 mHz to 100 kHz.	151
<b>Figure 89</b> X-Ray Diffraction (XRD) patterns for Mo <sub>2</sub> C and Mo <sub>2</sub> C-GO nanocomposites with various GO amount.	152
<b>Figure 90</b> Scanning electron microscope images of pure Mo <sub>2</sub> C (a) and Mo <sub>2</sub> C-GO nanocomposites with different GO loading amount (b) GO (0.1% wt), (c) GO (0.5wt%), and (d) GO (1.0 wt%)	154
<b>Figure 91</b> XPS (a) survey spectrum, (b)Mo3d spectrum, and (c) C1s spectrum for Mo <sub>2</sub> C-GO composites with different GO content.	156
<b>Figure 92</b> Raman spectra of Mo <sub>2</sub> C and Mo <sub>2</sub> C-GO nanocomposites with different amount of GO addition	157
<b>Figure 93</b> Resistivity data for Mo <sub>2</sub> C-GO electrocatalysts with different amount of GO content (GO=0.1, 0.5, 1.0 %)	159
<b>Figure 94</b> Linear sweep voltammetry (LSV) curves for Mo <sub>2</sub> C nanoparticles with different amount of GO content, the electrolyte was 0.5 M H <sub>2</sub> SO <sub>4</sub> , the was scan rate 20 mVs <sup>-1</sup> , the geometric area of the electrode was 1.0 cm <sup>2</sup> .	160

**Figure 95** Tafel plot; for Mo<sub>2</sub>C nanoparticles with different amount of GO content, the electrolyte was 0.5 M H<sub>2</sub>SO<sub>4</sub>, the was scan rate 20 mVs<sup>-1</sup>, the geometric area of the electrode was 1.0 cm<sup>2</sup>. ..... 161

**Figure 96** EIS spectra (Nyquist Plots) of Mo<sub>2</sub>C-GO nanocomposites with different η=0, 50mV, 100mV, 150mV, 200mV obtained in 0.5 M H<sub>2</sub>SO<sub>4</sub> at 25 0C in the frequency range of 100 mHz to 100 kHz. .... 163

**Figure 97** EIS spectra (Bode Plots) of Mo<sub>2</sub>C-GO nanocomposites with different GO amounts obtained at η=150mV in 0.5 M H<sub>2</sub>SO<sub>4</sub> at 25 0C in the frequency range of 100 mHz to 100 kHz. .... 164

**Figure 98** Electrical Equivalent circuit models for the EIs response of: two-time constant model, including the series resistance (R<sub>s</sub>), the charge transfer resistance (R<sub>ct</sub>), resistivity related to the porosity of the electrode surface (R<sub>p</sub>) and constant phase elements CPE1 and CPE2. .... 165

**Figure 99** Schematic representation of Mo<sub>2</sub>C-Go composites as an active electrocatalyst for HER ..... 166

## ACKNOWLEDGEMENT

During my doctoral dissertation and the research work, I would not have been able to finish without the support and help of many people. I would like to express my appreciation and acknowledgement throughout this long and fantastic journey.

First and foremost, I am extremely grateful to my supervisor, Prof. Jung Kun Lee, for giving me the opportunity to work in this evolving and highly demanding field of energy. I also thank him for his kind guidance, patience, endless support, and suggestions throughout this journey. His eagerness, passionate, diligence, the sharing of his extensive knowledge with me influenced my research and future goals. He was always showing endless support for his students to succeed in their research. I am impressed by his work enthusiasm, work ethic, deep knowledge in various fields, strong logic and creativity. I am amazed to see his sincerity, dedication, and punctuality even after achieving so much in his life. Without his perfect guidance in all aspects, it would be difficult for me to survive and finish my PhD study.

I would like to thank to esteemed committee members, Professor Ian Nettleship, Professor Youngjae Chun, and Professor Marcus Chmielus. Their kindness, feedbacks on my work and corrections always guided my PhD research.

I feel very lucky about having chance to work with great lab members in such an active research group: Dr. Bo Ding, Dr. Youngsoo Jung, Dr. Po Shun Huang, Dr. Hyun Soo Han, Dr. Gill San Han, Fen Quin, Lingtao Jiang, and Anqi Wang. They are hardworking, smart, diligent, and very much friendly. ‘

Thanks to my other colleagues and friends, who provide excellent research environment and collaboration: Dr. Ziyue Xiong, Dr. Hee-Suk Roh, Seongha Lee, and Matt Duff, who are patient, diligent, and very friendly. With their assistance, we conducted research in a friendly and productive laboratory environment.

Moreover, I would like to thank to Department of Mechanical Engineering and Materials Science, Materials Science Characterization Lab and Nano-Scale Fabrication and Characterization facility, and their staffs: Cole Van Ormer and Dr. Susheng Tan.

Finally, I would like to express my apologies, gratitude and love, to my mom, my brother and my sister, the only people in my life, who will love and support me no matter the situation and decisions I make and whose care and education helped me to get here

## **1.0 INTRODUCTION**

### **1.1 MOTIVATION**

Possible energy shortages and the impact of global warming on future weather patterns are growing of global concern. In 2010, the world's energy consumption summed up to J, analogous to a consumption rate of TW. The U.S. Department of Energy (DOE) predicts this number to be grow by 49% in next quadricentennial. Moreover in 2015, 86 % of world's energy demand was offset by fossil fuel-based energy sources. (Figure 1) Besides, a recent BP report of the 2030 Energy Outlook predicts that an additional 1.3 billion people will become new energy consumers by 2030. <sup>1</sup>

Fossil fuel-based energy sources have been the primary source of world's energy demand for the past bicentennial. Natural gas, petroleum and coal are the most common form of fossil fuels. Recent estimations about current reserves of fossil fuels project that global energy demand will be satisfied for several hundred years at a consumption rate of 30 TW/year. Yet, there is enough concern about quickly diminishing energy sources, and consequences of consuming fossil fuel such as pollution and climate change.

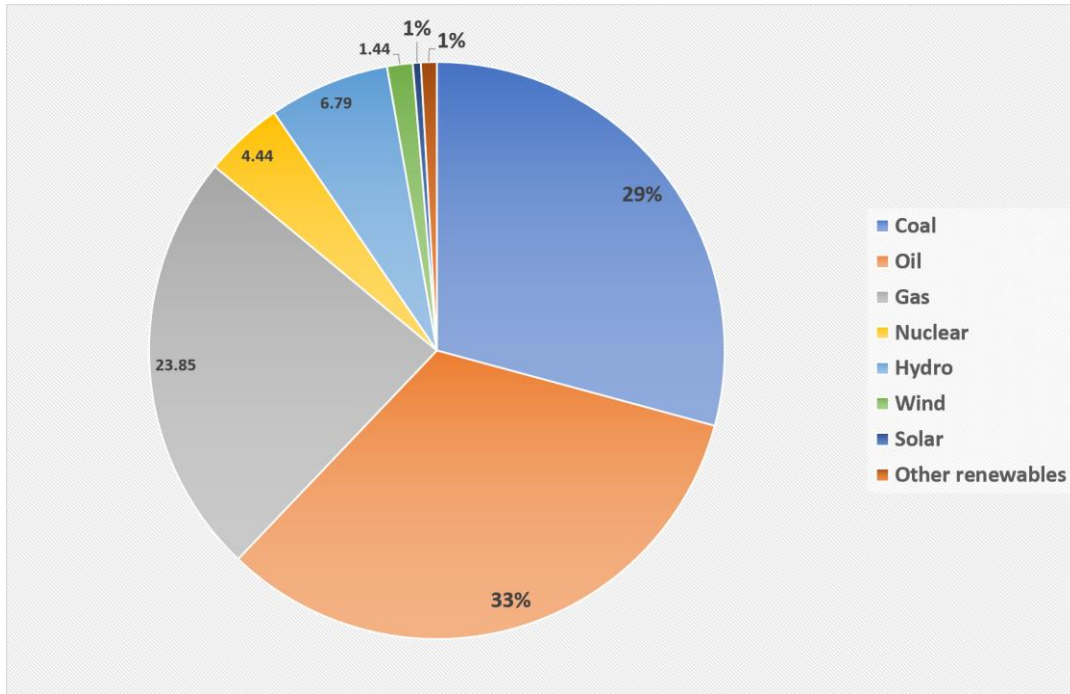


**Figure 1** World Energy Source Distribution in 2015.<sup>2</sup>

Coal is most pollutant among all fossil fuels, in which combustion for electric power and industry were responsible for producing 90 kg of carbon dioxide emissions per gigajoule of energy produced. Oil lists the second as producing 77 kg/GJ, and currently indispensable for road transport and petrochemical industries. Natural gas appears to be the cleanest of fossil fuels releasing about 50 kg/GJ. Despite of natural gas being the cleanest and seems to be innocent and environmentally friendly, all fossil-based energy resources contribute to greenhouse gas emissions and leading to global warming.

Fossil fuel dependence of a country is directly affect economic and national security. Global players for energy production and consumption are United States, China and Russia. Therefore, any conflict in politics may lead to threats of a country and monopoly of these global powers to other nations to be energy dependent. Although fossil fuels remain to be the primary source of world's energy demand, the environmental costs are high because of high levels of

carbon dioxide emission, and national and economic security concerns raised due to fossil fuel dependence of a nation. Consequently, the desire to be energy independent for security reasons and environmental pollutions concerns drives nations to look for alternatives to fossil fuels. Hence, renewable and cleaner energy sources appear to be prominent research objectives.

## **1.2 RENEWABLE ENERGY SOURCES**

Uranium and nuclear power is carbon free source of energy and already accounts almost 5 % of global consumption due to its high efficiency, moderate and predictable cost of electricity over service life and no CO<sub>2</sub> emission during life cycle. However, uranium resources are limited similar to the fossil fuel resources. Furthermore, the use of nuclear power faces other challenges such as high capital and compliance costs, public concerns about operation and final waste disposal, and finally liabilities in case of nuclear accident. Recent nuclear power accidents and detrimental causes lead to public protests and the fear of nuclear power against new nuclear power plants. Therefore, the concentrate of research turns into renewable energy sources: solar, wind, geothermal, hydro, and biomass. Solar, and wind are the two-prevalent renewable energy sources that convert these natural resources into energy. Figure 2 illustrates annual availability and consumption situation of renewable energy sources.

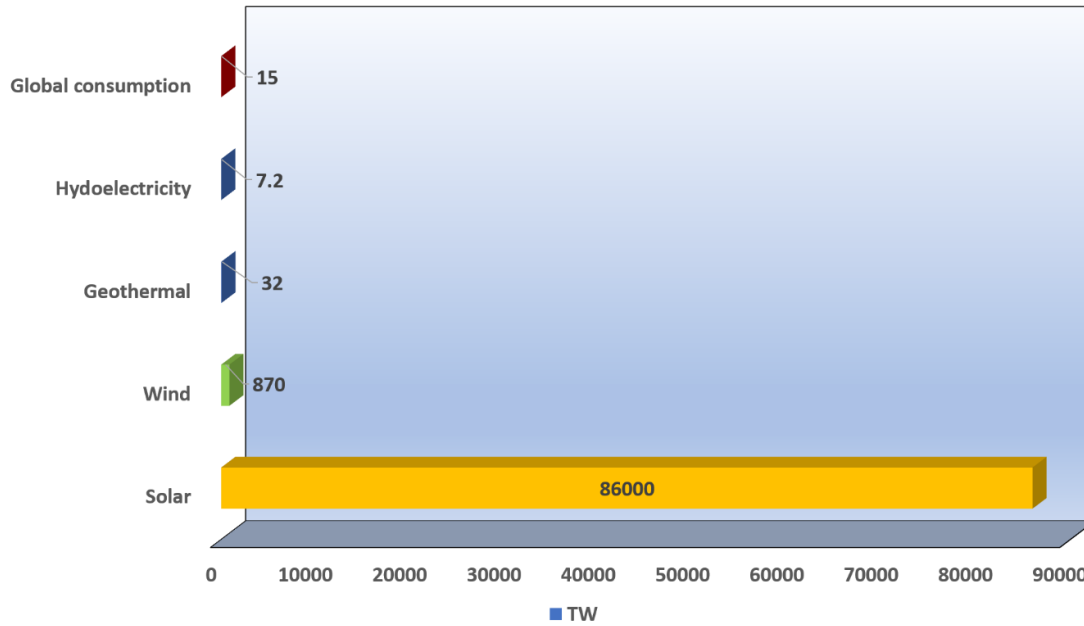


**Figure 2** Available yearly renewable energy sources and yearly global energy consumption.<sup>3</sup>

### 1.3 SOLAR ENERGY

Of all renewable energy sources, solar energy possesses the largest supply capacity. Every hour enough sunlight reaches the earth to meet the world’s energy demand for a whole year. Proposed usages of solar energy are; solar-fuel conversion, solar-thermal conversion and solar-electricity conversion. Several technologies have been used to capture solar irradiation and convert it to fuel, heat and electricity. Photovoltaics, conversion of solar energy into electrical energy, the most widely implemented type of solar energy technology. In photovoltaics, the absorbed photons of sun are converted into electrical current. However, the limitation with solar photovoltaics is relative low conversion efficiency. High most for material production, and installation of photovoltaics drive overall cost of solar-electricity conversion high. Nowadays, investing in solar photovoltaics with policies and subsidies is globally supported in favor of reducing carbon release.

Recent forecasts predict that solar energy will become an economically competitive energy source without any subsidies within a decade. Solar power production capacity is more than decupled between 2009 (23GW) and 2015 (227GW). (Figure 3) This is a significant sign of enormous interest in conversion solar irradiation into conventional energy.

Another limiting factor of solar energy is that Sun does not shine 24 hours/day. Therefore, storage of solar energy at night time becomes an essential part of a solar power system. Surplus energy needs to be collected and stored during daytime and redistributed at night time.

In this regard, photoelectrochemistry (PEC) appears as a promising method for solar light harvesting. It converts solar energy into chemical energy instead of electrical or thermal energy. Conversion into chemical energy offers automatic storage of solar energy and makes it available when the supplied power decreases.

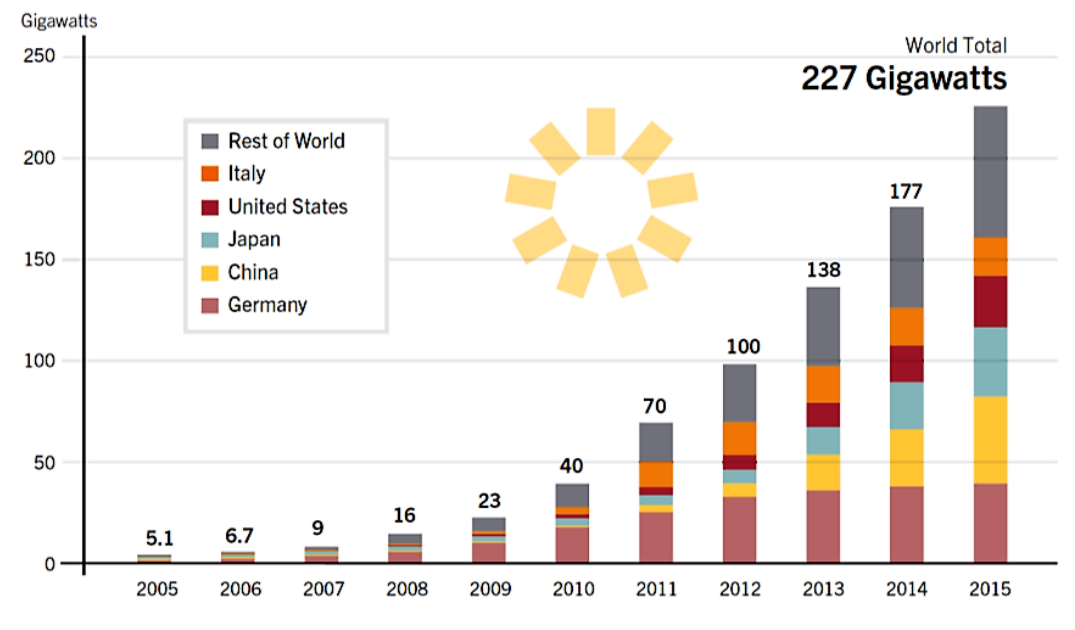


**Figure 3** Solar photovoltaics global capacity, by country/region, 2005-2015 <sup>4</sup>

## 1.4 HYDROGEN ECONOMY

Hydrogen economy means replacing fossil fuels with clean and storable hydrogen gas which neither produce pollutant nor leave a negative footprint on the environment.<sup>5</sup> Hydrogen is regarded as a promising fuel for future and the energy, stored in the form of hydrogen, can be used to supply the needs of a great variety of industrial activities and aspects of society from homes to electric utilities to business and industry, a typical hydrogen energy system is illustrated in Figure 4. Hydrogen has been appealing research material as it bears the highest energy content per unit weight.<sup>6</sup> The only byproduct of hydrogen combustion is water.<sup>7</sup>

As of today, however, hydrogen gas is mainly produced from fossil fuels such as alcohol, natural gas and petroleum. Though hydrogen itself is very clean, a hydrogen production process and its byproduct are not environment-friendly. In order to lessen carbon footprint and prevent further climate change, a low-carbon hydrogen generation process should be implemented. In addition, challenges in production, compression, distribution, transfer and storage must be addressed before hydrogen becomes a competitive alternative to other energy sources. In this regard, electrocatalytically driven hydrogen evolution reactions (HER) emerges as a prominent way of feasible and clean production of hydrogen, since HER uses only water to produce hydrogen.

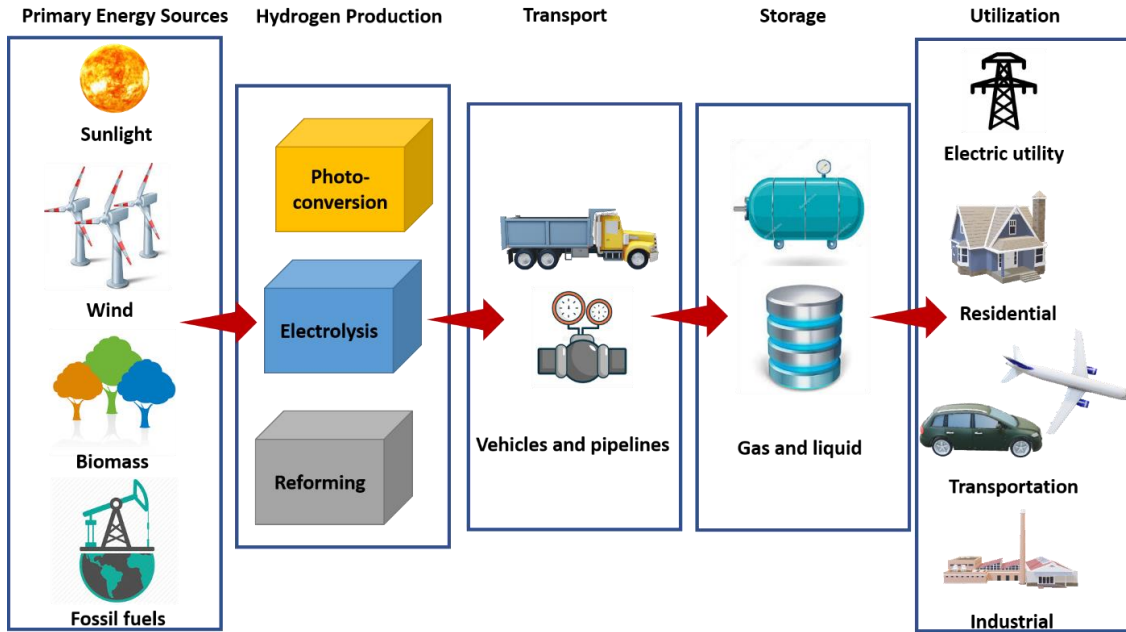


**Figure 4** Schematic presentation of “how hydrogen economy works “

## 1.5 CLASSIFICATION OF WATER SPLITTING SYSTEMS

Water splitting is the general term for a chemical reaction in which water is separated into oxygen and hydrogen. Efficient and economical water splitting would be a key technological component of a hydrogen based future economy. Various techniques for water splitting have been issued in water splitting processes which is illustrated in Figure 5. Basically, electrochemical and photo electrochemical ways appears to be two prominent ways to perform water splitting. Electrochemical splitting of water is the decomposition of water ( $H_2O$ ) into oxygen ( $O_2$ ) and hydrogen gas ( $H_2$ ) due to an electric current being passed through the water and in some cases with the aid of suitable catalysts. In solar water splitting or photoelectrochemical systems, hydrogen is produced from water using sunlight and suitable photocatalysts. However, there are several ways

and configurations one can use different electrochemical systems and catalysts or combine a specialized semiconductor to harvest and convert light and generate hydrogen and/or oxygen, which is illustrated in Figure 5.

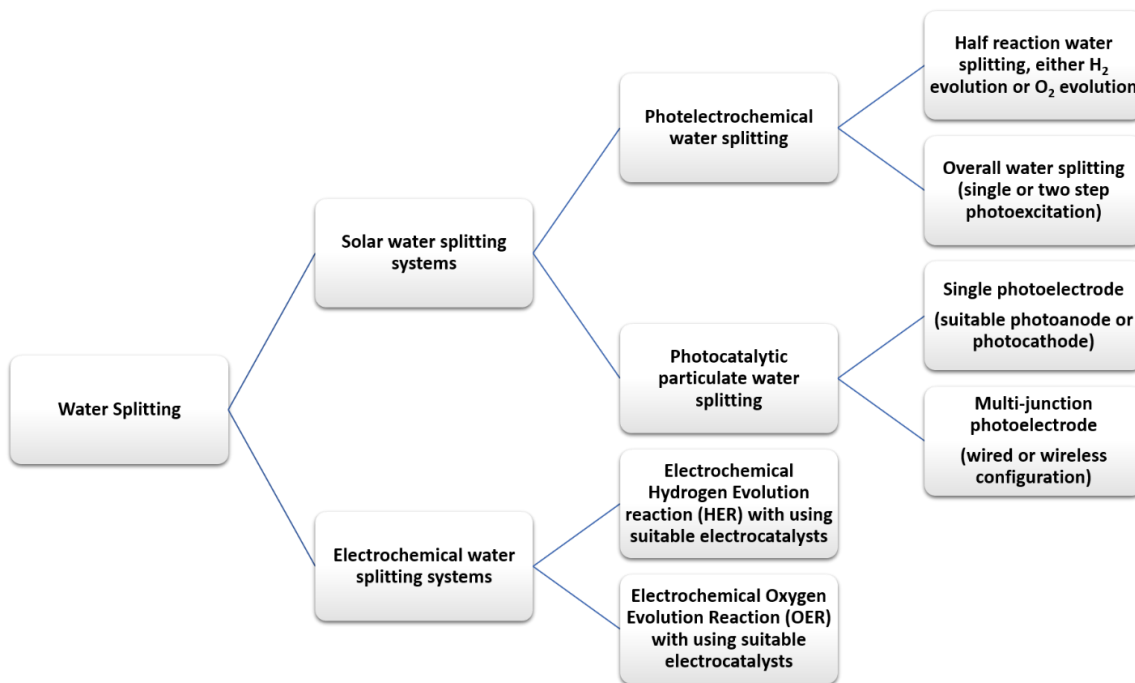


**Figure 5** Classification scheme for water splitting systems

## 1.6 THESIS OUTLINE

Following the introduction chapter, basic principles of PEC cell and HER reaction will be reviewed in Chapter 2. In addition, current semiconductor materials used as photoanode for PEC water splitting and HER reaction will be discussed, and special emphasis will be given to:

- i. Bismuth vanadate ( $\text{BiVO}_4$ ) thin films and plasmonic nanoparticles for PEC cell
- ii. Tin oxide ( $\text{SnO}_2$ ) nanowires and cadmium chalcogenides ( $\text{CdS}$ ,  $\text{CdSe}$ ) nanoparticles for PEC cell
- iii. Molybdenum carbide ( $\text{Mo}_2\text{C}$ ) and graphene oxide (GO) for HER reaction

Experimental procedures and characterization techniques to fabricate semiconductor photoelectrodes and evaluate their PEC and HER properties are stated in detail in Chapter 3.

Chapter 4 shows results on PEC performance of  $\text{BiVO}_4$  thin films coated with plasmonic particles. Then, the effect of plasmonic particles on light absorption and its effect on the performance of  $\text{BiVO}_4$  PEC cells are mainly discussed.

Chapter 5 shows results on PEC performance of  $\text{CdS}/\text{CdSe}$  coated  $\text{SnO}_2$  nanowires. Sequential coating of two different semiconductors and the effect of panchromatic light absorption on PEC performance are mainly discussed.

Chapter 6 shows results on electrolysis of water by molybdenum carbide ( $\text{Mo}_2\text{C}$ ) and graphene oxide (GO). Microwave-assisted synthesis of GO supported  $\text{Mo}_2\text{C}$  and its role in hydrogen evolution reaction (HER) will be mainly discussed.

Chapter 7 is conclusion of entire thesis and future remarks.

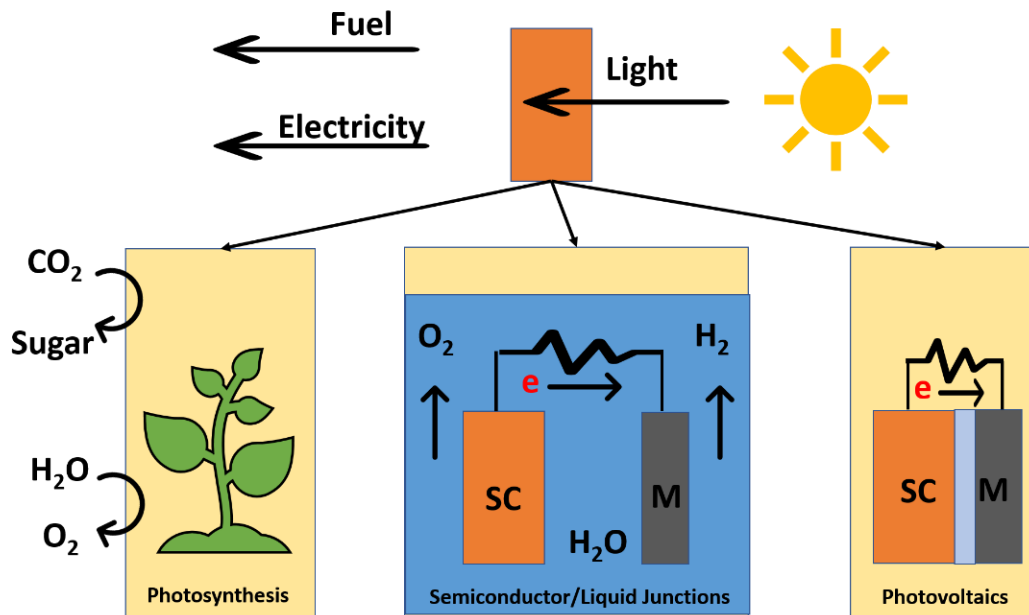
## **2.0 BACKGROUND AND THEORY**

In this chapter, basic principles of two water splitting systems (i.e. PEC cell and electrolysis cell) are explained in detail. The performance of PEC cell is restricted by various factors, generally associated to intrinsic material properties of the semiconductor photoelectrode, for instance the electronic bandgap and electronic transport properties. These limitations will be summarized first and current photoanode materials are reviewed. Then, previous studies on electrolysis of water and hydrogen evolution reaction (HER) on MoC<sub>2</sub> are discussed.

### **2.1 PHOTOELECTROCHEMICAL CELL (PEC)**

#### **2.1.1 Basic Principles**

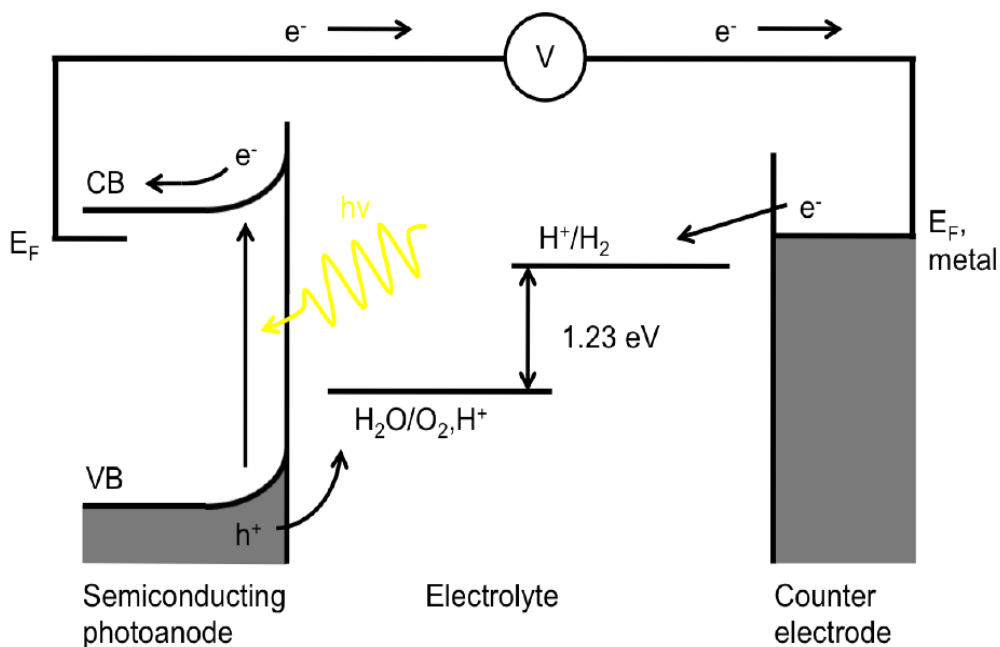
Hydrogen appears to be the best energy carrier which may secure sustainable energy future. Hydrogen is a clean and environmentally friendly energy source, as combustion of hydrogen leaves only water. However, hydrogen does not exist in large amounts in nature. It is commonly found as a part of large molecules such as water and hydrocarbon. Hence, a certain amount of energy is required to separate pure “hydrogen, H<sub>2</sub>”. Out of several methods to produce hydrogen, “solar water splitting” appears to be the most green and sustainable energy cycle.



**Figure 6** Energy conversion strategies from solar irradiation

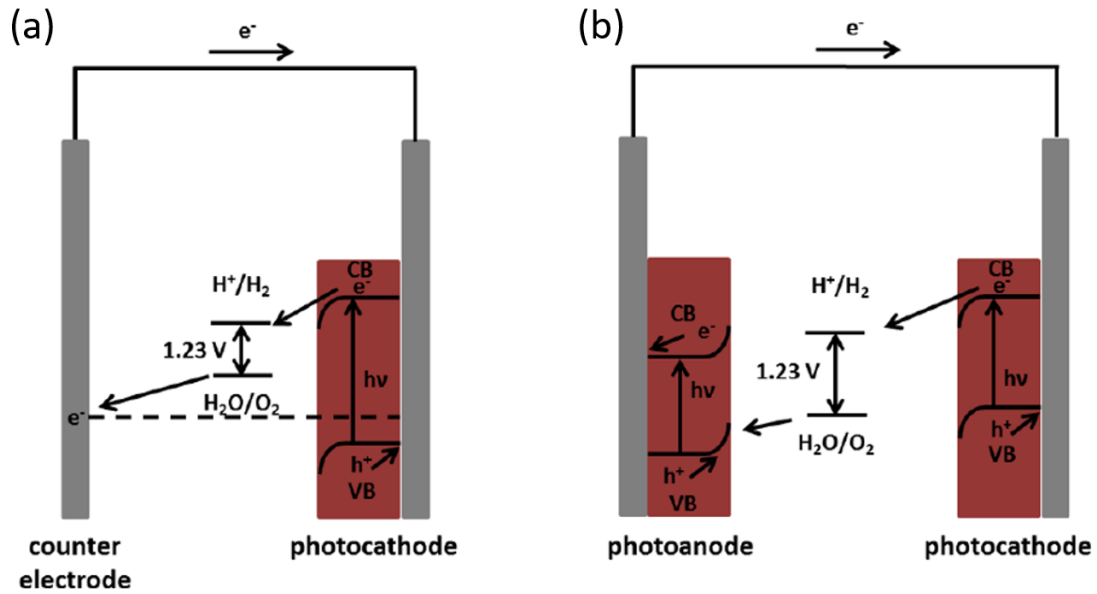
Figure 6 shows three energy conversion pathways from solar energy to fuel or electricity: natural photosynthesis, semiconductor/liquid junctions and photovoltaics. Semiconductor/liquid junction devices are commonly referred as photo-electrochemical cells or PECs which are solar cells which generate fuel from light. Photoelectrochemical hydrogen generation takes place on the Schottky junction that is formed at the interface between semiconducting material and aqueous electrolyte. Photoelectrodes absorb solar energy and generate electrons and holes, which split water molecules into  $\text{H}_2$  and  $\text{O}_2$ . A common PEC cell set-up is illustrated in Figure 7. It consists of an anode and cathode immersed in an aqueous electrolyte, of which at least one is made of a semiconductor exposed to light and able to absorb the light.

This type of PECs operates on a principle that there are two redox systems driven by high energy electrons or holes: for an n-type semiconductor (i) energetic holes associated with the oxygen-evolution half-reaction (OER) occurs at the surface of the semiconductor electrode, whereas (ii) energetic electrons associated with the hydrogen evolution half-reaction (HER) takes place at the counter-electrode (mainly metals). In this case, n-type semiconductor is called photoanode



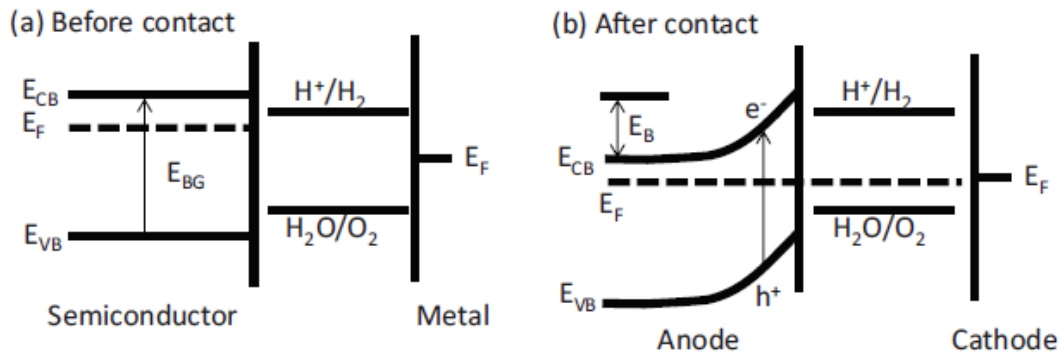
**Figure 7** Schematic on a water splitting diagram of a PEC cell consisting of the photoanode and the counter electrode.

If p-type semiconductor absorbs light, HER may also take place on a p-type semiconductor, a photocathode, where generated electrons are transported to the semiconductor-electrolyte junction thus reducing water to hydrogen gas. This p-type semiconductor is called photocathode. The conduction band edge of the photocathode has to be more negative than the hydrogen evolution potential. In both photoanode and photocathode, hydrogen and oxygen generation reactions are driven by minority carriers. An ideal water splitting system needs a tandem structure of photoanode and photocathode, which is illustrated in Figure 8.



**Figure 8** Energy diagrams of photoelectrochemical water splitting using a) a photocathode, and b) a photoanode and cathode in a tandem cell configuration.<sup>8</sup>

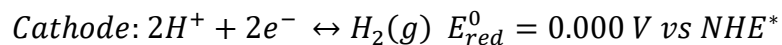
In order to be able to drive the water splitting reaction, not only the band gaps but also the relative position of the energy levels involved need to be well matched. Figure 9 (a) shows the energy diagram of a semiconducting electrode and a metal electrode before contact. Figure 9 (b) shows a change in the band diagram after the semiconductor surface contacts electrolyte. Fermi level alignment at the solid/liquid interface bends band edges of the semiconductors, which creates a main driving force for charge transport at the interface. When semiconductor electrodes absorb light, electron and holes are generated and one of them transports to the solid/liquid interface due to the band bending.

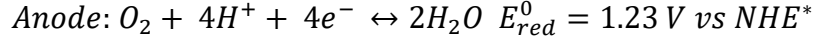


**Figure 9** Energy level diagram of the semiconductor/liquid/metal system (a) before contact and (b) after contact.

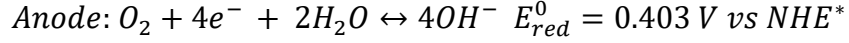
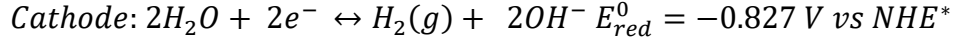
If the charge carriers reach the solid/liquid interface, it reacts with a water molecule, the possible water splitting half reactions and their redox potentials are given by;

When  $H^+$  activity is 1 ( $pH = 0$ )





When  $OH^-$  activity is 1 ( $pOH = 0$ )



### 2.1.2 Challenges

Several limitations of the PEC cell are attributed to physical properties of semiconductor photoelectrode and its interaction with the aqueous electrolyte. In an ideal condition, an electromotive force of the cell must be 1.23 V. The anode donates holes to water molecules, therefore produces oxygen gas and protons. These protons are reduced at the cathode where electrons have higher energy by 1.23eV. However, more EMF of PEC cell is required in real operation, due to a thermodynamic loss. At redox potential, the reactions are in equilibrium and a net reaction rate is zero. At room temperature 25<sup>0</sup>C (298 K) and concentrations (1 mol/L, 1 bar), thermodynamically the minimum applied electrochemical cell voltage  $\Delta E=1.229$  V corresponds to a  $\Delta G=+237$  kJ/mol H<sub>2</sub>. Considering the entropy term, the water-splitting reaction at the equilibrium state is a nonspontaneous reaction and thermodynamically uphill. Therefore, though the theoretical bandgap of the semiconductor for PEC is 1.23 V, a bandgap between 1.9 V and 2.0 V is needed to overcome the thermodynamic loss and proceed the reaction with fast reaction kinetics. However, if the bandgap is too large, the semiconductor absorbs only a part of the solar spectrum. Figure 10 shows the photon flux by solar irradiation and its relationship with photoelectrolysis.

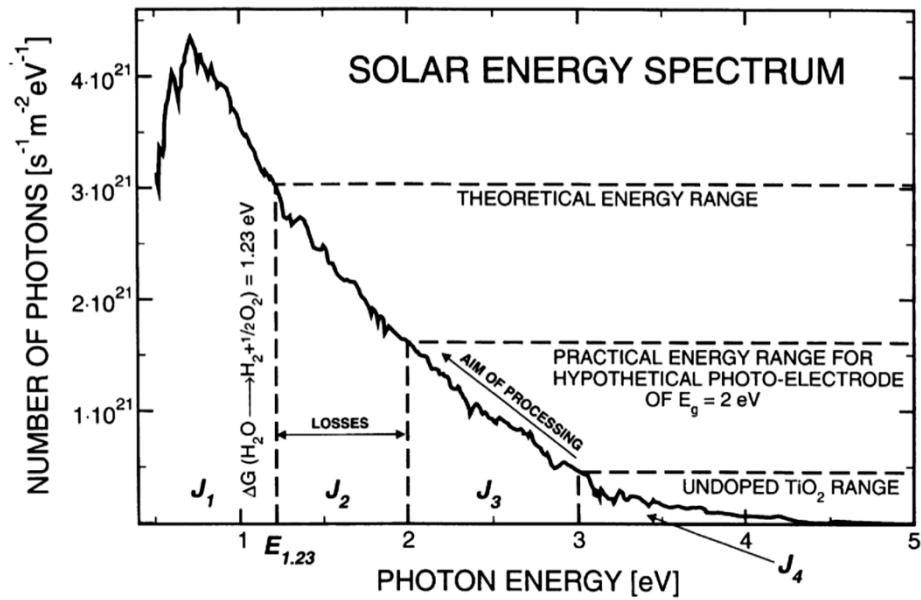


**Figure 10** Photon flux in the solar spectrum (AM1.5).

In addition to the bandgap, there are a few factors to be considered for semiconductors of PEC cell. First, high light absorption coefficient in the visible range is essential to take more photons using a same volume of materials. Second, the conduction and valence band edges must be well aligned with the oxidation and reduction potentials of water. The energy of the valence band edge should be lower than the oxidation potential for  $\text{H}_2\text{O}/\text{O}_2$  couple so that holes can be transferred into an aqueous electrolyte to generate oxygen. The energy of the conduction band must be higher than the reduction potential for  $\text{H}_2\text{O}/\text{H}_2$  couple so that electron is transferred into an aqueous electrolyte to produce hydrogen. Figure 11 shows the band edge positions of several semiconducting photoelectrodes and water splitting half reactions.

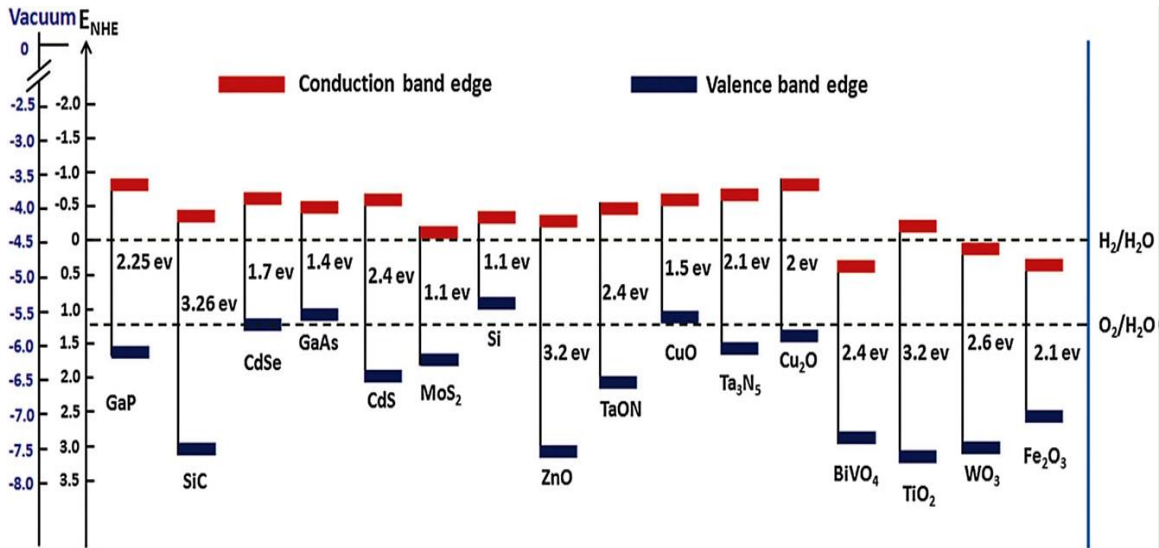


**Figure 11** Band edge positions of various semiconductors in contact with the aqueous electrolyte at pH=0 with respect to NHE and the vacuum level. For comparison water oxidation and reduction potentials are also depicted. (Adopted from literature <sup>9</sup>)

Besides the band gap size and band alignment restrictions, electric properties are also important such as efficient charge separation and transport of photogenerated charge carriers. Diffusion length of photogenerated carriers should be long enough so that minority carriers reach the semiconductor/electrolyte junction without losses such as charge recombination. Increasing the overlap of metal 3d orbitals with conduction band can enhance the lifetime. Corrosion resistance and stability of semiconductors in dark and light conditions are also important parameters for proper material selection. Water oxidation and reduction reactions can corrode the semiconductors and change their surface chemical composition. This leads to degradation of the photoelectrochemical properties. The corrosion problem makes conventional non-oxide solar cell materials such as GaAs, and GaP unsuitable for photoelectrochemical cells. Corrosion-resistant semiconductor metal oxides appear to be prominent photoelectrode materials. Another important

parameter is fast kinetics of carrier extraction reactions at the semiconductor/aqueous electrolyte. If not, holes or electrons are accumulated in the semiconductor surface.

Since the first report on a photoelectrochemical reactor of TiO<sub>2</sub>, several materials were selected and tested for photo-assisted water splitting reaction. In general, not a single type material can bear all the properties to meet conditions for efficient photoelectrolysis. The semiconductor and its interaction with electrolyte is the primary factor. Band gap, charge transport properties, stability are all important. Since the first PEC cell, there has been growing efforts to tuning electronic properties for efficient and economically viable cells.

### **2.1.3 Strategies for an Efficient Photoelectrochemical (PEC) Cell**

In order to improve total efficiency of photoelectrochemical water splitting systems possible strategies can be taken. First, it is necessary to develop a narrow bandgap semiconductor photoelectrode to absorb much more visible solar spectrum. Many ongoing efforts for improving stable wide bandgap semiconductors have been focused on extension of light absorption to visible region.<sup>10,11</sup> Efforts for narrower bandgap materials have focused on their stability in aqueous environment. On the other hand, fabrication of a tandem photoelectrode with doping or combining different semiconductors has also been extensively studied. Overall, these strategies can be summarized as follows:

- (i) Modification of the semiconductor with metal and/or nonmetal doping for narrower bandgap material: one of the most effective ways to modify the band gap of semiconducting material by creating impurity levels in the bandgap through ion doping, hence the large band gap material can benefit from visible light absorption. Figure 12

illustrates the scheme for how donor and acceptor ions function in wide bandgap of semiconductor material and a change results into visible light response of the wide band gap material in addition to UV light absorption.<sup>12,13</sup>

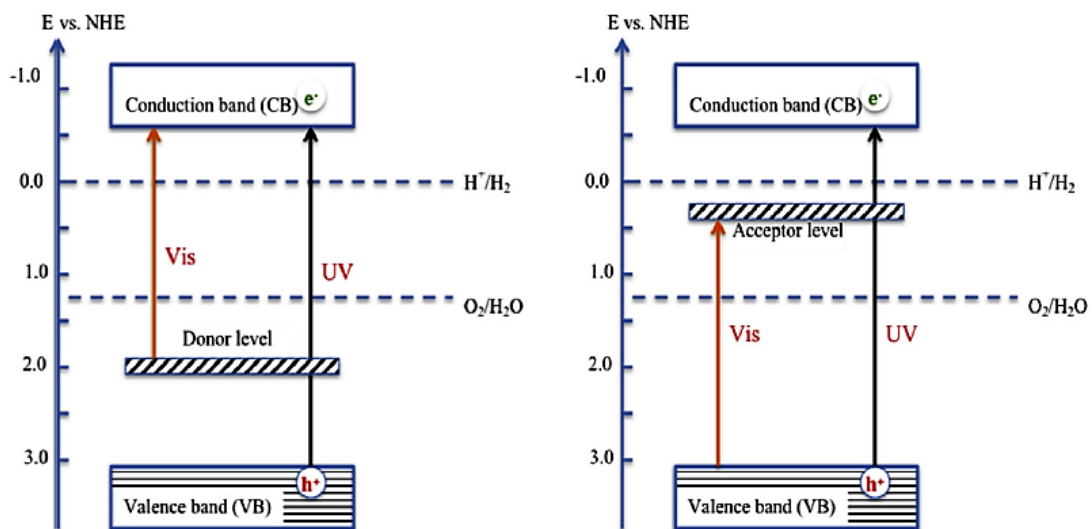


**Figure 12** Donor/acceptor level band gap modification formed by metal ion doping.

- (ii) Sensitization of the semiconductor photoelectrode with a compatible dye, quantum dots, or enhancement with a well-defined plasmonic nanoparticle: another powerful way of extending absorption spectrum range with suitable sensitizers such as dyes,<sup>14</sup> quantum dots,<sup>15</sup> and plasmonic particles.<sup>16</sup> Figure 13 illustrates how this sensitization works.

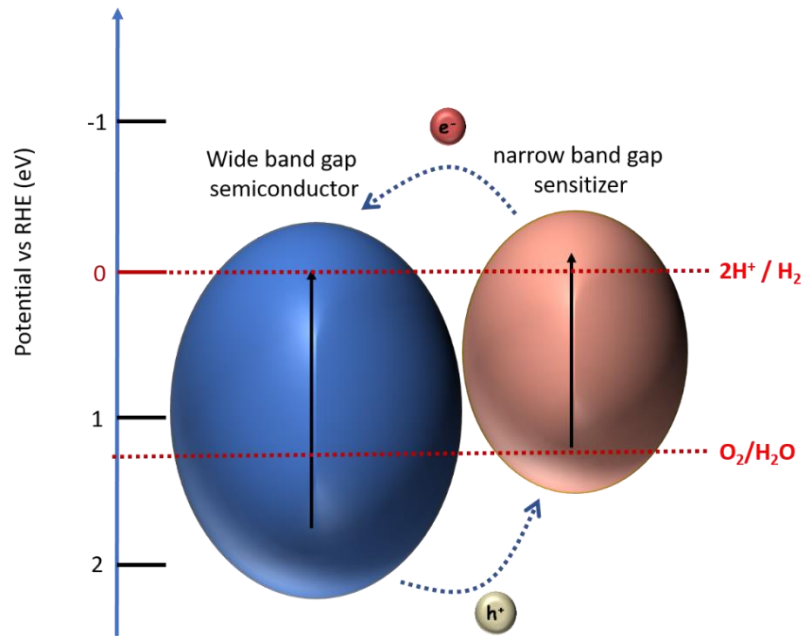


**Figure 13** Schematic illustration of the bandgap alignment between a wide bandgap semiconductor and a narrow bandgap sensitizer material. Sensitizer material enhances light absorption and enables easier electron transfer to the wide band gap semiconductor material.

- (iii) Fabrication of tandem or heterojunction cells by combining different bandgap semiconductors: employment of heterojunction structures is another way of benefiting properties of each component in the junction and reaching an improved overall efficiency. Several advantages accompany with formation of a heterojunction such as extension of solar light absorption, promotion of photo-generated charge carrier separation at the semiconductor/liquid interface, reduction of electron-hole recombination.<sup>17, 18</sup>

(iv) Modification of crystal structure and morphology of the semiconductor photoelectrode: modifying crystal structure mainly alters charge transfer and separation behavior of semiconductor material. In general materials crystallinity, defect structure, surface area, surface structure, and particle size are mainly important for efficient charge transport. Figure 14 shows examples of different types of nanostructures used as photoelectrodes in PEC systems.

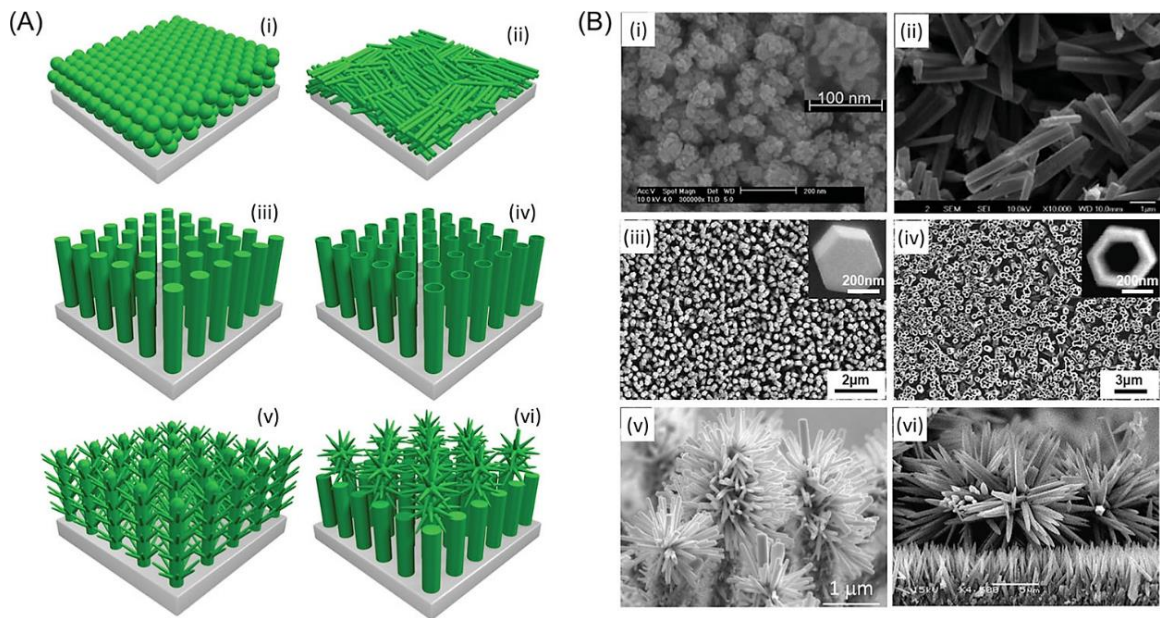


**Figure 14** (A) Scheme and (B) SEM images of different morphology of ZnO nanostructures coated on TCO substrate. (i) nanoparticles, (ii) disordered nanorods, (iii) array of nanorods, (iv) array of nanotubes, (v) array of nanoforests, (vi) array of bilayer nanostructures. (Adopted from literature <sup>19,20,21,22,23</sup> )

#### **2.1.4 Metal Oxide Semiconductors for Photoelectrochemical (PEC) Cell**

Various types of semiconductors have been used for photoelectrodes, amongst metal oxides draw attention a lot due to their chemical stability, suitable band edge positions, low cost and tunable bandgaps.<sup>24</sup> Oxides appear to be one of the most stable form of metal compounds in nature and can be synthesized via different methods. Generally, the VB and CB of metal oxides have O 2p character and transition metal (s, d, or p) character.<sup>25</sup> Combination of high ionic character of O 2p and electron rich metal orbitals leads to various types of metal oxides. In Figure 15, a typical PEC cell made by photoanodes of metal oxides coated on transparent conductive oxide materials (TCO) is illustrated. The rich diversity of metal oxides with multi-functional properties enable researchers to develop high performance PEC systems. Herein several outstanding semiconductor materials are evaluated and possible modification methods for an improved performance photoelectrochemical cell are explained.

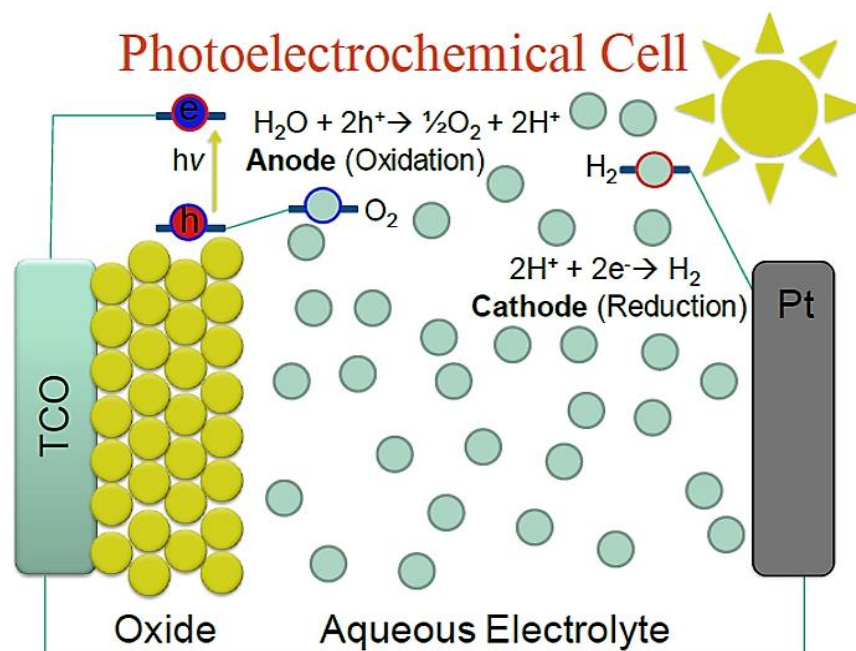


**Figure 15** A typical photoelectrochemical cell made of photoanode (semiconductor metal oxide material coated on transparent conductive oxide (TCO)), cathode (Pt), and aqueous electrolyte .

#### 2.1.4.1 Titanium dioxide ( $\text{TiO}_2$ )

Since the discovery of Fujishima and Honda in 1972, n-type  $\text{TiO}_2$  has become the most intensively studied system for photoelectrochemical water splitting. The electrochemically active phase of  $\text{TiO}_2$  are rutile which has a body-centered tetragonal structure, which is depicted in Figure 16. Therein  $\text{TiO}_6$  octahedra are connected by sharing one edge. Oxygen anions, on the other hand, show a coordination number of 3 with  $\text{OTi}_3$  trigonal planar slices.

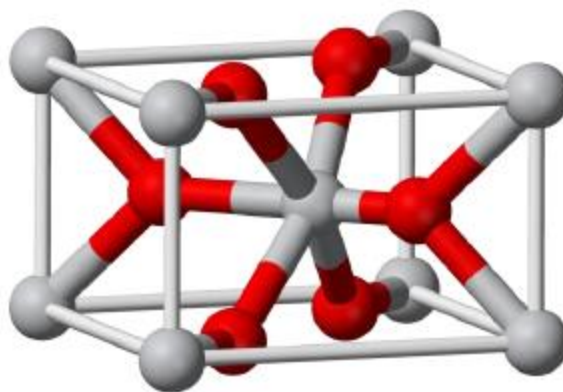


**Figure 16** Crystal structure of TiO<sub>2</sub> (rutile) unit cell

Photogenerated carriers on TiO<sub>2</sub> deliver enough energy to drive the overall water splitting reaction due to the favorable position of the valence and conduction bands. The chemical stability, abundancy and low production costs make TiO<sub>2</sub> attractive. The performance of TiO<sub>2</sub>, however, is limited due to its wide band gap (3.2 eV) and high electron hole recombination rate.<sup>26,27</sup> Many groups have demonstrated extension of the optical absorption spectrum edge of TiO<sub>2</sub> towards the visible range by doping transition metals such as iron or chromium or sensitizing TiO<sub>2</sub> with other low band gap semiconductors. Transition metal doping into TiO<sub>2</sub> leads indeed to the shift of absorption wavelength but does not result in the expected increase in efficiency, as impurity states act as recombination sites. In addition, various nanostructuring techniques have been applied to increase an active surface area and decrease the travel distance of photogenerated carriers to the semiconductor-electrolyte interface.<sup>28</sup> Different morphologies such as nanotubes, nanowires, nanoflakes, mesoporous and inverse opal films synthesized using different techniques such as sol-gel, chemical vapor deposition or electrodeposition. Combining nanostructured morphologies with selective doping can sufficiently enhance the photoelectrochemical performance of TiO<sub>2</sub>.

### 2.1.4.2 Bismuth Vanadate ( $\text{BiVO}_4$ )

$\text{BiVO}_4$ , a ternary metal oxide n type semiconductor has attracted a considerable amount of research interest in recent years as an attractive photoanode.  $\text{BiVO}_4$  has three main crystal structures, tetragonal zircon, tetragonal scheelite and monoclinic scheelite. Structures of zircon and scheelite are illustrated in Figure 17. Monoclinic scheelite  $\text{BiVO}_4$  is composed of non-interconnecting  $\text{VO}_4$  tetrahedra. 3d orbitals of V constitute the conduction band of  $\text{BiVO}_4$  and photogenerated electrons have to hop between  $\text{VO}_4$  tetrahedra in  $\text{BiVO}_4$ .

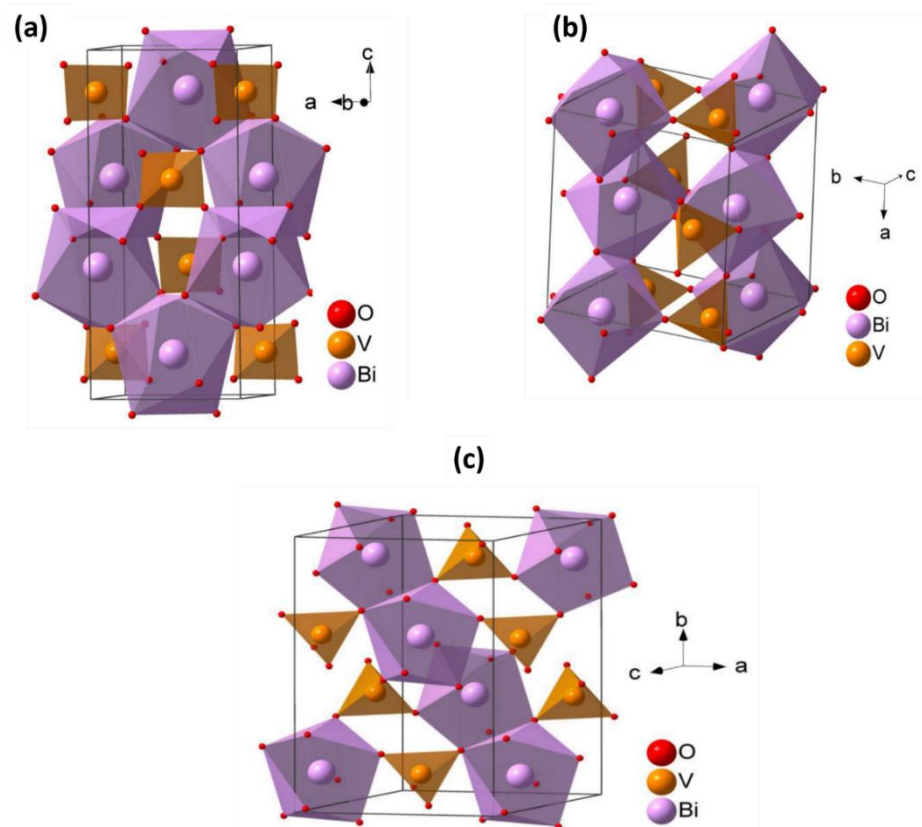


**Figure 17** Crystal structures of different  $\text{BiVO}_4$  polymorphs: (a) tetragonal scheelite and (b) tetragonal zircon, (c) monoclinic scheelite  $\text{BiVO}_4$

Scheelite-monoclinic  $\text{BiVO}_4$  (m- $\text{BiVO}_4$ ) appears to be the most important polymorph. m- $\text{BiVO}_4$  has n-type conductivity, bandgap of  $\approx 2.4$  eV and high photoactivity for  $\text{O}_2$  evolution. In contrast, the tetragonal zircon has band gap of 2.9 eV and its absorption band reaches near UV region. Band structures of monoclinic and tetragonal scheelite are compared in Figure 18.

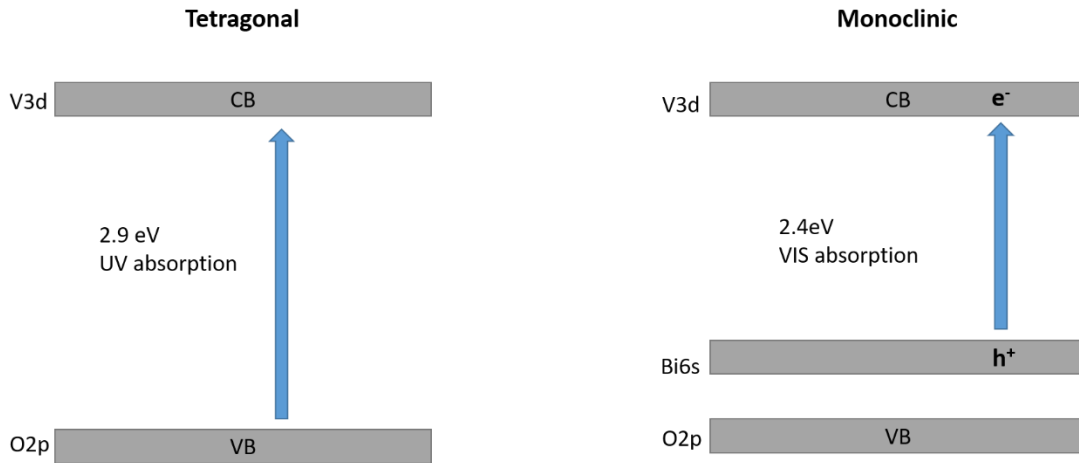


**Figure 18** The scheme of the  $\text{BiVO}_4$  tetragonal and monoclinic band structures

A theoretical maximum photocurrent density and a theoretical solar-to-hydrogen conversion efficiency is about  $7.5 \text{ mA/cm}^2$  and 9 % at AM 1.5 illumination condition for m- $\text{BiVO}_4$ .  $\text{BiVO}_4$  is cheap and abundant but suffers from poor electron transport and slow oxidation kinetics, requiring further modifications to assist in efficient photoelectrolysis. Bulk electron conductivity has been identified as one of major bottlenecks which limits the efficiency of the photoelectrochemical reaction. This limitation can be overcome by doping Mo and W. Impurities can increase the electron density, thereby improving the conductivity of  $\text{BiVO}_4$ . Recently  $\text{BiVO}_4$  has been reported to have the smallest onset potential of photocurrent for water oxidation among

all the reported visible light absorbing n-type photoanodes due to its favorable band edge alignment with the water redox potentials.<sup>29</sup> Oxygen evolution reaction (OER) is considered to be a rate determining step for water splitting. Therefore, BiVO<sub>4</sub> photoanodes of an excellent OER ability has increased an overall solar to fuel conversion efficiency of monolithic devices to 5 %. An obvious disadvantage of BiVO<sub>4</sub> is a low CB edge energy level. Increasing the energy level of CB edge is needed. Moreover, the poor charge transport limits separation of the photoinduced charge carriers, thus leading to poor photoactivity. To improve PEC performance, prolong photogenerated charge carrier lifetime and improve the photoinduced charge carrier separation, heterojunction structures such as WO<sub>3</sub>/BiVO<sub>4</sub>, SnO<sub>2</sub>/WO<sub>3</sub>/BiVO<sub>4</sub>, BiVO<sub>4</sub>/Co<sub>3</sub>O<sub>4</sub>, and Bi<sub>2</sub>O<sub>3</sub>/BiVO<sub>4</sub> have been studied.<sup>30</sup>

#### **2.1.4.3 Tin dioxide (SnO<sub>2</sub>)**

The material of choice in this work was tin (IV) oxide. It is a wide (direct) band-gap, n-type semiconductor with a bandgap of 3.6 eV at room temperature. The mineral form of SnO<sub>2</sub> is called cassiterite (in German, common names are Kassiterite or Sperlingschnabel). The unit cell contains two tin cations and four oxygen anions. The Sn<sup>4+</sup> cations are coordinated by six O<sup>2-</sup> anions, forming slightly distorted octahedra, whereas the oxygens are surrounded by three tin ions, forming an almost regular triangle, its crystal structure is shown in Figure 19. The electronic structure of SnO<sub>2</sub> is a key factor for optoelectronic device fabrication. 1D nanostructures have unique electronic, optical, and mechanical properties due to their low dimensionality and the quantum confinement effect.<sup>31</sup> 1D SnO<sub>2</sub> can be fabricated in different forms of tubes,<sup>32</sup> belts,<sup>33</sup> rods, wires<sup>34</sup> and sheet, and these structures with high aspect ratio offer better crystallinity, higher integration density, and

lower power consumption. 1D SnO<sub>2</sub> nanostructures have been synthesized by a variety of techniques such as electrodeposition,<sup>35</sup> hydrothermal treatment,<sup>36</sup> thermal decomposition and thermal evaporation,<sup>37</sup> and template free synthesis.<sup>38</sup>

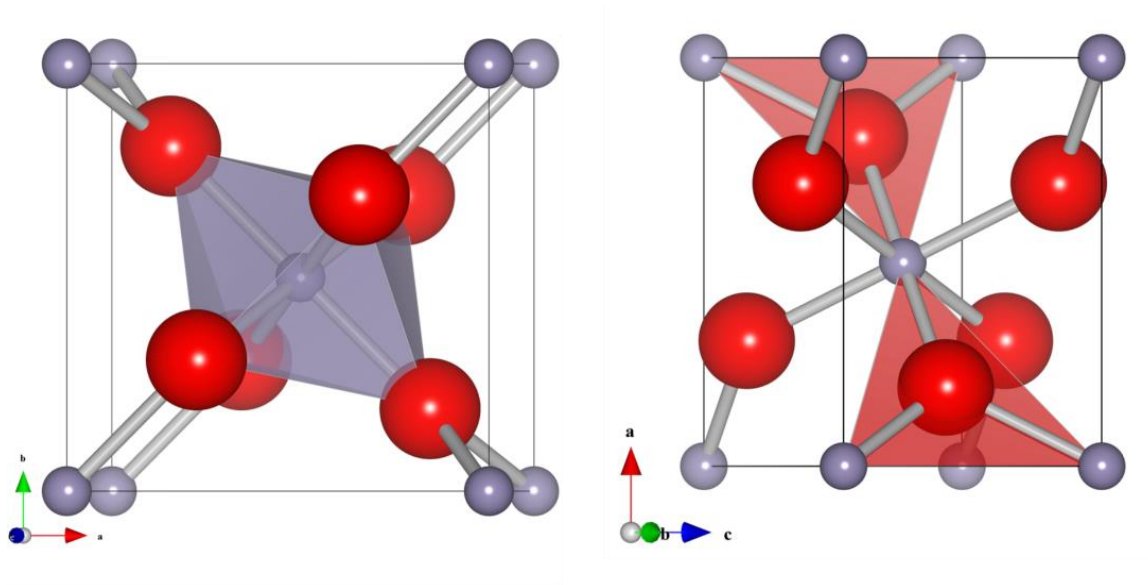


**Figure 19** Unit cell and coordination polyhedral of SnO<sub>2</sub>: (a) Octahedral coordination of tin cations; (b) Triangle around the oxygen anions.

This material has been used as a key functional material for various applications such as gas sensor<sup>39</sup>, optoelectronic devices<sup>40</sup>, catalysts, transparent conducting electrodes,<sup>41</sup> and antireflecting coatings. SnO<sub>2</sub> based transparent conductive oxide materials (TCO) can be beneficial due to high conductivity and large band gap and it is a low-cost alternative to indium tin oxide films in various optoelectronic devices. Advantages of nanostructures such as SnO<sub>2</sub> nanowires/nanobelts/nanorods, make SnO<sub>2</sub> as an ideal alternative material for optoelectronic devices, due to better electron mobility,  $\sim 100\text{-}200\text{ cm}^2\text{ V}^{-1}\text{ s}^{-1}$  and electronic conductivity which is

much higher than that of TiO<sub>2</sub> (~0.1-1 cm<sup>2</sup> V<sup>-1</sup> s<sup>-1</sup>) and photo-stability compared to TiO<sub>2</sub>, and it has a more negative conduction band edge (0.40 eV, compared to anatase TiO<sub>2</sub>) assisting efficient charge injection and charge collection from the photosensitizer. SnO<sub>2</sub> gets less attention in PEC hydrogen production than that of TiO<sub>2</sub>, because the conduction band edge of SnO<sub>2</sub> is lower than the reduction potential of water. One potential solution to this problem is to make the type II band alignment by connecting SnO<sub>2</sub> and TiO<sub>2</sub>. SnO<sub>2</sub>/TiO<sub>2</sub> heterojunction is a promising photoelectrode for solar cells,<sup>42</sup> photocatalysis,<sup>43</sup> and photoelectrochemical water splitting reactions.<sup>44</sup> Moreover, one-dimensional metal oxide architectures can promote the charge transport behavior and improve the charge collection efficiency. Charge carriers, with minimum recombination losses, can be separated across the metal oxides interfaces of appropriate positions. Therefore, utilization of various 1D metal oxide nano-architectures and heterojunction of them with different semiconducting light absorbers can lead to a superior hetero-nanostructure which provides efficient charge separation, with minimum recombination losses, and as results higher power conversion efficiencies can be achieved.

#### **2.1.4.4 Advanced Nanostructured Metal Oxide Semiconductors for Energy Applications**

Previously described energy devices will be benefited from better design of material properties. Most commonly used semiconductors for photovoltaic applications suffer from poor charge carrier transport properties and limited absorption which limits the resultant device's energy conversion efficiency. On the other hand, materials used for other energy devices such as batteries, supercapacitors, and fuel cells experience inadequate energy/power output because of poor charge and mass transport properties and high cost and complex fabrication processes. As a result,

advanced nanostructured metal oxide materials show up as a promising material in the fields of photovoltaics, semiconductors, and renewable energy. These nanomaterials can show wholly different characteristic properties compared to the ordinary bulk counterparts. Nanostructured metal oxide nanostructures have attained great interest in energy related applications since they can overcome the limitations of the standard electrodes and can show high conductivity, charge carrier mobility, low charge recombination rates, and high crystallinity. Besides metal oxide nanostructures are one of the most widely available materials on Earth due their unique shapes, compositions, chemical and physical properties, making them spotlight of present research efforts in nanomaterials science.<sup>45</sup> As previously mentioned they have been widely used in energy related applications such as Lithium ion batteries,<sup>46</sup> fuel cells,<sup>47</sup> solar cells,<sup>48</sup> transistors/FETs,<sup>49</sup> light emitting devices,<sup>50</sup> hydrogen production by water photolysis, electrolysis and its storage,<sup>51,52</sup> water and air purification by degradation of organic/inorganic pollutants,<sup>53,54</sup> gas, humidity and temperature sensors,<sup>55,56</sup> and photodetectors.<sup>57</sup>

There are several methods for producing well defined nanostructured metal oxide semiconductors. Nanostructured metal oxide semiconductors can be deposited on any type of substrate such as metals, semiconductors, polymers, flexible substrates. Depending on fabrication process different shapes and morphologies of metal nanostructures can be synthesized such as nanowires, nanorods, nanotubes, nanocombs, nanorings, nanohelices, nanosprings, nanocages, nanosheets and nanostars.

The deposition techniques can usually be divided into two main categories as chemical and physical deposition methods. Pulsed laser deposition (PLD), molecular beam epitaxy (MBE), and sputtering can be categorized into physical deposition techniques. Whereas, chemical methods are mainly gas phase deposition methods and solution techniques such as chemical vapor deposition

(CVD), metal organic chemical vapor deposition (MOCVD), atomic layer deposition (ALD), while spray pyrolysis, sol-gel, spin- and dip-coating methods. Different methods come with both advantages and disadvantages depending on ease of use, cost, time, and quality and quantity of growth.

Sputter deposition is a common method of metal oxide film deposition. It involves bombardment of a target (metal or metal-oxide) with a plasma (usually a noble gas, such as Argon). The main advantage is low operating temperature which makes sputtering one of the most flexible deposition techniques. When an energetic particle strikes a surface (the target), a plume of material is released, like the shower of sand when a golf ball lands in the bunker. This effect is known as 'sputtering' and is a good method for depositing smooth, uniform films that exhibit good adhesion to the growing substrate. Film grown rate is well controllable allowing the reproducibility of the samples thickness. Growth rate are also high and comparable to evaporation techniques.

Pulsed laser deposition (PLD) has been used to deposit films of a variety of materials. It is a promising technique to develop complex-oxide heterostructures, superlattices, and well-controlled interfaces. Figure 20 shows a typical PLD system. Pulsed beam of a high power ultraviolet laser is focused on a target inside a vacuum chamber. The target is usually sintered ceramics and the chemical composition of the target is same as that of the film to be deposited. A significant removal of material occurs in the target above a certain threshold energy density of the laser (depending on the material, and laser wavelength and pulse duration). Pulses of the focused laser transform the removed solid to plasma. Expansion of the ablated material cools the plasma and reverts it to gas that is carried to the substrate where the delivered material condenses to solid and the film growth happens. The crystal structure and orientation of films grown by PLD are highly dependent on a thermodynamic stability. In PLD, the precise control of the processing

parameters (such as species fluxes) is also difficult to realize, which is helpful for understanding the nucleation and growth mechanisms of thin films.

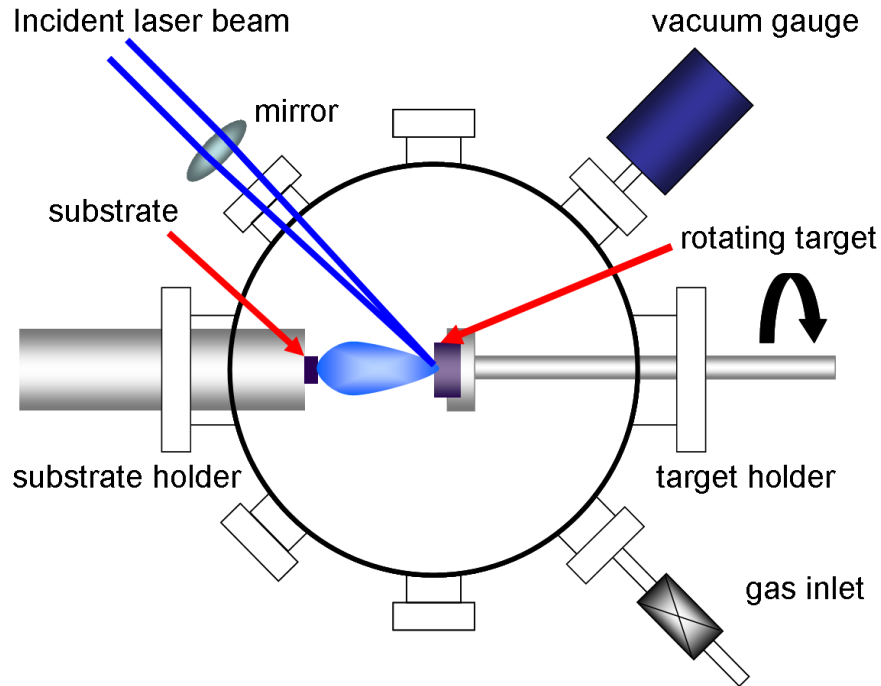


**Figure 20** Schematic illustration of the pulse layer deposition (PLD) system used for thin films depositions.

Chemical vapor deposition (CVD) is another widely used materials-processing technology. In Figure 21 common CVD system is shown, where a precursor gas or gases flow into a coating chamber. Chemical reactions occur on and near hot substrate surface, resulting in the deposition of a thin film on the substrate. By-products of the chemical reactions are exhausted out of the chamber along with unreacted precursor gases. Precursor molecules must have high vapor pressure so that source gas is transported to the reaction chamber. In addition, evaporated precursor gases

must have high thermal stability to prevent particle formation in the gas phase. In this method, controllable film growth rate and smooth films are attainable. CVD is done in hot-wall reactors and cold-wall reactors, at sub-torr pressures to above-atmospheric pressures, with and without carrier gases, and at temperatures typically ranging from 200-1600 °C. CVD processes can be categorized according to a type of: (i) application, (ii) process and reactor used, or (iii) precursor and chemical reaction used. Derivatives of CVD terminology are metal-organic chemical vapor deposition (MOCVD) or, less commonly, organo-metallic chemical vapor deposition (OMCVD).

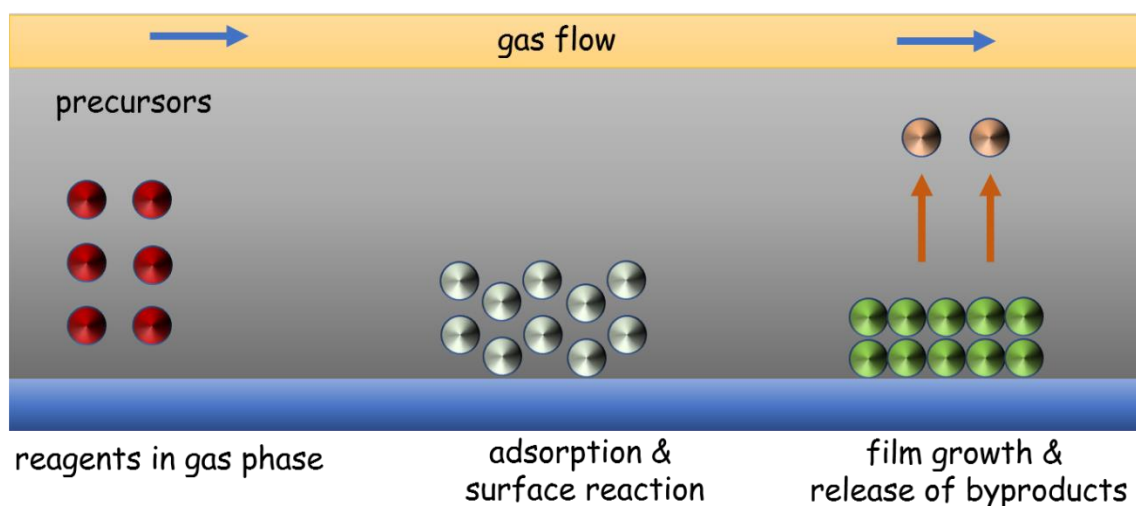


**Figure 21** Schematics of steps of Chemical Vapor Deposition (CVD)

Atomic Layer Deposition (ALD), also known as atomic layer epitaxy (ALE) or atomic layer chemical vapor deposition (ALCVD), is a vapor phase technique to deposit thin films layer-by-layer. ALD was developed in Finland in 1970s by T. Suntola. Figure 22 shows schematics of ALD process. In ALD reactant gases are sequentially introduced to a chamber and thin film grows on substrate surface through self-limiting surface reactions. This results in highly uniform and

conformal film with an accurately controlled thickness. In particular, sequential, self-limiting reactions of ALD offer exceptional conformality on high-aspect ratio structures, thickness control at Angstrom level, and tunable film composition. Reactant species are enabled to reach into open cavities and evenly cover complicated structures. ALD technique allows depositing a wide variety of compounds such as oxides, nitrides and sulfides, as well as pure metals.

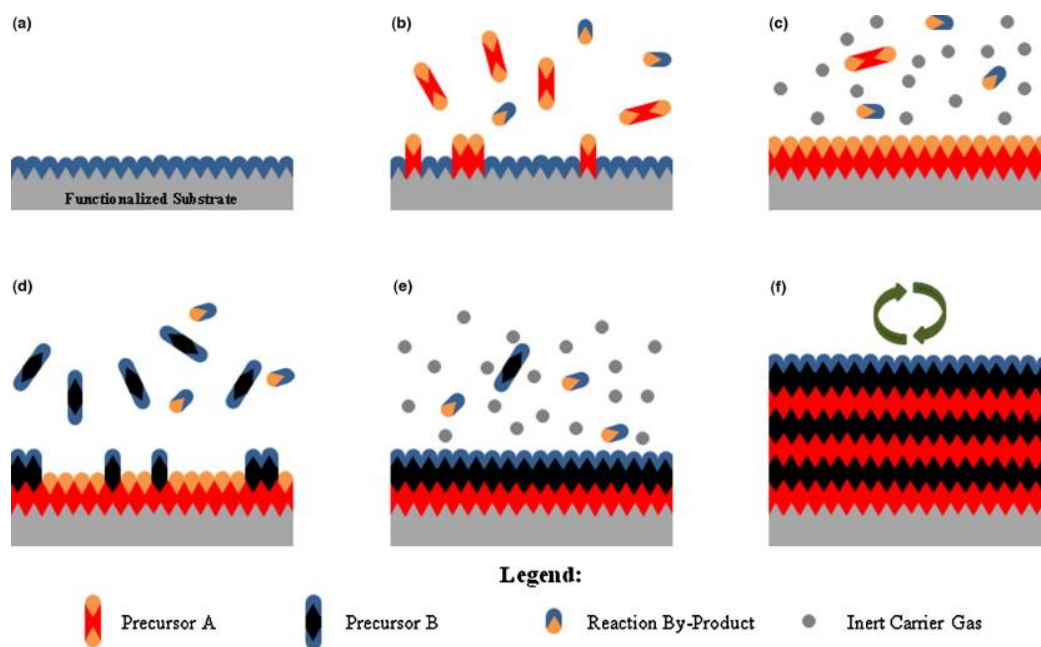


**Figure 22** Schematic of ALD process. (a) Functionalized substrate surface. (b) Pulse of precursor A and reaction at the surface. (c) Excess precursor and reaction by-products are purged with inert gas carrier. (d) Pules of precursor B and reaction at the surface. (e) Excess precursor and reaction by products are purged with inert carrier gas. (f) Sequential steps in order to have desired material thickness and film quality. (Adopted from literature<sup>58</sup> )

Electrodeposition is a facile method for achieving high quality films at low temperatures and low production cost. In an electrodeposition process, ions drift in an electrolyte solution by applying electric field and reduced to thin film on a top of metal substrate. Numerous non-oxide (group III-V, II-IV) and oxide semiconductors (oxides of Ni, Cu, Zn, Fe, Mn, Ti, W) have been prepared by electrodeposition. These thin films have many applications including transistors, piezoelectric devices, gas sensors, electrocatalysis, and solar water splitting.<sup>59</sup> Binary oxides, mixed oxides and metal/oxide nanocomposites have also been prepared by the electrodeposition method. Basic steps of the electrodeposition are 1) a heterogeneous electron transfer step between WE and electroactive species and 2) a transition of metal ions into crystalline material by a reduction reaction. Electrodeposition of metal oxides is mainly performed in alkaline aqueous solutions containing ionized metal complexes. Major processing variables to control the composition, morphology and spatial orientation of electrodeposited films are pH, electrolyte composition, current density, potential, temperature, annealing conditions, etc. Precise tuning of these variables can optimize growth direction, morphology and crystallinity of thin films.

Advantages of electrodeposition techniques are:

- i. Deposition temperature is low (Since a maximum deposition temperature is usually limited by the boiling point of the electrolyte, molten salts are used to increase the deposition temperature.)
- ii. Products of redox reactions are tuned by changing electric potential or current.
- iii. Composition and quality of deposited films are controlled by changing the composition and viscosity of electrolyte.
- iv. Simple experimental setup can provide high quality films at low cost.

The simplest form of the electrodeposition cell is 2-electrode system that consists of a cathode and an anode. In the 2-electrode system, voltage is measured between these electrodes, and current is measured anywhere in the circuit. However, the most commonly used method is using 3-electrode system composed of the following:

- i. Working electrode (WE): this is anode of the cell and an electrically conducting substrate for film deposition is normally used as WE,
- ii. Counter electrode (CE): this is cathode of the cell and a plate or wire of inert metal such as Pt or Au is used as CE,
- iii. Reference electrode (RE): this is standard electrode composition and used to measure absolute potential of WE,
- iv. Electrolyte solution: this contains electrolyte, electroactive ions, and additives to maintain pH of the solution stable

A schematic diagram of a general 3-electrode electrodeposition system is shown in Figure 23.

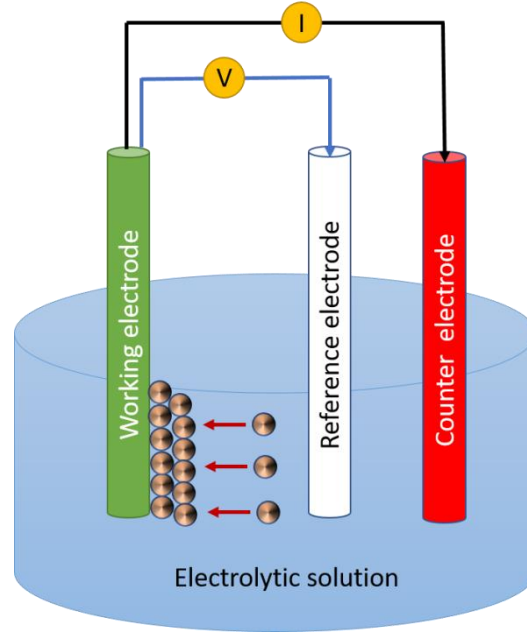


**Figure 23** Illustration of how electrochemical deposition works in a 3-electrode system

## 2.1.5 Promising Methods to Improve Overall Photoelectrochemical (PEC) Cell Efficiency

### 2.1.5.1 Plasmonic Photovoltaics

Photovoltaics still need several innovations to reduce cost and accomplish grid parity. Major requirements are to choose earth abundant semiconductors and decrease the semiconductor volume. Important progress can be made by developing thin-film devices. In addition to lower material cost, thin semiconductor films can suppress the electron-hole recombination. However, a decrease in the thickness of light absorber reduces the amount of absorbed light.<sup>60</sup> In Figure 24, the light absorption spectrum of 2  $\mu\text{m}$  thick silicon film is shown. Light is poorly absorbed in such a thin-film photovoltaic device; as a result, the overall efficiency goes down. In this case, there is

a tradeoff between semiconductor bulk for full absorption and semiconductor film for negligible carrier recombination and low material cost. In this regard, additional light trapping techniques appears to be a proper solution for an advanced light management of thin semiconductor films. Thus, thin films absorb more light and at the same time their good charge transport behavior is retained. Employment of plasmonic nanoparticles is a prominent way of enhanced light trapping in thin film photovoltaics.

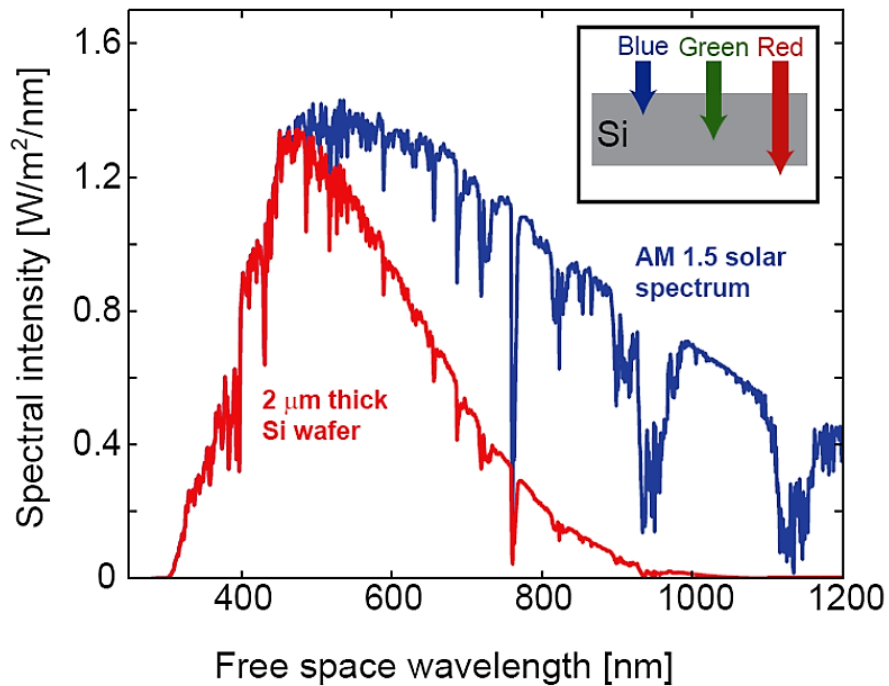


**Figure 24** Solar spectrum absorbed in a 2 mm thick Si. (Adopted from literature<sup>60</sup>)

Plasmonic nanostructures concentrate electromagnetic fields, scatter electromagnetic radiation, and convert the energy of photons into heat. Surface plasmons indicate an electromagnetic wave mode that can exist on metal/dielectric interface or inside metallic nanostructures. Energy of incident light can be transferred to evanescent waves by surface

plasmons. If semiconductor is next to metal nanostructures, the energy of the surface plasmons can be absorbed by the semiconductor. In solar cells, it is highly desirable to excite surface plasmons with visible light. Surface plasmons can be classified into two groups: (i) propagating surface plasmon polaritons (SPPs), and (ii) non-propagating localized surface plasmon resonances (LSPRs). Figure 25 shows SPP and LSPR mechanisms. In SPPs, the resonance wave propagates along the metal/dielectric interface where a pair of electric fields decay exponentially along a normal direction of the interface. In order to get SPPs excited, attenuated total internal reflection or grating coupling methods are used. LSPRs are non-propagating excitations of conduction electrons within a metal nanostructure. A typical example of LSPRs is to illuminate metallic nanoparticles with light of a resonance wavelength. Then both absorption and scattering of metal nanoparticles are greatly enhanced.

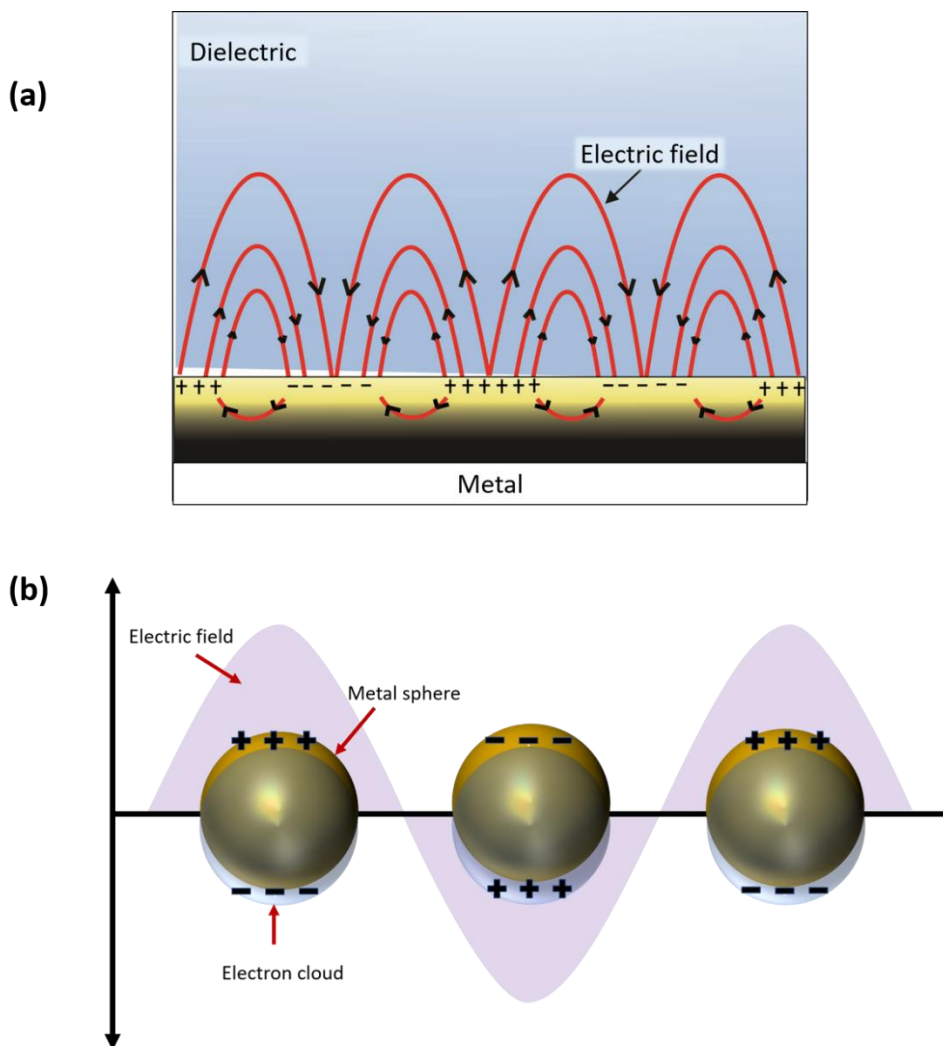


**Figure 25** Schematic diagrams illustrating (a) a surface plasmon polariton (SPP), and (b) a localized surface plasmon resonance (LSPR).<sup>61</sup>

Strong electric field of the surface plasmons increases light absorption in visible and infrared regions. Understanding the fundamental mechanisms behind plasmonic metal nanoparticle / semiconductor interaction is essential for this change in electric field. Figure 26 shows how this change in the electric field can improve a water splitting reaction depending on

where the plasmonic metal nanoparticle is placed whether it is in direct contact with the semiconductor or separated from the semiconductor with an insulating layer.

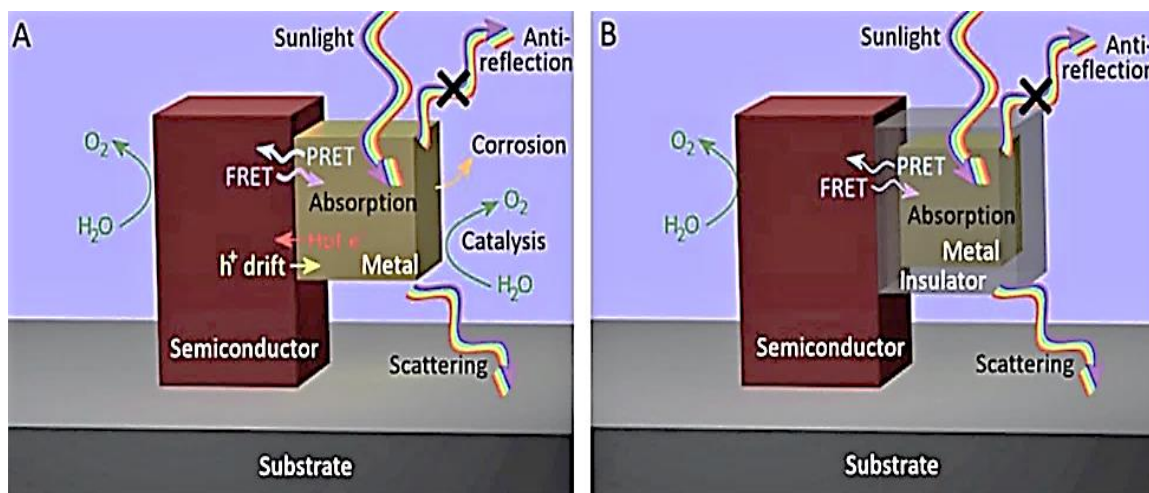


**Figure 26** Schematics for several energy transfer mechanisms in a plasmonic solar water splitting system. N-type semiconductor nanostructure in contact with (a) pure metal nanoparticle, and (b) metal core – insulator shell nanoparticle. (adapted from literature <sup>62</sup>)

Firstly, three main steps take place in the interaction of light with semiconductor electrode; absorption by semiconductor, excitation of a plasmonic resonance, and reflection of light. Later, surplus energy of excited electrons in the metal nanostructures can be transferred to the neighbor semiconductor to trigger plasmonic resonance effect in metal nanoparticle within the composite electrode. The plasmonic resonance can follow different pathways;

- i. It can be re-radiated (scattering); when a surface plasmon resonance decays, light can be scattered or absorbed. Scattering enables controlling of the flow of electromagnetic energy in a water splitting device. Scattering of light at the surface of the semiconductor can also increase the light's path length through the semiconductor, which is very

- essential for thin films with small absorption. In generally scattering occurs into a material with higher dielectric constant, and this scattering can be tuned depending on the position of plasmonic particle and semiconductor.
- ii. Energy transfer to the semiconductor PRET (plasmon resonance energy transfer); an important characteristic of a surface plasmonic particles is considered as a reaction of the surface plasmon to excite an electron-hole pair within semiconductor. When the plasmonic particle is in contact with semiconductor, plasmonic particles near field act as a light concentrator and locally enhance the electron-hole generation rate within the semiconductor. This PRET enhancement is effective only for plasmonic particles having resonance frequency that corresponds to the band gap of the semiconductor.
  - iii. Production of hot  $e^-$  in which these hot electrons injected into the semiconductor or couple to phonons and thermalize. When a plasmon is neither scattered nor undergoes PRET, it will be absorbed by the metal nanoparticles, producing hot electrons or holes. When these hot electron/hole has a sufficient energy and are in contact with an n-type semiconductor, they can be transferred into the conduction band of the semiconductor where they can take place in the corresponding water splitting half reaction.<sup>63</sup>

### **2.1.5.2 Metal Chalcogenide Sensitization**

Widely studied metal oxide semiconductors are  $\text{TiO}_2$ ,  $\text{ZnO}$ ,  $\text{Fe}_2\text{O}_3$ , and  $\text{WO}_3$  due to their favorable band edge position, excellent chemical stability, and large photo-corrosion resistance and low cost, which are summarized in Table 1. However, PEC performance of typical metal oxide semiconductors suffers from two major problems: limited visible light absorption due to large band

gap which restricts light in UV region and fast recombination of photogenerated charge carriers because of short diffusion lengths of photogenerated carriers. Utilization of narrow band gap semiconductor materials such as CdS,<sup>64</sup> CdS,<sup>65</sup> CdS/CdSe,<sup>66</sup> CdTe<sup>67</sup>, PbS,<sup>68</sup> and PbSe<sup>69</sup> appear to be a prominent solution to address this problem.

**Table 1** Energy band parameters of most commonly used materials for sensitization

<b>Semiconductors</b>	<b>Band Gap (eV)</b>	<b>Conduction Band Edge (eV)</b>	<b>Valence Band Edge (eV)</b>
<b>CdS</b>	2.4	-3.98	-6.38
<b>CdSe</b>	1.74	-4.1	-5.84
<b>TiO<sub>2</sub></b>	3.2	-4.21	-7.41
<b>SnO<sub>2</sub></b>	3.5	-4.5	-8
<b>ZnO</b>	3.2	-4.19	-7.39

Associated with a well-defined nanostructure (nanowire, nanorod, nanoparticle), and sensitization of narrow band gap materials; as a result, having a multiple-component semiconductor nanostructure is the most potential way to achieve combination of large light absorption (both in visible and ultraviolet), fast charge carrier transportation, and well-matched energy levels simultaneously, consequently an improved PEC water splitting performance. Various combinations of deposition sequences can be employed to design optimum

photoelectrochemical performance heteronanostructures. For direct growth, chemical batch deposition (CBD),<sup>70</sup> successive ion layer deposition (SILAR)<sup>71</sup> and electrodeposition (ED)<sup>72</sup> methods are preferred because of their simplicity and convenience. A fabrication process of heterogeneous structures by common sequential or simultaneous deposition techniques is illustrated in Figure 27.

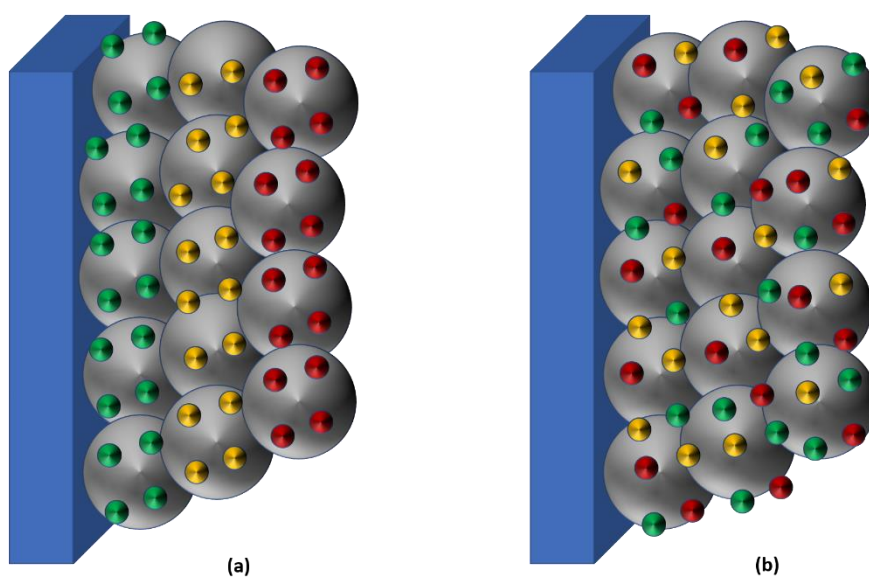
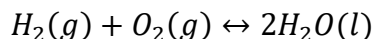


**Figure 27** Schematic illustration of multicomponent heteronanostructures formed by (a) sequential and (b) simultaneous deposition of narrow band gap materials with different light absorbing regions: green (495-570nm), yellow (570-590 nm), red (620-750 nm).

## 2.2 HYDROGEN EVOLUTION REACTION (HER)

### 2.2.1 Hydrogen as a Fuel

Greenhouse gas formation is currently a major global concern. Toxic NO<sub>2</sub> and SO<sub>2</sub> (which can cause acid rain) are formed in the combustion of fossil fuels, as well as man-made CO<sub>2</sub> which has been largely attributed to be the cause of global warming, an environmental and political issue. A further disadvantage of using fossil fuels is their non-renewability which will lead to eventual depletion of available sources, which may start in as early as 2050 in the case of petroleum. Hence, catalysts which promote PEC splitting of water at low cost become more important to decrease the dependence on fossil fuels. In addition, an alternative to the internal combustion engine (i.e. the common petrol or diesel engine) used in the vast majority of automotive vehicles, is a fuel cell which requires hydrogen as a fuel and good catalysts for hydrogen or dissociation. They are PEMFCs (polymer electrolyte membrane fuel cells), SOFCs (solid oxide fuel cells), MCFCs (molten-carbonate fuel cells), PAFCs (phosphoric acid fuel cells) and AFCs (alkaline fuel cells). The advantage of these fuel cells includes a more environmentally friendly fuel than combustion engines. The overall reaction in a hydrogen fuel cell can be given by the following equation:



By-product of the reaction is pure water, making the fuel cell leave no pollution. This is another strength in comparison to burning fossil fuels.

### 2.2.2 Electrocatalysis

Catalysis appears to be one of the most important part of green chemistry processes, it basically serves as crucial role in almost all industrial chemical processed and basic natural processes in life. Typically, a catalytic process can be described as where a tiny amount of an alien material can change the rate of a chemical reaction without being consumed and the remaining parts for the overall chemical reaction is unchanged. As illustrated in Figure 28, firstly the reactants are adsorbed on the surface of suitable catalysts. Then those species undergo a chemical reaction to form a product with assistance of catalysts and the catalysts itself are regenerated at the end of an overall process.

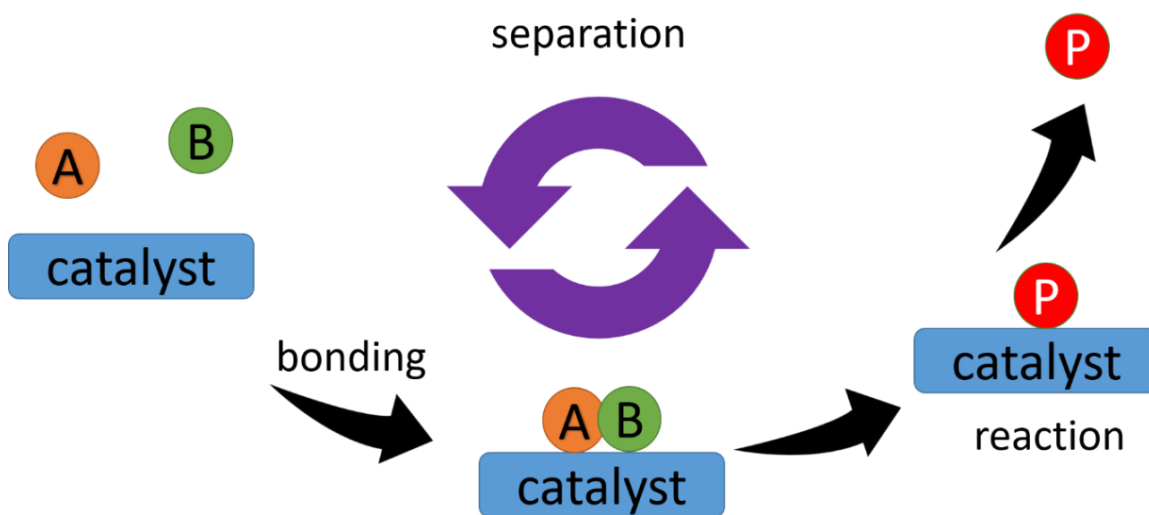


**Figure 28** Schematic illustration of a catalytic process. A and B react on surface of catalyst and product P is formed, and the cyclid is regenerated with separation of catalyst.

There are numerous advantages that a catalyst can offer to a given reaction system:

- i. Promotion of an energetically more favorable alternative pathway for a given reaction.
- ii. Lowering activation energy significantly compared to uncatalyzed reaction.
- iii. Significant impact on the kinetics of a reaction but no change in equilibrium constant for a thermodynamically favorable reaction. Therefore, no change in overall Gibbs free energy.
- iv. Catalysts can be utilized in different mediums such as liquids, gases or at the surface of solids.

Electrochemical reactions are widely used in large-scale industry in order to transform electrical energy into chemical energy. Utilization of a proper catalyst can also be good way of increasing the rate of electrochemical reactions. There is a type of catalysts, named as electrocatalysts. Today, the electrocatalysis is extensively used in electro-organic synthesis, high-tech electrochemical reactions, electrochemical sensors, fuel cells, and battery applications.<sup>73</sup> This process takes an important part of clean energy technologies such as fuel cells, water electrolysis cells, and CO<sub>2</sub> to fuel conversion systems.<sup>74</sup> Especially for the water splitting reaction, oxygen evolution reaction (OER) and hydrogen evolution reaction (HER), electrocatalysts play a crucial role and there has been extensive research on affordable materials which decreases the overpotential of the reaction as much as platinum and palladium.

Numerous factors can influence the overall performance of the electrocatalysts:

- i. Activity: The catalytic activity of the catalyst to increase rate of reaction. In general adsorption and desorption rates of reactants and products is crucial for the activity of a catalyst.

- ii. **Selectivity:** Most of electrocatalysts able to promote only the rate of a particular reaction to yield particular products and excluding other undesired reactions and products. Selectivity is sometime considered to be more important than activity and sometimes it is more difficult to achieve.
- iii. **Conductivity:** Most electrochemical reactions take place at the interface between an electronic and ionic conductor, such as solid/liquid, solid/polymer, solid/solid. Electric conductivity of electrolytes and electrocatalysts is important for the overall electrocatalytic performance. The conductivity of electrolyte can affect charge diffusion and accumulation at the interface. The electronic conductivity of the electrocatalyst loaded on electrode is also substantially important for overall electrocatalytic processes.
- iv. **Stability:** In addition to the electrocatalytic activity and electronic conductivity, the chemical stability of the electrocatalyst is also crucial for a specific electrochemical reaction. Especially for large scale industrial applications, the stability is a very important property of electrocatalysts and is still quite challenging for electrocatalysts. In general, the overpotential of the catalytic reaction should not increase even after long-term operation.
- v. **Electronic structure:** The activity and selectivity of an electrocatalyst is very much related with the electronic band structure of the material. The binding energies, especially for metals because of wide variety of oxidation states and electron accommodation abilities in their d-band, may vary since neighboring metals in the periodic table can exhibit a difference in binding energy for a given adsorbate, which means that while one metal might be chemically inert for a particular

catalytic transformation, its first neighbor in the periodic table might be very reactive and efficient in that reaction. For a given electrochemical reaction, reaction rate on a substrate having different d-band character and work function can be theoretically assessed and the effect of electronic structure on the overall electrochemical reaction can be predicted by d-band model.<sup>75</sup> Based on d-band predictions, electronic structure engineering and predictive electronic structure-reactivity relationships can be employed to identify optimal materials for a given reaction.

- vi. **Surface structure:** Surface morphology and crystallinity can significantly affect the overall electrochemical reaction. Shape of particles, crystallographic orientation of surface planes, the type and concentration of defects play vital role in electrocatalysis depending on the mechanism of an electrocatalytic reaction.

### **2.2.3 The Hydrogen Evolution Reaction (HER)**

Hydrogen evolution reaction (HER) of water is a simple way to produce hydrogen. This is a cathode reaction which competes with metal deposition reactions. The electrolysis of water to hydrogen and oxygen cannot replace the production of hydrogen from petroleum, because the cathode of HER is made of expensive materials including Pt, Pd, Au and Ag. Also, water electrolysis requires electrical energy which is currently obtained from fossil fuels. Reforming process is a chemical reaction to collect hydrogen atoms from hydrocarbon organic compounds. As mentioned earlier, residual compounds of the reforming process are CO<sub>2</sub> which causes a greenhouse effect and CO which is absorbed on the surface of catalysts to block further catalytic

reaction. Hence, research efforts to find more effective or less expensive catalyst are on-going for obvious economic and environmental motivations. In addition, non-fossil fuel sources such as photovoltaics have been connected to the electrolysis. Nuclear energy (though public is not assured of its safety to human and environment) is another possible energy source for the electrocatalysis.

The hydrogen evolution reaction is a simple reaction where two protons and two electrons combine to form hydrogen, the overall reaction is simply given by:

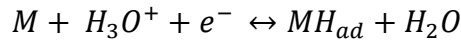
In acid solution;



In base solution;

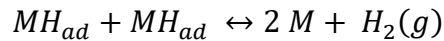


In an initial reaction stage, a proton and an electron react to form an adsorbed hydrogen atom. This is called Volmer reaction:

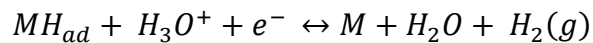


where M is metal (or cathode material) which catalyzes the reaction.

Volmer reaction can be followed by Tafel reaction that is a Langmuir-Hinselwood type reaction. Two adsorbed H atoms on metal react associatively and a hydrogen molecule is released:



or Heyrovsky reaction which is an Eley-Reidel type reaction takes place. In Heyrovsky reaction, a proton and an electron react directly with an adsorbed atomic H atom to form a hydrogen molecule.



The exact reaction path is not simply deduced, and even the same material can exhibit different HER reaction paths by changing surface crystal planes. The mechanism of the HER is

examined using cyclic voltammogram (CV). In the cyclic voltammogram of water electrolysis there is an oxygen adsorption peak, and the oxygen adsorption peak is partly overlapping with the oxygen evolution peak. A typical cyclic voltammogram with different reaction steps are shown in Figure 29. The cyclic voltammogram is a method to measure current while increasing potential to the maximum value at a certain rate and then decreasing potential to a predetermined minimum value. By using this technique, different reaction steps can be identified. A common cyclic voltammogram for water electrolysis starts with the adsorption of oxygen atom on the catalyst surface when positive potential is applied. As more positive potential is biased, adsorbed oxygen atoms coalesce on the catalyst and oxygen molecule is released from the catalyst. Then, backward scanning of the potential reduces adsorbed oxygen atom on the catalyst surface (i.e. the oxygen atom is desorbed). In low potential region, hydrogen atom is adsorbed on the catalyst and a further decrease in the potential causes the evolution of hydrogen molecule. As the potential is rebounded, hydrogen atom is oxidized (or ionized) and a full scanning cycle ends. With this technique, the reaction steps of electrochemical reactions can be well observed.

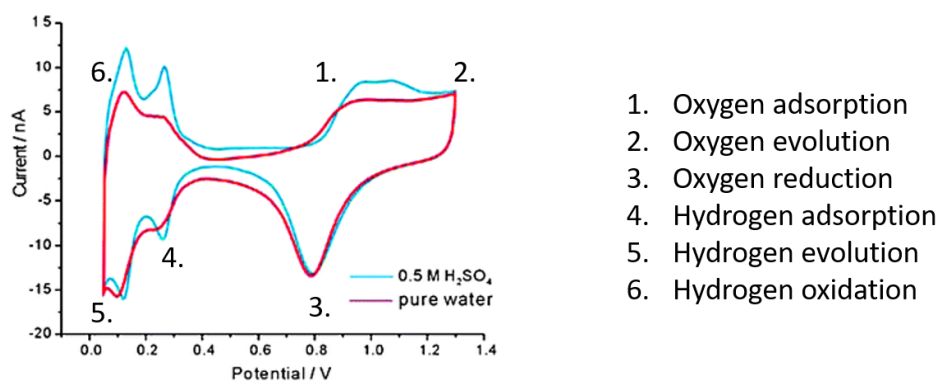


**Figure 29** Cyclic voltammogram for pure water and H<sub>2</sub>SO<sub>4</sub> on Pt micro-disk electrodes. A scanning rate is 80 mV/s. A DHE/PEM system is used as a reference electrode. (Adopted and

edited from literature)<sup>76</sup>

## 2.2.4 HER Catalyst Materials

According to Figure 30, so-called volcano plot which is produced by plotting the exchange current density for HER versus free energy of hydrogen adsorption,<sup>77</sup> the most active catalysts for HER are platinum (Pt) or platinum-group composite materials which are at the top of volcano plot, at which hydrogen binding at the surface is very strong. Platinum-group materials are also very stable in corrosive environment and due to high stability and activity, platinum is used in various applications in corrosive environments. For example, catalysts of low temperature PEM are platinum and platinum alloys. A problem of platinum is limited supply and high cost and it is thus crucial to have alternative catalysts that are comparable to Pt.

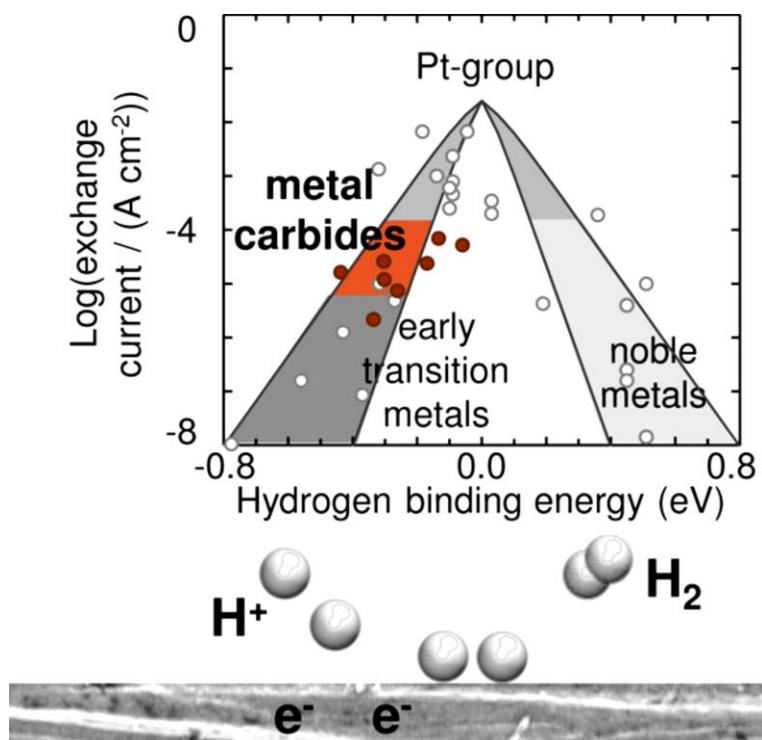


**Figure 30** Volcano plot for the most active HER catalysts (Adopted from literature<sup>78</sup>)

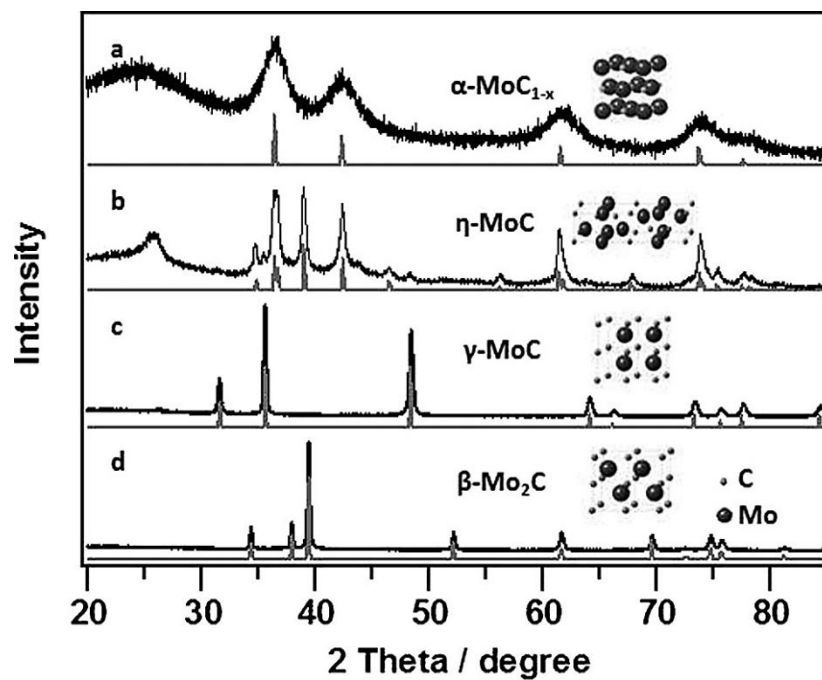
Besides Pt-group composite materials, transition metal carbides (TMC) and transition metal nitrides (TMN) have gained special attention due to their unique chemical and physical properties. Especially, TMC catalysts such as tungsten carbide (WC-W<sub>2</sub>C), and molybdenum carbide (MoxCy), are known to be Pt-like electronic and catalytic properties which can be seen very close to Pt-group in volcano plot, appear to be good alternative nonprecious electrode materials for electrochemical energy conversion applications, such as H<sub>2</sub> fuel cells or electrochemical cells. TMC catalysts possess high melting points, high corrosion stability, superior electric, magnetic, and catalytic properties which make them good and cheap alternative to Pt and noble metal catalysts, making them to be active for HER and not so poisoning and susceptible to easy deactivation as noble metals,<sup>79</sup> especially for catalysis of the dissociation of H<sub>2</sub> in the presence of H<sub>2</sub>O under ambient conditions or catalysis for HER.<sup>80</sup>

In general, geometric and electronic factors are essential for synthesizing the appropriate structure of carbides and nitrides. Basic crystalline structures of these compounds can be found as face-centered cubic (fcc), hexagonal closed packed (hcp) and simple hexagonal (hex) structure. Synthesis of transition metal carbides (TMC) and nitrides (TMN) have some limitations like large particle size, low crystallinity, contamination of unreacted O, C, and N. These drawbacks significantly affect the catalytic performance of those TMC or TMN. Thus, considerable attention is needed to control the size, crystallinity and shape of TMC and TMN particles. For the last decade, remarkable efforts have been made to improve the synthesis method of TMC and TMN for HER application.<sup>81,82,83</sup>

### 2.2.5 Mo<sub>x</sub>C<sub>y</sub> as a Promising Material for Hydrogen Evolution Reaction (HER)

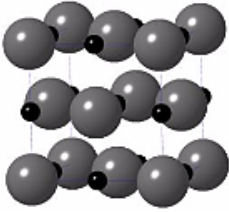
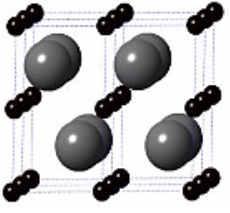
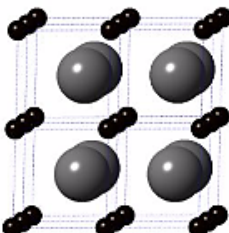
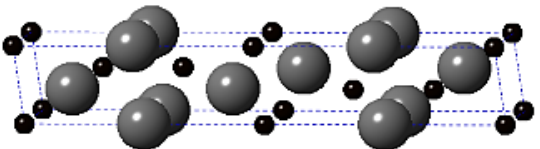
Recently, molybdenum-based materials, such as Mo<sub>2</sub>C,<sup>84</sup> MoO<sub>2</sub>,<sup>85</sup> MoP,<sup>86</sup> MoS<sub>2</sub>,<sup>87</sup> and MoN<sup>88</sup> have attracted much attention being used as electrocatalyst for HER due to their low cost, high durability and high activity. Among them, molybdenum carbide (Mo<sub>x</sub>C<sub>y</sub>) materials appears to be promising electrocatalysts systems for HER because of their unique d-band electronic structures, similar catalytic properties to Pt-based catalysts, low cost, high melting point, good conductivity, and catalytic activity.<sup>89</sup> Molybdenum is much more abundant than Pt in the Earth's crust, and thus as a cheap and more abundant alternative to Pt; investigating methods for the synthesis of molybdenum-based catalysts with high HER activity and long-term durability is important. Tunable phases and composition of molybdenum carbides (Mo<sub>x</sub>C<sub>y</sub>) have attracted researchers who search for noble-metal free catalysts.

Molybdenum carbide is a general name of multiple phases of Mo<sub>x</sub>C<sub>y</sub>. The basic unit of Mo<sub>x</sub>C<sub>y</sub> closely packed molybdenum whose interstitials are filled with carbon atoms. Molybdenum carbide includes MoC, Mo<sub>2</sub>C and Mo<sub>3</sub>C<sub>2</sub>. Out of several phases ( $\alpha$ -MoC<sub>1-x</sub>,  $\beta$ -Mo<sub>2</sub>C,  $\eta$ -MoC, and  $\lambda$ -MoC),  $\beta$ -Mo<sub>2</sub>C (Fe<sub>2</sub>N structure) is the most common phase in HER study.  $\beta$ -Mo<sub>2</sub>C,  $\eta$ -MoC, and  $\lambda$ -MoC have similar hexagonal crystal structures but their hexagonal packing sequences are different.  $\beta$ -Mo<sub>2</sub>C has an ABAB hexagonal packing of metallic planes, whereas  $\eta$ -MoC shows ABCABC and  $\lambda$ -MoC exhibits AAAA packing sequence. Atomic structures of different molybdenum carbide phases are summarized in Table 2. XRD patterns of different phases of molybdenum carbide are also found in Figure 31.



**Figure 31** X-ray diffraction (XRD) patterns for a  $\alpha\text{-MoC}_{1-x}$  (JCPDS 01-089-2868), b)  $\eta\text{-MoC}$  (JCPDS 01-089-4305), c)  $\lambda\text{-MoC}$  (JCPDS 00045-1015), and d)  $\beta\text{-Mo}_2\text{C}$  (JCPDS 00-011-0608), where insets show the corresponding crystal structure. (Adopted from literature <sup>90</sup>)

**Table 2** Summary of four phases of molybdenum carbide.

Phase	Structure	Stacking sequence	Space group	Crystal view
$\alpha$ -MoC <sub>1-x</sub> (NaCl type)	Cubic	ABCABC	Fm $\bar{3}$ m	
$\beta$ -Mo <sub>2</sub> C (Fe <sub>2</sub> N type)	Hexagonal	ABAB	P63/mmc	
$\gamma$ -MoC (WC type)	Hexagonal	AAAA	P $\bar{6}$ m2	
$\eta$ -MoC (MoC type)	Hexagonal	ABCABC	P63/mmc	

Nanostructural modification of Mo<sub>x</sub>C<sub>y</sub> is essential to design novel morphologies and structures, and thus trigger the performance of Mo<sub>x</sub>C<sub>y</sub> for HER. In general, the aim is to synthesize Mo<sub>x</sub>C<sub>y</sub> nanoparticles with higher number of catalytically active sites by constructing composite structures. The well-defined size and shape Mo<sub>x</sub>C<sub>y</sub> nanoparticles can be controlled by modification of the reactants and the reaction temperatures.<sup>91</sup> At very low temperatures, carburization of

molybdenum is not sufficient yet while very high temperatures may induce phase transformation, sintering and aggregation, which can be demonstrated in the Mo-C phase diagram. (Figure 32).

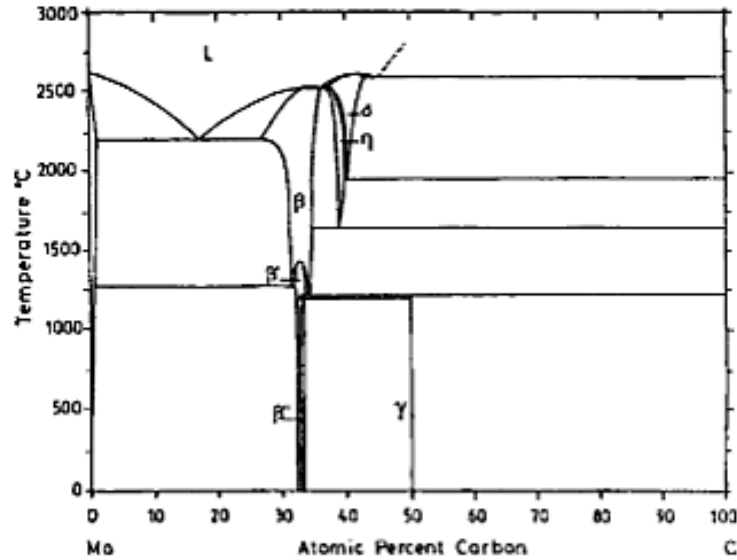


**Figure 32** Phase diagram for  $\text{Mo}_x\text{C}_y$  (Adopted from literature<sup>92</sup>)

For this reason, reaction temperature has a crucial role in formation of desired crystalline structure and morphology of  $\text{Mo}_x\text{C}_y$  during carburization process. Conventionally, the synthesis procedure of  $\text{Mo}_x\text{C}_y$  materials consists of two steps: (i) preparation of the precursor and (ii) subsequent fabrication of desired electrocatalyst under high temperature carburization in an inert atmosphere. Several synthetic methods including for the  $\text{Mo}_x\text{C}_y$  composites can be summarized in Table 3.

**Table 3** Several synthetic methods for the  $\text{Mo}_x\text{C}_y$  composites.

<b>Precursor</b>	<b>Reaction Condition</b>	<b>Crystallinity</b>	<b>Morphology</b>	<b>Reference</b>
$(\text{NH}_4)_6\text{Mo}_7\text{O}_{24}\cdot 4\text{H}_2\text{O}$ , glucose, NaCl	annealing at 850 °C in $\text{N}_2$ for 2 hr	$\beta$ - $\text{Mo}_2\text{C}$	$\text{Mo}_2\text{C}$ /graphene porous foam	93
$\text{MoO}_3$ , $\text{CH}_4/\text{H}_2$ , $\text{C}_2\text{H}_6/\text{H}_2$	1100 °C for 2hr	$\alpha\beta$ - $\text{Mo}_2\text{C}$ ,	nanoparticles	94
$\text{MoCl}_5$ , urea	thermal heating at 800 °C for 3 hr under $\text{N}_2$	$\alpha$ - $\text{Mo}_2\text{C}$ , $\gamma$ - $\text{Mo}_2\text{N}$	nanoparticles	95
$(\text{NH}_4)_6\text{Mo}_7\text{O}_{24}\cdot 4\text{H}_2\text{O}$ , $(\text{C}_2\text{H}_2\text{O}_4\cdot 2\text{H}_2\text{O})$	calcination at 900 °C for 2 hr in $\text{N}_2$	$\alpha$ - $\text{MoC}$ , $\beta$ - $\text{Mo}_2\text{C}$	hierarchically mesoporous nanomaterials	96

## 2.2.6 Graphene for Hydrogen Evolution Reaction

Graphene, an allotrope of carbon atoms in the form of two-dimensional sheet of  $sp^2$ -hybridized atoms tightly bound within a honeycomb structure, has gained special attention in recent electrochemical studies due to its remarkable properties. It has large surface area (specific surface area (SSA)= $2630 \text{ m}^2/\text{g}$ ), high thermal conductivity ( $5000 \text{ Wm}^{-1}\text{K}^{-1}$ ), high optical transmittance (97.7%), high stability, high mechanical strength, zero band gap, high current density sustainability, and high hole drift mobility.<sup>97</sup> However, pristine graphene shows poor catalytic activity.<sup>98</sup>

In electrochemistry, graphene is commonly used as a high-surface area scaffold to host different types of electrocatalysts.<sup>99</sup> In this regard, composites of graphene or graphene derivatives such as graphene oxide (GO) are fabricated combining with highly active catalytic nanoparticles,<sup>100,101</sup> Since exfoliation of graphene introduces oxygen related defects possessing both Lewis acidic and basic sites, exfoliated graphene can show high catalytic activity. Heteroatom doping into graphene can also improve the catalytic activity significantly and was found to be economically favored alternative catalyst for HER, especially avoiding usage of precious transition and noble metal catalysts.<sup>102</sup> In addition, when graphene makes a composite with other nanomaterials, a synergetic catalytic effect is observed. In the electrocatalytic hydrogen production, graphene appears as a multi-functional material. Exfoliated or doped graphene or a composite of graphene with metal nanoparticles exhibit following functionalities: (i) enhanced conductivity providing accelerated charge transfer kinetics for HER, (ii) highly dispersed catalyst loading thus providing more catalytic active sites, and (iii) synergistic interaction between graphene and catalyst providing modulated electronic structure for a better catalytic performance. Both approaches can adjust the electronic structure of the resultant composite and hence more active

surface sites leading to high activity for HER. Various types of commonly used graphene-based electrodes used for electrocatalytic water splitting is shown in Figure 33.

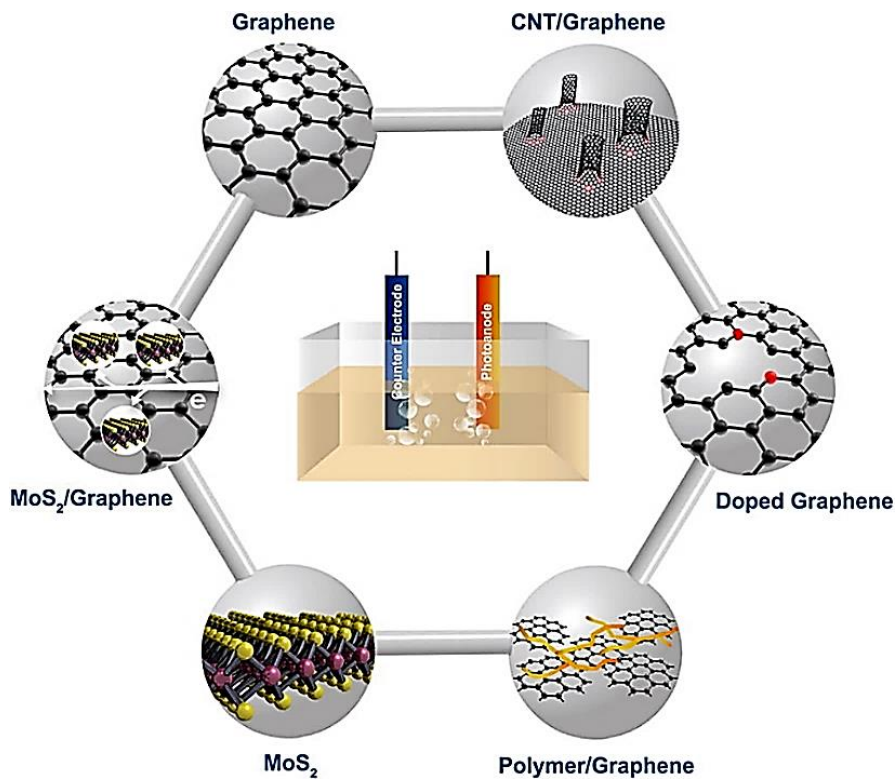


**Figure 33** Schematic illustration of various graphene-based electrodes for electrocatalytic water splitting

### **3.0 EXPERIMENTAL METHODS**

In this chapter, material preparation methods are described in details and their characterization techniques is summarized. There are three main material synthesis parts: (i) plasmonic nanoparticle preparation and bismuth vanadate thin film fabrication process, (ii) synthesis of CdSe/CdS coated SnO<sub>2</sub> nanowires, and (iii) preparation of Mo<sub>2</sub>C and Mo<sub>2</sub>C-GO nanocomposite. Material and device characterization tools include XRD, SEM, TEM, RAMAN, XPS, UV-Vis, photoelectrochemical measurement and electrochemical measurement.

#### **3.1 SAMPLE PREPARATION**

##### **3.1.1 Plasmonic Nanoparticles Decorated BiVO<sub>4</sub> Thin Films**

###### **3.1.1.1 Synthesis of Plasmonic Nanoparticles**

Preparation of SiO<sub>2</sub>@Ag core@shell and SiO<sub>2</sub>@Ag@SiO<sub>2</sub> core@shell@shell plasmonic nanoparticles were conducted to similar to the literature. SiO<sub>2</sub> spheres with uniform diameters were synthesized by Stober method. Pure ethanol (C<sub>2</sub>H<sub>6</sub>O), ammonium hydroxide (NH<sub>4</sub>OH) and tetraethyl orthosilicate (TEOS) were mixed together and stirred vigorously at room temperature for 24 h. By varying the volume ratio of these chemicals, the diameter of the silica spheres could

be controlled. Synthesis of  $\text{SiO}_2@Ag$  core@shell and  $\text{SiO}_2@Ag@SiO_2$  core@shell@shell nanoparticles were performed following seed-mediated two step method. The synthesized  $\text{SiO}_2$  nanospheres were decorated with tiny layer of gold (Au) shell in order to serve as a seed for the growth of silver (Ag) shell. Gold-decorated  $\text{SiO}_2$  colloid was added to a 0.15 mM silver nitrate ( $\text{AgNO}_3$ ) aqueous solution, and the mixture was submitted to magnetic stirring at 400 rpm. The formaldehyde ( $\text{CH}_2\text{O}$ ) reducing agent was then added, and vigorously stirred. Ammonium hydroxide ( $\text{NH}_4\text{OH}$ ) was added to the mixture, and an immediate color change was observed. The samples were stirred for 30 s. They were then cleaned by centrifugation several times with deionized water and ethanol respectively.

### **3.1.1.2 Fabrication of $\text{BiVO}_4$ Thin Films**

Pulse laser deposition (PLD) is a well-known fabrication method for the preparation of oxide thin films of complex stoichiometry. First, the  $\text{BiVO}_4$  target was synthesized by a solid-state reaction method from  $\text{Bi}_2\text{O}_3$  (99.9 %), and  $\text{V}_2\text{O}_5$  powders. The  $\text{BiVO}_4$  photoanodes were deposited on fluorine-doped tin oxide (FTO)/glass substrate (TEC8, 8 ohm/square, Pilkington) from the  $\text{BiVO}_4$  target via PLD. A KrF excimer laser, emitting at a wavelength of  $\lambda=248$  nm, was used. The excimer laser focused on a target inside a vacuum chamber and evaporates to the target so that a vapor cloud of the  $\text{BiVO}_4$  material is created. The substrate is positioned close to target and collects some of the materials, hence allowing thin film growth of surface of substrate. The desired stoichiometry of the material of interest transfers from the target to the substrate surface by the aid of rapid thermal heating of the target's surface. The rapid thermal heating causes very high evaporation rates so that almost all of the constituents substantially evaporate at the same rate. PLD also enables

us to heat and rotate the substrate during deposition. The best performing  $\text{BiVO}_4$  photoanode was obtained to be  $\sim 800$  nm thickness.

### 3.1.1.3 Decoration of $\text{BiVO}_4$ Thin Films with Plasmonic Nanoparticles

As synthesized core shell and core shell nanoparticles were coated on PLD fabricated  $\text{BiVO}_4$  thin films via simple spin coating method, where the optimum amount of nanoparticle solution is applied on the center of the substrate, then the substrate is then rotated at high speed in order to uniformly spread the coating material by centrifugal force. The resultant coated  $\text{BiVO}_4$  thin films further baked on hot plate. Figure 34 shows the steps; for preparations of plasmonic nanoparticles decorated  $\text{BiVO}_4$  thin films.

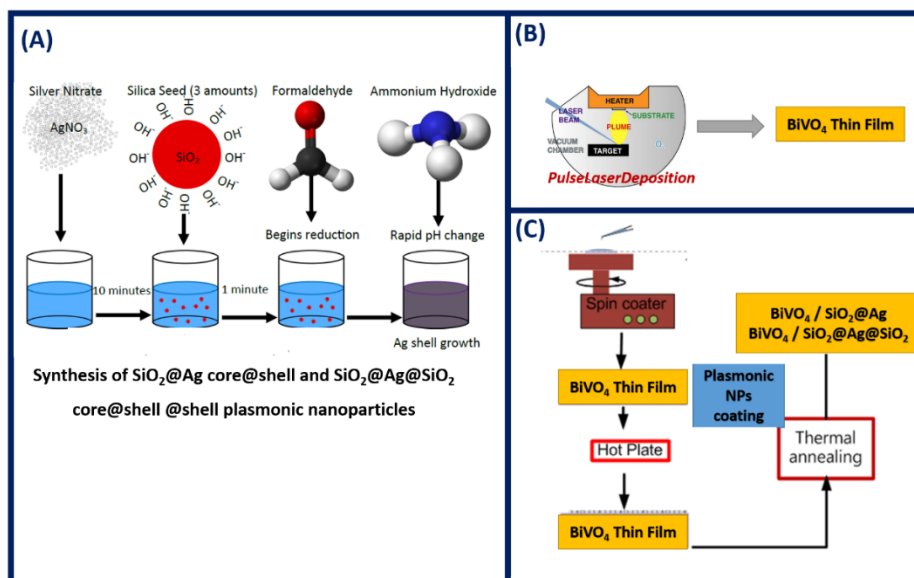


**Figure 34** Schematic illustration of the preparation of plasmonic nanoparticles decorated  $\text{BiVO}_4$  thin films (a) preparation of plasmonic nanoparticles, (b) fabrication of  $\text{BiVO}_4$  thin films, (c) decoration of  $\text{BiVO}_4$  thin films with plasmonic nanoparticles.

### 3.1.2 Fabrication of SnO<sub>2</sub>/CdS/CdSe Heteronanostructures

#### 3.1.2.1 Synthesis of SnO<sub>2</sub> and Sb-SnO<sub>2</sub> Nanowire Arrays

Tin oxide (SnO<sub>2</sub>) nanowire arrays were grown on commercial FTO/glass substrates (10 Ω per square) by vapor-liquid-solid (VLS) method in a horizontal vacuum tube furnace. (Figure 35) High purity tin (99.99%, ACS reagent) metal powder with and without 5%, 10%, 15% atomic ratios of antimony (Sb) powder (99.99 %, ACS reagent) were loaded into a quartz boat and was placed at the center of quartz tube. Au (~1.5 nm) coated FTO film/glass substrates were placed at several centimeters distance from the mixed powder. The system was heated to 800 °C at a rate of 10 °C/min while maintaining the base pressure at below 1.5 mTorr. The temperature of hot zone where the metal source was placed was 800 °C and the temperature where the FTO film/glass substrates located was under 600 °C. The oxygen gas was flowed through the tube with a flow rate of 0.5 sccm during the growth process for 40 min, followed by natural cooling.

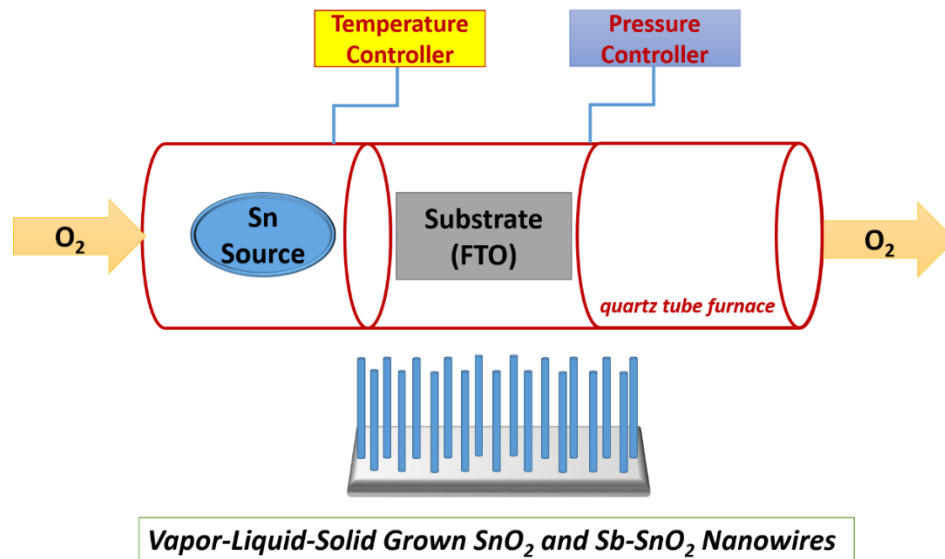


**Figure 35** Illustration of VLS growth method for SnO<sub>2</sub> nanowires.

### 3.1.2.2 Preparation of SnO<sub>2</sub>/CdS/CdSe Heteronanostructures

Firstly, TiO<sub>2</sub> layer with a thickness of 10 nm was conformally deposited on the surface of as prepared SnO<sub>2</sub> and Sb-SnO<sub>2</sub> nanowires using atomic layer deposition (ALD) system (Savannah S100, Cambridge Nano Tech Inc.) at 200 °C. Titanium isopropoxide [Ti(OCH(CH<sub>3</sub>)<sub>2</sub>)<sub>4</sub>] and water vapor were alternatively pulsed into the reaction chamber for the TiO<sub>2</sub> coating of the SnO<sub>2</sub> and Sb-SnO<sub>2</sub> electrodes. Before running the system, the chamber was evacuated to a pressure below 0.3 Torr and then purged with ultrahigh purity nitrogen at a mass flow rate of 20 sccm. The growth rate of TiO<sub>2</sub> layer was 0.3 Å/cycle. Finally, the samples were annealed at 450 °C in air for 1h.

Secondly, the electrodeposition method has been well developed for the fabrication of semiconductor hybrid materials for PEC cell application, typically metal oxide/CdX (X= S, Se, Te) heterostructures. Electrodeposition of CdS was carried out at a constant potential of -0.7 V vs. Ag/AgCl in an aqueous solution containing 0.67 M CdCl<sub>2</sub> and 0.17 M Na<sub>2</sub>S<sub>2</sub>O<sub>3</sub> with a pH of 2.0 at 70 °C. After electrodeposition, the as prepared sample was washed with distilled water several times, and then dried at room temperature in open air.

For electrodeposition of CdSe, the electrolyte was an aqueous solution of 0.02 M Cd(CH<sub>3</sub>COOH)<sub>2</sub>, 0.04 M of ethylene diamine tetraacetic acid disodium salt (EDTA), and 0.02 M of Na<sub>2</sub>SeSO<sub>3</sub> (which is prepared by refluxing 0.48 g of Se powder and 2.0 g of Na<sub>2</sub>SO<sub>3</sub> in water at 100 C for 3 h), with the solution pH around 8. The electrodeposition was performed at 0.67 mA cm<sup>-2</sup> for 10 min on SnO<sub>2</sub> electrode or as prepared SnO<sub>2</sub>CdS electrode to get SnO<sub>2</sub>/CdSe or SnO<sub>2</sub>/CdS/CdSe, respectively, followed by rinsing with distilled water and drying in air at room temperature.

### 3.1.2.3 Polystyrene Treatment for Sequential Deposition of CdSe/CdS Layers on SnO<sub>2</sub> Nanowires

Figure 36 illustrates fabrication steps for polystyrene (PS) treated CdSe/CdS/SnO<sub>2</sub> heteronanostructure. Firstly, synthesis of polystyrene solution was performed with a conventional styrene oligomerization method. Styrene oligomer solution was prepared by mixing styrene with azobisisobutyronitrile as an initiator solution for free radical polymerization of styrene into polystyrene. Obtained styrene oligomer solution was heated at 140 °C and then the resultant solution was spin-coated onto the as-grown SnO<sub>2</sub> nanowire films. Polymerization of the styrene oligomer layer conducted via baking the final film at 70 °C for 30 mins. Polystyrene layer inside the SnO<sub>2</sub> nanowire arrays was sequentially removed by dipping the film in ethylacetate for 30 seconds. Then electrodeposition of first CdS layer was conducted as previously mentioned. In order to fully removal of polystyrene layer for CdSe layer deposition the film was immersed into ethyl acetate for 10 minutes. Finally, electrodeposition of CdSe layer was performed as described above.

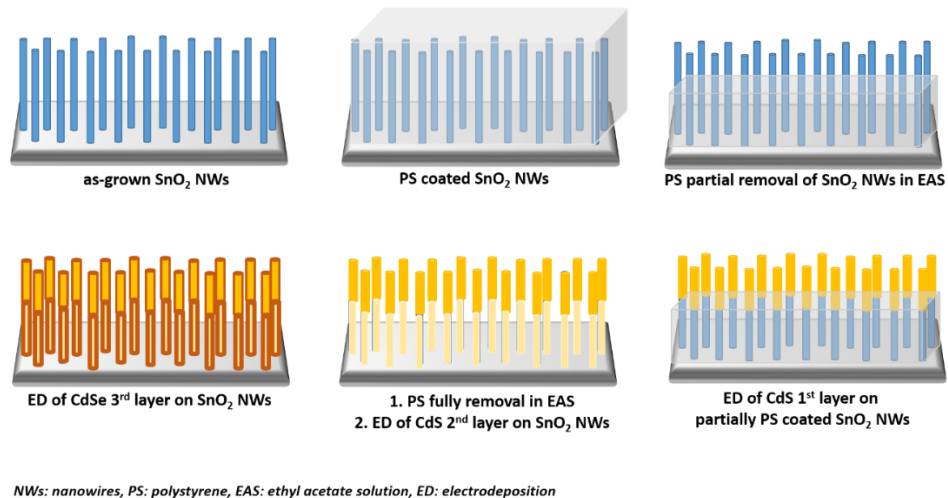


**Figure 36** Fabrication process for polystyrene coating and removal on SnO<sub>2</sub> nanowires and electrodeposition of CdS and CdSe layers on SnO<sub>2</sub> nanowires

### **3.1.3 Fabrication of Mo<sub>2</sub>C/Graphene Oxide Composites**

#### **3.1.3.1 Preparation of Mo<sub>2</sub>C via Microwave Assisted Method**

Molybdenum chloride (MoCl<sub>5</sub> 95%, Sigma Aldrich), ethanol (200 proof, Decon), and urea (Sigma Aldrich) were used to synthesize Mo<sub>2</sub>C nanoparticles. In a typical process, pure ethanol was mixed with MoCl<sub>5</sub> and a different amount of urea was added into the mixture. The precursor solution was stirred and loaded in a teflon reaction vessel. The sealed teflon reaction vessel was irradiated with microwave (Mars, CEM). During the reaction, the temperature was controlled to be 150 °C. A pressure sensor was used to monitor any change in pressure inside the vessel. After the microwave reaction, solid nanoparticles were collected using a centrifuge and annealed at 600, 700, 800 and 870 °C for 3 hrs.

#### **3.1.3.2 Preparation of Mo<sub>2</sub>C Films**

A facile screen printing method was used to coat Mo<sub>2</sub>C films from Mo<sub>2</sub>C nanoparticle paste onto FTO substrate. The NSG ETCTM FTO substrate was chosen as the substrate of Mo<sub>2</sub>C with a resistivity of 8 Ω/sq. Prior to each film coating FTO glass was washed by acetone, ethanol, and DI water respectively. Mo<sub>2</sub>C nanoparticle paste was a mixture of Mo<sub>2</sub>C nanoparticles, ethanol, α-terpineol and ethyl cellulous. Mo<sub>2</sub>C nanoparticles were first fully separated in mixture of ethanol and DI water solvent by repeatedly stirring and ultrasonic dispersion. The Mo<sub>2</sub>C paste was coated on FTO glass through a screen printing process, and organic parts in the paste were burned at 220~250 °C.

### 3.1.3.3 Preparation of Mo<sub>2</sub>C/Graphene Oxide Composites

Commercially available graphene oxide (powder, Sigma Aldrich) was directly added into as-synthesized Mo<sub>2</sub>C nanoparticles with different weight ratios (0.3, 1.5, 3 wt%). The mixture was fully dispersed with ultrasonic dispersion and loaded in a teflon reaction vessel. The sealed teflon reaction vessel was irradiated with microwave (Mars, CEM). The microwave reaction conditions were same as the above mentioned for Mo<sub>2</sub>C nanoparticle synthesis.

Finally, Mo<sub>2</sub>C-GO nanoparticle paste was prepared. The paste was a mixture of Mo<sub>2</sub>C-GO nanoparticles, ethanol,  $\alpha$ -terpineol and ethyl cellulous. The resultant paste was coated on FTO glass via screen printing similar as mentioned above, and then baking at 220-250 C was performed. Illustration of overall process for preparation of Mo<sub>2</sub>C and Mo<sub>2</sub>C-GO composites given in Figure 37.

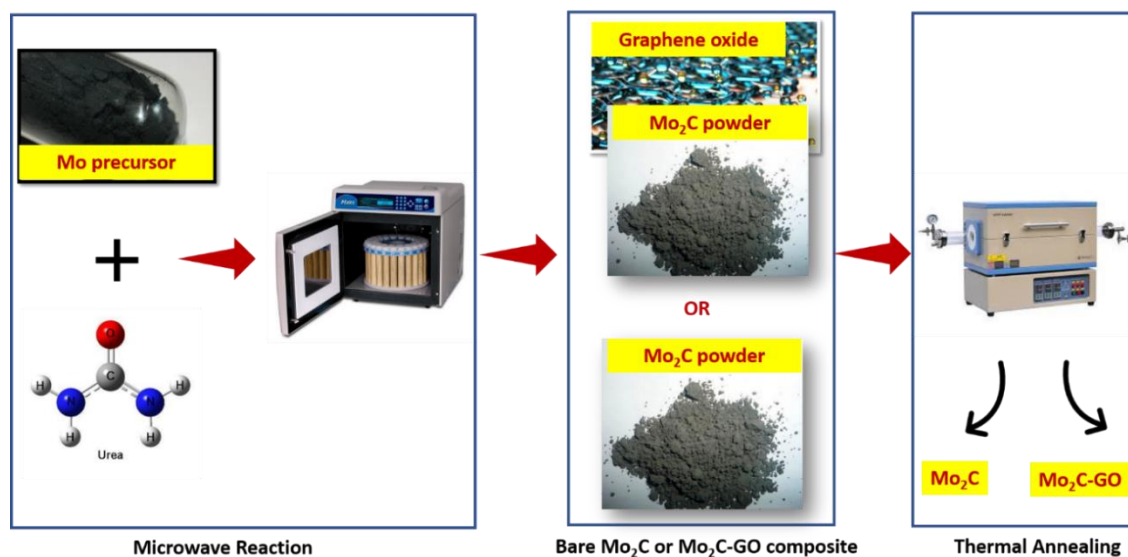


**Figure 37** Schematic illustration of microwave assisted synthesis of Molybdenum Carbide (Mo<sub>2</sub>C) and Molybdenum Carbide-Graphene Oxide (Mo<sub>2</sub>C-GO) nanocomposite synthesis

## **3.2 PHYSICAL CHARACTERIZATION**

Plasmonic nanoparticles, plasmonic nanoparticles decorated BiVO<sub>4</sub> thin films, SnO<sub>2</sub> nanowires, SnO<sub>2</sub>/CdS/CdSe heteronanostructures, Mo<sub>2</sub>C nanoparticles and GO-Mo<sub>2</sub>C nanocomposites, were analyzed using multiple characterization tools.

### **3.2.1 X-Ray Diffraction (XRD)**

The crystal structure and phase composition of the samples was analyzed by using X-ray diffraction (XRD). PANanalytical X-Ray diffractometer, Co-K radiation,  $\lambda = 1.79 \text{ \AA}$ ., a step size of 0.0170 and step time of 20 s. The diffraction patterns were recorded in the range of  $2\theta = 20 \sim 80^\circ$ . Peak identification was performed by comparing the obtained XRD patterns with electronic JCPDS file by using JADE software.

### **3.2.2 Scanning Electron Microscope (SEM), Energy Dispersive X-Ray Analysis (EDXA), Transmission Electron Microscopy (TEM)**

The microstructure, thickness and 3D morphology of nanomaterials were characterized by microscopy using High Resolution SEM (FEI Apreo). Energy dispersive X-ray spectroscopy (EDAX) analyzer (attached with the SEM machine) analysis and elemental mapping information was also performed by using SEM-EDAX (FEI\_Apreo) by detecting and measuring the energy of X-Ray emitted from the interaction of the electron with samples. The structure of nanomaterials was studied using high resolution transmission electron spectroscopy (HR\_TEM) by (FEI-Tecnai).

### **3.2.3 Ultraviolet–visible spectroscopy (UV-Vis)**

To obtain light absorption and reflection of the semiconductor nanomaterials for photoanode, diffuse spectra were recorded in the range of 300-800 nm with 100 UV-Visible spectrophotometers (Perkin Elmer, model) in 1 cm pathlength quartz cuvettes, equipped with a 150 mm integrated sphere and using spectralon as a reference material. The reflectance (R) and transmittance (T) spectra were obtained by the air reference from 300 to 800 nm. The light absorption (A, %) was obtained from  $A = 100 - R - T$ , where R is the total reflectance, and T is the total transmittance

### **3.2.4 Raman Spectroscopy**

Raman spectroscopy was used for identification and structural characterization of the samples. Room temperature Raman spectra were collected on a thin film and on a powder sample with a microprobe Raman system type Horiba spectrometer, using a 630-nm wavelength excitation line.

### **3.2.5 X-Ray Photoelectron Spectroscopy (XPS)**

X-Ray photoelectron spectroscopy (XPS) has been employed in this study to obtain more information about the structure, chemical composition and the valence states of the resulted phases.

## **3.3 PHOTOELECTROCHEMICAL CHARACTERIZATION**

Photoelectrochemical characterization of plasmonic nanoparticles decorated BiVO<sub>4</sub> thin films was carried out in an aqueous 0.5 M potassium phosphate buffer, using KH<sub>2</sub>PO<sub>4</sub> (Sigma-Aldrich, Reagent grade, 1.0 M) solution and K<sub>2</sub>HPO<sub>4</sub> solution (Sigma-Aldrich, Sigma-Aldrich, Reagent

plus, 1.0 M) buffered to  $\text{pH} \approx 7 \pm 0.02$  and CdS and CdSe sensitized  $\text{SnO}_2$  nanowires was carried out in an aqueous 0.35 M  $\text{Na}_2\text{SO}_3$  and 0.24 M  $\text{Na}_2\text{S}$  buffered to  $\text{pH} \approx 12 \pm 0.05$  at 25 °C using three-electrode configuration. The potential scan rate of  $50\text{mVs}^{-1}$  of the working electrode was controlled by an electrochemical workstation (CH Instruments, CHI 660C). An Ag/AgCl electrode (Accumet, Fisher Scientific) and a coiled Pt wire were used as the reference and counter electrodes, respectively. The potentials vs Ag/AgCl were converted to the reversible hydrogen electrode (RHE) using the following Nernst equation,

$$E(\text{RHE}) = E(\text{Ag}/\text{AgCl}) + E^0(\text{Ag}/\text{AgCl vs NHE}) + 0.059\text{pH}$$

*where  $E^0(\text{Ag}/\text{AgCl vs NHE}) = 0.207\text{ V}$  at 25 °C*

The electrolyte solution was purged with Argon for about an hour before each measurement. Illumination was performed under simulated AM 1.5 solar illumination ( $100\text{mA}/\text{cm}^2$ ) with a Newport Solar Simulator using appropriate filters and calibrated using Si photodiode. The illuminated area was  $0.28\text{ cm}^2$ . A typical setup for PEC cell is shown in Figure 38, composed of working electrode (WE), reference electrode (RE), and counter electrode (CE).

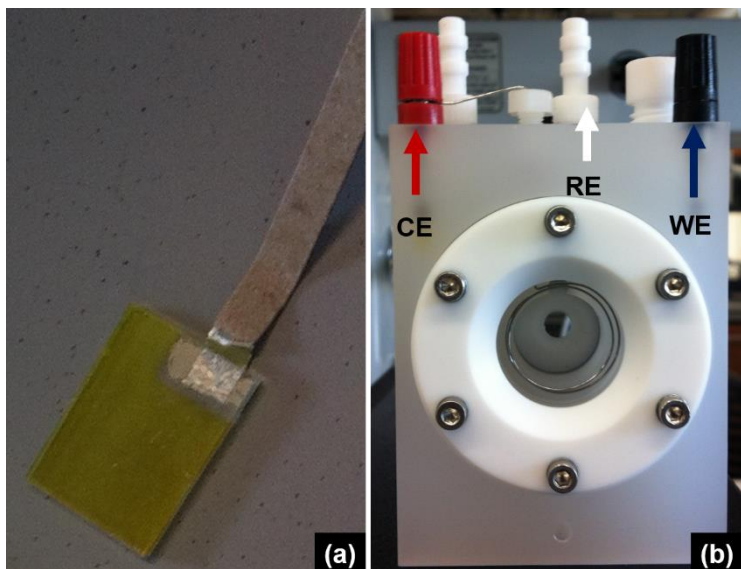


**Figure 38** Typical thin film semiconductor photoelectrode (a) and assembled cell (b) for PEC measurements

Another approach to measure the performance of a PEC cell or photoanode is to determine the photocurrent as a function of wavelength. A common way to for this measurement is Incident Photon to Current Efficiency (IPCE), which is also equivalent to external quantum efficiency. To determine IPCE, a measurement was performed using a 300 W Xenon arc lamp (Oriel) which is coupled with a grating monochromator (Newport) which is depicted in Figure 39.

IPCE is calculated based on the following equation:

$$IPCE (\%) = \frac{1240 \times J_{sc} (A/cm^2)}{P(Watt/cm^2) \times \lambda(nm)} \times 100\%$$

where “J<sub>sc</sub>” is the photocurrent density at a specific wavelength, is “λ” the wavelength of the incident light, and “P” is the light intensity. A calibrated Si photodiode (Newport) was used to measure illumination intensity.

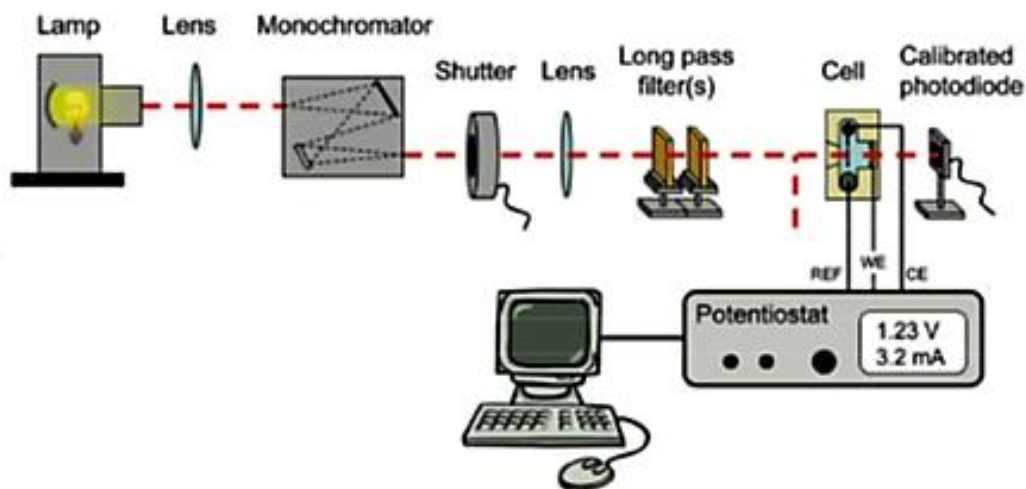


**Figure 39** Schematics of the experimental setup to measure is Incident Photon to Current Efficiency (IPCE) of a photoanode

### 3.4 ELECTROCHEMICAL CHARACTERIZATION

Electrochemical properties of  $\text{BiVO}_4$ ,  $\text{CdSe/CdS}$  and  $\text{Mo}_2\text{C}$  samples were measured in a proper electrolyte for each composition at constant temperature using amperometry technique conducted in a three-electrode system shown in Figure 40. Amperometry generally refers to all electrochemical techniques in which a current is measured as a function of either time (potentiostatic amperometry) or applied electrode potential (voltammetry). In this research, we perform potentiostatic amperometry where current is measured at a constant potential with variation of the deposition time for nanowire coating. An electrochemical station (CH Instruments) is used is connected to an FTO/glass substrate as the working electrode and a platinum wire as a counter electrode, with the potential kept fixed with respect to an  $\text{Ag/AgCl}$  reference electrode.

The electrocatalytic activity and electrochemical performance were tested by a cyclic voltammetry (CV) measurement technique. A CV work station needs three electrodes: reference electrode, working electrode and counter electrode. This is also called a three-electrode setup. In the measurement, we use saturated calomel electrode (SCE) as a reference electrode and Pt electrode as counter electrode (sometimes called auxiliary electrode). Three different pH states of electrolytes were used during the test including 0.5M H<sub>2</sub>SO<sub>4</sub>, 0.5M Phosphate buffer and 1M NaOH.

We performed both potentiostatic amperometry (LSV) or voltammetry (amperometric i-t test). The overpotential and long-term stability of the working electrode were measured from LSV and amperometric test, respectively. Applied potential at the current density of 10 mA/cm<sup>2</sup> in I-V curve is defined as the overpotential which reflects the activity of electrocatalyst for HER. In LSV measurement, we set the potential range from -1.0 V to +1.0 V to find the potential corresponding to 10 mA/cm<sup>2</sup>. For I-t stability test, we fixed the potential at 0.5V and measured a change in electric current of the working electrode. In the case of Mo<sub>2</sub>C electrode, the electrode dissolves rapidly in alkaline state electrolyte and 1M NaOH is not used as the electrolyte.

Polarization curve can be obtained by using LSV data. After measurement of the above electrochemical tests, we plot Tafel plot and calculate the Tafel slope. The overpotential and Tafel slope are chosen as main factors showing the performance of the electrocatalysts.

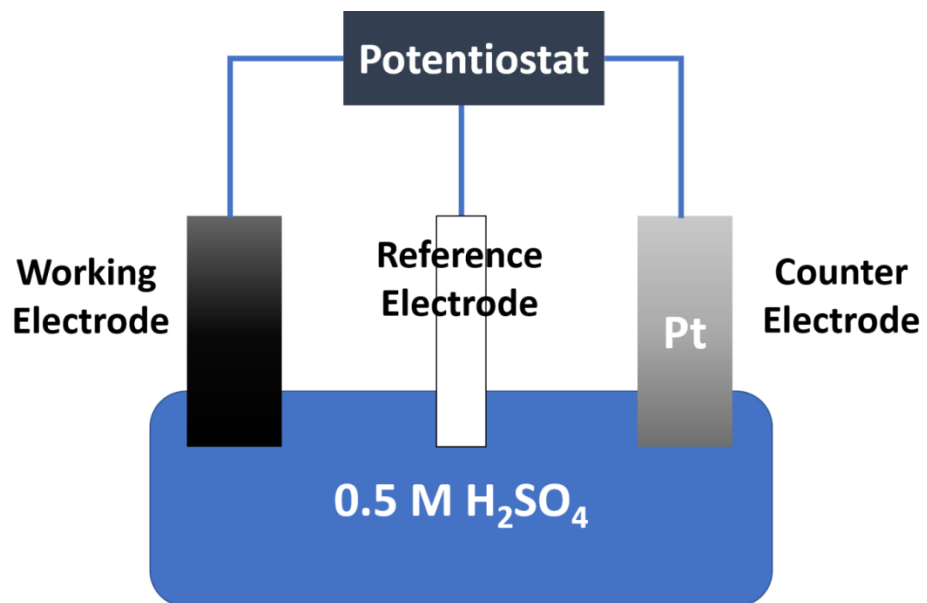


**Figure 40** Electrode setup used for all electrochemical measurements. WE (working electrode, CE (counter electrode), RE (reference electrode)

## **4.0 CONCENTRATED LIGHT ABSORPTION AND ITS EFFECT ON PHOTOELECTROCHEMICAL REACTION IN PLASMONIC NANOPARTICLES DECORATED BiVO<sub>4</sub> PHOTOANODES**

### **4.1 OBJECTIVES**

Binary metal oxides such as TiO<sub>2</sub>, ZnO, WO<sub>3</sub>, Fe<sub>2</sub>O<sub>3</sub> have been extensively tested as a photoelectrode of PEC cells. However, a small number of binary oxides can offer large photocurrent density (> 1 mA/cm<sup>2</sup>) using solar light,<sup>103</sup> and most of them have limitations to build an efficient PEC cell such. Some of them have too large band gaps to absorb a sufficient fraction of the solar spectrum, low lying valence bands below water oxidation potential, conduction band lying above water reduction potential, instability in acidic or basic aqueous solution, or short carrier lifetimes due to extensive recombination and/or poor charge transport.<sup>104</sup> Although efforts are still ongoing to overcome limitations of binary metal oxides, material search is extended to focus more on complex metal oxides, such as ternary metal oxides. With ~50 nominee metals in the periodic table, there are many combinations of ternary and quaternary compounds are possible, which clearly improves the possibility of finding an ideal semiconductor electrode for PEC water splitting.<sup>105</sup> One of promising ternary metal oxides for photoanodes which produce oxygen using solar energy is bismuth vanadate BiVO<sub>4</sub>. It consists of abundant elements, non-toxic and very

stable during a photoelectrochemical reaction at a wide pH range (3 - 11). In addition, BiVO<sub>4</sub> has a bandgap of 2.4 eV which can absorb visible light and its band edge positions match water redox reaction potentials better than other well-known metal oxides such as titanium oxide, hematite or tungsten oxide. BiVO<sub>4</sub> exhibits a low onset potential and high photocurrent even in the low-bias region, as a result complete water splitting can be achieved with a relatively small external bias with using BiVO<sub>4</sub>.<sup>106</sup> Moreover, BiVO<sub>4</sub> photoanodes do not depend upon very acidic or basic media to achieve good PEC performance. Despite appealing intrinsic properties, photocurrent densities of BiVO<sub>4</sub> photoelectrodes do not reach its theoretical photocurrent density of 7.5 mA/cm<sup>2</sup>. One of the main limitations of BiVO<sub>4</sub> is slow transfer of photogenerated holes from BiVO<sub>4</sub> to the electrolyte. Since the kinetics of a water oxidation process is slow, holes accumulate at the BiVO<sub>4</sub>/electrolyte and the catalytic activity decreases. Another limitation is poor carrier transport within BiVO<sub>4</sub>. A charge transport mechanism is small polaron hopping and a drift mobility of holes in single-crystal BiVO<sub>4</sub> is as low as 0.2 cm<sup>2</sup>/V/s.<sup>107</sup> Therefore, photogenerated carriers easily recombine and a charge separation efficiency of BiVO<sub>4</sub> is low.<sup>108</sup> In addition a modest light absorption coefficient near the band gap is a problem to be addressed.

Several solutions have been proposed to improve the overall PEC performance of BiVO<sub>4</sub> photoelectrodes. Oxygen evolution catalysts (OECs) such as RhO<sub>2</sub>, cobalt phosphate (Co-Pi), iron oxyhydroxide (FeOOH) have been coated on the surface of BiVO<sub>4</sub> to solve low catalytic activity for water oxidation and slow charge transfer across the interface. These OECs generally lead to improved photocurrent density, cathodic onset potential shift, higher charge transfer efficiency across the interface and improved stability. A general way of improving conduction in a semiconductor is introducing dopants. Donor dopants (W and Mo<sup>109</sup>) have been incorporated to BiVO<sub>4</sub> to increase the carrier concentration and the electric conductivity. A typical dopant

concentration is in the range of 1-10 %, however, its activation efficiency is not high, and a high concentration of neutral impurities work as a scattering center. Therefore, it is important to maintain a balance between advantageous and disadvantageous implications of doping. In addition, other efforts to compensate for the poor charge transport is to use nanostructured BiVO<sub>4</sub>, which can reduce the diffusion length of photogenerated has been widely used. In order to secure enough light absorption, the thickness of BiVO<sub>4</sub> film has to be increase. However, simply increasing the film thickness does not optimize the photocurrent, since the hole diffusion length of most BiVO<sub>4</sub> films is around 100 nm. As long as the BiVO<sub>4</sub> feature sizes are smaller than reported diffusion length, photogenerated holes can reach to the interface and be separated from electrons. However, as the thickness of BiVO<sub>4</sub> film becomes larger than the hole diffusion length, the recombination of photogenerated charge carriers within BiVO<sub>4</sub> film becomes significant. Hence, BiVO<sub>4</sub> nanostructures with several synthesis techniques have been fabricated in order to address this problem and to ensure high carrier separation efficiencies, and high optical absorption despite the small thickness of the BiVO<sub>4</sub> layer.

In a typical PEC water splitting cell, light is absorbed in three different parts of semiconductors: (i) a space charge layer where photogenerated electrons and holes can be separated with the assistance of a built-in potential as soon as they are produced, (ii) a diffusion layer where photogenerated electrons and holes can diffuse in an opposite direction till they reach a space charge layer, (iii) bulk layer where most of photogenerated carriers recombine before they reach the semiconductor/electrolyte interface. Only the charge carriers generated in first and second regions contribute to photocurrent. A distance between a boundary of the bulk region and a boundary of the space charge region corresponds to a minority carrier diffusion length. In order

to get desired solar to hydrogen conversion efficiency; it is essential to manipulate light absorption locally, particularly in first and second regions of the semiconductor.

Nanophotonic structures such as plasmonic nanoparticles are combined with the semiconductor to increase total light absorption or confine the light absorption region within space charge and diffusion layers. This provides existing semiconductors with new opportunities for improving the power conversion efficiency of PEC cells. The nanophotonic structures which can generate surface plasmon resonances (SPR) act as light antennas and localize radiation energy near the metal/dielectric interface.

In this study, core-shell type plasmonic particles are coated on the surface of  $\text{BiVO}_4$  and the effect of the surface plasmons on light absorption, carrier transport and water redox reaction of  $\text{BiVO}_4$  is examined. Compared with spherical metal nanoparticles, the plasmonic resonance frequency and width of metal nanoshells can be tuned by changing the size of the metal core and insulating nanoshells. Ag is chosen a metal component because it is less expensive than other plasmonic metals such as Au, Pt and the plasmonic frequency of Ag can be tailored to a perfect match with absorption spectrum of  $\text{BiVO}_4$ . Different types of plasmonic nanoparticles are employed to examine a change in the light absorption coefficient, the carrier separation efficiency, and the catalytic efficiency in plasmonic particle decorated  $\text{BiVO}_4$  photoanode. We observe that the surface plasmonic can localize the light absorption to the sub-surface region of  $\text{BiVO}_4$  and increase the absorption coefficient at the band edge. The water splitting efficiency is tightly related to the enhancement of light absorption by the surface plasmons. Plasmonic particle coated  $\text{BiVO}_4$  increases the separation efficiency of PEC cell and harness more light at the band edge, leading to 40% improvement of the photocurrent.

## 4.2 RESULTS AND DISCUSSION

### 4.2.1 Microstructure and Crystal structure of BiVO<sub>4</sub> Film and Plasmonic Nanoparticles

Photoelectrochemical activity of PEC cell is sensitive to microstructure and crystal structure of semiconductor and plasmonic particles. These properties heavily depend on a synthesis method. In this study, we chose BiVO<sub>4</sub> films grown by a pulsed laser deposition technique and plasmonic particles synthesized by a solution method. The microstructure and crystal structure of BiVO<sub>4</sub> films and plasmonic nanoparticles are characterized by electron microscope and XRD.

The crystal structure and phase purity of BiVO<sub>4</sub> films were characterized by XRD. Figure 41 (c) shows XRD pattern of BiVO<sub>4</sub> films. Peaks at 17.5°, 22°, 46.5°, 55° of 2θ correspond to (002), (112), (004), (200), (020) peaks of monoclinic scheelite BiVO<sub>4</sub>. This indicates that BiVO<sub>4</sub> has a monoclinic structure. In addition, XRD patterns show strong peaks of FTO film that was coated between BiVO<sub>4</sub> film and glass substrate as a transparent electrode. Relative peak intensities of BiVO<sub>4</sub> films are different from those of BiVO<sub>4</sub> bulk. This means that BiVO<sub>4</sub> film has a textured structure with a preferred growth direction. It is theoretically predicted that the carrier transport along BiVO<sub>4</sub> along [001] direction experiences less bulk and surface recombination. This, in turn, improves interfacial charge transfer from BiVO<sub>4</sub> film OER activity because of its favorable surface electronic properties and atomic structure. Therefore, we performed the photoelectrochemical study in BiVO<sub>4</sub> film which was epitaxially along [001] direction. BiVO<sub>4</sub> film was grown by pulsed laser deposition method. Since (101) plane of FTO and (001) plane of BiVO<sub>4</sub> have a structural similarity, (101) FTO/glass substrate was chosen to grow (001) plane of BiVO<sub>4</sub> which was normal to [001] direction. Morphology of BiVO<sub>4</sub> films are shown in Figure 41 (a) and (b). BiVO<sub>4</sub> films were ~ 800 nm thick and consisted of columnar grains with rounded edges.

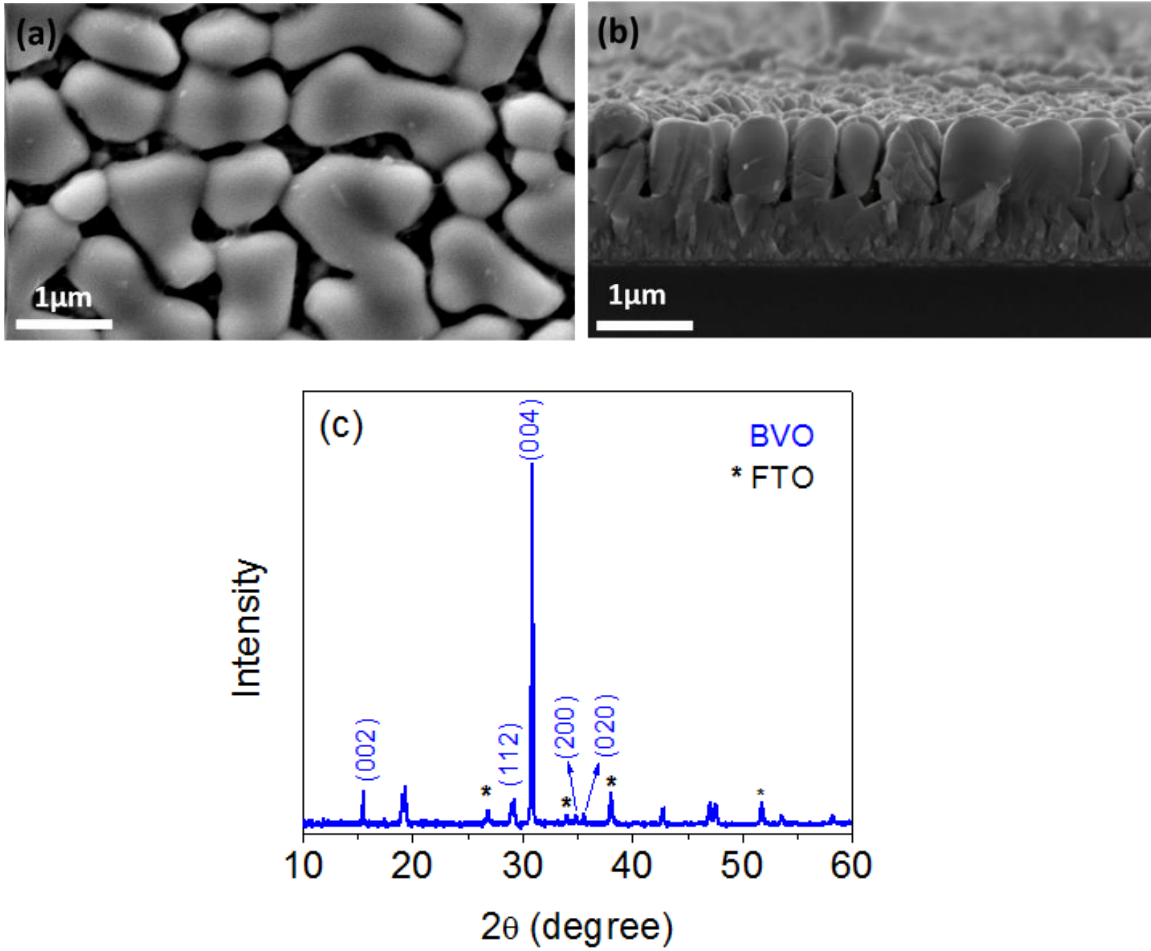


**Figure 41** Characterization of the  $\text{BiVO}_4$  sample; scanning electron microscopy (SEM) morphology of bare as-synthesized  $\text{BiVO}_4$  thin films, (a) top view (b) cross sectional view and (c) X-ray diffraction (XRD) of the samples

Figure 42 (a) schematically explains the sequential growth of Ag and  $\text{SiO}_2$  layer on  $\text{SiO}_2$  cores. In this study, core size and shell thickness were controlled by changing deposition time and concentration of precursor solutions. The particle size of pure  $\text{SiO}_2$ ,  $\text{Ag@SiO}_2$  and  $\text{SiO}_2@\text{Ag@SiO}_2$  was analyzed by dynamic light scattering (DLS), which is shown in Figure 42 (b). The average particle size increases from 90 nm (pure  $\text{SiO}_2$ ) to 142 nm ( $\text{SiO}_2@\text{Ag@SiO}_2$ ),

which indicates that the thickness of each shell is 10 nm. SEM image of  $\text{SiO}_2@\text{Ag}@\text{SiO}_2$  is shown in Figure 41 (c). The particle size of SEM image is consistent with DLS analysis.

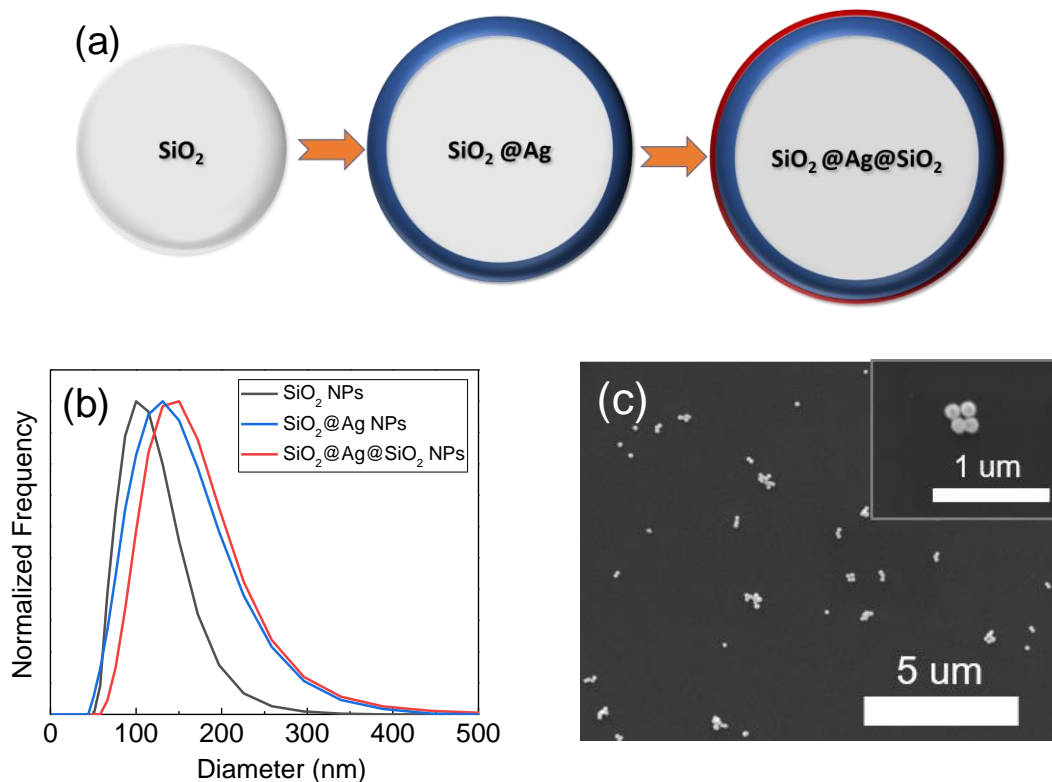


**Figure 42** Characterization of core shell nanoparticles: (a) schematic representation of core shell particles evolution starting from  $\text{SiO}_2$  particles to  $\text{SiO}_2@\text{Ag}@\text{SiO}_2$ , (b) a size distribution of  $\text{SiO}_2$ ,  $\text{Ag}@\text{SiO}_2$  and  $\text{SiO}_2@\text{Ag}@\text{SiO}_2$  particles, (c) SEM image of  $\text{SiO}_2@\text{Ag}@\text{SiO}_2$  particles.

TEM images in Figure 43 show the growth sequence of the plasmonic nanoparticles. Figure 43 (a) shows that uniform  $\text{SiO}_2$  nanoparticles with a core diameter of 90 nm were synthesized first. In Figure 43 (b) and (c), small seeds were coated on the surface of  $\text{SiO}_2$  to nucleate 10 nm thick Ag layer. The thickness of the outermost  $\text{SiO}_2$  shell was 15 nm in Figure 43 (d).

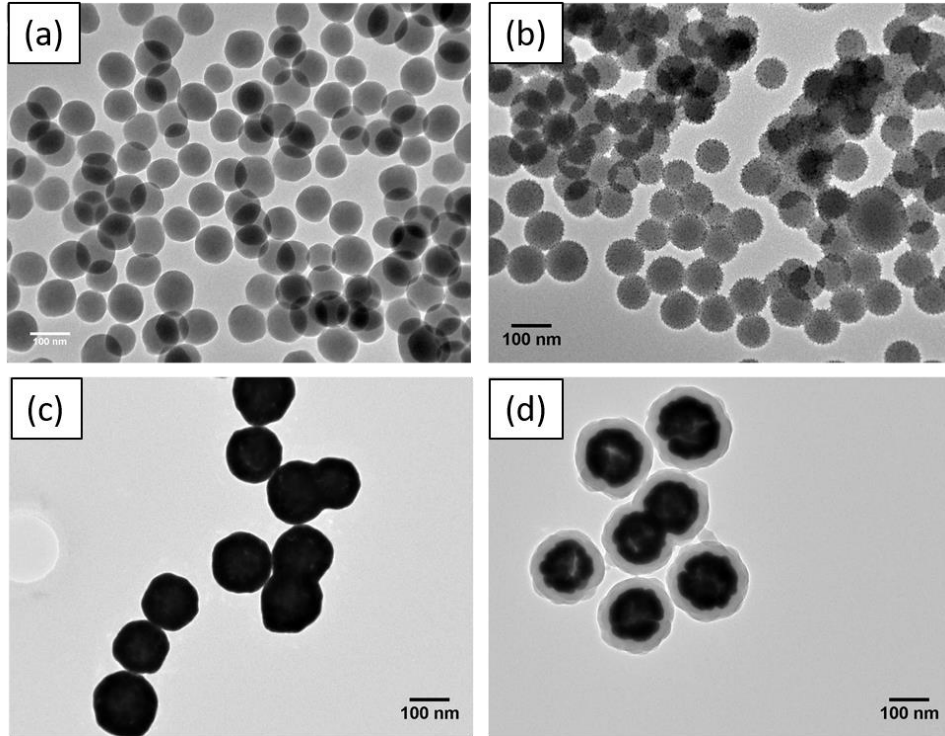


**Figure 43** Transmission electron microscopy (TEM) images of (a) SiO<sub>2</sub> spheres, (b) SiO<sub>2</sub>@Au seeds, (c) SiO<sub>2</sub>@Ag core shell particles, and (d) SiO<sub>2</sub>@Ag@SiO<sub>2</sub> core shell shell particles.

For optimal integration of the plasmonic particles with the BiVO<sub>4</sub>, plasmonic nanoparticles were uniformly coated on the surface of BiVO<sub>4</sub> by spin coating method. Figure 44 (a) and (b) shows SEM images of the nanoparticles decorated BiVO<sub>4</sub> in plan-view and cross-section modes. The plasmonic nanoparticles were evenly distributed on BiVO<sub>4</sub> thin films. X-ray diffraction analysis was also performed to see any changes after BiVO<sub>4</sub> thin films were coated with plasmonic nanoparticles. XRD patterns in Figure 44 (c) show that BiVO<sub>4</sub> maintains a monoclinic scheelite structure. SiO<sub>2</sub> and Ag were not detected in XRD analysis, due to their amorphous structure or very fine size.

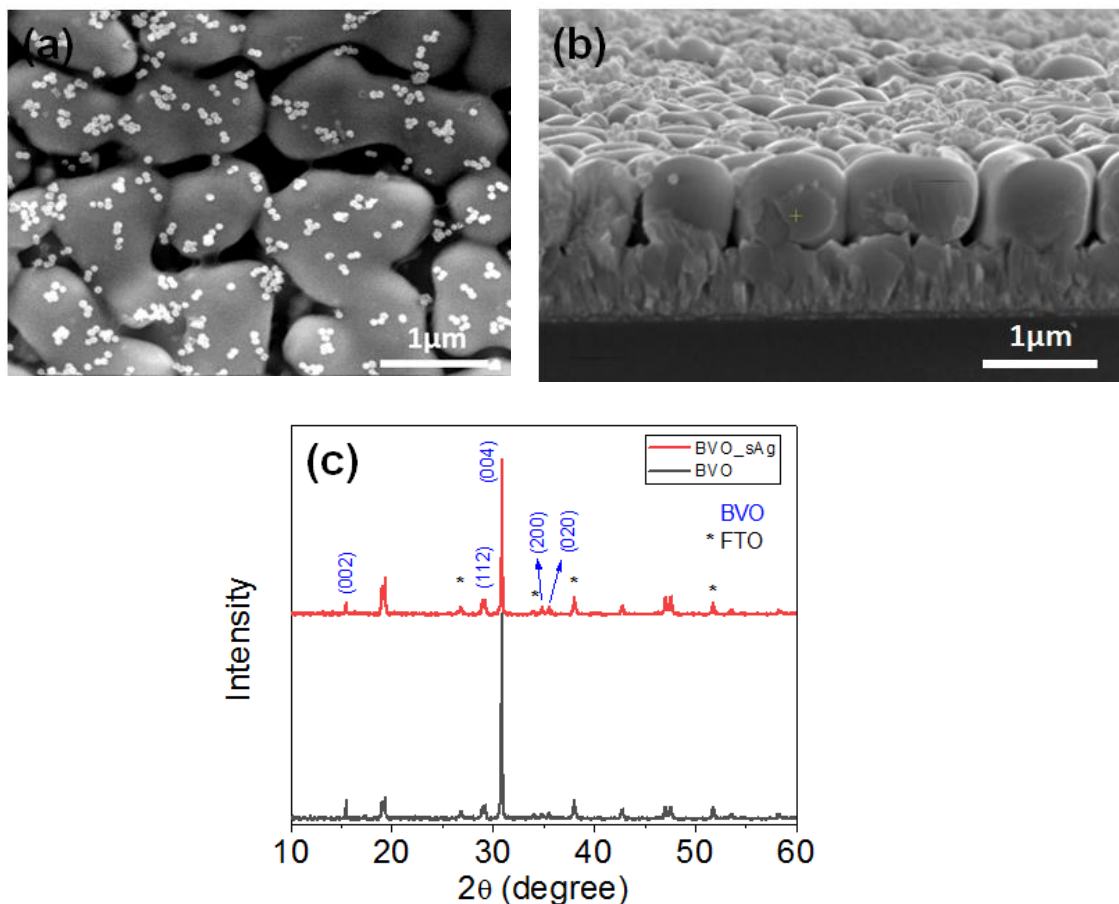


**Figure 44** Characterization of the core shell particles coated  $\text{BiVO}_4$  samples; Scanning electron microscopy (SEM) morphology of core shell particles coated  $\text{BiVO}_4$  thin films, (a) top view (b) cross sectional view and (c) X-ray diffraction (XRD) of the samples,



#### 4.2.2 Optical Property of $\text{BiVO}_4$ Films and Core-Shell Plasmonic Particles

$\text{BiVO}_4$  has attracted an increasing interest because of its interesting optical properties.  $\text{BiVO}_4$  exhibits greenish-yellow color and the band gap of  $\text{BiVO}_4$  is reported 2.4 eV. UV-vis absorption spectra of the  $\text{BiVO}_4$  samples are illustrated in Figure 45. The experimentally measured absorption spectrum of  $\text{BiVO}_4$  film in this study is close to the calculated absorption spectrum of  $\text{BiVO}_4$  film

using the refractive index in the literature. As expected, BiVO<sub>4</sub> does not absorb light whose wavelength is longer than c.a. ~ 530 nm. A dramatic change in the range of 500 ~ 520 nm corresponds to the band gap of bulk BiVO<sub>4</sub> (~2.4 eV). Therefore, BiVO<sub>4</sub> film does not effectively harness green and red light which accounts for a significant portion of solar energy. This is a problem in applying BiVO<sub>4</sub> film to photoelectrochemical applications.

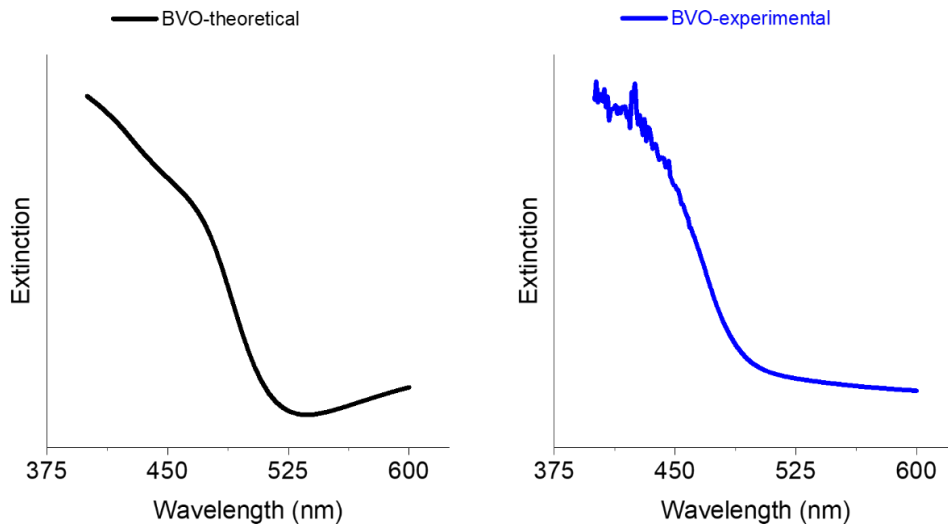


**Figure 45** Experimental measured and theoretically calculated extinction spectra of 800 nm thick BiVO<sub>4</sub> films on FTO/glass substrate (the calculation was performed using FTDT simulation).

In this study, two different types of spherical plasmonic particles are used. One is Ag shell – SiO<sub>2</sub> core (SiO<sub>2</sub>@Ag) and the other is Ag shell – SiO<sub>2</sub> core (SiO<sub>2</sub>@Ag@ SiO<sub>2</sub>). In both cases, the plasmonic behavior is originated at Ag - SiO<sub>2</sub> interface. From the electromagnetic theory; also, well known as Mie theory, we expect these plasmonic spheres to create resonance modes at sub-wavelength and wavelength scale dimensions. These resonance modes lead to resonant optical

antenna effects that significantly contribute the optical absorption and overall photoelectrochemical efficiency.

Experimentally measured and theoretically calculates absorption spectra of two different plasmonic particles which are dispersed in water are illustrated in Figure 46. Experimental and theoretical results are consistent. Broad absorption spectra of both particles range from 400 nm to 800 nm. Surface plasmon peaks of  $\text{SiO}_2@Ag$  ( $\text{SiO}_2$  core diameter: 90 nm, Ag shell thickness: 10 nm) and  $\text{SiO}_2@Ag@SiO_2$  ( $\text{SiO}_2$  core diameter: 90 nm, Ag shell thickness: 10 nm,  $\text{SiO}_2$  shell thickness: 10 nm) are found at  $\sim 500$  nm where the absorption coefficient of  $\text{BiVO}_4$  dramatically decreases.

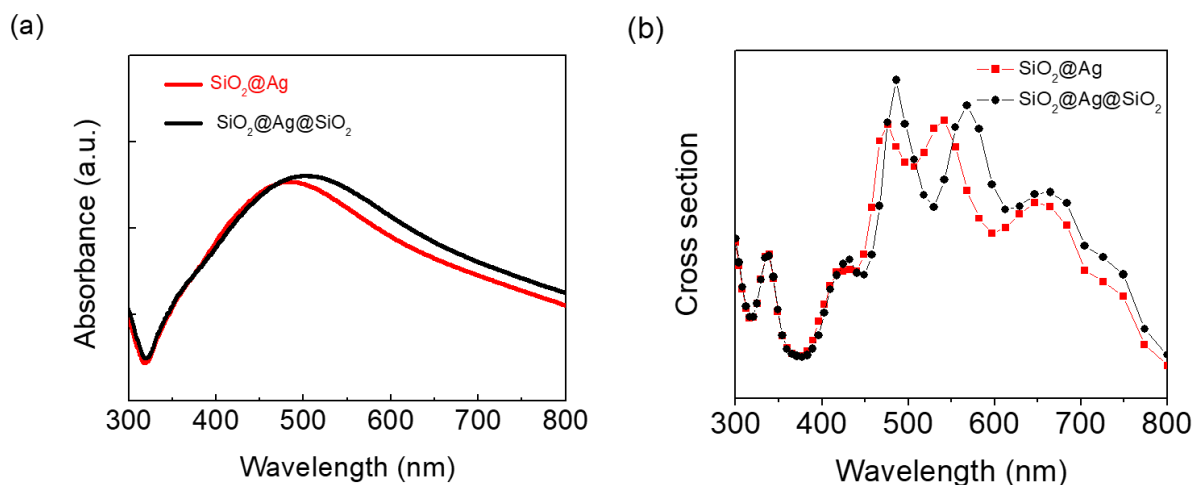


**Figure 46** UV-vis absorbance spectra of experimental (a) and theoretical data calculated by FDTD simulations of 110 nm core shell particles in aqueous solution.

In order to explore the effects of the plasmonic nanoparticles on the optical properties of  $\text{BiVO}_4$  films, the extinction spectra of bare and plasmonic particle coated  $\text{BiVO}_4$  films are measured. A film thickness of  $\text{BiVO}_4$  film is 800 nm. Monoclinic phase  $\text{BiVO}_4$  has a band gap of  $\sim 2.4$  eV which corresponds to the light wavelength of 518 nm. The absorption edge of bare  $\text{BiVO}_4$

film shown in Figure 47 is also at  $\sim 520$  nm. Figure 47 shows that the plasmonic nanoparticles ( $\text{SiO}_2@Ag$  and  $\text{SiO}_2@Ag@SiO_2$ ) facilitate light absorption of  $\text{BiVO}_4$  film near the band edge where the extinction coefficient of the plasmonic particles is found. Consequently, light transmittance decreases by a half at the wavelength of 500 nm at which  $\text{BiVO}_4$  film can convert photons to electron-hole pairs. This enhanced absorption of the plasmonic particle coated  $\text{BiVO}_4$  film suggests that the plasmonic nanoparticles can promote the photocatalytic activity of  $\text{BiVO}_4$  film using photons of the band edge. It is noted that the transmittance of even base  $\text{BiVO}_4$  film does not get close to 100 % for red light which is far beyond the band edge of  $\text{BiVO}_4$  film. This is attributed to the presence of defect levels, the additional scattering of the  $\text{BiVO}_4$  supporter which has a large refractive index<sup>110</sup>, the formation of an indirect charge transfer band and additional energy states within the bandgap of  $\text{BiVO}_4$ .

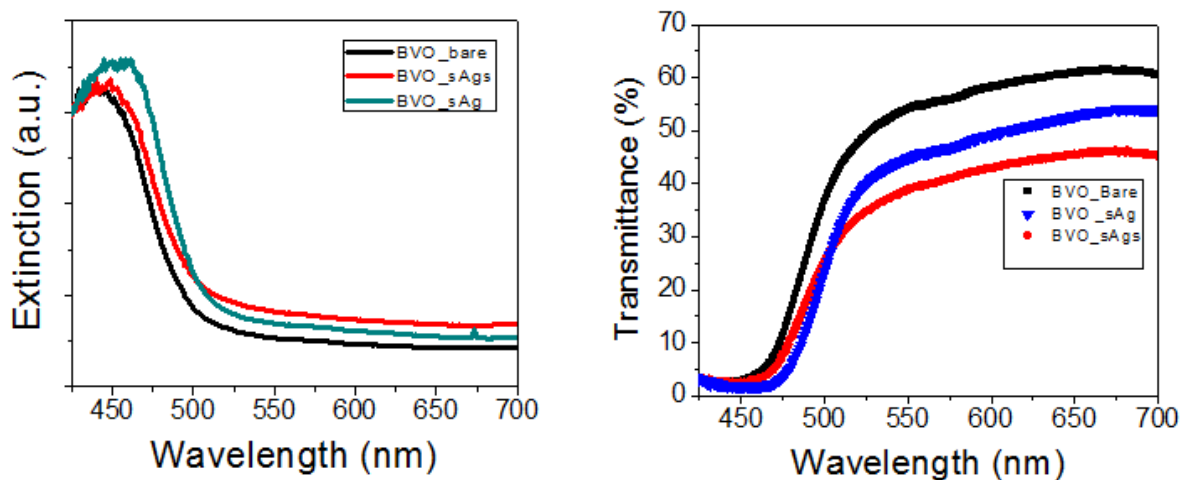


**Figure 47** UV-visible extinction (left) and transmittance spectra (right) of bare and plasmonic particle coated  $\text{BiVO}_4$  thin film. BVO:  $\text{BiVO}_4$ , sAg:  $\text{SiO}_2@Ag$ , sAgs:  $\text{SiO}_2@Ag@SiO_2$

Experimental results in Figure 47 are verified using FDTD simulation. Figure 48(a) shows the absorption spectra of bare and plasmonic particle coated BiVO<sub>4</sub> thin film. Enhancement of light absorption near the band edge of BiVO<sub>4</sub> thin film is clearly confirmed in both cases of SiO<sub>2</sub>@Ag and SiO<sub>2</sub>@Ag@ SiO<sub>2</sub> particles. The absorption spectra of the plasmonic particle coated BiVO<sub>4</sub> film has a local maximum peak at  $\lambda = 465$  nm which is not found in the absorption spectra of bare BiVO<sub>4</sub>. Enhanced light absorption by the surface plasmons and its effect on the photoelectrochemical reaction have been extensively studied. When plasmonic nanoparticles is illuminated with light at their resonance frequency, electrons in the plasmonic particles resonate and change local electric field intensity and light propagation direction.<sup>111</sup> If the plasmonic particles are in contact with the semiconductor, the surface plasmon resonance increases electric field intensity near the plasmonic particles and enhances light absorption of the semiconductor at the metal – semiconductor interface.<sup>112</sup> This is called a near-field effect. In addition, the plasmonic particles on the semiconductor scatter incident photons and elongate the photon path in the semiconductor. This, in turn, increases the effective absorption thickness of the semiconductor and causes the semiconductor to absorb more light, which is called a far-field effect. The third effect of the surface plasmon resonance is generation of hot carriers in the metal part. If these hot electrons (or holes) have sufficient energy, they can move into the conduction band of n-type semiconductor (or the valence band of p-type semiconductor) and contribute to the electrochemical reaction at the semiconductor – electrolyte interface.

In this study, all three effects can influence the enhanced absorption. To examine the role of the near-field effect, the absorption contour of bare and plasmonic particle coated BiVO<sub>4</sub> film are also simulated at  $\lambda = 465$  nm. We chose this wavelength because the plasmonic effect is clearly absorbed in the absorption spectra and light transmittance is close to 0 even in 800 nm thick bare

BiVO<sub>4</sub> film. Figures 48 (b-1), (b-2) and (b-3) show absorption contour plots of bare and plasmonic particle coated film. When plasmonic particles are added, light absorption of BiVO<sub>4</sub> film increases dramatically near the surface of plasmonic particles. In bare BiVO<sub>4</sub> film, 200 nm thick layer is required to absorb most of incident blue light. However, in plasmonic particle coated BiVO<sub>4</sub> film, strong absorption occurs from the surface to 100 nm deep region of the film. Regardless of plasmonic particle coating, absorption of 465 nm light at the bottom of 800 nm thick BiVO<sub>4</sub> film is negligible. This suggests that the role of the plasmonic nanoparticle in the absorption of blue light is to confine the location of absorption to the surface region of the semiconductor through the near-field effect. In addition, the absorption of silver nanoshell is also found in the simulation results of Figures 48 (b-2) and (b-3). This indicates that hot electrons are produced in the nanoshell by 465 nm light. However, the effect of scattering on the light absorption is not found in our simulation results.

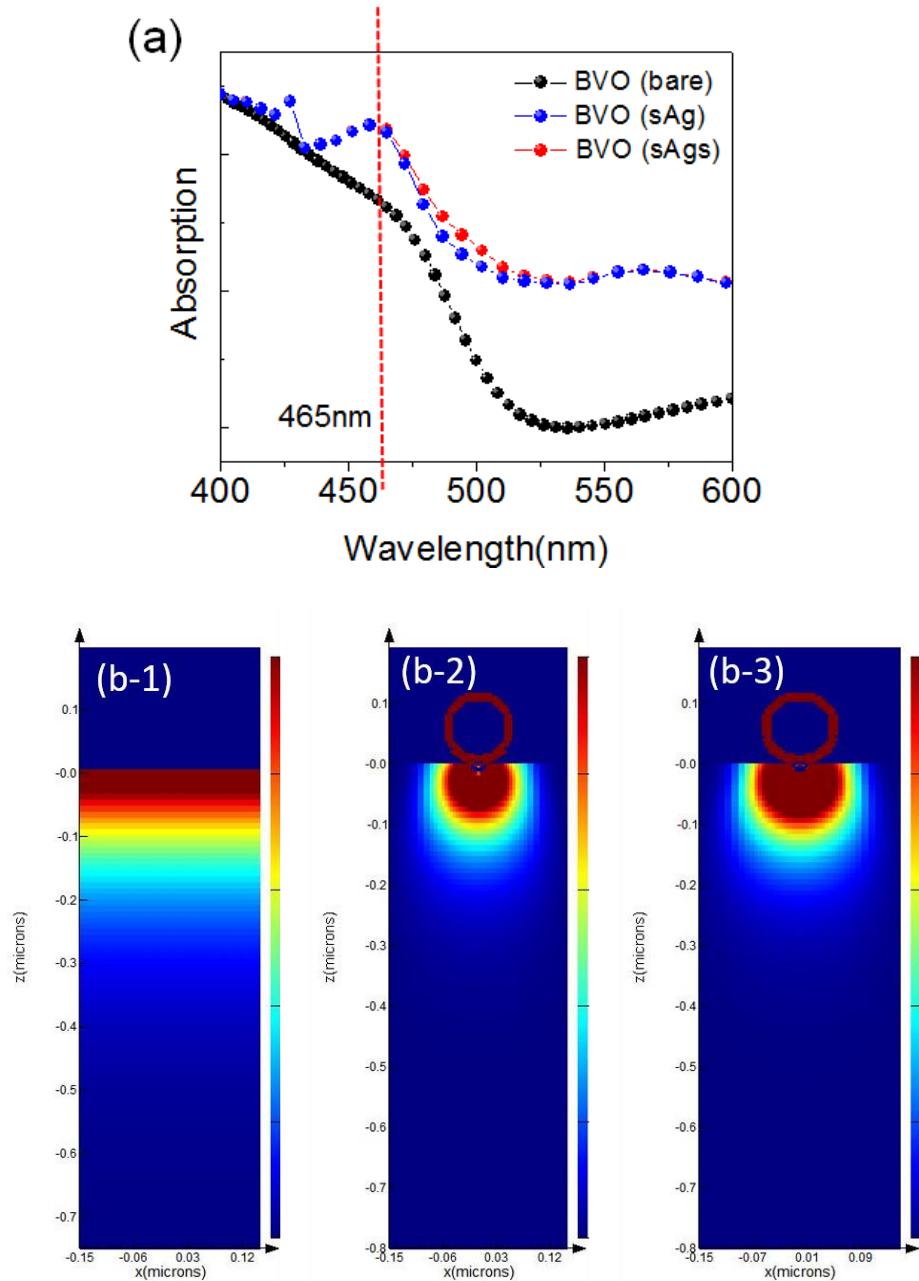


**Figure 48** Calculated light absorption of bare and plasmonic particle coated BiVO<sub>4</sub> films using FDTD simulation results (light is illuminated from the top surface) ; (a) Absorption spectra of bare and plasmonic particle (SiO<sub>2</sub>@Ag and SiO<sub>2</sub>@Ag@SiO<sub>2</sub>) coated BiVO<sub>4</sub> film, (b) absorption contour plot (b-1: bare BiVO<sub>4</sub> film, b-2: SiO<sub>2</sub>@Ag coated BiVO<sub>4</sub> film, b-3: SiO<sub>2</sub>@Ag@SiO<sub>2</sub> coated BiVO<sub>4</sub> film).

### 4.2.3 Effect of Plasmonic Nanoparticles on Photoelectrochemical Performance of BiVO<sub>4</sub> Film

Electrochemical properties of bare and plasmonic nanoparticles modified BiVO<sub>4</sub> photoelectrodes were examined both in a dark condition and a solar illumination condition. Current density vs. voltage (J-V) curves of bare, SiO<sub>2</sub>@Ag and SiO<sub>2</sub>@Ag@SiO<sub>2</sub> coated BiVO<sub>4</sub> photoanodes under simulated solar light (AM1.5G, 100mW/cm<sup>2</sup>) are shown in Figure 49. For this measurement, pH of the buffered electrolyte was controlled to be 7. As the applied positive potential increases, all samples exhibit a steady increase of the photocurrent responses with negligible dark currents. By imposing a positive bias to BiVO<sub>4</sub> film/rear FTO contact, the minority charge carrier (hole) and the majority charge carrier (electron) are driven toward BiVO<sub>4</sub>/electrolyte interface and BiVO<sub>4</sub>/FTO interface, respectively. Holes at BiVO<sub>4</sub>/electrolyte participate in water oxidation reaction and oxygen evolves.

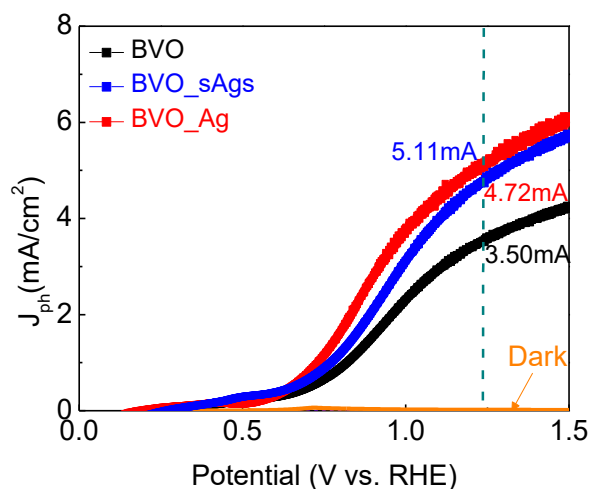


**Figure 49** J-V curves of bare and plasmonic nanoparticle coated BiVO<sub>4</sub> thin films at AM 1.5 condition (light is illuminated from the electrolyte – BiVO<sub>4</sub> interface or the electrolyte – plasmonic particle/BiVO<sub>4</sub> interface). BVO: BiVO<sub>4</sub>, sAg: SiO<sub>2</sub>@Ag, sAgs: SiO<sub>2</sub>@Ag@SiO<sub>2</sub>

At 1.23V vs. RHE, photocurrent density of bare BiVO<sub>4</sub> photoanode is 3.50 mA/cm<sup>2</sup> which is higher than most of BiVO<sub>4</sub> photoanodes in previous studies. This higher photocurrent is attributed to preferentially [001]-oriented growth and facet engineering of BiVO<sub>4</sub> film. Given that randomly oriented polycrystalline BiVO<sub>4</sub> photoanodes suffers from poor charge transport and low electron-hole separation efficiency, this result indicates that the controlled growth along [001] orientation greatly improves charge transport and suppresses electron-hole recombination. A further remarkable increase in the photocurrent is observed in plasmonic particle coated photoanodes. The photocurrent density of SiO<sub>2</sub>@Ag coated BiVO<sub>4</sub> photoanode and SiO<sub>2</sub>@Ag@SiO<sub>2</sub> coated BiVO<sub>4</sub> photoanode increases to 5.11 /cm<sup>2</sup> and 4.74 mA/cm<sup>2</sup>. Compared with bare BiVO<sub>4</sub> photoanode, 46% (SiO<sub>2</sub>@Ag) and 35% (SiO<sub>2</sub>@Ag@SiO<sub>2</sub>) improvement of PEC performance are found.

As explained in section 4.2, the surface plasmons of SiO<sub>2</sub>@Ag and SiO<sub>2</sub>@Ag@SiO<sub>2</sub> particles can increase PEC performance via three different ways; near-field effect, scattering and hot electrons. The near-field effect of the surface plasmons is to strengthen the electric field near the nanoparticle. One of mechanisms to cause the near-field is plasmon resonance energy transfer (PRET). In addition, the nanostructured metal can affect PEC performance by improving a catalytic efficiency at the semiconductor – electrolyte interface or changing local temperature (thermal heating). To examine the role of the surface plasmon on PEC performance, incident photon to current conversion efficiency (IPCE) was measured. Figure 50 shows IPCE of bare, SiO<sub>2</sub>@Ag and SiO<sub>2</sub>@Ag@SiO<sub>2</sub> BiVO<sub>4</sub> film under front illumination. Positive bias (1.23 V vs. RHE) was applied to BiVO<sub>4</sub>/FTO side using a three-electrode system. IPCE of bare BiVO<sub>4</sub> photoanode is around 60% at  $\lambda = 350 - 460$  nm and drops to 0 % at  $\lambda = 520$  nm that matches the

band edge of BiVO<sub>4</sub>. Photocurrent density from the Integration of IPCE closely coincides with the current density of *J–V* curve at 1.23 V vs. RHE (Figure 49).

When the plasmonic particles are coated, the IPCE spectrum shows two apparent changes. First, the photon - electron conversion near the band edge ( $460 \text{ nm} < \lambda < 520 \text{ nm}$ ) increases. At  $\lambda = 480 \text{ nm}$ , IPCE increases from 30 % to 51 % (SiO<sub>2</sub>@Ag) and 55 % (SiO<sub>2</sub>@Ag@SiO<sub>2</sub>). This change is due to an increase in the light absorption near the band edge by the surface plasmons. A change in the light absorption itself is experimentally measured and theoretically calculated (Figures 47 and 48). Since the surface plasmon resonance frequency of Ag nanoshell coincides with the band edge of BiVO<sub>4</sub>, the light absorption coefficient of BiVO<sub>4</sub> film is promoted by the Ag nanoshell. Second, the plasmonic particle coating increases IPCEs of BiVO<sub>4</sub> to 70 ~ 80 % at  $\lambda = 350 - 460 \text{ nm}$  where even bare BiVO<sub>4</sub> film exhibits 0 % transmittance. Given that both bare and plasmonic particle coated BiVO<sub>4</sub> films absorb all incident photons, an increase in IPCE at  $\lambda = 350 - 460 \text{ nm}$  cannot be explained by a change in light absorption.

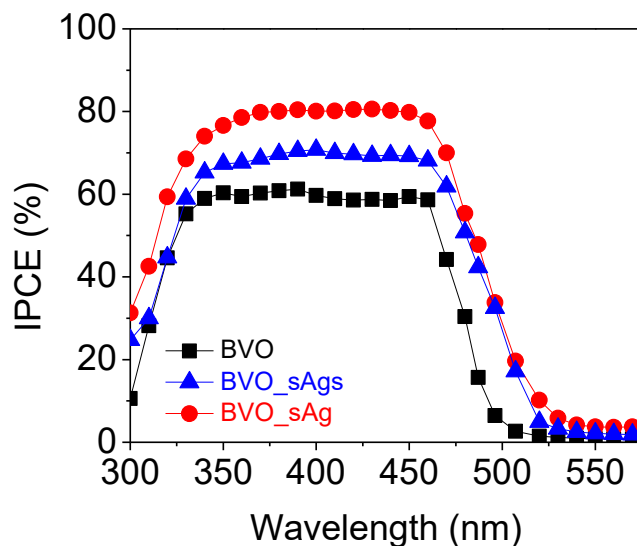
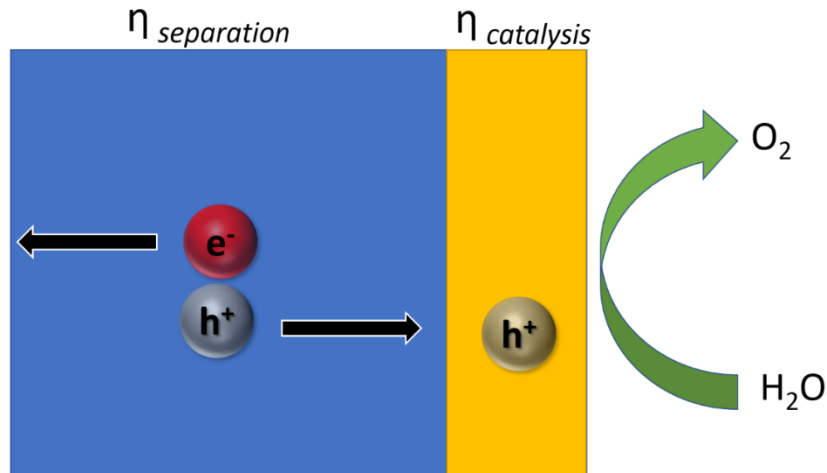


**Figure 50** Incident photon to current conversion efficiency (IPCE) measured at 1.0 V vs RHE of the bare BiVO<sub>4</sub>: BVO, SiO<sub>2</sub>@Ag/BiVO<sub>4</sub> (sAg) and SiO<sub>2</sub>@Ag@SiO<sub>2</sub> /BiVO<sub>4</sub> (sAgs).

Although employment of plasmonic particles significantly enhances the PEC performance of BiVO<sub>4</sub> photoanode, it is difficult to fully elucidate the improvement performance from a viewpoint of total amount of absorbed photons. To better understand the improvement of photocurrent, the charge separation and surface catalysis of bare and plasmonic nanoparticle coated BiVO<sub>4</sub> films are examined. The conversion of incident photon to photocurrent ( $J_{ph}$ ) requires three fundamental processes of a photoanode: light absorption expressed as current density ( $J_{abs}$ ), charge separation efficiency in BiVO<sub>4</sub> ( $\eta_{separation}$ ) and catalysis efficiency at BiVO<sub>4</sub> – electrolyte interface for water oxidation ( $\eta_{catalysis}$ ). A relationship between  $J_{ph}$  and three processes are given by:

$$J_{ph} = J_{abs} \times \eta_{separation} \times \eta_{catalysis}$$

$J_{abs}$  is calculated from the light absorption spectrum and the solar irradiance curve at AM1.5G condition. Contributions of  $\eta_{separation}$  and  $\eta_{catalysis}$  to PECs are evaluated by conducting the photoelectrochemical measurements in the presence of 0.5 M H<sub>2</sub>O<sub>2</sub>. H<sub>2</sub>O<sub>2</sub> is an effective hole scavenger and the photooxidation of H<sub>2</sub>O<sub>2</sub> is 10 times faster than H<sub>2</sub>O. Therefore, holes fully participate in the photoelectrochemical reaction and  $\eta_{catalysis}$  is assumed to be 100 %. A procedure to calculate  $J_{abs}$ ,  $\eta_{separation}$  and  $\eta_{catalysis}$  is schematically explained in Figure 51.



$$J_{\text{H}_2\text{O}} = J_{\text{abs}} \times \eta_{\text{separation}} \times \eta_{\text{catalysis}}$$

$$J_{\text{H}_2\text{O}_2} = J_{\text{abs}} \times \eta_{\text{separation}} \quad (\text{catalytic efficiency assumed to be 100 \%})$$

**Figure 51** A schematic explanation of separation and catalysis on photoanodes and equations to calculate  $J_{\text{ph}}$ ,  $J_{\text{abs}}$ ,  $\eta_{\text{separation}}$  and  $\eta_{\text{catalysis}}$ .

Figure 52 shows the change in  $J_{\text{abs}}$ ,  $\eta_{\text{separation}}$  and  $\eta_{\text{catalysis}}$  of  $\text{BiVO}_4$  photoanodes. It is noted that the plasmonic particles increases  $J_{\text{abs}}$ ,  $\eta_{\text{separation}}$  and  $\eta_{\text{catalysis}}$ .  $J_{\text{abs}}$  of the photoanode well matches the absorption spectra. The plasmonic particles increase  $J_{\text{abs}}$  by promoting the light absorption near the band edge ( $460 \text{ nm} < \lambda < 520 \text{ nm}$ ), which suggests that the theoretical photocurrent of the plasmonic particle coated  $\text{BiVO}_4$  photoanode is larger than that of bare  $\text{BiVO}_4$  photoanodes.

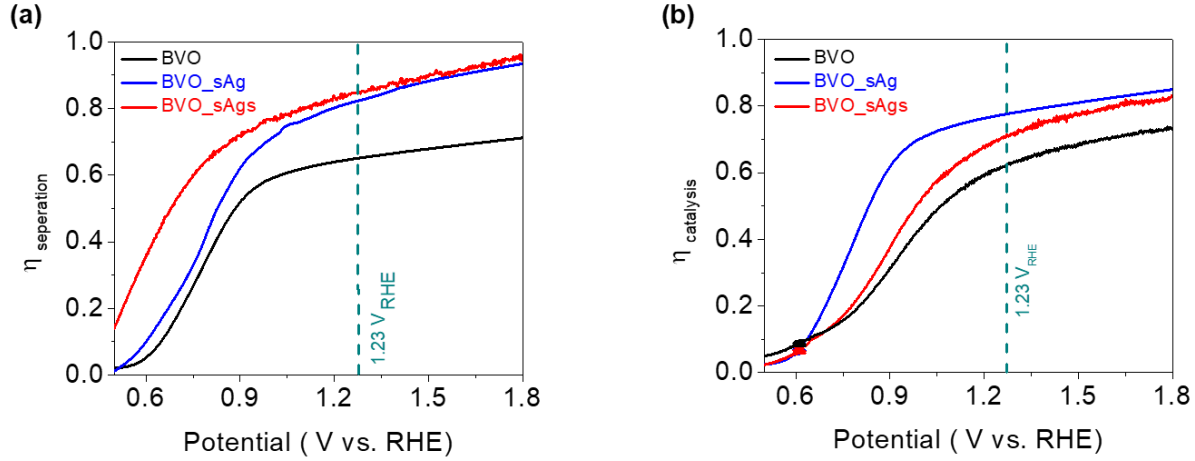


**Figure 52** Separation (a) and catalysis (b) efficiencies of bare  $\text{BiVO}_4$ ,  $\text{SiO}_2@\text{Ag}@\text{SiO}_2$  and  $\text{SiO}_2@\text{Ag}$  plasmonic particles decorated  $\text{BiVO}_4$  thin films.

In  $300 \text{ nm} < \lambda < 460 \text{ nm}$ , all three photoanodes exhibit similar  $J_{\text{abs}}$ . However, an improvement  $\eta_{\text{separation}}$  and  $\eta_{\text{catalysis}}$  is found in the plasmonic particle coated photoanodes. While  $\eta_{\text{separation}}$  of bare  $\text{BiVO}_4$  photoanode is 65 %,  $\text{SiO}_2@\text{Ag}$  and  $\text{SiO}_2@\text{Ag}@\text{SiO}_2$  coated photoanode is 85 % and 81 %, respectively. This suggests that the plasmonic particles control not only the absorption coefficient but also the carrier transport. Given that the light absorption is confined toward the  $\text{BiVO}_4$  - electrolyte interface in the plasmonic particles, an improvement of  $\eta_{\text{separation}}$  results from a shorter transport distance of electrons and an electric bias at the depletion region of  $\text{BiVO}_4$  film. Bare  $\text{BiVO}_4$  and plasmonic particle coated  $\text{BiVO}_4$  absorb a same amount of photons at  $300 \text{ nm} < \lambda < 460 \text{ nm}$ . However, our theoretical study in Figure 48 shows that light penetration depth at which the light intensity falls to  $1/e$  of the incident light intensity is  $\sim 200 \text{ nm}$  for Bare  $\text{BiVO}_4$  and  $\sim 100 \text{ nm}$  for plasmonic particle coated  $\text{BiVO}_4$ . Since the depletion region width of  $\text{BiVO}_4$  at the  $\text{BiVO}_4$  - electrolyte interface is  $\sim 100 \text{ nm}$ , the shorter penetration depth of the plasmonic nanoparticle coated  $\text{BiVO}_4$  photoanodes suggests that most photogenerated electron -

hole pairs can be separated. In bare BiVO<sub>4</sub> photoanode, however, more electron - hole pairs are produced outside the depletion region and  $\eta_{\text{separation}}$  becomes smaller.

The plasmonic particles also increase  $\eta_{\text{catalysis}}$  due to the catalytic effect of noble Ag shell.  $\eta_{\text{catalysis}}$  at 1.23 V vs. RHE is 62 % for bare BiVO<sub>4</sub> photoanode and 72 % for SiO<sub>2</sub>@Ag@SiO<sub>2</sub> coated BiVO<sub>4</sub> photoanode. Though an outer thin layer of SiO<sub>2</sub> suppresses the catalytic reaction, the Ag nanoshell of SiO<sub>2</sub>@Ag@SiO<sub>2</sub> still promotes the water oxidation. The improvement is more obvious in SiO<sub>2</sub>@Ag coated BiVO<sub>4</sub> photoanode, since the Ag nanoshell is directly exposed to the electrolyte without a shielding layer. A change in  $\eta_{\text{catalysis}}$  is also supported by a negative shift of the onset potential in J-V curves of Figure 49. This indicates that the quasi Fermi level of the photoanode depends on the plasmonic particle coating. While the onset potential is 280mV vs. RHE in bare BiVO<sub>4</sub> photoanode, the plasmonic particle coated BiVO<sub>4</sub> photoanodes exhibit a negative shift. After the plasmonic particles are coated, it is 190 mV vs. RHE (SiO<sub>2</sub>@Ag) and 210mV vs. RHE (SiO<sub>2</sub>@Ag@SiO<sub>2</sub>), respectively.

Stability under illumination for certain periods of time is an important parameter especially for feasible energy conversion systems. In order to check the stability of samples upon illumination, photocurrent vs. time performance of bare-BiVO<sub>4</sub>, BiVO<sub>4</sub>\_SiO<sub>2</sub>@Ag and BiVO<sub>4</sub>\_SiO<sub>2</sub>@Ag@SiO<sub>2</sub> films were tested for several cycles of 30 s intervals light off and on and under continuous irradiation at 1.23 V vs. RHE under AM 1.5G illumination for 15 mins. The chronoamperometric current vs time (i-t) curves are shown in Figure 53 and Figure 54 respectively. We observed fast and uniform photocurrent responses for each switch on and switch off event for all electrodes. Fast and uniform photocurrent responses are observed for each switch-on and switch-off mode for all electrodes. The maximum current of the chopped light LSV is approximately linear and is reached spontaneously upon illumination. In addition to these LSV

behaviors chopped LSV measurements give much better idea about the stability of the resultant plasmonic modified BiVO<sub>4</sub> films. Normally the stability of bare BiVO<sub>4</sub> films decrease within few minutes. This low stability is can be explained by accumulation of photoinduced holes at the surface of BiVO<sub>4</sub> photoanode, these accumulated photogenerated holes may result in oxidation of solution species (absorbed H<sub>2</sub>O molecules or OH- groups) at the surface of BiVO<sub>4</sub>, due to sluggish kinetics of water oxidation and poor carrier transport properties of BiVO<sub>4</sub> and due to the poor catalytic nature of BiVO<sub>4</sub> for water oxidation.<sup>113</sup>. For each bias potential, the data are compared with bare BiVO<sub>4</sub> and plasmonics particle decorated BiVO<sub>4</sub>. The stability of plasmonic particles decorated BiVO<sub>4</sub> is enhanced compared to the bare-BiVO<sub>4</sub> samples. Within 15 mins the decay is only about 4%, which is significantly improved ( $\approx 10$  times) compared with 40% decay for the bare-BiVO<sub>4</sub> samples. Moreover; bare BiVO<sub>4</sub> samples were diagnosed by the initial “spiked” and subsequent decay photocurrent-time profiles which can be attributed to trap mediated recombination prevails. In contrast, these spikes are absent for plasmonics particle decorated BiVO<sub>4</sub> at the same potential indicating that the better surface quality of plasmonics particle decorated BiVO<sub>4</sub> and suppressed recombination at the surface. The photocurrent spikes are mainly related with the charge carrier generation and recombination behavior of the photoanode material of interest. Plasmonic particles decorated BiVO<sub>4</sub> can consume all holes reaching its surface for water oxidation and therefore is shown to be stable for water oxidation. And the accumulated holes at the semiconductor electrolyte interface believed to trigger the photo-corrosion and therefore resulting low stability. Deposition of plasmonic particles suppress the recombination possibility of photoinduced electrons and holes and this improvement can be attributed to enhanced photoinduced charge carrier transport within the semiconductor and electrolyte interface. Therefore, the photostability of bare BiVO<sub>4</sub> films can be significantly improved by surface

modification with SiO<sub>2</sub>@Ag core shell plasmonic particles. During performance of the stability experiments; O<sub>2</sub> bubbles collected on photoanode surface were removed by manual shaking which may cause fluctuation of photocurrent. The amount of deposited SiO<sub>2</sub>@Ag nanoparticles should not be too high, because Ag can form a disadvantageous, smooth surface and bigger agglomerates, which absorb in the IR range <sup>114</sup>.

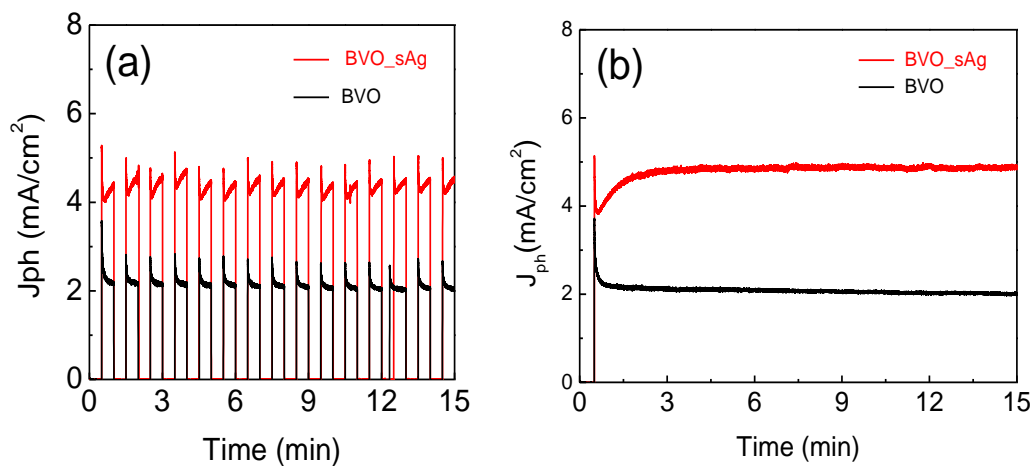


**Figure 53** Amperometric i-t measurements for BiVO<sub>4</sub> and core shell particles decorated BiVO<sub>4</sub>.

BiVO<sub>4</sub> (BVO), BiVO<sub>4</sub>\_SiO<sub>2</sub>@Ag (BVO\_sAg) and BiVO<sub>4</sub>\_SiO<sub>2</sub>@Ag@SiO<sub>2</sub> (BVO\_sAgs)

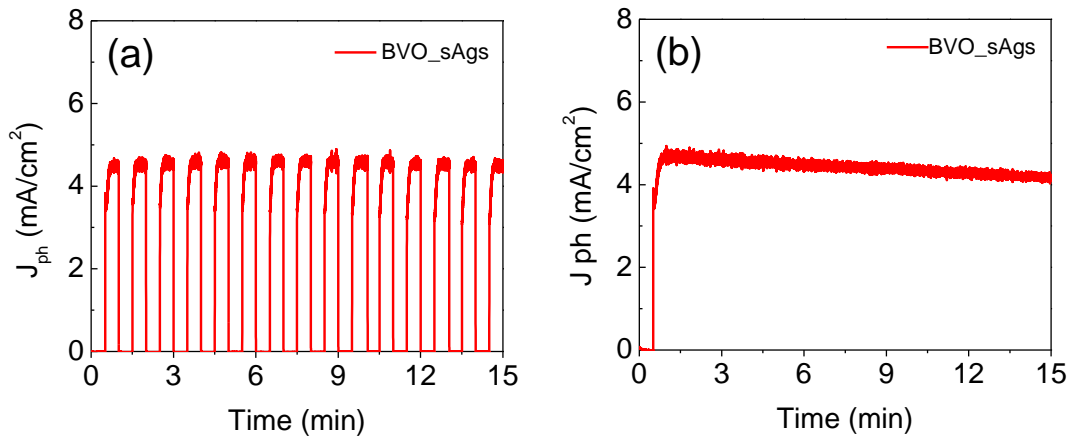


**Figure 54** Amperometric i-t measurements for  $\text{BiVO}_4$  and core shell shell particles decorated  $\text{BiVO}_4$ .  $\text{BiVO}_4$ : BVO,  $\text{SiO}_2@Ag$  (sAg) and  $\text{SiO}_2@Ag@SiO_2$  (sAgs)

#### 4.2.4 Discussion on the Effect of Confined Light Absorption on Overall PEC Performance

According to our proposed model plasmonic nanoparticles (PNPs) decorated on  $\text{BiVO}_4$  thin films work mainly in two ways to enhance light subwavelength metal nanoparticles decorates on either front or back of the semiconductor light absorbing material scatters incident light into various angles, increasing the path length of the light within the absorbing layer. (Figure 55)

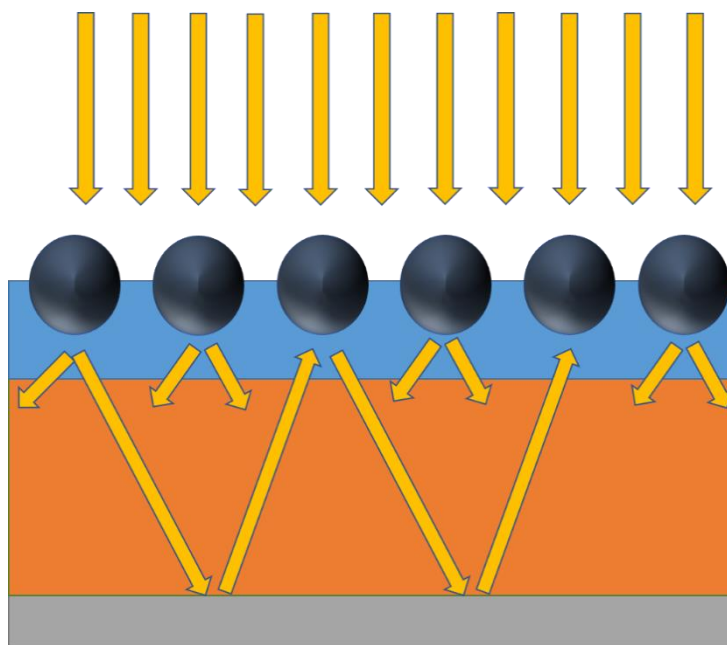


**Figure 55** Light trapping by plasmonic nanoparticles from metal nanoparticles on the top surface of the semiconductor thin film ( $\text{BiVO}_4$ )

Accompanying efficient scattering, PNPs also contribute to localized enhancement of the electric field especially at the surface of  $\text{BiVO}_4$ .  $\text{BiVO}_4$  surface proximate to the Ag plasmonic PNPs confronts an enhanced electric field, which illustrated in FDTD-calculated simulation results at different wavelengths in Figure 56. This localized field enhancement also contributes to electron-hole pair formation and diminishes recombination rate. The highest localized field effect can be seen in the neighborhood of Ag plasmonic nanoparticles, which suggests PNPs induced electron-hole pair formation should be the enormous essentially at the  $\text{BiVO}_4$ -electrolyte interface. The benefits of surface decoration of  $\text{BiVO}_4$  with PNPs hence electron-hole pair formation near semiconductor-electrolyte interface instead of bulk  $\text{BiVO}_4$  can be summarized as follows; *firstly* efficient charge carrier separation under the influence of surface potential which suppresses recombination rate, and *secondly* efficiently separated charge carriers with less recombination can

migrate to the surface in a shorter distance than in bulk case; resulting in improvement in photocatalytic efficiency. So as a result, our BiVO<sub>4</sub>/PNPs system has an improved PEC performance due to intense localized electric field, increased electron-hole pair formation rate at the BiVO<sub>4</sub> surface and reduced recombination rate proximate to the surface, outcoming as large PEC improvements.

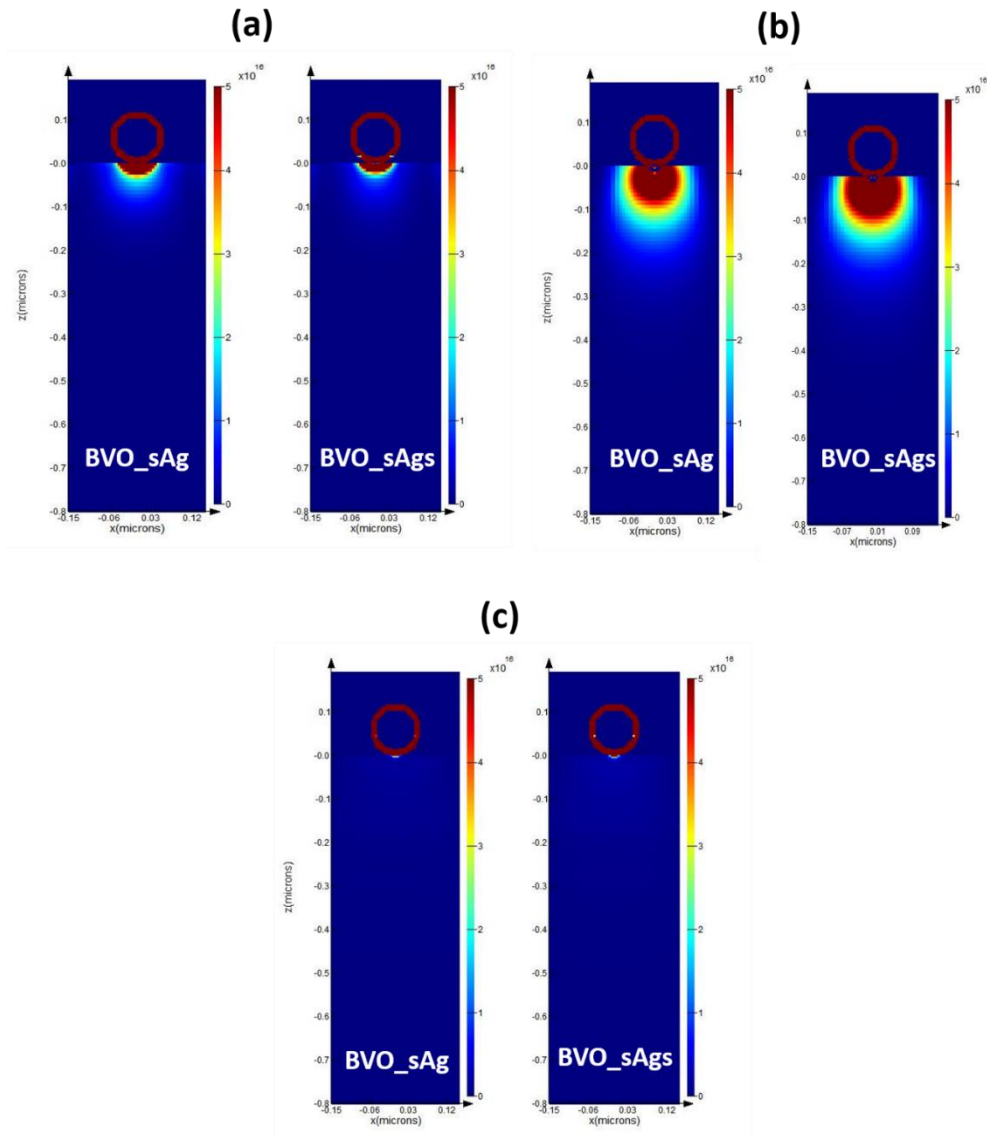


**Figure 56** FDTD calculated simulation results for plasmonics effect at a contour plot of absorption at different wavelengths (a)  $\lambda=400$  nm, (b)  $\lambda=465$  nm, and (c)  $\lambda=600$  nm.

BiVO<sub>4</sub>: BVO, SiO<sub>2</sub>@Ag (sAg) and SiO<sub>2</sub>@Ag@SiO<sub>2</sub> (sAgs)

## **5.0 PANCHROMATIC PHOTOELECTROCHEMICAL CELLS USING VERTICAL ALIGNMENT OF CdS AND CdSe ON SnO<sub>2</sub> NANOWIRES**

### **5.1 OBJECTIVES**

A fundamental problem of nanoparticles-based photoelectrochemical (PEC) cells is that there is a mismatch between the solar spectrum and the light absorption spectrum of quantum dots (QD). Since the absorption spectrum of nanoparticles is much narrower than the solar spectrum, a single type of QDs absorbs only part of solar spectrum and a large portion of the solar energy is not harvested by PEC cells. To circumvent this problem, we will selectively position the multiple kinds of QDs along the longitudinal direction of nanowires (NWs) so that different QDs absorb different parts of the solar light. For photoelectrochemical (PEC) hydrogen production, low charge transport efficiency of a photoelectrode is one of the key factors that largely limit the PEC performance enhancement. We have studied tin-oxide (SnO<sub>2</sub>) nanowires array (NWs) based CdSe/CdS/TiO<sub>2</sub> multi-shelled heterojunction photoelectrode. SnO<sub>2</sub> is a promising wide band gap metal oxide nanostructure because of its good electronic mobility, conductivity, and good stability due to its large bandgap. SnO<sub>2</sub> has higher electronic mobility (240 cm<sup>2</sup>/Vs) and better electronic conductivity compared to most widely used metal oxides TiO<sub>2</sub> and ZnO. Furthermore, it is a good charge acceptor because its conduction band minimum is more negative conduction band edge

(0.40 eV compared to anatase TiO<sub>2</sub>) and this can promote effective charge separation and transportation from a narrow band gap semiconductor especially light sensitizer such as PbS, PbSe, and metal chalcogenides. Moreover, the morphology and structure of photoanode is another important aspect affecting the resultant PEC device performance. Nanoparticles based photoelectrodes provide enough catalytic active sites and sites for sensitizer absorption, but they suffer from poor electron transport rate and poor photogenerated charge carrier efficiency. Alternatively, one dimensional metal oxide nanostructures provide better charge collection efficiency, increased surface area, a direct conductive pathway for charge carriers hence improved interfacial charge transfer. Photoelectrochemical cells composed of only semiconducting light sensitizers show inferior performance due to serious recombination losses because the electron transport route referred as random walk and low stability in aqueous media. Heterojunction with a wide band metal oxide nanostructure is a convenient way to suppress this limitation and a better power conversion efficiency. Although chalcogenide-based semiconductors are not able to carry out unassisted solar water splitting since they quickly photocorrode in aqueous solutions, this limitation can be overcome by adding sacrificial agents (i.e., Na<sub>2</sub>SO<sub>3</sub> or Na<sub>2</sub>S) into an aqueous solution. Once the heterojunction is formed between wide band gap metal oxide and narrow band gap sensitizer, it not only improves the separation of photogenerated charge carriers, but also suppresses recombination of electron-hole pairs and prolongs the lifetime of photogenerated charge carriers.

In this regard, efficient sunlight-driven water splitting devices can be fabricated by pairing two light sensitizers of different bandgaps. These heteronanostructures with different bandgap materials may provide new opportunities such as, utilization of a larger fraction of solar spectrum and formation of additive photovoltages by each absorber material which can meet the water

electrolysis energy demand. Herein we demonstrate that multi-shelled one-dimensional (1-D) heterojunction photoelectrode has a superior charge transport efficiency, leading to a greatly improved photocurrent density ( $\sim 16.2 \text{ mA/cm}^2$  at 1.0 V vs. RHE).  $\text{SnO}_2$  NWs with an average length of  $\sim 15 \text{ }\mu\text{m}$  are grown on FTO/glass substrate by vapor-liquid-solid method. Subsequently, the  $\text{TiO}_2$  and CdSe/CdS shell layers are deposited by an atomic layer deposition (ALD) and a facile electrochemical deposition method, respectively.

For an efficient PEC cell design using CdSe, CdS and  $\text{SnO}_2$  heterojunction, two important criteria should be taken into account. The first one is the light absorption range of the semiconductor in use which is responsible for light harvesting capability of the PEC cell. The second criterion is the electron levels of the conduction band edge of semiconductor materials in the heterojunction. This will have an impact on the electron injection efficiency and charge recombination at the semiconductor/semiconductor junction and semiconductor/electrolyte interface. The conduction band edge of wide band gap materials should be lower position than narrower band gap sensitizers and a high charge carrier mobility, CdS and CdSe have higher level conduction band edges with respect to  $\text{SnO}_2$  which may result in higher electron injection efficiency.<sup>115</sup>

The specific objective is to demonstrate an efficient tandem device using  $\text{SnO}_2$  nanowires as a main scaffold for different band gap light absorbing materials coating and carrier collection. CdS and CdSe are semiconductors with direct bandgap of 2.25 and 1.70 eV. There has been extensive study on the coating of sensitizers along the radial direction of nanowires. However, the sequential coating of semiconductors along the longitudinal direction of the nanowire has not been explored. If different kinds of semiconductors harvesting blue and green effectively, are selectively positioned along the longitudinal direction, blue and green light can be absorbed at different parts

of the nanowire array. Given that light with a longer wavelength experiences less scattering, the semiconductor absorbing longer wavelength light is preferred to stay at the bottom of nanowires to minimize the scattering loss.

In this study, CdS absorbing only blue light is placed at the top of the nanowire array and CdSe absorbing blue and green light is placed at the bottom of the arrays. In comparison to the traditional heterojunction structure of CdSe and CdS where CdSe absorbs most of high energy photons, our new design suppresses the absorption of higher energy photon (blue light) by the lower band gap semiconductor (CdSe). This indicates that hot electrons in CdSe have less surplus kinetic energy and thermalization loss is reduced. For the sequential coating along the longitudinal direction, polystyrene (PS) layer is used as a sacrificial layer. Coating and removal of PS layer are performed repeatedly in order to get CdS and CdSe coated vertically along the longitudinal direction of nanowires. This new photoelectrode exhibits panchromatic light absorption capability, low energy loss of hot electrons (i.e. low thermalization loss) and good carrier transport behaviors, all of which contribute to high photocurrent density in PEC reaction.

## **5.2 RESULTS AND DISCUSSION**

### **5.2.1 Microstructure and Crystal Structure of SnO<sub>2</sub> Nanowires Before and After CdS and CdSe Coating Along the Radial Direction**

Figure 57 shows SEM images of SnO<sub>2</sub> nanowires which were grown for 40 minutes and 1 hr. It is clearly seen that SnO<sub>2</sub> NW arrays are grown on the 1.5 nm thick Au layer coated FTO through a vapor-liquid-solid (VLS) mechanism. In this process, Au catalyzes the conversion of Sn vapor and

O<sub>2</sub> to 1-dimensional SnO<sub>2</sub> nanowire. Au metal catalyst forms liquid Au-Sn alloy droplets at elevated temperatures (800 °C). Supersaturation of Sn in Au causes the precipitation of Sn from Au-Sn alloy. The 1D nanowire continue growing as long as the vapor source supplied. After 1 hr growth, SnO<sub>2</sub> NWs have an average length of ~15 μm and a diameter of ~100 nm. A growth time is an important parameter for VLS growth method. Figure 57(b) indicates that 30-minute-long growth reaction produces SnO<sub>2</sub> nanowires with an average length of ~ 6μm.

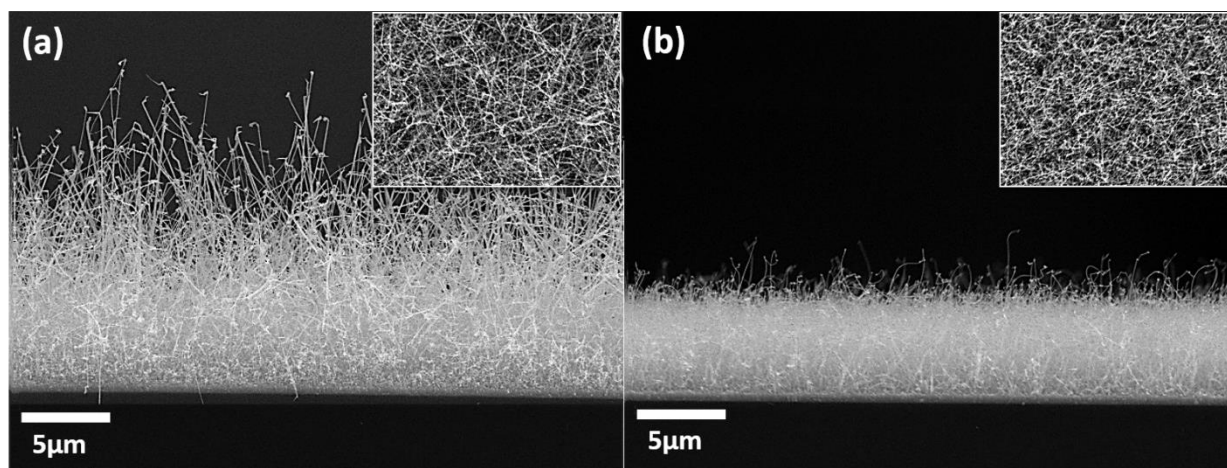


**Figure 57** Cross-sectional SEM images of SnO<sub>2</sub> nanowires that were grown on the Au coated FTO for 1 hr (a) and 30 minutes (b); insets of plan-view images.

We examined the crystal structure of SnO<sub>2</sub> nanowires using XRD. Figure 58 shows the XRD pattern of 1 hr long grown SnO<sub>2</sub> nanowires. Diffraction peaks are indexed as (110), (101), (200), (111), (210), (211), (220) and (002) planes of rutile SnO<sub>2</sub> that has a tetragonal structure. The lattice constant of rutile SnO<sub>2</sub> is  $a = 4.864$  and  $c = 3.249$  (JCPDS: SnO<sub>2</sub>-41-1445). No characteristic peaks of metal phases are observed, though oxygen partial pressure during the growth ambience

is 50mTorr. The strong and sharp peak is an evidence for high crystallinity of SnO<sub>2</sub> nanowires. Rutile tetragonal structures, respectively, were confirmed for SnO<sub>2</sub> nanowires.

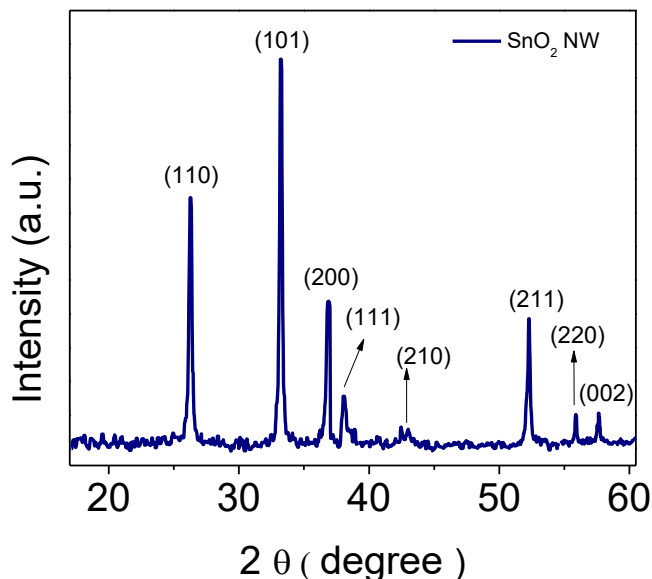


**Figure 58** X-ray Diffraction (XRD) patterns of 1hr long grown SnO<sub>2</sub> nanowires.

In addition to pure SnO<sub>2</sub> nanowires, Sb doped SnO<sub>2</sub> nanowires were synthesized to increase the electric conductivity of SnO<sub>2</sub> nanowires. In Figure 59, the morphologies of pure SnO<sub>2</sub> and Sb-SnO<sub>2</sub> nanowires are compared. The length of the nanowires is controlled to be in the range of ~20 μm. Since Sb doping increased the nanowire length in this study, the growth time of Sb-SnO<sub>2</sub> nanowires was shorter than pure SnO<sub>2</sub> nanowires. A change in the growth rate may be attributed to a change in the melting/solidification temperature in Sn-Sb-Au phase diagram. This has an impact on a driving force for growth of NWs from Au-Sn-Sb liquid.

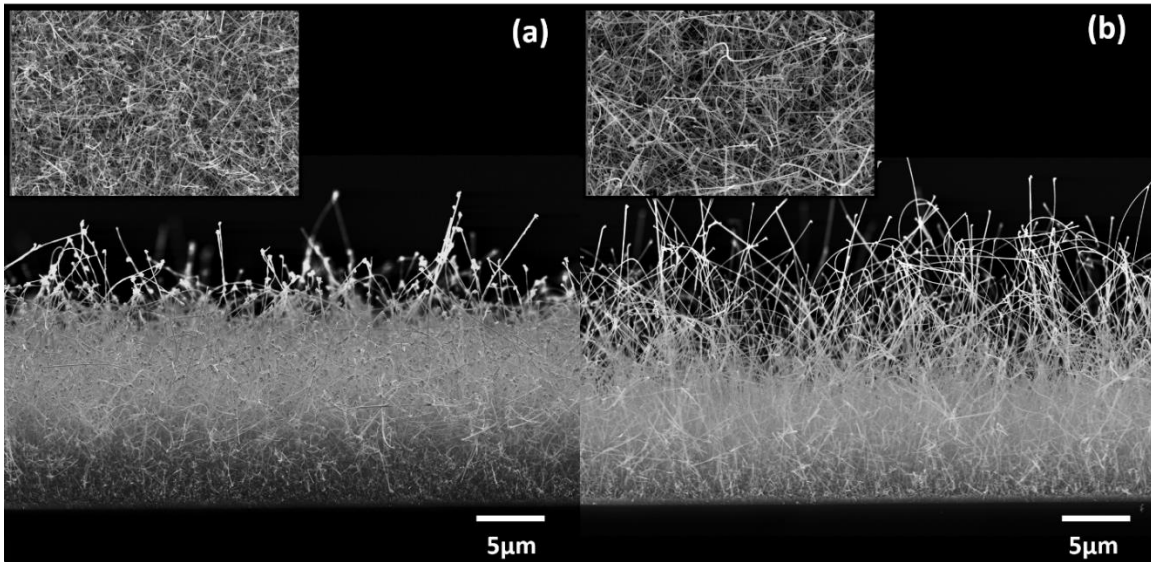


**Figure 59** Cross-sectional SEM images of SnO<sub>2</sub> nanowires (a) and Sb-doped SnO<sub>2</sub> nanowires (both were grown for 1 hr); insets of plan-view images.

The chemical composition of SnO<sub>2</sub> and Sb-SnO<sub>2</sub> nanowires was analyzed using EDAX analysis. Figure 60 shows typical EDAX spectra for pure SnO<sub>2</sub> and Sb-SnO<sub>2</sub> nanowires. In Sb-SnO<sub>2</sub> nanowires, Sb/Sn ratio is 10 wt % which is similar to Sb/Sn ratio in a melting pool. This indicates that the content of Sb in SnO<sub>2</sub> can be tuned by changing the composition of the melting pool.

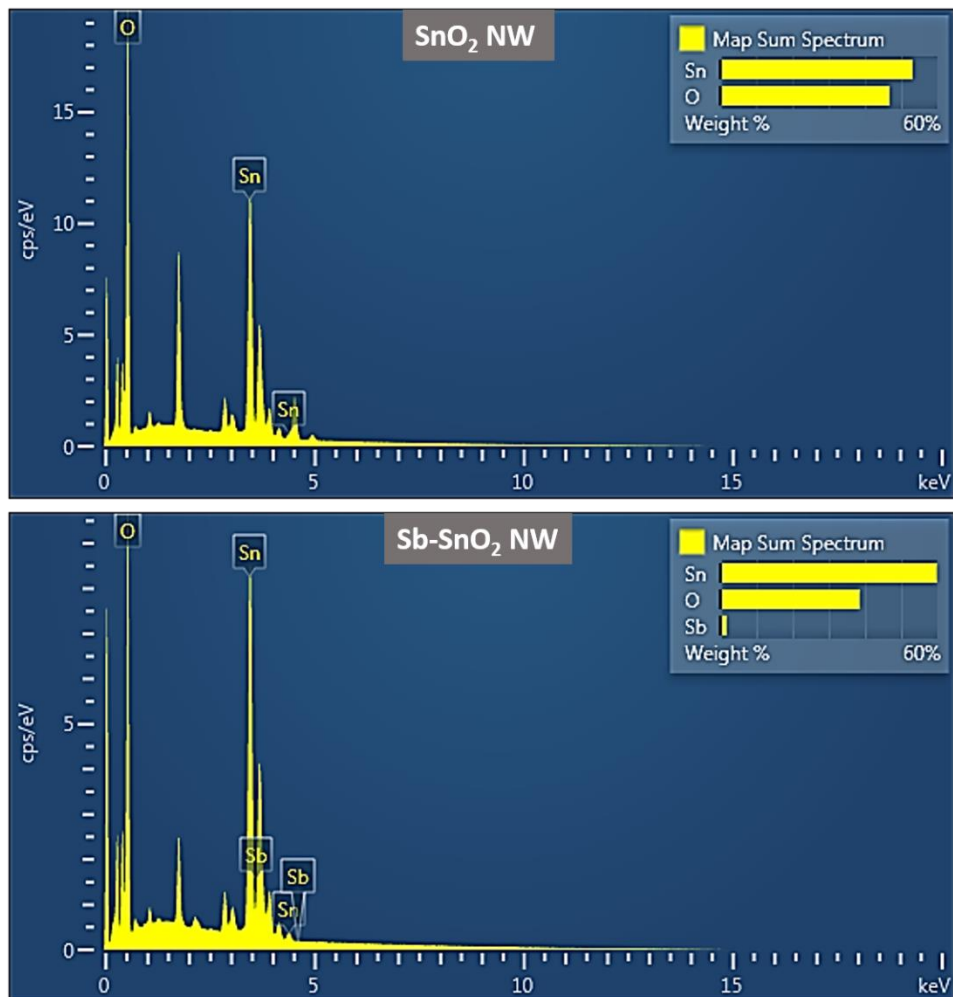


**Figure 60** EDAX results for as grown SnO<sub>2</sub> and Sb-SnO<sub>2</sub> nanowires

To fabricate PEC cell on the nanowires, light absorbing materials (CdS and CdSe) are coated on SnO<sub>2</sub> nanowires using the electrodeposition method. Figure 61 shows SEM images of only CdS coated SnO<sub>2</sub>, only CdSe coated SnO<sub>2</sub> and SnO<sub>2</sub> which are sequentially coated with CdS (first) and CdSe (second). CdS, CdSe, and CdS/CdSe layers uniformly cover the surface of the nanowire surfaces. The electrodeposition rate of CdS is slower than that of CdSe and the CdS layer has a more particle-like morphology. Compared with only CdS or only CdSe coated NWs, the

surface of CdS/CdSe/NWs becomes smooth. In the electrodeposition of the semiconductor, the amount of the coated semiconductor is determined by the total amount of charge that flowed during the electrodeposition ( $Q = \int i t dt$ ,  $Q$ : total charge,  $i$ : electric current,  $t$ : electrodeposition time). The parameters of electrodeposition such as current and time, were carefully controlled. Previous spectrophotometric study reports that if same deposition parameters are used for a same precursor, the total amount of the semiconductor coated on substrates of different surface area is same.<sup>116</sup>

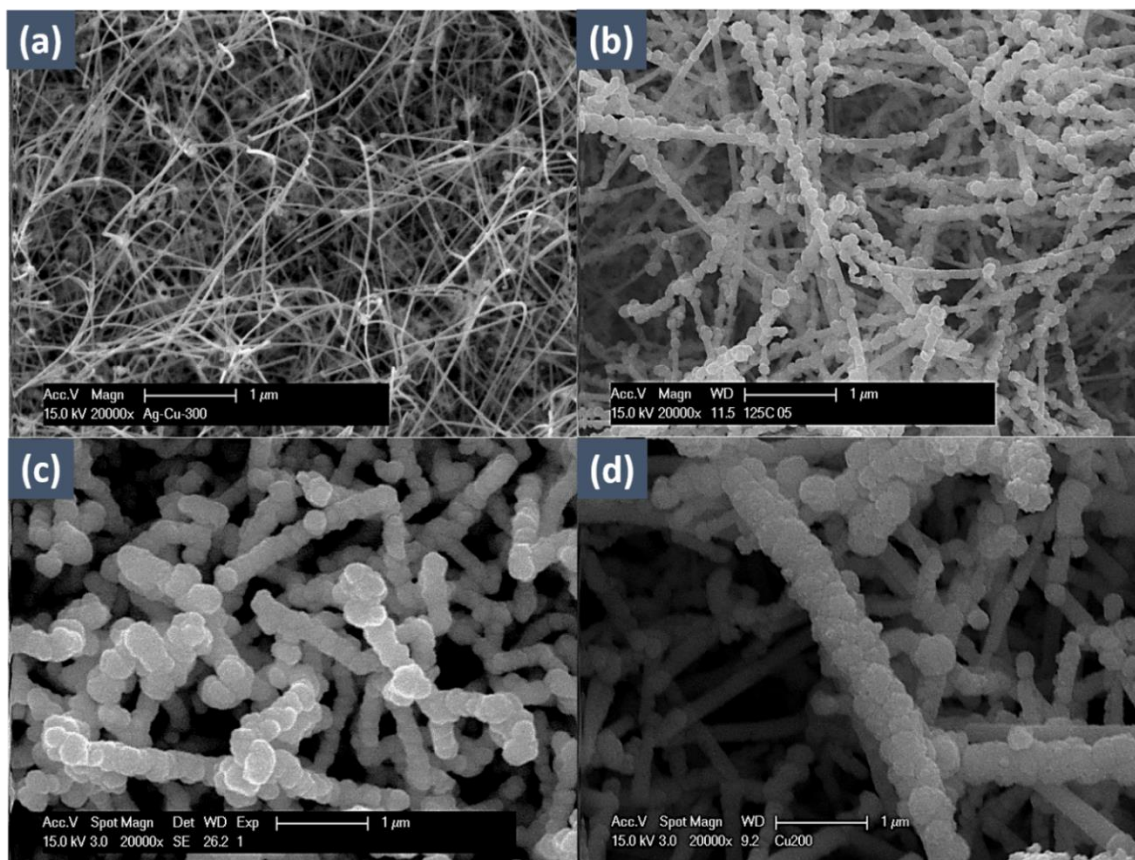


**Figure 61** SEM image of (a) bare SnO<sub>2</sub> nanowires, (b) CdS coated SnO<sub>2</sub> nanowires, (c) CdSe coated SnO<sub>2</sub> nanowires, and (d) SnO<sub>2</sub> nanowires sequentially coated with CdS and CdSe.

The chemical composition of CdS and CdSe was also examined using EDAX analysis. Figure 62 shows EDAX spectra of CdS, CdSe and CdS/CdSe coated on SnO<sub>2</sub> nanowires. EDAX results testifies that CdS, CdSe and CdS/CdSe are coated on SnO<sub>2</sub> nanowires as expected and the ratio of Cd/S and Cd/Se is close to a stoichiometric composition.

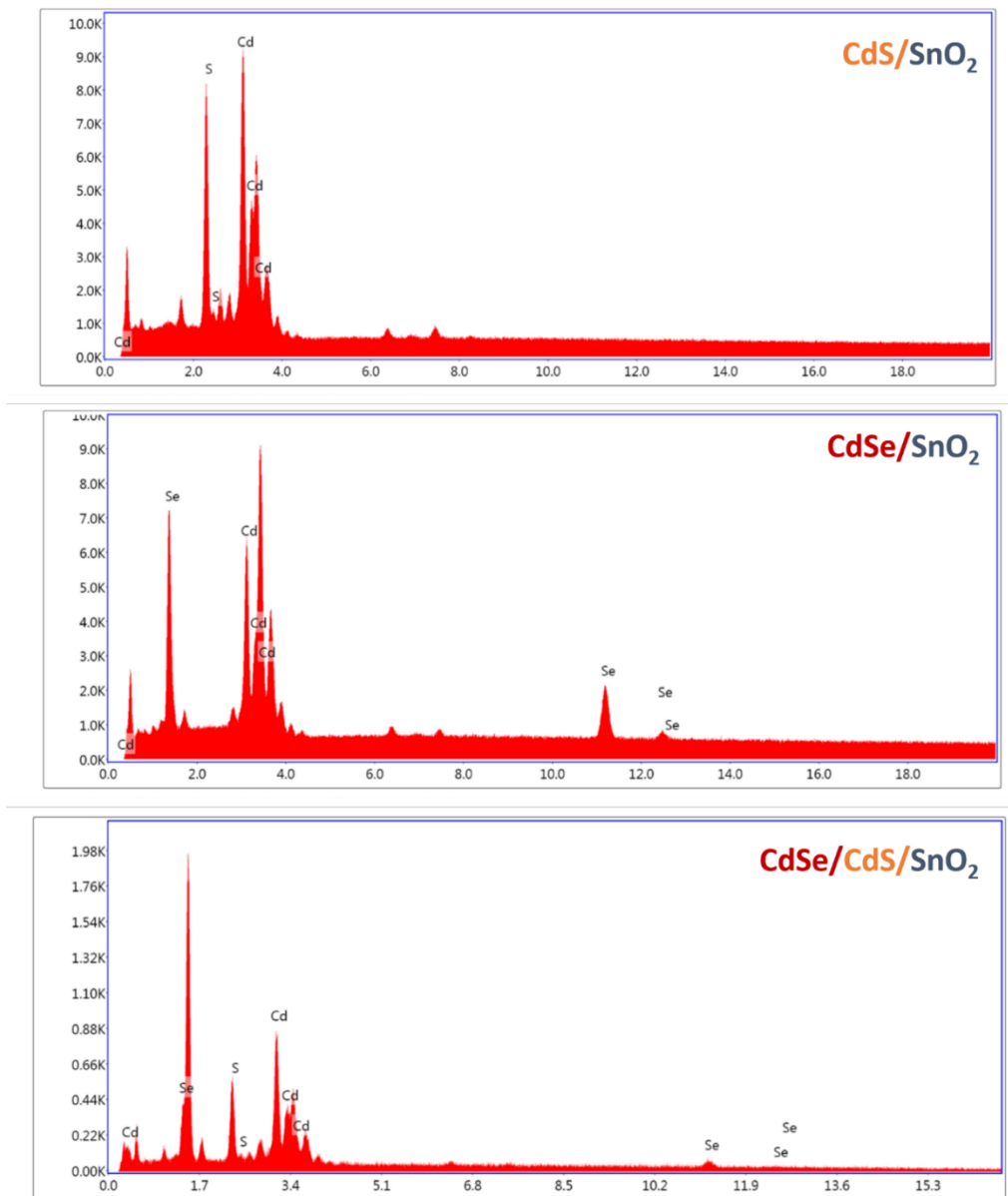


**Figure 62** EDAX results for CdS, CdSe and CdS/CdSe coated on SnO<sub>2</sub> nanowires

### 5.2.2 Sequential Coating of CdS and CdSe Along the Longitudinal Direction of Nanowires

To place CdS and CdSe at different parts of the nanowire surface, two materials were sequentially coated using polystyrene as a sacrificing layer. A goal is to stack CdS (top) and CdSe (bottom) vertically along the longitudinal direction of nanowires. Polystyrene treatment enables partially decorating of SnO<sub>2</sub> NWs with different semiconductor. For sequential coating along the longitudinal direction of NWs, PS was coated first. Figure 63 shows SEM images of polystyrene coated SnO<sub>2</sub> nanowires at different spin-coating conditions. An increase in the spinning rate decreased the thickness of the polystyrene layer. Then, the top half of the polystyrene layer was etched out by soaking the sample in ethyl acetate solution and CdS was deposited on the top bare half of the nanowire surface by the electrodeposition. After the top half of the nanowire surface was coated, the remaining polystyrene was completely removed and the electrodeposition of CdS was resumed for additional 5 minutes. As a last step, CdSe was electrodeposited onto nanowires coated with CdS layer of a different thickness. Due to a large electric resistance difference between a thin CdS region (the bottom half of NWs) and a thick CdS region (the top half of NWs), CdSe nanoparticles were mainly deposited only on the thin CdS region of higher electrically conductivity. The sequential deposition process of this study is schematically explained in Figure 64. During the electrodeposition, the amount of coated materials depends on total electric charges that flow through NWs. Hence, the relative amount of deposited nanoparticles can be estimated by integrating current over time. UV/Vis absorption spectra of the deposited material were measured to confirm a correlation between the coated material amount and the total electric charge.

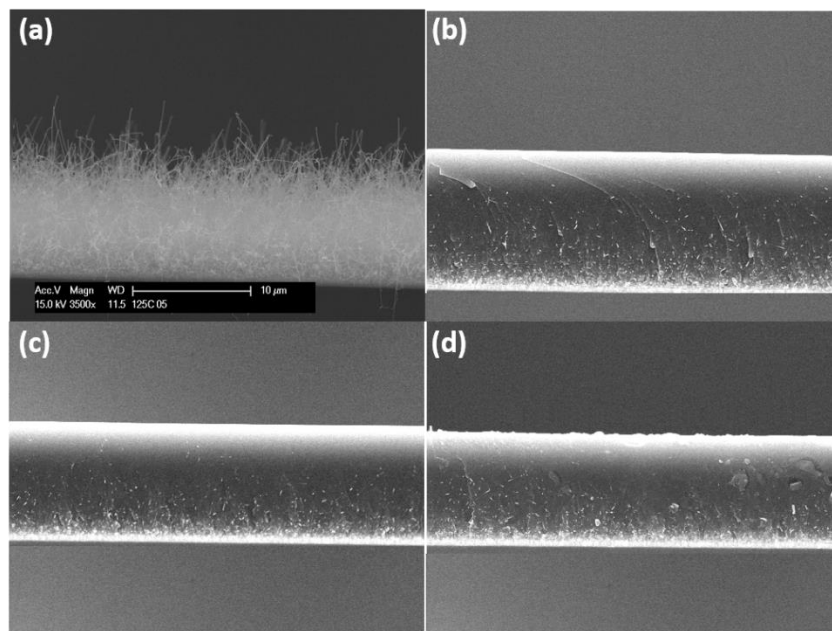
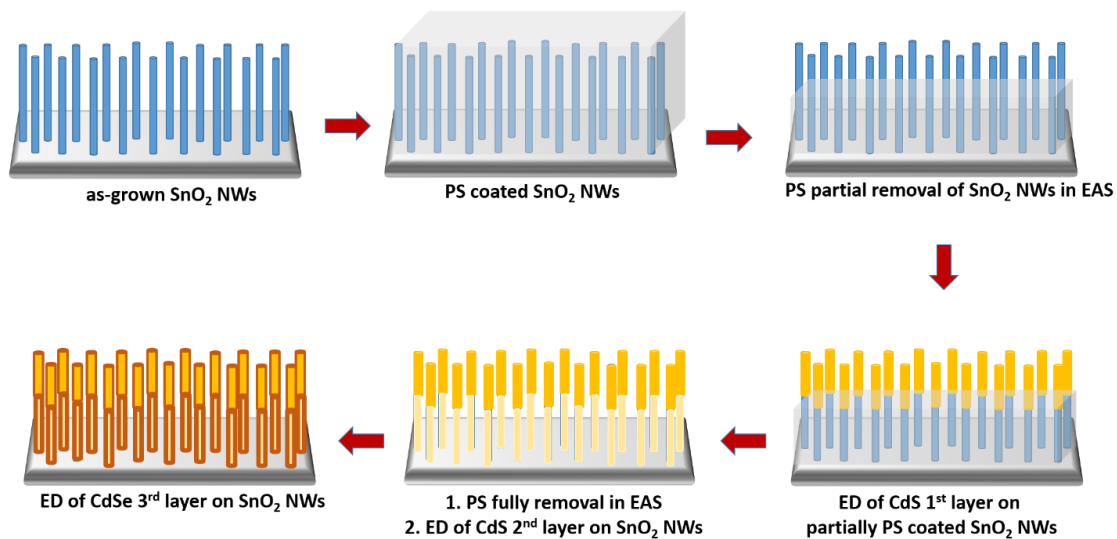


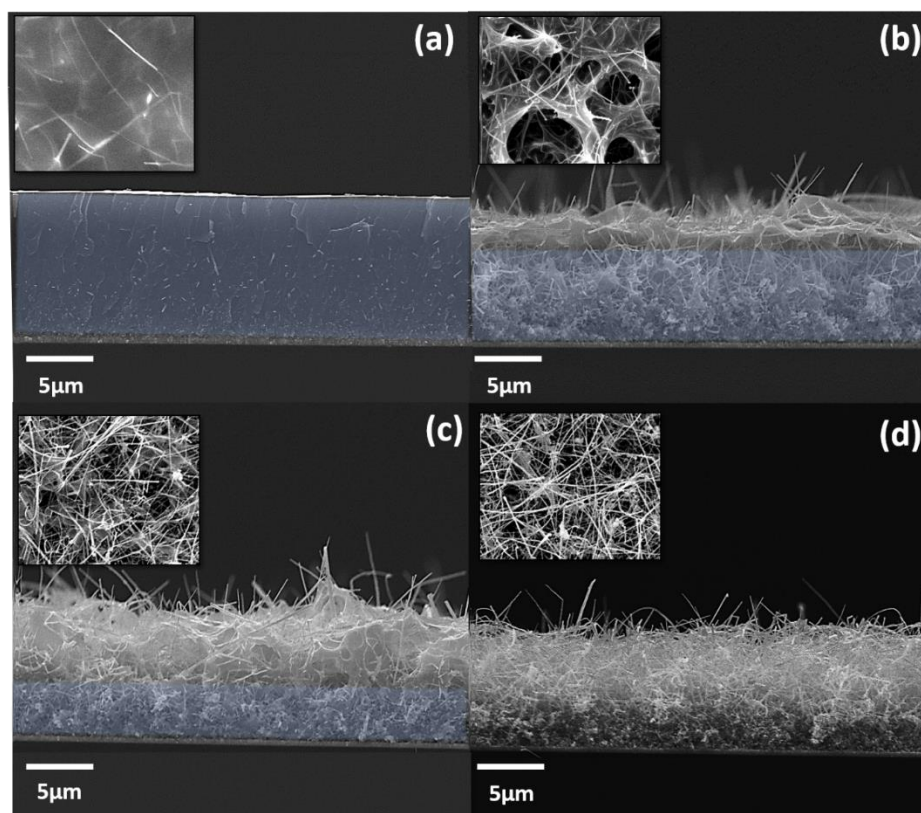
**Figure 63** Cross-sectional SEM image of (a) bare SnO<sub>2</sub> nanowires, (b-d) SnO<sub>2</sub> nanowires spin-coated with polystyrene for 30 sec; (b) at 2000 rpm, (c) at 3000 rpm, (d) at 4000 rpm.



*NWs: nanowires, PS: polystyrene, EAS: ethyl acetate solution, ED: electrodeposition*

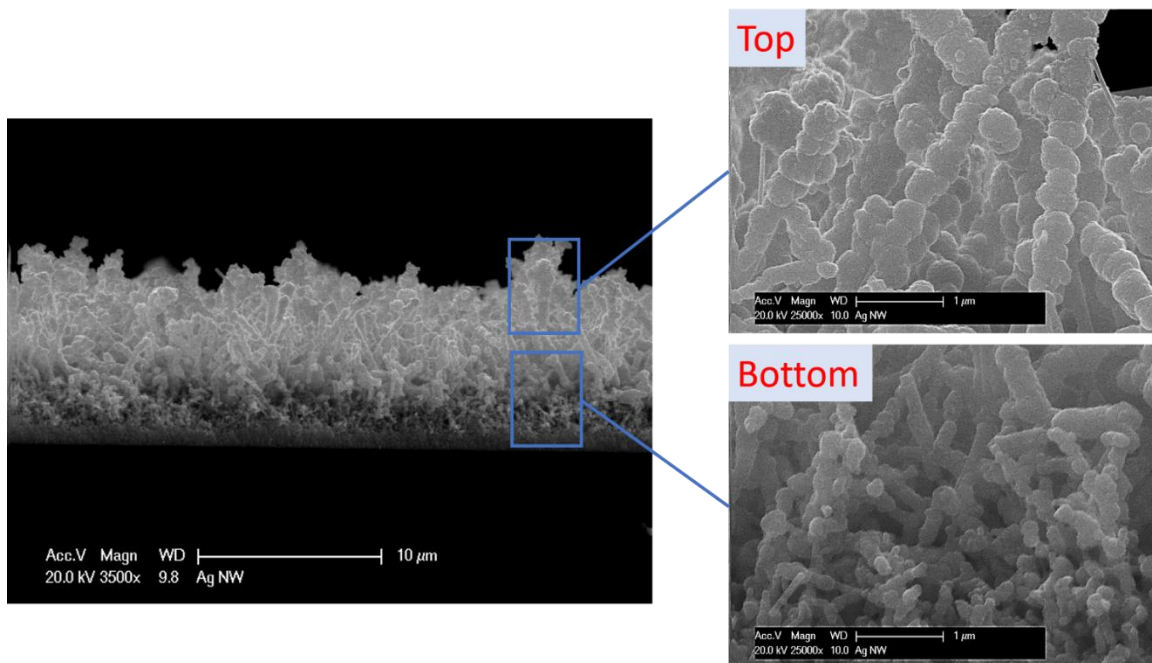
**Figure 64** Schematic representation of polystyrene treatment of SnO<sub>2</sub> nanowires for sequential deposition of CdS and CdSe layers

Figure 65 shows the removal procedure of the polystyrene layer in ethyl acetate solution as a function of a soaking time. Initially, nanowires were completely buried under the polystyrene. As the polystyrene layer was soaked longer, the top part of the nanowires started being exposed to ambient. After 1-minute etching, the polystyrene layer was removed even at the bottom of the nanowire layer.



**Figure 65** Cross-sectional SEM images of the polystyrene coated SnO<sub>2</sub> nanowire arrays (insets show the plan-view images): (a) after spin-coating of the polystyrene layer, (b)-(d) after soaking the polystyrene layer in ethyl acetate solution for (b) 10 sec, (c) 30 sec, (d) 60 sec.

Results of the sequential coating along the longitudinal direction of the nanowires are shown in Figure 66. The morphology of the sequentially coated nanowires in the top region is similar to that of only CdS coated nanowires. A thicker and smoother coating layer is observed. The bottom half of the nanowires exhibit the morphology that is found in only CdSe coated nanowires. The coating layer was thinner and more particle-like. The composition of the coating layer was also analyzed using EDAX. Figure 67 shows EDAX analysis results for Cd, Se and S at the top and bottom parts of the nanowire arrays. The atomic ratio of S/Se is 1.98 at the top part and 0.32 at the bottom part. This indicates that CdS was dominantly deposited at the top part of the interwire space and CdSe was a major constituent filling the bottom half of the interwire space. Our results confirm that the semiconductor composition can be controlled by partially covering the surface of the nanowires and locally changing the electric resistance. Therefore, it is expected that CdS in the top region of the sequentially coated nanowires absorbs blue light and CdSe in the bottom region of the sequentially coated nanowires absorbs green light. This will decrease the scattering of blue light and the thermalization loss of incident solar energy.



**Figure 66** Cross-sectional SEM images of CdSe/CdS/SnO<sub>2</sub> nanowires which were sequentially coated with CdS and CdSe along the longitudinal direction of the nanowires.

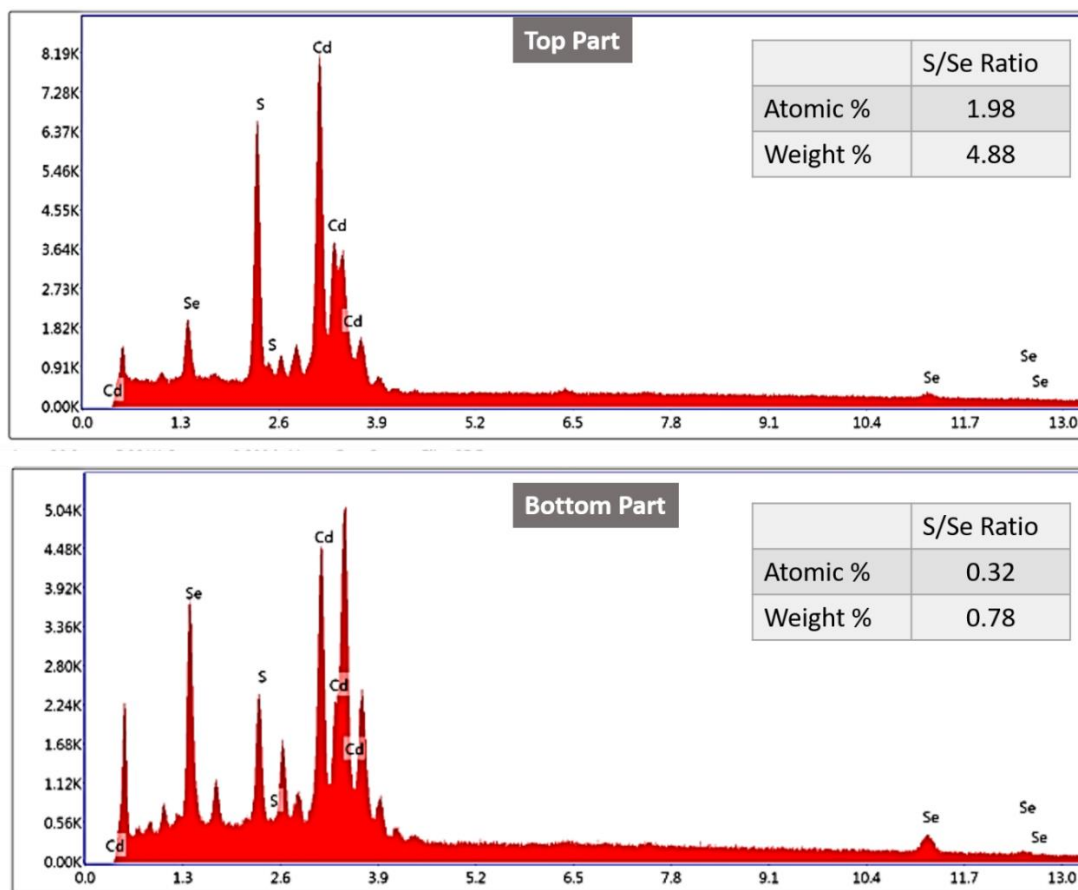


**Figure 67** EDX analysis results of the top and bottom parts of the coating layer which was sequentially deposited along the longitudinal direction of the nanowires.

### 5.2.3 Optical Properties of CdS and/or CdSe Coated SnO<sub>2</sub> Nanowires

The optical properties of the as-grown and sensitized nanowires are shown in Figure 68. All measurements were conducted using UV-vis spectrophotometer equipped with an integrating sphere. The absorption edge is determined from the intersection of the sharply decreasing region of the spectrum and its baseline.<sup>117</sup> As shown in Figure 68, the pristine SnO<sub>2</sub> does not absorb visible light, due to its wide band gap  $\sim 3.6$  eV. SnO<sub>2</sub> crystal is transparent for visible region,

however, SnO<sub>2</sub> nanowires scatter UV and visible light and decreases transmittance. CdS/SnO<sub>2</sub>, CdSe/SnO<sub>2</sub> and CdS/CdSe/SnO<sub>2</sub> clearly absorb visible light. Upon sensitization of CdS and CdSe, the sharp absorption edges are found at ~520 nm and ~630 nm which is in agreement with the band gap of bulk material ( $E_{g,CdS} \approx 2.4$  eV,  $E_{g,CdSe} \approx 1.7$  eV).

It is also noted that co-sensitization of CdS and CdSe causes the red shift of the absorption edge and the band edge of the sequentially coated sample does not depend on the sequential coating direction. Both sequential coating along the radial or longitudinal direction of the nanowire end up being the similar absorption edge at ~ 670 nm. In addition, two sequentially coated samples exhibit a negligible change in the transmittance at  $\lambda > 700$  nm.

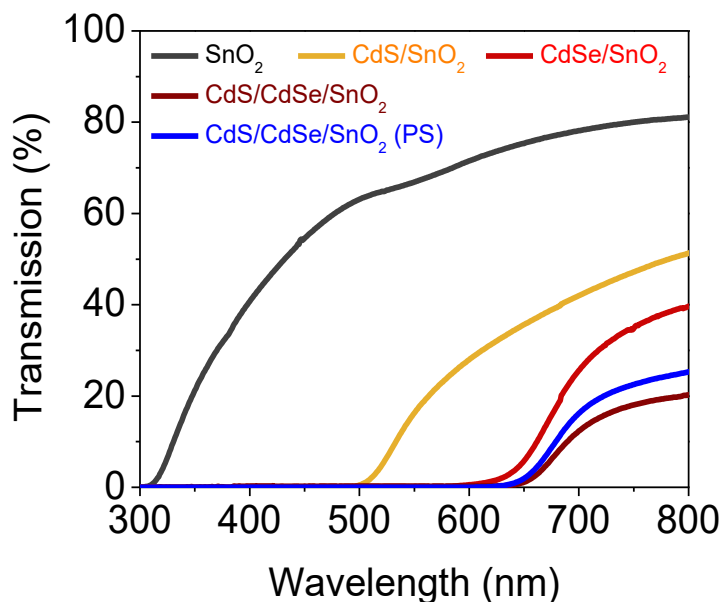


**Figure 68** Diffuse transmittance spectrum of bare SnO<sub>2</sub>, CdS/SnO<sub>2</sub>, CdSe/SnO<sub>2</sub>, CdS/CdSe/SnO<sub>2</sub> nanowires (sequential coating along the radial direction of the nanowire, and PS: sequential coating along the longitudinal direction of the nanowire).

Photos of SnO<sub>2</sub> nanowires, CdS/SnO<sub>2</sub>, CdSe/SnO<sub>2</sub> and CdSe/CdS/SnO<sub>2</sub> heteronanostructures are shown in Figure 69. The color of CdS/SnO<sub>2</sub> and CdSe/SnO<sub>2</sub> was yellow and brown. After CdSe was coated on the top of CdS, the color turned into dark red. This color change is consistent with the fact that the cosensitization of CdS and CdSe extended the absorption edge to 650 nm. In this study, SnO<sub>2</sub> nanowires were cosensitized to increase the absorption of visible light for PEC application.

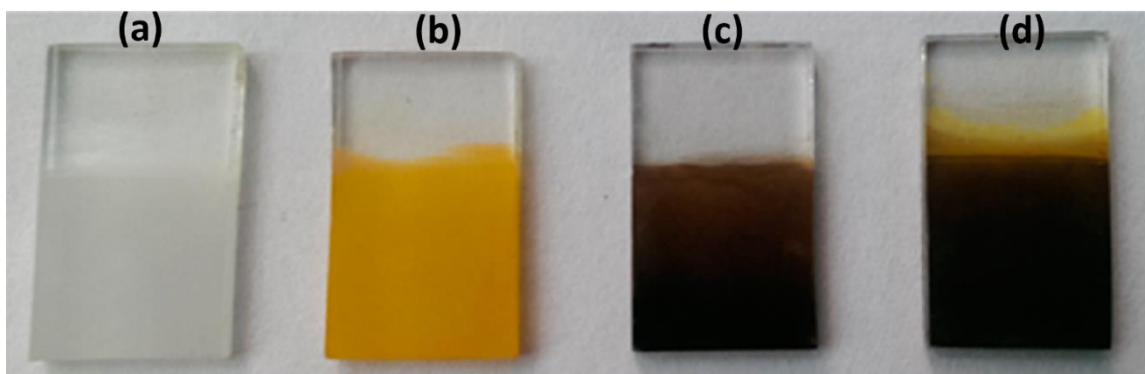
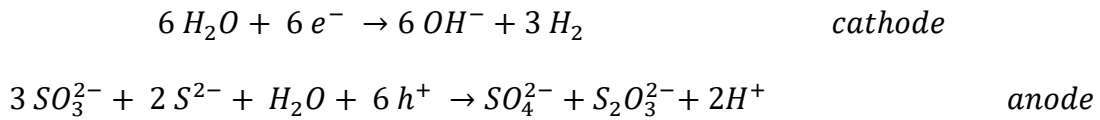


**Figure 69** Photos of (a) SnO<sub>2</sub> nanowires, (b) CdS/SnO<sub>2</sub>, (c) CdSe/SnO<sub>2</sub> and (d) CdSe/ CdS/SnO<sub>2</sub> heteronanostructures.

#### 5.2.4 Photoelectrochemical (PEC) Performance of Differently Sensitized SnO<sub>2</sub> Nanowires

Cadmium chalcogenides e.g., CdS, CdSe, CdTe, band gap fits well into the water splitting redox potential, still these types of semiconductors are not active for water splitting due to photocorrosion. Photocorrosion happens when the anion from the semiconductor itself is oxidized by photogenerated holes instead of water. Therefore, a photoelectrochemical system for water

reduction in a sulfide/sulfite ( $S^{2-}/SO_3^{2-}$ ) aqueous solution was used as electrolyte and sacrificial reagent to maintain the stability of CdS and CdSe. The oxidation reaction on CdS and CdSe upon solar irradiation occurs through the reaction of photogenerated holes with  $S^{2-}$  and  $SO_3^{2-}$  in the electrolyte. Photogenerated holes in the valence band oxidize  $SO_3^{2-}$  and  $S^{2-}$  to form  $SO_4^{2-}$  and  $S_2^{2-}$ . This reaction removes excess holes from chalcogenide semiconductors and stabilizes the surface of sulfide catalysts. The possible mechanisms for the reactions taking place on the cathode and photoanode can be given as follows.<sup>118</sup>

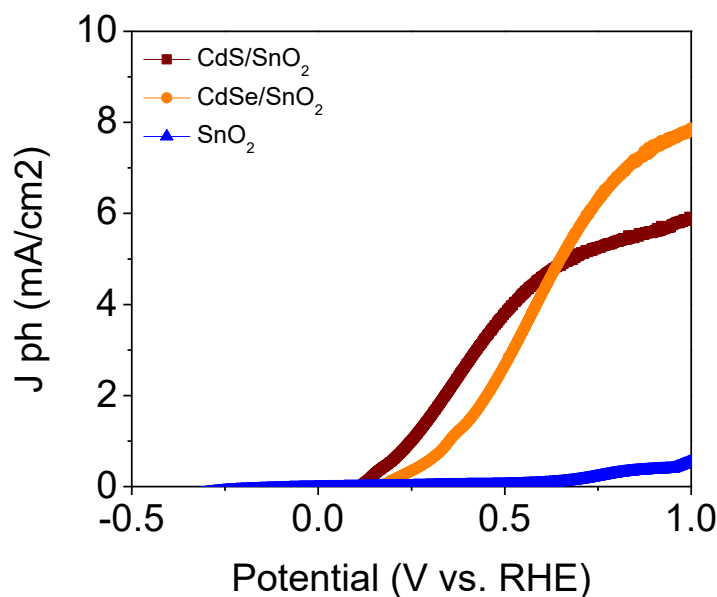


The oxidation reactions on the surface of differently coated nanowires were examined using linear sweep voltammogram in a three-electrode setup. A coiled Pt wire was a counter electrode and an Ag/AgCl electrode was a reference electrode. A voltage scan rate was 100 mV/s and the chalcogenide layers were illuminated with the simulated solar light at AM1.5G condition (100 mW/cm<sup>2</sup>) for PEC measurement. pH of an aqueous electrolyte was 12.5. To maintain the chemical stability of CdS and CdSe layers, the electrolyte contained 0.25 M Na<sub>2</sub>S and 0.35 M Na<sub>2</sub>SO<sub>3</sub> as the electrolyte and sacrificial agent. The working area of the photoanode is about 1.8 cm<sup>2</sup>. Electric potential which was applied to the working electrode was converted to the RHE scale ( $E_{RHE}$ ) using the Nernst equation, where  $E_{Ag/AgCl}$  is the potential difference between the working electrode and the Ag/AgCl reference electrode,  $E_{RHE}$  is the converted potential with respect to the reversible hydrogen electrode (RHE),  $E_{Ag/AgCl}^0$  is the standard potential between

Ag/AgCl reference electrode and RHE at 25 °C (which is 0.1976 V). Theoretically, the oxidation reaction of sulfur in the electrolyte reaches the equilibrium when  $E_{RHE}$  is 1.0V in the dark condition.

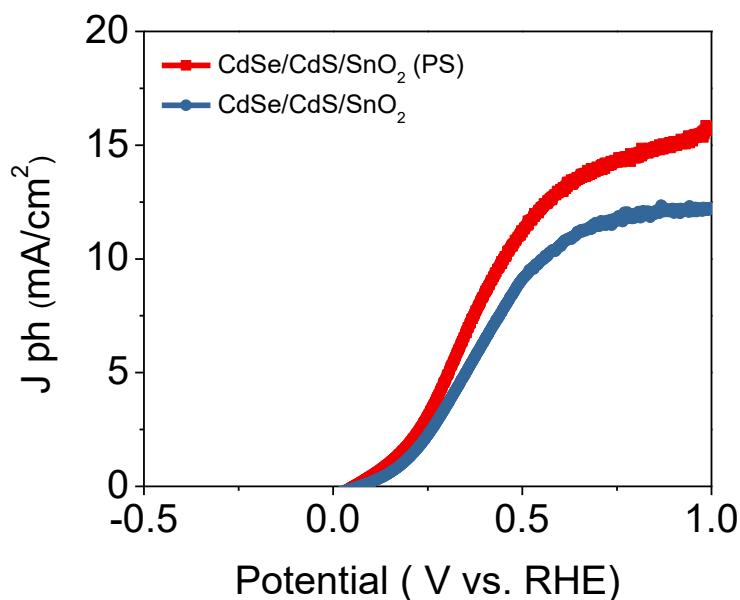
$$E_{RHE} = E_{Ag/AgCl} + 0.059pH + E_{Ag/AgCl}^0 \quad \text{Nernst Equation}$$

Figure 70 shows J-V curves of SnO<sub>2</sub> NWs, CdS coated SnO<sub>2</sub> NWs and CdSe coated SnO<sub>2</sub> NWs in the dark and illuminated conditions. Results of the dark measurement show that a very small current flow at 1 V (vs. RHE). This is because CdS and CdSe have a catalytic effect. Once the samples were exposed to the light, a noticeable photocurrent density was measured in sensitized nanowires. The photocurrent density at 1 V (vs. RHE) was 7.8 mA/cm<sup>2</sup> for CdSe coated SnO<sub>2</sub> NWs and 5.9 mA/cm<sup>2</sup> for CdS coated SnO<sub>2</sub> NWs. Higher photocurrent density of CdSe coating results from the smaller band gap of CdSe.



**Figure 70** Linear sweep voltammograms of pure SnO<sub>2</sub> nanowires, CdS coated SnO<sub>2</sub> nanowires and CdSe coated SnO<sub>2</sub> nanowires at a scan rate of 100 mVs<sup>-1</sup> at applied potentials from -0.9 to +0.3 V vs. Ag/AgCl under illuminated (AM1.5G) conditions.

Figure 71 shows J-V curves of SnO<sub>2</sub> nanowires coated sequentially with CdS and CdSe. They exhibit higher photocurrent than only CdSe coated nanowires and the effect of the coating method on the photocurrent density is found.



**Figure 71** Linear sweep voltammograms of photoanodes fabricated from CdSe/CdS/SnO<sub>2</sub> NWs (with, PS, and without PS) at a scan rate of 100 mVs<sup>-1</sup> at applied potentials from -0.9 to +0.3 V vs. Ag/AgCl, under illuminated (AM1.5G) conditions.

When CdS and CdSe are sequentially along the radial direction of NWs, the photocurrent density is 12.2 mA/cm<sup>2</sup>. More absorption of small energy photons (see the absorption spectra of Figure 68) and a cascade band structure increase the photocurrent from 7.8 mA/cm<sup>2</sup> to 12.2 mA/cm<sup>2</sup>. The cascade structure of the band edges facilitates the separation of photogenerated electrons and holes and promotes the carrier transfer at the CdS - CdSe interface. Figure 72 depicts

the schematic representation of cascade hetero-nanostructure and process of electron transport in CdS/CdSe co-sensitized SnO<sub>2</sub>/TiO<sub>2</sub> nanowire photoelectrodes. Upon solar irradiation, the semiconductor photoelectrode SnO<sub>2</sub> nanowire and CdS/CdSe layers absorb the photons and generation of electron hole-pairs triggered. At equilibrium, the Fermi levels of semiconductors, will be aligned with electrolyte solution as shown in the simplified energy diagram. Conduction band edges of CdSe and CdS are higher than SnO<sub>2</sub>, and TiO<sub>2</sub>, which allows efficient charge transfer of photoexcited electrons from CdS and CdSe to SnO<sub>2</sub> NWs. CdS has a higher conduction band edge position and CdSe has a higher valence band edge position compared to large band gap SnO<sub>2</sub> and TiO<sub>2</sub>, which is favorable for photo-generated charge transfer. The cascade hetero-nanostructure provides a stepwise band alignment between CdS/CdSe and SnO<sub>2</sub>/TiO<sub>2</sub> and facilitates the photogenerated charge separation and transfer process, hence charge carrier recombination rate is reduced. Besides high electron mobility and high conductivity of SnO<sub>2</sub> nano-scaffold provides a better charge collection efficiency. The photocurrent density in this study is compared with previous studies chalcogenide sensitized photoelectrodes in Table 4.

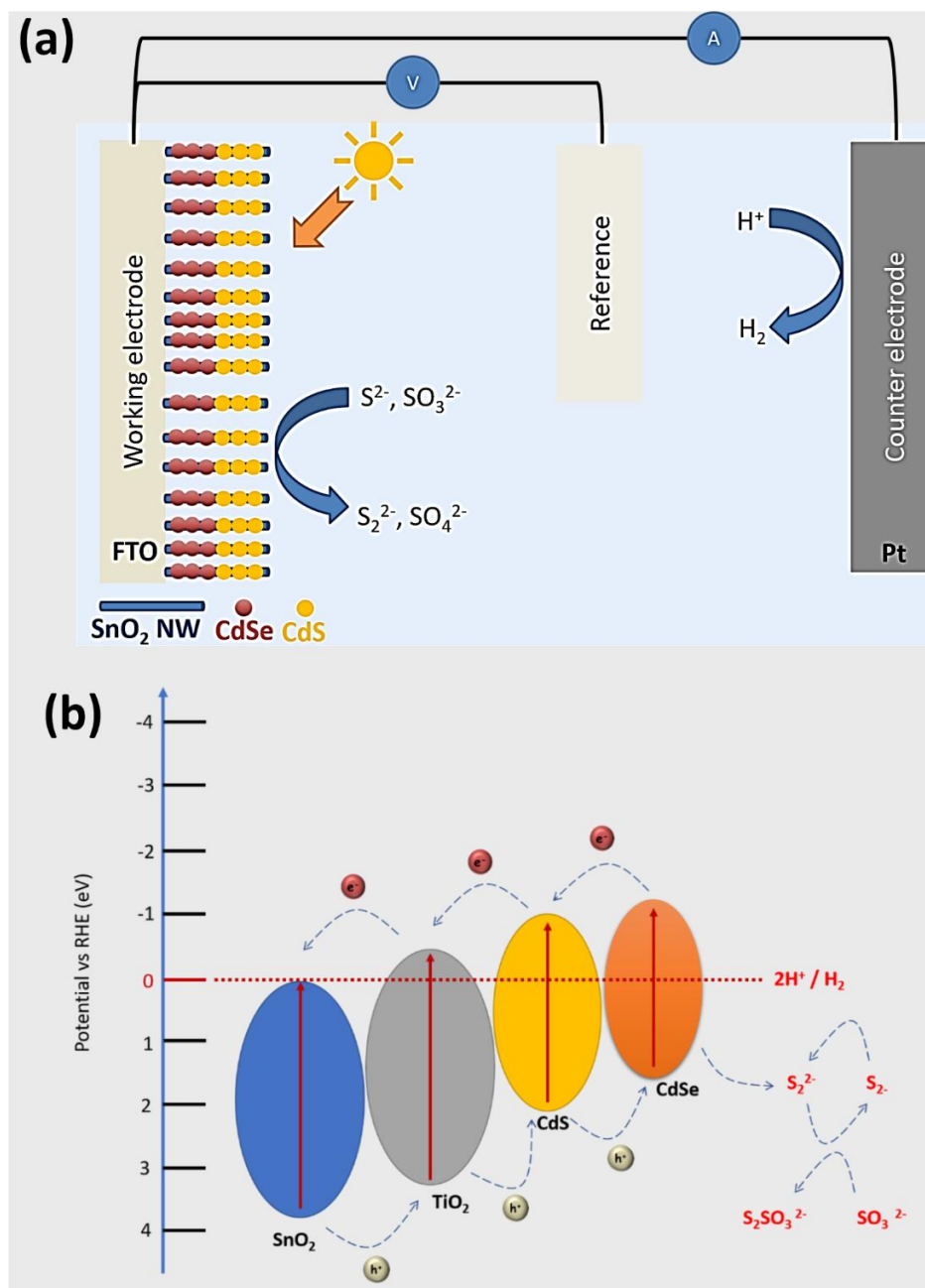


**Figure 72** Schematic illustration of band alignment and charge transfer at CdS/CdSe coated SnO<sub>2</sub> nanowires during the photoreaction.

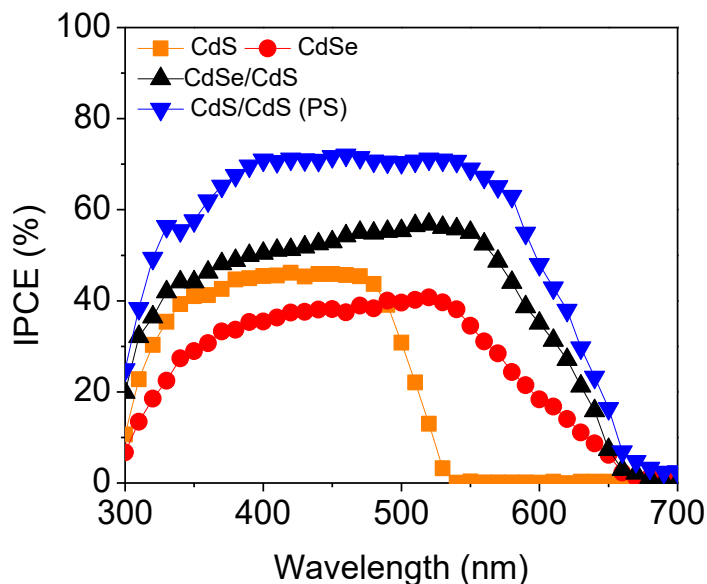
**Table 4** Comparison of the PEC activity of metal chalcogenide sensitized metal oxide semiconductor photoelectrodes reported recently for PEC water splitting

<b>Photoelectrode</b>	<b>Current density (mA/cm<sup>2</sup>)</b>	<b>Electrolyte</b>	<b>Morphology</b>	<b>Method</b>	<b>Ref.</b>
CdS/CdSe/SnO <sub>2</sub> and CdSe/CdS/Sb-SnO <sub>2</sub>	12.2, 15.7, 16.40, 18.87 respectively at 1.0 V vs. RHE	0.25 M Na <sub>2</sub> S 0.35 M Na <sub>2</sub> SO <sub>3</sub>	SnO <sub>2</sub> nanowires CdS and CdSe nanoparticles	ED	This work
CdS/CdSe co-sensitized 3D SnO <sub>2</sub> /TiO <sub>2</sub>	6 at 1.4 V vs. RHE	0.25 M Na <sub>2</sub> S 0.35 M Na <sub>2</sub> SO <sub>3</sub>	SnO <sub>2</sub> / TiO <sub>2</sub> sea urchin nanotubes	SILAR	119
3D SnO <sub>2</sub> /TiO <sub>2</sub> /CdS multi-heterojunction structure	8.75 at 1.0 V vs. RHE	0.25 M Na <sub>2</sub> S 0.35 M Na <sub>2</sub> SO <sub>3</sub>	SnO <sub>2</sub> nanowires /TiO <sub>2</sub> nanoneedles/CdS quantumdots	CBD	120
Quantum Dot Based Heterostructures	8 at 0 V vs. Ag/AgCl	0.25 M Na <sub>2</sub> S 0.35 M Na <sub>2</sub> SO <sub>3</sub>	TiO <sub>2</sub> hallow NWs sensitized by CdS and CdSe QDs	CBD and SILAR	121
CdS/CdSe Sensitized TiO <sub>2</sub> Nanocable Arrays	6.57 at 0 V vs. Ag/AgCl	0.25 M Na <sub>2</sub> S 0.35 M Na <sub>2</sub> SO <sub>3</sub>	TiO <sub>2</sub> nanorod and nanocable arrays	ED	122

The improvement of the photocurrent is more pronounced in SnO<sub>2</sub> nanowires of the sequential coating along the longitudinal direction. When CdS and CdSe are coated using the partial etching of the polystyrene layer, the photocurrent density is as large as 15.7 mA/cm<sup>2</sup> at 1.0 V vs. RHE. To explain the effect of the coating direction on the photocurrent, IPCEs of differently sensitized SnO<sub>2</sub> nanowires were measured at 1.0 V vs. RHE. Figure 73 shows that the cascade band structure clearly increases IPCE at  $\lambda > 500$  nm where CdSe absorbs visible light. In addition, the longitudinal direction coating provides higher IPCE over visible light than the radial direction coating, though transmittance of visible light is almost 0 % in both samples. In particular, the larger improvement of IPCE for blue light (400 to 500 nm) is intriguing. This indicates that the increase in IPCE by the longitudinal direction coating is related to the enhanced carrier transport rather than the improved light absorption.

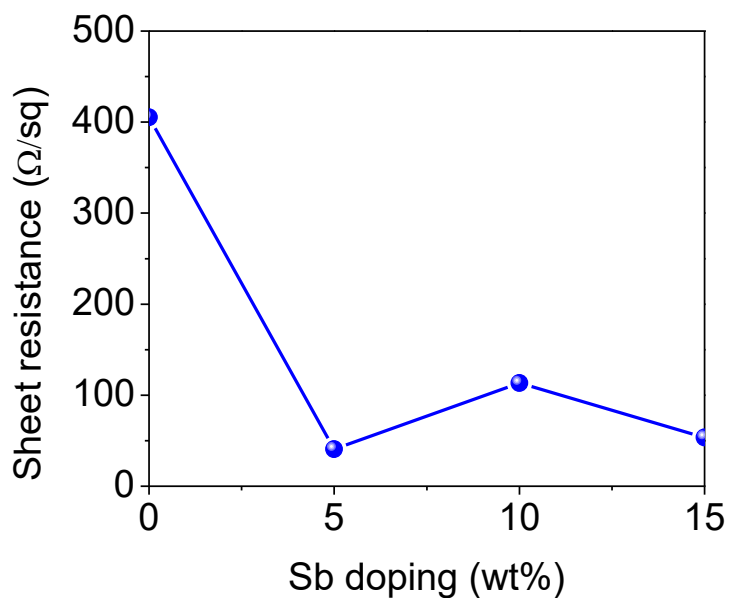
The improvement of PEC performance by the selective positioning of semiconductors along the longitudinal direction of nanowires is due to a decrease in the non-radiative recombination of photogenerated carriers. If photon energy is larger than bandgap of semiconductor, kinetic energy of photogenerated electrons and holes is not zero. This kinetic energy of hot carriers is relaxed through phonon generation, which often causes a non-radiative recombination of carriers and a decrease in the collection efficiency of devices. This is called thermalization loss. In solar cells, the thermalization problem is addressed by stacking multiple semiconductors with different band gap. The semiconductor of wider band gap is placed on the top of the semiconductor stack and the semiconductor of narrower band gap is placed at the bottom of the semiconductor stack. Similarly, selective positioning of semiconductor along the longitudinal direction in this study helps large energy photons to be absorbed by the large bandgap semiconductor on the top half of nanowires. Consequently, the thermalization loss is reduced, the

carrier recombination is suppressed, and the photocurrent is increased. In a case of the radial direction coating, however, the small band gap semiconductor absorbs high energy photons and excess kinetic energy of photogenerated electrons is lost in a form of phonons.



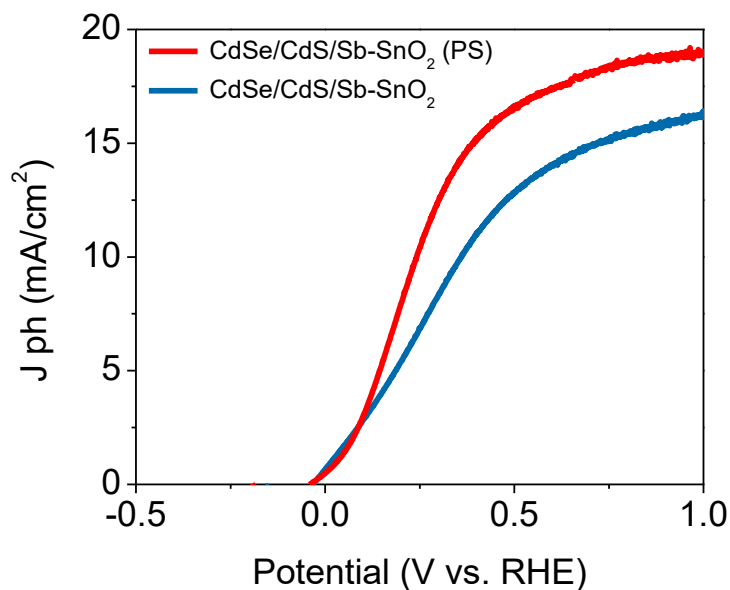
**Figure 73** IPCE spectra of CdS/SnO<sub>2</sub> nanowires, CdSe/SnO<sub>2</sub> nanowires and CdSe/CdS/SnO<sub>2</sub> nanowires (sequential coating along the radial or longitudinal direction) at 1.0 V vs. RHE.

Successful doping of SnO<sub>2</sub> nanowires with Sb shows an improvement of their electrical conductivity. Figure 74 shows doping of Sb into SnO<sub>2</sub> nanowires further increases the electrical conductivity. The increased electrical conductivity improves charge transfer and collection rates and hence improvement in photocurrent density upon Sb doping.



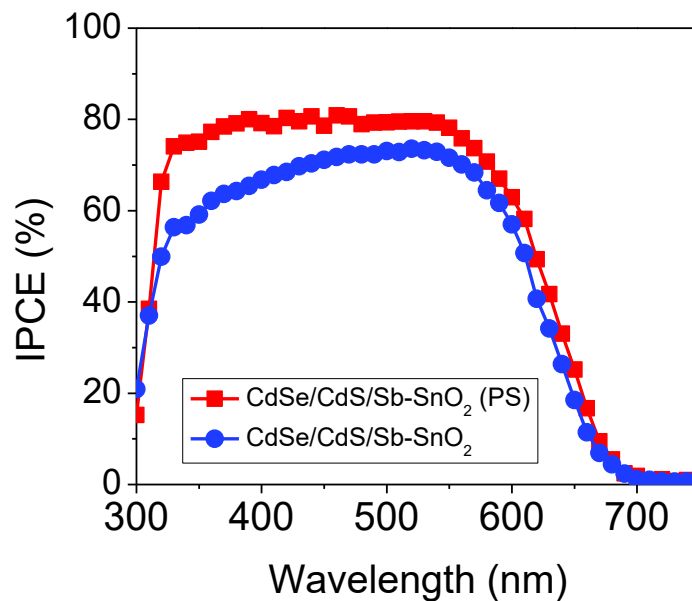
**Figure 74** Conductivity of SnO<sub>2</sub> nanowire as a function of Sb doping content

Figure 75 shows the J-V curve for Sb-doped samples. In a case of the longitudinal direction coating onto Sb doped SnO<sub>2</sub> nanowires, the photocurrent reaches 16.7 mA/cm<sup>2</sup> (without PS), whereas 18.8 mA/cm<sup>2</sup> (with PS) (at 1 V vs. RHE. Highly conductive Sb-doped SnO<sub>2</sub> nanowires facilitates the electron transport and provides a better conductive pathway to photogenerated charge carriers.



**Figure 75** Linear sweep voltammograms of photoanodes fabricated from CdSe/CdS/Sb-SnO<sub>2</sub> NWs (with and without polystyrene treatment), at a scan rate of 100 mVs<sup>-1</sup> at applied potentials from -0.9 to +0.3 V vs. Ag/AgCl, under a light intensity of 100 mWcm<sup>-2</sup>.

Moreover, the IPCE of the Sb-doped photoelectrodes were also evaluated in Figure 76 and showed significant enhancement compared to the undoped photoelectrodes. Undoped photoelectrodes exhibit 45 % (without PS) and 70 % (with PS) between 400-500 nm. Whereas the Sb-doped photoelectrodes reaches 65 % (without PS) and 80 % (with PS) within the same wavelength region. This clearly indicates that IPCE is enhanced at visible region for Sb-doped samples. This implies that the Sb-doping is improving charge collection for photons that penetrate deeper in the nanowires. All of the positive factors with Sb doping will account for a better PEC performance fulfilling the requirements of host scaffold e.g high electronic conductivity with high transparency in the visible region of solar spectrum, in constructing efficient composite photoelectrodes for PEC devices.



**Figure 76** Measured IPCE spectra of CdSe/CdS/Sb-SnO<sub>2</sub> and CdSe/CdS/Sb-SnO<sub>2</sub> (PS) samples, from 300-800 nm at a potential of 1.0 V vs. RHE

The stability issues associated with chalcogenide materials are one of the obstacles in PECs based on semiconductors such as CdS, CdSe, PbS etc. Use of n-type CdS and CdSe may result in photoanodic dissolution yielding Cd<sup>2+</sup> ions and elemental S or Se to the aqueous solution, and this is an irreversible decomposition encountered serious problems in practical application of PEC cells.<sup>123</sup> We try to address these issues upon illuminating the PEC system for extended time. Figure 77 shows the amperometric i-t curves of the consequent photoanodes collected under chopped light illumination (30s period of light and dark cycle) at an applied external bias of 1.0 V vs. RHE. Photoresponse and photoswitching occur quickly when light is turned on and off. It is noticed that a dark current and voltage of mA/cm<sup>2</sup> and V could be observed during the off-illumination cycles, respectively. When the light is turned on, a spike/dip type of photocurrent is observed and the J<sub>sc</sub> and

$V_{oc}$  jumped to a higher value of mA/cm<sup>2</sup> and V, respectively. The sharp spike/dip in the photocurrent response upon light on-off conditions shows that; rapid transfer of the photogenerated electrons from CdS/CdSe to SnO<sub>2</sub>/TiO<sub>2</sub> heteronanostructure and fast transfer of photogenerated charge carriers within SnO<sub>2</sub> nanowire network. Moreover, the CdS/CdSe cosensitized Sb-SnO<sub>2</sub> NWs photoanode shows remarkable photostability with a small decrease under continuous light illumination (Figure 78) Current decreases 30 % within 1 minute and does not show a change for 15 minutes.

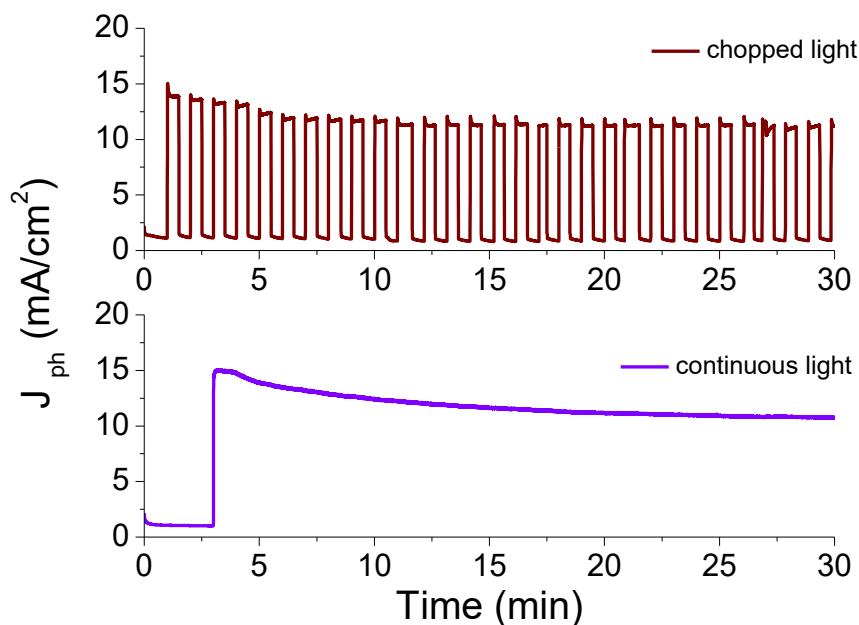


**Figure 77** The photocurrent responses (amperometric i-t curves, light on-off mode) of SnO<sub>2</sub>CdS/CdSe (without polystyrene treatment) samples, chopped and continues light mode, at an applied potential of 1.0 V versus RHE

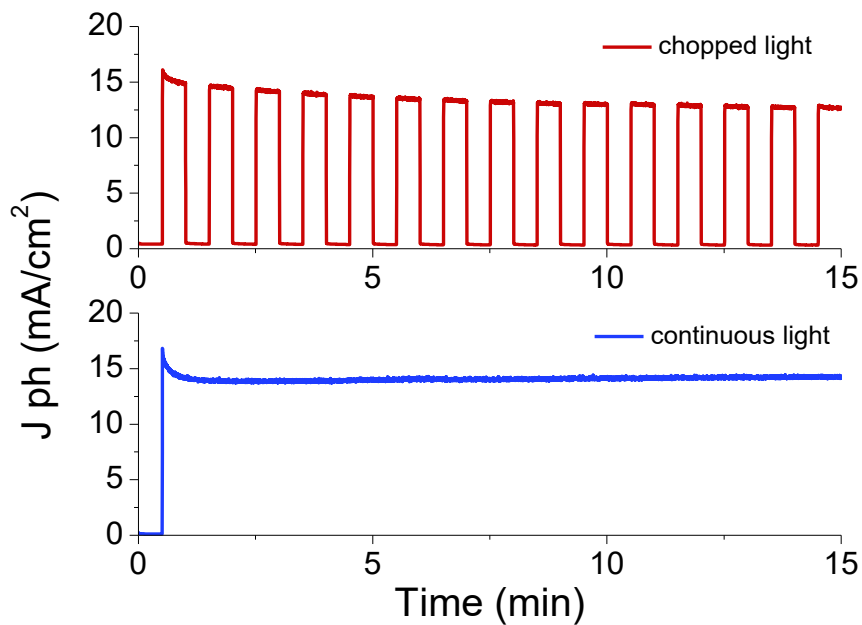


**Figure 78** The photocurrent responses (amperometric i-t curves, light on-off mode) of Sb-SnO<sub>2</sub>CdS/CdSe (without polystyrene treatment) samples, chopped and continuous light mode, at an applied potential of 1.0 V versus RHE

## **6.0 Mo<sub>2</sub>C AND Mo<sub>2</sub>C-GO NANOCOMPOSITE FOR HIGH PERFORMANCE HYDROGEN EVOLUTION REACTION**

### **6.1 OBJECTIVES**

Molybdenum carbide (mainly referring to Mo<sub>2</sub>C) is one important class of transition metal carbides (TMCs). Recent studies in the past few years have shown that molybdenum carbides are active in a variety of catalytic reactions including desulfurization, water - gas shift, and hydrogenation. Vrubel and Hu reported that after removal of surface oxides, the commercial molybdenum carbide (Mo<sub>2</sub>C) was a very active hydrogen evolution reaction (HER) catalyst in both acidic and basic conditions. The performance of HER electrocatalysts greatly depends on the surface state, composition, and crystal structures of Mo<sub>2</sub>C. The surface area plays an important role in the HER activity. Use of agglomerated Mo<sub>2</sub>C microparticles may provide less surface area for catalytically active sites and hinder the transport of electrons or protons during the reaction. Consequently, the catalytic activity of Mo<sub>2</sub>C significantly decreases. Recently, Sasaki et al. demonstrated that Mo<sub>2</sub>C nanoparticles on carbon nanotubes were a highly active and durable electrocatalyst for hydrogen production. Moreover, the nanostructured Mo<sub>2</sub>C on 2D graphitic supports has also been developed to increase the overall electric conductivity which is essential for excellent HER activity.

To meet requirements of high surface area and electric conductivity, Mo<sub>2</sub>C nanoparticles and Mo<sub>2</sub>C-graphene oxide (GO) nanocomposites are synthesized via facile microwave reaction and their electric and electrochemical properties are studied. With the assistance of the microwave radiation, highly Mo<sub>2</sub>C nanoparticles are synthesized at 800 °C. In Mo<sub>2</sub>C-GO composites, 2D GO tailor the size of Mo<sub>2</sub>C nanoparticles by preventing agglomeration and facilitates the exposure of active sites for electrocatalysis. In addition, the interconnected GO structure provides a conductive pathway for rapid electron transport and Mo<sub>2</sub>C-GO composites turns out to be an excellent electrocatalyst for HER.

## **6.2 RESULTS AND DISCUSSION**

### **6.2.1 Molybdenum Carbide (Mo<sub>2</sub>C) Nanoparticles as Electrocatalyst**

#### **6.2.1.1 Structural Analysis of Mo<sub>2</sub>C from Microwave-Assisted Reaction**

To synthesize Mo<sub>2</sub>C, molybdenum chloride and urea were mixed in pure ethanol and the mixture was irradiated with the microwave. After the microwave reaction, solid nanoparticles were collected using a centrifuge and annealed at 600, 700 and 800 °C for 3 hrs. In the synthesis process, one important variable was a ratio (R) of urea/molybdenum chloride. As the thermal annealing at 800 °C, synthesized particles were characterized by XRD and their crystal structure was analyzed. Figure 79 shows XRD patterns of synthesized particles as a function of urea/molybdenum chloride ratio. The XRD pattern of the sample synthesized at R=7 shows sharp diffraction peaks which are indexed  $\alpha$ -Mo<sub>2</sub>C. The peaks at  $2\theta = 34, 38, 39, 52, 62, 69, 74, \text{ and } 76$  correspond to (100), (002), (101), (102), (110), (103), (200) and (112) planes of hexagonal Mo<sub>2</sub>C (JCPDS patterns: Mo<sub>2</sub>C-

0871)). Samples from different R conditions exhibit broad diffraction peaks of Mo<sub>2</sub>C and additional peaks of second phases such as MoC. Increase in the peak broadness suggests that nanoparticles synthesized from precursors of R = 5, 9 have smaller crystallite size or residual strain. The broad peak at 17 ° was ascribed to carbon. Our study confirms that the microwave reaction of the precursor of R = 7 and the subsequent annealing at 800 °C enable the formation of highly crystalline Mo<sub>2</sub>C. 800 °C is much lower than the crystallization temperature in previous studies. The typical way of Mo<sub>2</sub>C synthesis requires temperature programmed reaction (TPR) at elevated temperatures (usually T>800 °C) with a given amount of a mixture of carbon source.<sup>124</sup> On the other hand, in the TPR process, employing a large amount of flammable gas at high temperature can be dangerous. For these reasons, microwave assisted low temperature synthesis method is a favorable method to get desired crystalline Mo<sub>2</sub>C.

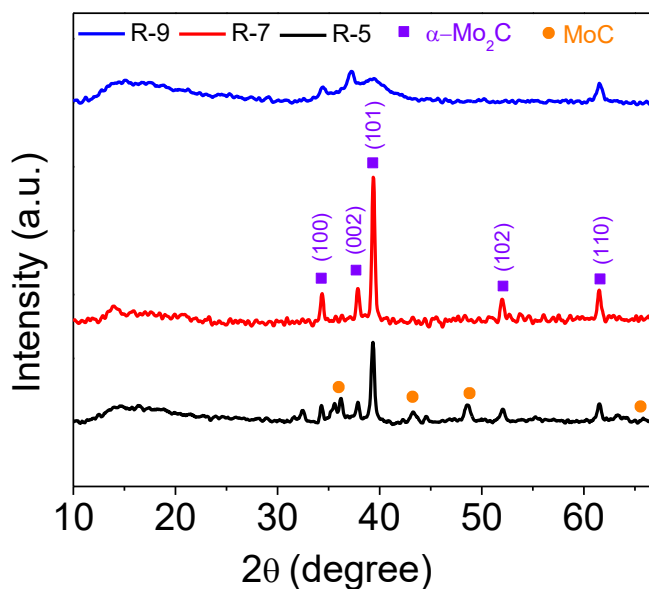


**Figure 79** X-Ray Diffraction (XRD) patterns for Mo<sub>2</sub>C nanoparticles with different amount of urea content (R).

In addition to the crystallinity, a particle size is an important parameter determining the performance of the electrocatalyst. Therefore, a change in the particle size from the precursor of  $R = 7$  was examined as a function of the thermal annealing temperature. The particle size after the microwave reaction is relatively large, since particles are still amorphous. Figure 80 shows, as the crystallization of the amorphous phase proceeds, the particle size decreases and the minimum particle size of 120 nm is found at 600 °C. Increase in the annealing temperature from 600 °C to 800 °C enlarges  $\text{Mo}_2\text{C}$  nanoparticles. XRD and SEM show that well-dispersed and highly crystalline  $\text{Mo}_2\text{C}$  with a size of 200 nm can be obtained by annealing the microwave-reacted product at 800 °C.

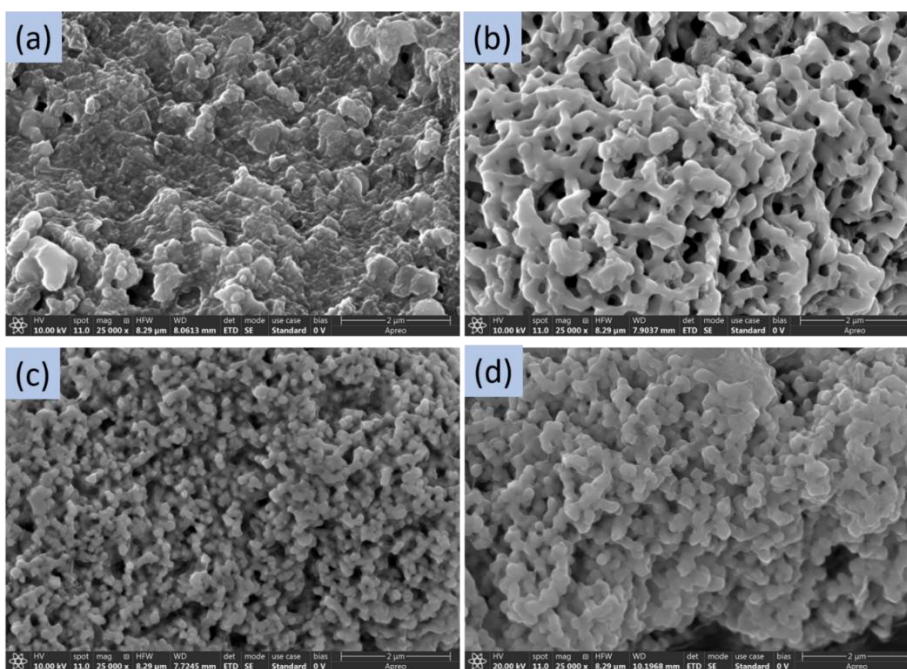


**Figure 80** SEM images of as-synthesized particles and thermally annealed particles (a) as synthesized after the microwave reaction, (b) annealed at 400 °C (b) annealed at 600 °C and (d) annealed at 800 °C ( $R$  of the precursor = 7).

While XRD is sensitive to the long-range order in crystalline solids, it cannot detect the short-range order of the atomic arrangement. In addition, XRD is not a powerful tool to characterize the crystallization of excess carbon into the solid phase which accompanies the reaction of Mo and C. To monitor the short-range order in the crystalline solid and the status of excess carbon, Raman analysis of Mo<sub>2</sub>C particles was performed in the range of 500 - 2500 cm<sup>-1</sup>. Figure 81 shows Raman spectra of Mo<sub>2</sub>C particles which were synthesized in different conditions. First, nanoparticles from the microwave reaction and the sol-gel method were compared to study the effect of the microwave radiation. Same precursor and thermal annealing method were used to synthesize these nanoparticles. Both samples show Raman peaks of Mo<sub>2</sub>C at 670 cm<sup>-1</sup>, 840 cm<sup>-1</sup> and 990 cm<sup>-1</sup>. In addition, D- and G-bands of carbon are found at 1350 and 1590 cm<sup>-1</sup>. D-band originates from the atomic vibration of a disordered graphitic carbon phase and G-band is attributed to the E<sub>2g</sub> vibration (a stretching mode) of carbon atoms in sp<sup>2</sup> bonds. Though the same composition and amount of the precursor was used, the D- and G-bands of the microwave reaction are much stronger. This indicates that the microwave radiation promotes the solidification of carbon from the precursor and Mo<sub>2</sub>C nanoparticles were mixed with fine graphitic particles which were not detected by XRD.

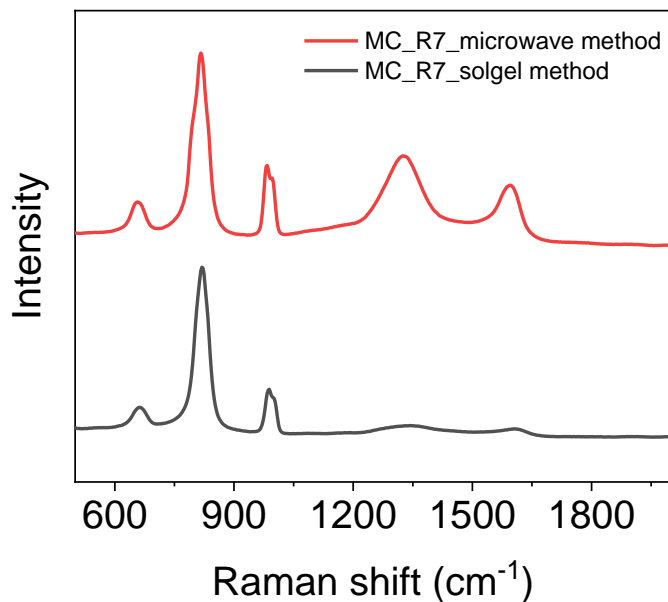


**Figure 81** Raman spectra of Mo<sub>2</sub>C synthesized by the microwave reaction and the sol-gel method (after the chemical reaction, products were thermally annealed at 800 °C).

In addition, the effect of R and annealing temperature on the short-range order was analyzed in nanoparticles from the microwave reaction. Figure 82 shows Raman spectra of Mo<sub>2</sub>C nanoparticles from the microwave reaction at different R. As-received nanoparticles were annealed at 600 °C or 800 °C. Raman peaks of Mo<sub>2</sub>C are found in all samples, but their intensity is the strongest in nanoparticles of R = 7. Increase in the annealing temperature also increases the intensity of Mo<sub>2</sub>C peaks. A change in the intensity ratios of D-band, G-band and Mo<sub>2</sub>C is negligible, regardless of R and annealing temperature. This suggests that the crystallization of Mo<sub>2</sub>C nanoparticles and the solidification of carbon to graphitic particles are strongly connected and the reaction producing the seeds of Mo<sub>2</sub>C also forms the seeds of the graphitic particles.

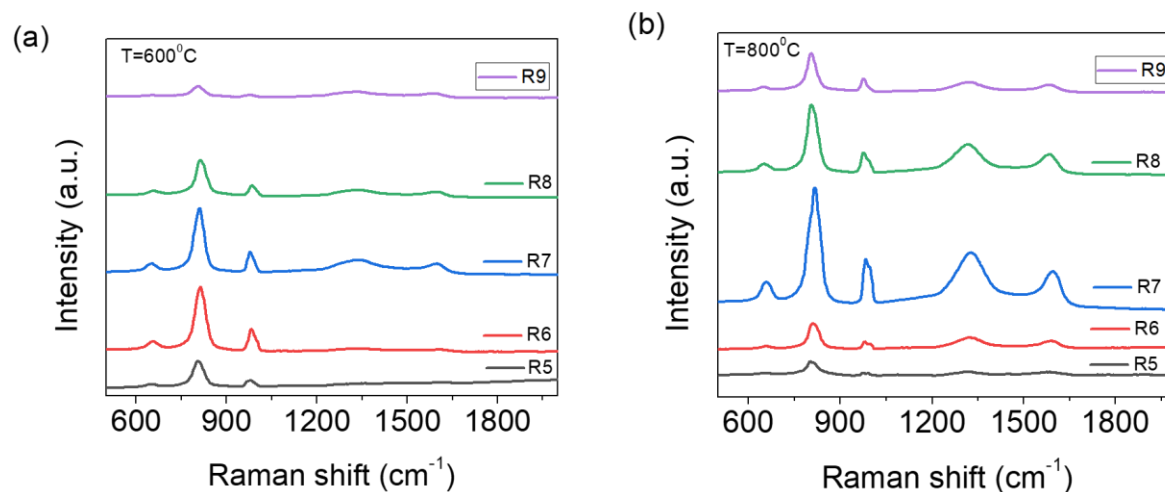


**Figure 82** Raman spectra of Mo<sub>2</sub>C nanoparticles from the microwave reaction at different R: as-received nanoparticles were annealed at 600 °C or 800 °C.

Since the HER performance of transition metal-based materials is closely related with the chemical environment of the metal, the surface chemical state and composition of the MoC<sub>2</sub> samples were also analyzed by X-ray photoelectron spectroscopy (XPS). Figure 83 shows the XPS spectrum of Mo<sub>2</sub>C from the precursors of R=7. In the survey region (Figure 83 (a), 100 - 700 eV), Mo, C and O are found. The high-resolution Mo 3d spectrum (Figure 83 (b)) can be well fitted into broad Mo 3d peak consists of the characteristic peaks of Mo<sup>2+</sup>, Mo<sup>3+</sup> and Mo<sup>6+</sup>, which is consistent with previous studies on the surface state of molybdenum carbide. Mo<sup>2+</sup> and Mo<sup>3+</sup> are associated with binding energies 228.0-229.0 and 231.0-232.0 eV can be assigned to carbides in Mo<sub>2</sub>C which is known to be active sites for HER, whereas Mo<sup>6+</sup> species result from the inactive oxides of Mo, MoO<sub>3</sub> which are commonly observed as carbides are exposed to air.<sup>125</sup> The deconvoluted C<sub>1s</sub> peak (Figure 83 (c)) shows a peak centered at 283.7 eV is the main peak and can be assigned as C from Mo-C bond and its intensity is the highest for R = 7. Whereas graphitic

carbon C=C ( $sp^2$ ) peak around 284.5 eV may overlap with the C from Mo-C. As consistent with the Raman data,  $Mo_2C$  shows both carbide and graphitic carbons C=C ( $sp^2$ ) around 284.5 eV and C-C ( $sp^3$ ) around 286.0 eV. Moreover, C1s peak of R = 7 has additional peaks which can be assigned to C=O peak around 288 which can be attributed to surface oxidation products.

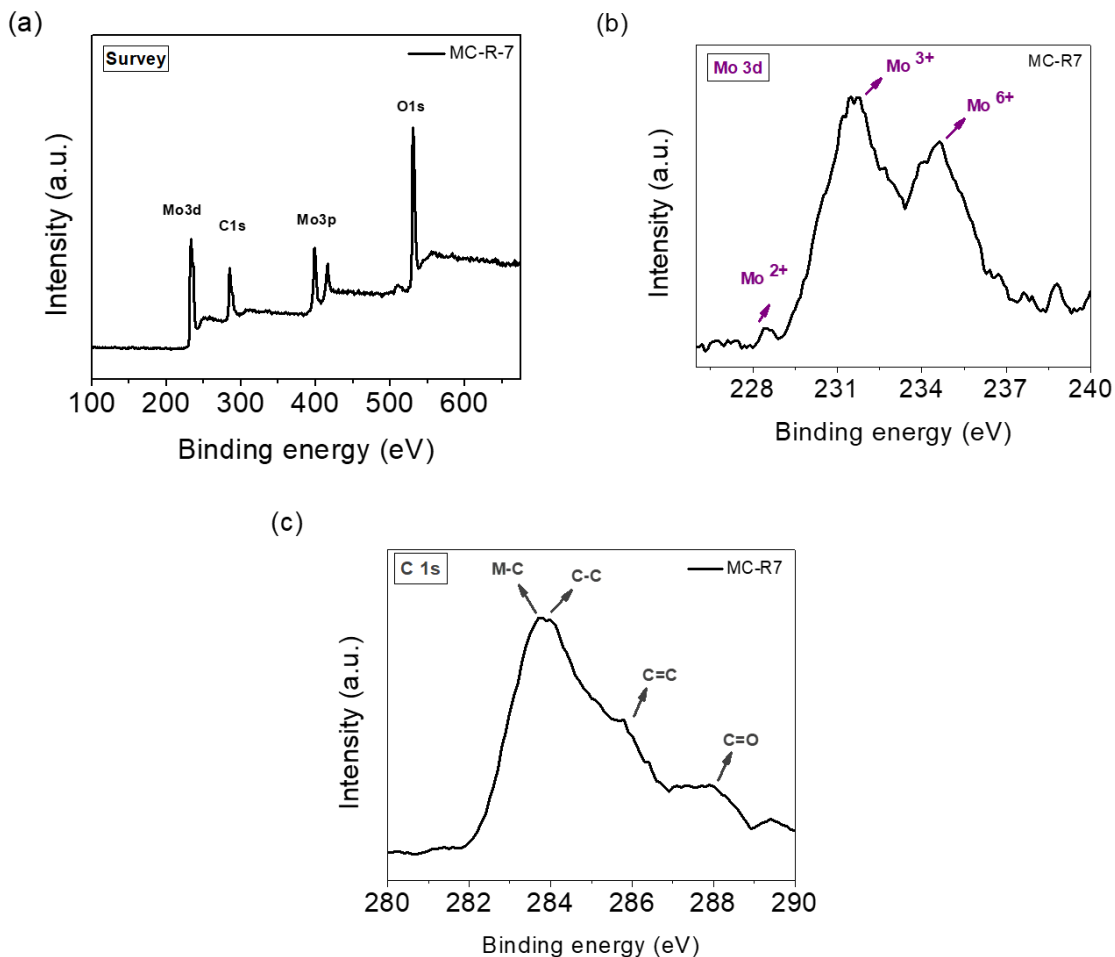


**Figure 83** XPS (a) survey spectrum, (b) Mo 3d spectrum and (c) C 1s spectrum of  $Mo_2C$  with different urea content (R=5, 7, 9)

$Mo_2C$  has attracted a significant amount of interest as a HER electrocatalyst. An outstanding ability of  $Mo_2C$  to produce  $H_2$  is related to its electronic structure that is very close to

that of Pt - group elements. Therefore, Mo<sub>2</sub>C exhibits a strong metallic character, which is different from most of ionic and covalent bonding materials. Mo<sub>2</sub>C acts as a conducting metal-like solid. In this regard, we performed the electrical conductivity measurements of Mo<sub>2</sub>C nanoparticles which were synthesized at different R. Nanoparticle were mixed with terpineol and screen-printed on glass substrates. Printed thick films of the nanoparticles were thermal annealed to remove residual organics before the 4-point probe electric conductivity measurement. Figure 84 shows I-V curves of Mo<sub>2</sub>C of different R. Mo<sub>2</sub>C-R7 exhibits the highest electric conductivity. In metal films like Mo<sub>2</sub>C films, the electric conductivity heavily depends on a change in the mobility of metals rather than their electron concentration. This is because the electron concentration is determined by the electron band structure which is not sensitive to a change in the crystallinity or microstructure of materials. A dependence of the electric conductivity on R suggests that the high crystallinity of Mo<sub>2</sub>C-R7 increases the electron mobility by decreasing the defect concentration within Mo<sub>2</sub>C grains.

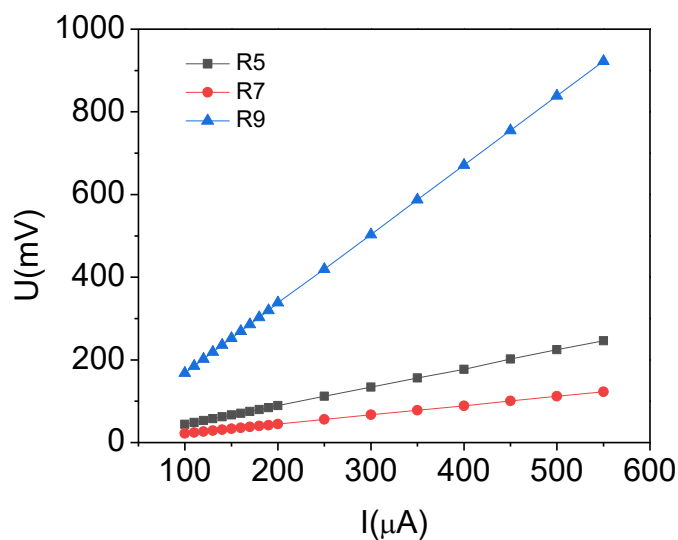


**Figure 84** I-V curves of Mo<sub>2</sub>C synthesized at different R (=5, 7, 9).

### 6.2.1.2 Hydrogen Evolution Reaction (HER) Performance and Electrochemical Characterization of Pure Mo<sub>2</sub>C

HER activity of Mo<sub>2</sub>C is measured by a three-electrode method: reference electrode, working electrode and counter electrode. In the measurement, we use Ag/AgCl electrode as the reference electrode and Pt electrode as the counter electrode. While our sample Mo<sub>2</sub>C electrode is the working electrode. From the three electrode measurements, several criteria to evaluate the performance of electrocatalysts are measured. The first one is electric current flowing in the PEC cell when applied electric potential is equivalent to the theoretical free energy of the redox reactions. As the electrocatalyst promotes the redox reaction, electric current of the three electrode measurement increases. The second is applied potential at which the redox reaction starts. In practice, water electrolysis and oxygen evolution on the anode does not occur by applying the

theoretical redox potential. Factors impeding the hydrolysis include the activation energy of a chemical reaction, the barrier for carrier transfer at the interface, the slow diffusion of ions in the electrolyte and the surface polarization. An additional potential to overcome such barriers is called the overpotential which is decreased by adding the electrocatalyst on the surface of the electrode. A definition of the overpotential ( $\eta$ ) is given by equation;

$$\eta = E_{\text{applied}} - E_t$$

$$\eta = \text{overpotential} \quad E_{\text{applied}} = \text{applied potential (V)}$$

$$E_t = \text{theoretical potential from thermodynamics (V)}$$

In electrochemistry, Tafel plot, is used to get a better grasp on the kinetics of electrochemical reactions for both anode and cathode. A Tafel slope gives information on the rate determining step in an electrochemical reaction. It is an inherent property of the electrode material. To better understand HER mechanism of various catalysts, polarization curves are fitted to the Tafel equation ( $\eta = a + b \times \log j$ ), where  $j$  is the current density and  $b$  is Tafel slope. Tafel slope ( $b$ ) is an inherent property of a catalyst and is determined by the rate-determining step of HER. In an acidic solution, hydrogen evolves through a multi-step process on the surface of catalyst.

The empirical values of the Tafel slopes extracted from the Tafel plot can provide insight into the probable mechanism for the HER on the catalytic surface.

$$\eta = \beta \times \log\left(\frac{i}{i_0}\right)$$

$$\beta = \text{Tafel slope } \left(\frac{mV}{dec}\right) \quad i = \text{current density } \left(\frac{A}{m^2}\right) \quad i_0 = \text{exchange current density } \left(\frac{A}{m^2}\right)$$

The overpotential and Tafel plot directly affect the energy efficiency and HER activity of electrodes, and it is the most important parameter to evaluate the performance of electrodes and electrodes. In general, the potential at 10 mA/cm<sup>2</sup> current density is used to evaluate overpotential of the resultant electrode, which is a useful metric for comparing electro-catalysts for solar to hydrogen production. The lower the overpotential, the higher the HER activity. Nanoparticle synthesis is essential for improving the HER performance by increasing the number of catalytically active sites available on the surface of catalyst. It is known that molybdenum carbide nanoparticles exhibit good electrocatalytic activity toward the HER. Mo<sub>2</sub>C nanoparticles synthesized by the microwave radiation not only result an increased number of catalytically active sites with unique surface facets but also introduced graphitized carbon into the cathode. This enhances the electric conductivity and accordingly improves their electrocatalytic activity for HER.

Mo<sub>2</sub>C nanoparticles synthesized at different conditions were tested for the electrochemical HER activity. LSV experiments were performed in 0.05 M H<sub>2</sub>SO<sub>4</sub> at various scan rates 100 mVs<sup>-1</sup>, 50 mVs<sup>-1</sup>, 20 mVs<sup>-1</sup>, and 10 mVs<sup>-1</sup> within various applied potential range. The optimum condition for all LSV measurements set to be a scan rate of 20 mVs<sup>-1</sup> and an applied potential of -0.8 V to 0 V. The catalytic activity of carbide materials is known to depend on their surface structure and composition. For this purpose, we prepared two different sets of samples. First set of samples composed of pure Mo<sub>2</sub>C nanoparticles synthesized with different R content. Figure 85

presents the voltammograms for the molybdenum nanoparticles with varying R content. The reported current density was obtained using a geometrical surface area of an electrode ( $1 \text{ cm}^2$ ) with the same amount catalyst loading ( $0.54 \text{ mg/cm}^2$ ).

R of the precursor affects HER activity of  $\text{Mo}_2\text{C}$ . The overpotential at  $10 \text{ mA/cm}^2$  ( $\eta_{10}$ ) is  $473 \text{ mV}$  for  $R = 9$ , but it decreases to  $220 \text{ mV}$  for  $R = 7$ . This shows that  $\text{Mo}_2\text{C} - \text{R7}$  possesses the highest catalytic activity. This suggests that synergic enhancement for molybdenum and carbon species for  $\text{Mo}_2\text{C-R7}$  sample.

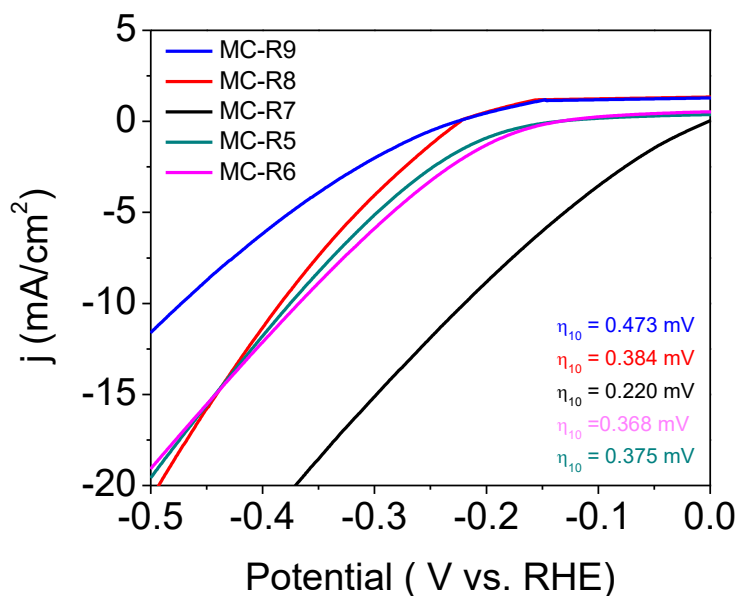
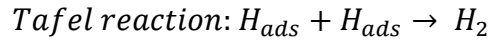
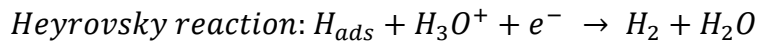
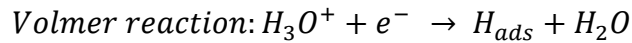


**Figure 85** Linear sweep voltammetry (LSV) curves for  $\text{Mo}_2\text{C}$  nanoparticles with different amount of urea content (R), the electrolyte was  $0.5 \text{ M H}_2\text{SO}_4$ , the scan rate  $20 \text{ mVs}^{-1}$ , the geometric area of the electrode was  $1.0 \text{ cm}^2$ .

Figure 86 displays the Tafel plots for HER on Mo<sub>2</sub>C with different R content. Tafel slopes obtained from the polarization curves of -0.8 V to 0 V of Mo<sub>2</sub>C electrode. Tafel slope is 177 mV/dec for Mo<sub>2</sub>C-R9 electrode, but it decreases to 120 mV/dec for Mo<sub>2</sub>C-R7 electrode. The small Tafel slope indicates a fast increase of the hydrogen generation rate with applied overpotential, which corresponds to the high activity presented in LSV curves. According to the classical theory, the HER in acidic media proceeds in two steps including the Volmer, the Heyrovsky, and the Tafel reaction, which can elucidate the electron transfer kinetics.<sup>126</sup> The possible reactions are given as follows:



The first step is Volmer-reaction where electrochemical reduction (H<sup>+</sup> reduction) takes place at the Tafel slope of b~120 mVdec<sup>-1</sup>, and the second step is hydrogen desorption reaction either the ion and atom reaction (Heyrovsky-reaction) at the Tafel slope of b~40 mVdec<sup>-1</sup> or adsorbed atom combination reaction (Tafel reaction) at the Tafel slope of b~30 mVdec<sup>-1</sup>.<sup>127</sup>

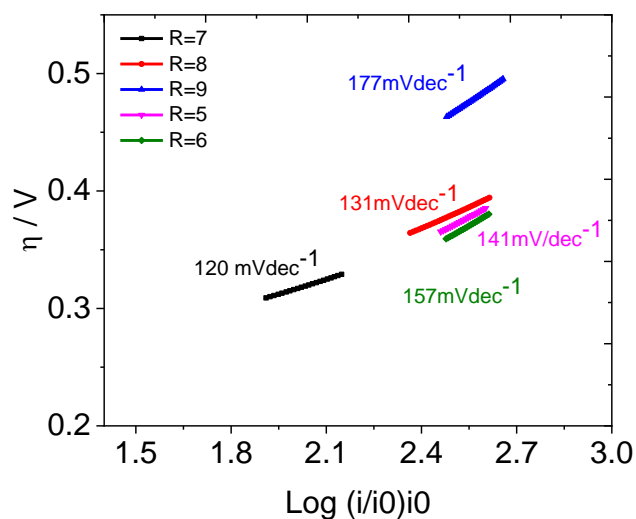


**Figure 86** Tafel plot; for  $\text{Mo}_2\text{C}$  nanoparticles with different amount of urea content (R), the electrolyte was 0.5 M  $\text{H}_2\text{SO}_4$ , the scan rate was  $20 \text{ mVs}^{-1}$ , the geometric area of the electrode was  $1.0 \text{ cm}^2$ .

Electrochemical impedance spectroscopy (EIS) measurements were carried out to further elucidate the mechanism of charge transfer processes at different frequency ranges with the different catalysts. Representative Nyquist plots and corresponding Bode plots of  $\text{Mo}_2\text{C}$  from different R (R= 5, 7, 9) are shown in Figure 87 and 88 respectively. Nyquist plots shown in Figure 87 indicates that the semicircle at low frequency depends on applied bias and represents RC relaxation of the charge transfer. This is directly connected to the kinetics of HER process. The second semicircle is due to material transport toward and from the surface of the cathode. Among three catalysts, MC-R7 exhibits the lowest charge-transfer resistance, suggesting that the highly crystalline and electrically conductive cathode improves the kinetics of HER reaction on the surface of  $\text{Mo}_2\text{C}$ . From Bode plots in Figure 88, it can be concluded that three catalysts with

different urea content reveal the presence of two time-constants at the applied potential of 0, 150, 200 mV.

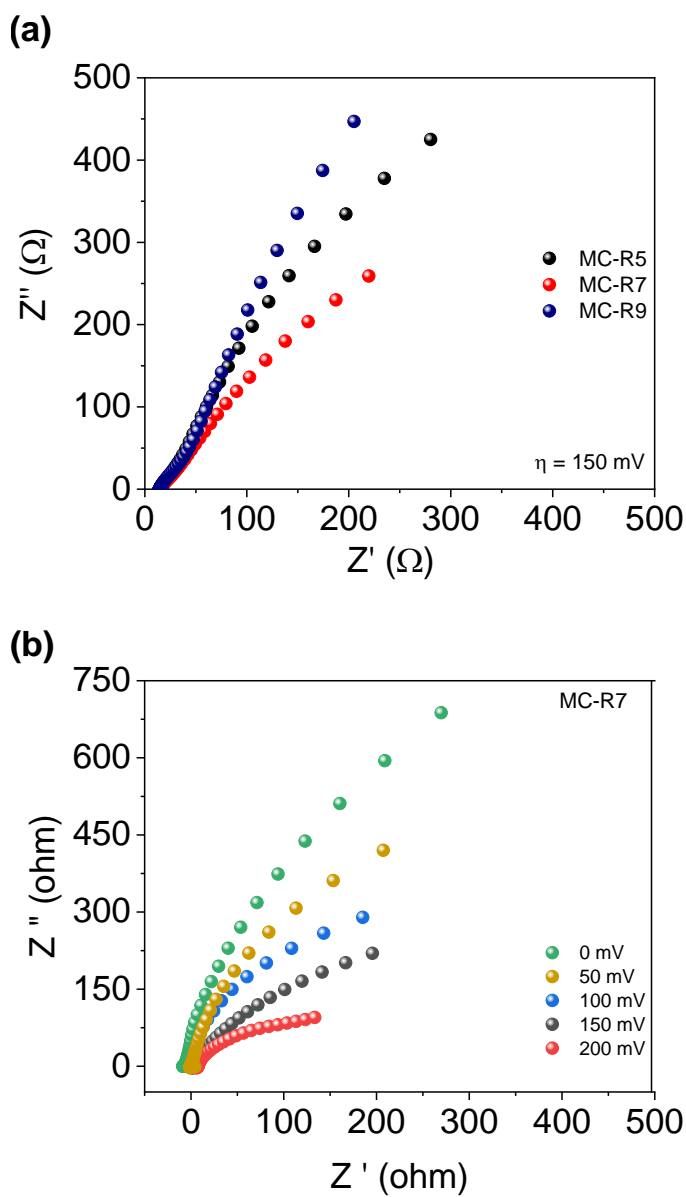


**Figure 87** EIS spectra (Nyquist Plots) of Mo<sub>2</sub>C nanoparticles of (a) different R (R = 5, 7, 9) under external bias of 150 mV and (b) R=7 sample under external bias of 0, 50, 100,150, and 200mV (electrolyte: 0.5 M H<sub>2</sub>SO<sub>4</sub>, a frequency range of 100 mHz to 100 kHz).

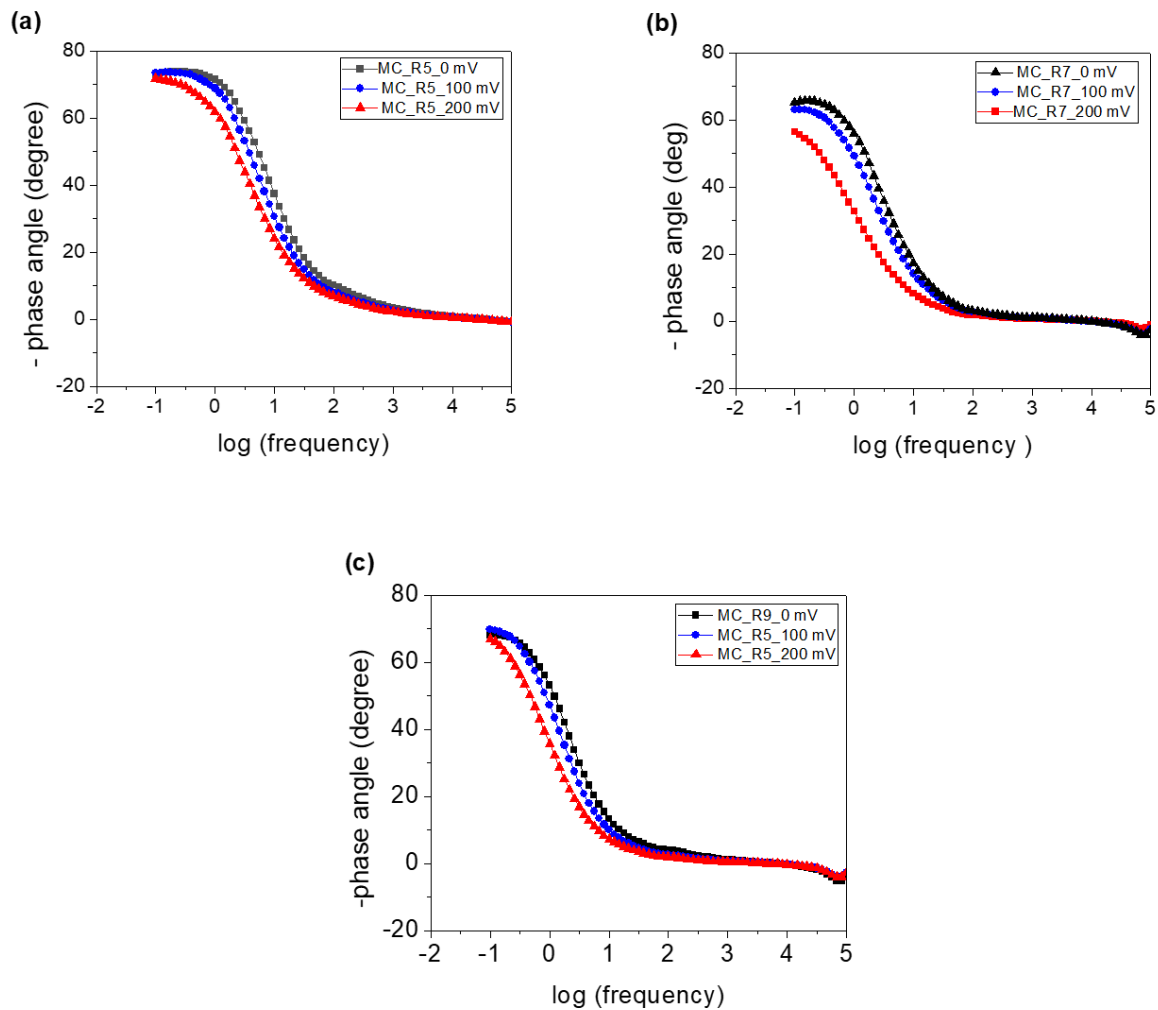


**Figure 88** EIS spectra (BodePlots) of Mo<sub>2</sub>C nanoparticles of different R (R = 5, 7, 9) under external bias of 0, 100, and 200 mV (electrolyte: 0.5 M H<sub>2</sub>SO<sub>4</sub>, a frequency range of 100 mHz to 100 kHz).

## 6.2.2 Molybdenum Carbide ( $\text{Mo}_2\text{C}$ )-Graphene Oxide (GO) Nanocomposite as Electrocatalyst

### 6.2.2.1 Structural Analysis of $\text{Mo}_2\text{C}$ – Graphene Oxide (GO) Nanocomposite

Figure 89 shows XRD patterns of synthesized nanocomposites as a function of GO content in  $\text{Mo}_2\text{C}$ . Upon addition of graphene oxide to the molybdenum carbide crystallinity of samples decreases. Crystallinity decrease with increasing GO content.  $\text{Mo}_2\text{C}$  with 0.3 wt % GO shows the best crystallinity. Incorporation of GO into  $\text{Mo}_2\text{C}$  decreases the crystallinity. The sharp and strong peaks and highly exposed planes indicate the good crystallization of  $\text{Mo}_2\text{C}$  nanoparticles while the unobvious diffraction peaks of graphite carbon in the pattern can be attributed to the limited content of graphitic carbon.

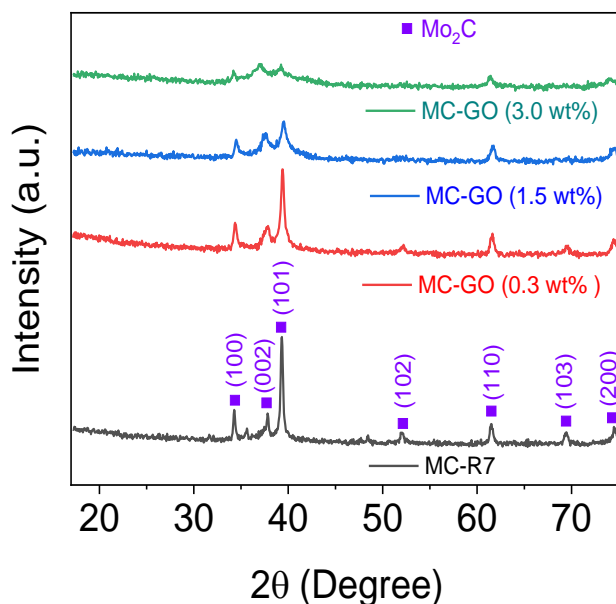


**Figure 89** X-Ray Diffraction (XRD) patterns for  $\text{Mo}_2\text{C}$  and  $\text{Mo}_2\text{C}$ -GO nanocomposites with various GO amount.

Open structure of graphene oxide (GO) material renders more interfacial contact with the electrolyte. All these advantages of GO can benefit the HER performance when used as carbon support for the electro catalyst material. Without any template for growing, Mo<sub>2</sub>C nanoparticles tend to form agglomerations and particles with random morphology. The coalescence of nanoparticles into bigger sized particles could lessen electrocatalytic activity as well as penetration of the electrolyte into catalytically active sites. In order to eliminate these problems, originate from agglomerated Mo<sub>2</sub>C nanoparticles, GO can be used as a proper supporting material for tailoring and curtailing the size of Mo<sub>2</sub>C nanoparticles to increase the catalytically active area and hence promoting the overall HER activity.

Moreover, we performed systematic analysis of GO addition into Mo<sub>2</sub>C nanoparticles and the resultant morphology change was observed. Figure 90 shows the effect of various amounts of GO (0.3 wt%, 1.5 wt%, and 3.0 wt%) added into Mo<sub>2</sub>C nanoparticles. Bare Mo<sub>2</sub>C shows larger particles around 200 nm and aggregation can be observed. Upon addition of GO into the system, the size is reduced up to 100 nm with 3.0 wt% GO. These results also consistent with the HER activity performances, which can be deduced that anchoring Mo<sub>2</sub>C morphology upon addition of GO provides reduction in size and increased number or catalytically active sites which enhances overall catalytic activity.

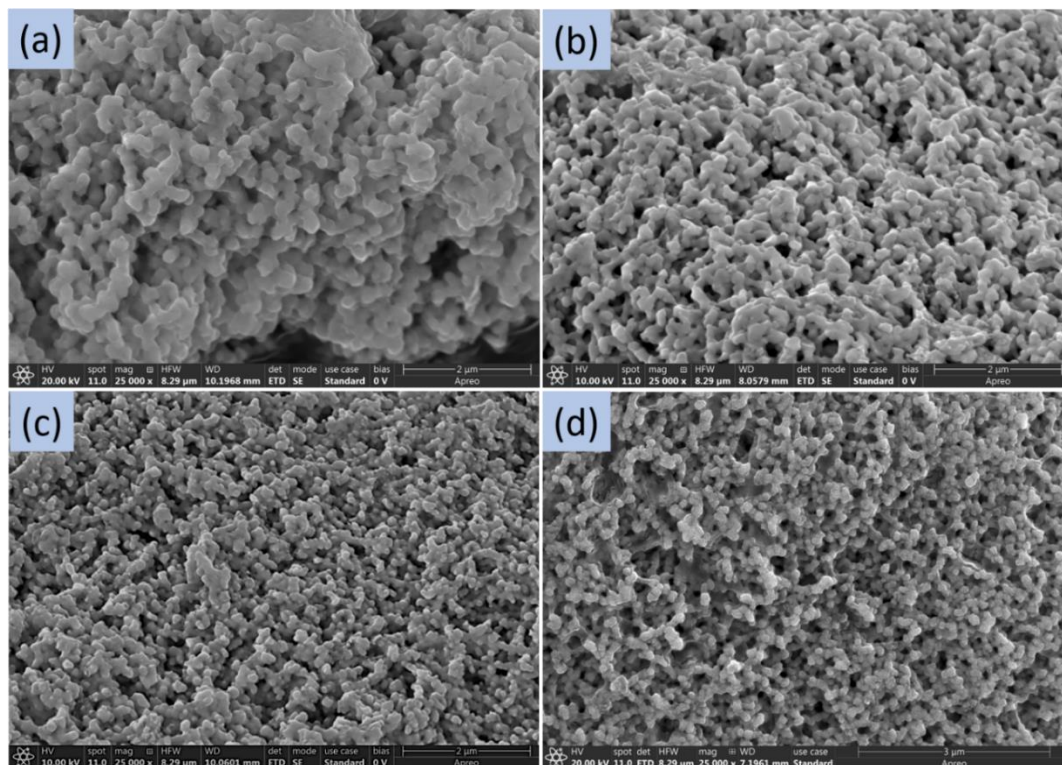


**Figure 90** Scanning electron microscope images of pure  $\text{Mo}_2\text{C}$  (a) and  $\text{Mo}_2\text{C}$ -GO nanocomposites with different GO loading amount (b) GO (0.3 wt%), (c) GO (1.5wt%), and (d) GO (3.0 wt%)

The HER performance of transition-metal-based materials is highly correlated with the chemical environment of the metal. Thus, XPS measurements were performed to study the surface chemical compositions and oxidation states of the samples. In accordance with the previous studies, the surface of the Mo catalysts can be contaminated with molybdenum oxides ( $\text{MoO}_2$  and  $\text{MoO}_3$ ). The survey, Mo 3d, O1s, and C1s spectra are presented in Figure 91. The peaks in the range of 224–240 eV can be assigned to Mo core level and oxidation states of molybdenum present in  $\text{Mo}_2\text{C}$ -GO composite samples can be given as:  $\text{Mo}^{2+}$  (228.0-229.0 eV),  $\text{Mo}^{3+}$  (231.0-232.0 eV), and  $\text{Mo}^{6+}$  (235.4 eV).  $\text{Mo}^{2+}$  and  $\text{Mo}^{3+}$  are focus point because they are the active centers for

hydrogen evolution reaction (HER). The  $\text{Mo}^{3+}/\text{Mo}^{2+}$  mole ratios can provide useful information to understand the nature of active sites. Variation of  $\text{Mo}^{3+}/\text{Mo}^{2+}$  will influence the HER activity, related to the different electron density around  $\text{Mo}^{3+}$  and  $\text{Mo}^{2+}$ . The  $\text{Mo}^{6+}$  species result from the inactive  $\text{MoO}_3$ , which are commonly observed as carbides are exposed to air. C1s peak in Figure 91 (c) is also composed of several peaks. A peak centered at 283.5 eV is assigned as C from Mo-C bond. Other peaks 284.0 eV and 285 eV can be assigned to amorphous carbon atoms (C=C  $\text{sp}^2$  and C-C  $\text{sp}^3$ ) which is also correlated with Raman data showing presence of  $\text{sp}^2$  and  $\text{sp}^3$  carbon bonding. The peak around 288.5 eV associated with C=O testify the surface oxidation upon incorporation of GO into  $\text{Mo}_2\text{C}$ .

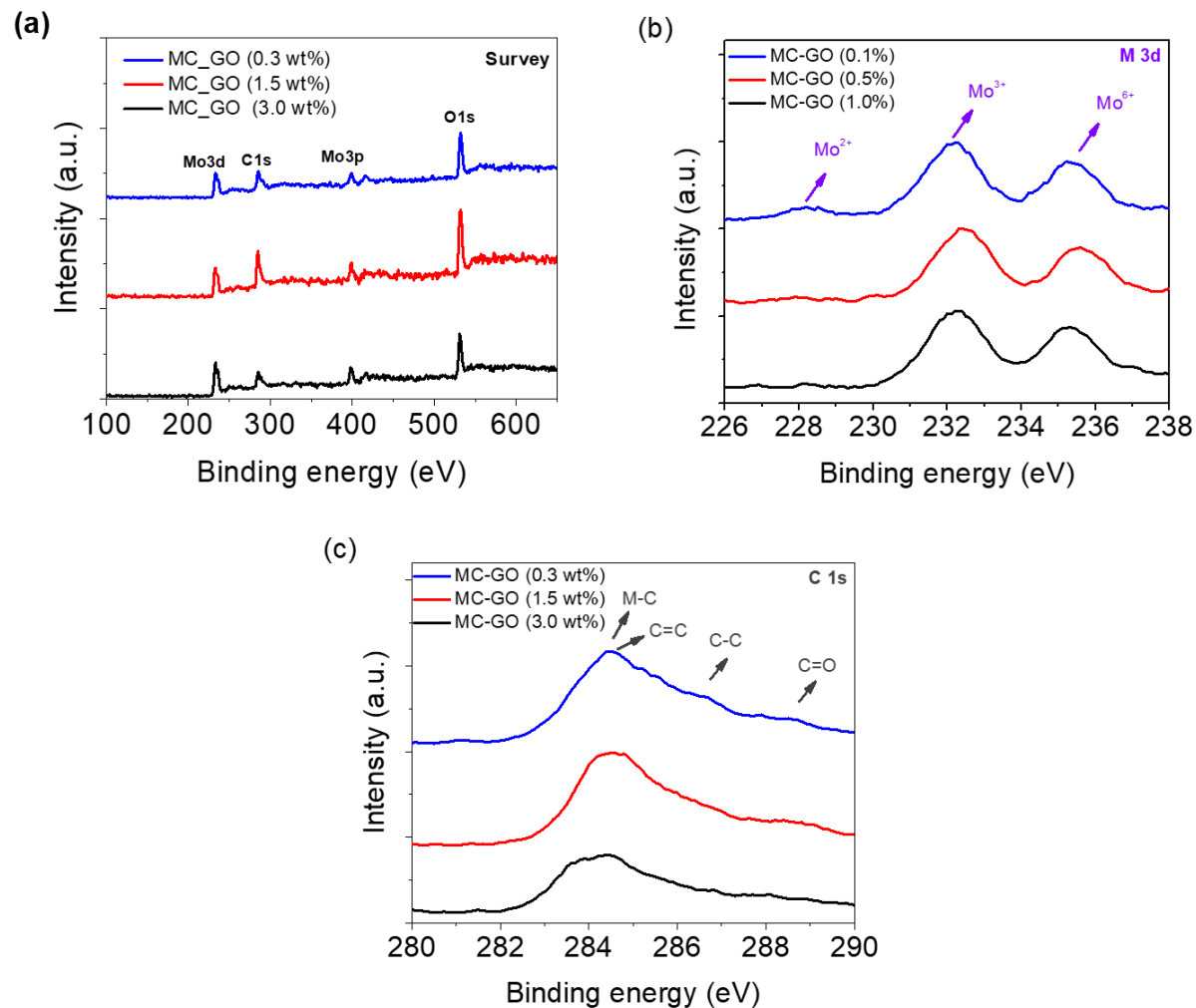


**Figure 91** XPS (a) survey spectrum, (b) Mo<sub>3d</sub> spectrum, and (c) C<sub>1s</sub> spectrum for Mo<sub>2</sub>C-GO composites with different GO content.

A comparison of the Raman spectra of Mo<sub>2</sub>C and Mo<sub>2</sub>C-GO composites in the 500-2500 cm<sup>-1</sup> range is shown in Figure 92. The D band at 1350 cm<sup>-1</sup> assigned to A<sub>1g</sub> symmetry, characterizes graphite plane disordering and defect incorporation into the pentagon and heptagon graphitic structures. The band observed at about 1580 cm<sup>-1</sup> is the G band which corresponds to splitting of the E<sub>2g</sub> graphite stretching mode and reflects the structural intensity of the sp<sup>2</sup>-hybridized carbon

atoms. The Raman spectra of the above Mo<sub>2</sub>C and Mo<sub>2</sub>C-GO samples display the D- and G-bands of carbon at 1350 and 1590 cm<sup>-1</sup>, respectively, confirming the presence of free carbon. Both Mo<sub>2</sub>C and Mo<sub>2</sub>C-GO showed characteristic peaks of molybdenum carbide located at 670 cm<sup>-1</sup>, 840 cm<sup>-1</sup>, and 990 cm<sup>-1</sup>, which is consistent with the XRD pattern. The values of the D/G ratio were usually applied to judge the graphitization degrees. The intensity of the D band has increase, indicating the generation of disordered graphitic carbon or defects during the annealing process. As going from Mo<sub>2</sub>C to Mo<sub>2</sub>C-GO samples, the relative peak intensity of molybdenum carbide peaks to D-G peaks decreases, which indicates incorporation of more graphitic carbon into the system and also consistent with XRD crystallinity change. D/G ratio decreases from Mo<sub>2</sub>C to Mo<sub>2</sub>C-GO samples. The decrease in D/G ratio indicates a decrease of the microstructural disordering and defects on increasing the amount of carbon source, thus the overall electrical conductivity was enhanced on going from low C content to high carbon content, which also facilitates charge transfer during electrochemical testing.

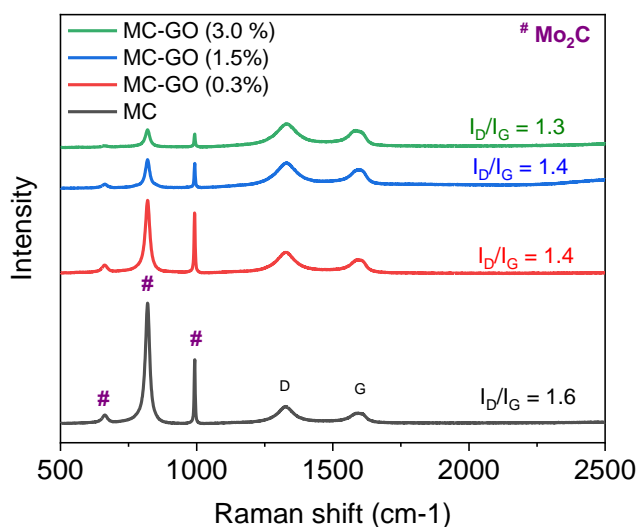


**Figure 92** Raman spectra of Mo<sub>2</sub>C and Mo<sub>2</sub>C-GO nanocomposites with different amount of GO addition

As previously mentioned, graphene based functional materials has been reported to be ideal HER electrocatalyst especially when coupled with other metal-based materials such as Mo<sub>2</sub>C. Graphene oxide expected to affect overall HER activity because of its high electric/thermal conductivity and large specific surface area.<sup>128</sup> The as-synthesized Mo<sub>2</sub>C-GO composite films may show a highly dispersed distribution of nanoparticles on the graphene support, which provides a large surface area and high conductivity to the Mo-compounds, thus increasing the HER catalytic activity through enhanced mass and charge transfer. In this regard, we performed the electrical conductivity measurements of Mo<sub>2</sub>C-GO nanocomposites which were synthesized at different amount of GO additions. Nanocomposites were mixed with terpineol and screen-printed on glass substrates. Printed thick films of the nanocomposites were thermal annealed to remove residual organics before the 4-point probe electric conductivity measurement. Figure 93 shows I-V curves of Mo<sub>2</sub>C of various amount of GO. Mo<sub>2</sub>C-GO (3.0%) exhibits the highest electric conductivity. In metal films like Mo<sub>2</sub>C films, the HER activity is limited by its poor electrical conductivity. Poor electrical conductivity is dependent on low mobility and low electron transfer capability which is originated from the electron band structure. A dependence of the electric conductivity on GO amount suggests that introducing the highly conductive graphene oxide substrates into Mo<sub>2</sub>C increases surface area and accelerates the electron transfer by increasing the electron mobility within Mo<sub>2</sub>C-GO nanocomposite material.

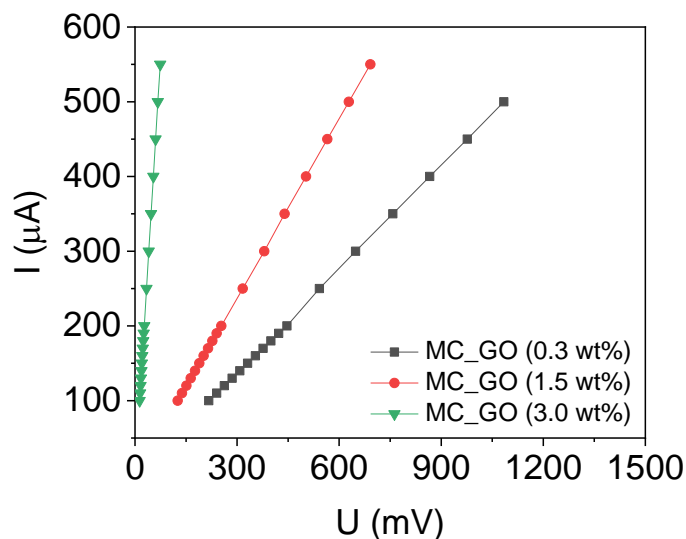


**Figure 93** Resistivity data for Mo<sub>2</sub>C-GO electrocatalysts with different amount of GO content (GO=0.3, 1.5, 3.0 wt%)

### 6.2.2.2 Role of GO on Hydrogen Evolution Reaction (HER) Performance and Electrochemical Characterization

The nanocomposite materials prepared at different temperatures and different synthetic methods are expected to possess different electrocatalytic activities. The graphene itself barely shows electrocatalytic activity towards HER, but graphene oxide incorporation into Mo<sub>2</sub>C shows dramatic enhancement in the overall HER activity. Figure 94 shows the corresponding LSV curves for Mo<sub>2</sub>C-GO nanocomposites. Mo<sub>2</sub>C -3.0 wt% GO shows the best HER performance with a small overpotential ( $\eta_{10}$ ) 125 mVs<sup>-1</sup>. Mo<sub>2</sub>C-GO (3.0 wt%) shows the smallest particle size under SEM which supports the increased number of active sites available on the surface. This superior catalytic activity of Mo<sub>2</sub>C-GO nanocomposites compared to pure Mo<sub>2</sub>C catalysts can be attributed to enhanced electrical conductivity, increase surface area hence more readily available

electrocatalytically active sites upon incorporation of GO to Mo<sub>2</sub>C. The presence of 1nm of graphitized carbon surrounding Mo<sub>2</sub>C particles improved the conductivity and accordingly electron transfer.

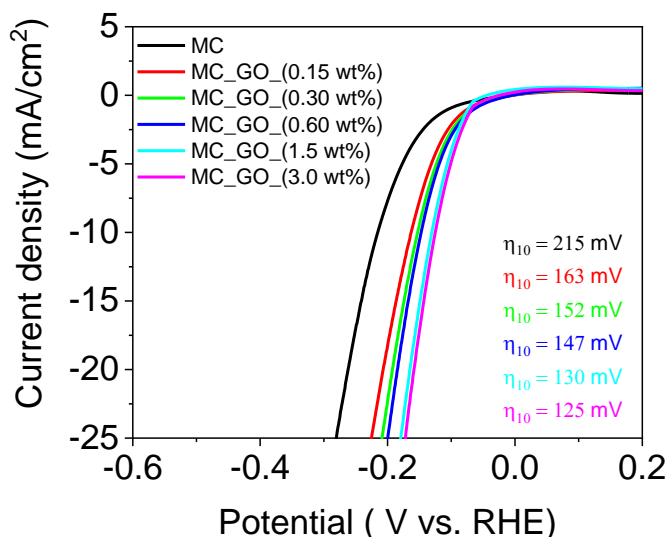


**Figure 94** Linear sweep voltammetry (LSV) curves for Mo<sub>2</sub>C nanoparticles with different amount of GO content, the electrolyte was 0.5 M H<sub>2</sub>SO<sub>4</sub>, the scan rate 20 mVs<sup>-1</sup>, the geometric area of the electrode was 1.0 cm<sup>2</sup>.

Linear Tafel plots are employed to evaluate HER kinetics and elucidate the HER mechanism by fitting the data to the equation ( $\eta = b \log(j) + a$ , where  $j$  is the current density and  $b$  is the corresponding Tafel slope). Figure 95 displays the Tafel plots for HER on Mo<sub>2</sub>C-GO nanocomposites with different GO content. Generally, two mechanisms are involved in the HER process in acidic media as mentioned previously. First one is combination of hydronium ion (H<sub>3</sub>O<sup>+</sup>) with an electron to form adsorbed hydrogen on the surface of electrocatalyst. (Volmer reaction, H<sub>3</sub>O<sup>+</sup> + e<sup>-</sup> = H<sub>ads</sub> + H<sub>2</sub>O) The second step can be associated with either combination of adsorbed H

with hydronium ion to form H<sub>2</sub> (Heyrovsky reaction), or binding with another adsorbed H to give H<sub>2</sub> at the Tafel slope (Tafel reaction). Tafel slopes obtained from the polarization curves of -0.8 V to 0 V of the molybdenum-based nanocomposites were in the range of 90-150 mV dec<sup>-1</sup> and these values are consistent with previously reported values, which suggests that the discharge mechanism is slow and the Volmer step is the rate determining step. The Tafel slope for Mo<sub>2</sub>C is 129 mVdec<sup>-1</sup> which is relatively larger than that of Mo<sub>2</sub>C-GO nanocomposites. Mo<sub>2</sub>-GO (3.0 wt%) shows the smallest Tafel slope, which suggests faster HER rate with the increased overpotentials and relatively faster proton discharge kinetics compared to pure Mo<sub>2</sub>C.

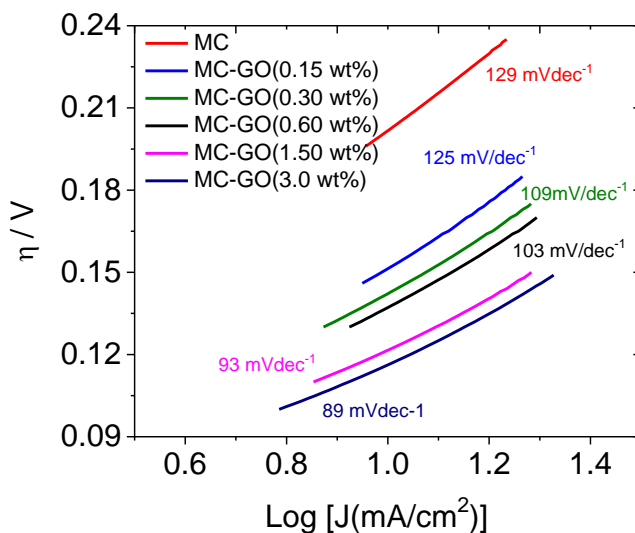


**Figure 95** Tafel plot; for Mo<sub>2</sub>C nanoparticles with different amount of GO content, the electrolyte was 0.5 M H<sub>2</sub>SO<sub>4</sub>, the scan rate was 20 mVs<sup>-1</sup>, the geometric area of the electrode was 1.0 cm<sup>2</sup>.

Electrochemical impedance spectroscopy (EIS) at different HER overpotentials ( $\eta=0, 50, 100, 150, 200$  mV) was further conducted from 100000 Hz to 0.01 Hz on Mo<sub>2</sub>C-GO electrocatalysts to investigate the origin of improved HER performance. The remarkable electrocatalytic activity HER performance of resultant Mo<sub>2</sub>C-GO nanocomposites might have resulted from faster electron transfer. Figure 96 and 97 represents Nyquist and Bode plots for Mo<sub>2</sub>C-GO nanocomposite samples. Consistent with the previous reports, Bode plots recorded at  $\eta=150$  mV and 200 mV suggest a classical two-time-constant model was proposed with EIS Nyquist plots. The proposed model is illustrated in Figure 98. The model consists of a series resistance.  $R_s$ ,  $R_c$ : the contact resistance between the electrode and catalyst layer,  $R_{sol}$  represents the solution resistance, connects in series with two additional branches; one at high frequency related to the surface porosity, CPE1-Rp; one at low frequency related to the charge transfer process CPE2-Rct. As  $R_{ct}$  showed strong correlation with the electrochemical performance, the Nyquist plots were fit and compared. MC-GO nanocomposites exhibit the minimum charge-transfer resistance when compared to MC, indicating the fast electron/mass transfer between the electrocatalyst and the electrolyte, and thus leading to an acceleration of HER kinetics. The charge transfer resistance  $R_{ct}$ , which can be determined from the semicircle recorded at low frequencies, reflects the details of HER kinetics, where a small  $R_{ct}$  value is associated with faster reaction kinetics.  $R_{ct}$  of Mo<sub>2</sub>C-GO is  $\Omega$  at  $\eta= 150$  mV, lower than for Mo<sub>2</sub>C suggesting faster reaction kinetics for Mo<sub>2</sub>C-GO. The charge-transfer resistance values ( $R_{ct}$ ) of both catalysts decrease rapidly as the overpotential decreases. Since  $R_{ct}$  decrease with increasing applied potential, much faster HER kinetics will occur at higher applied overpotential which can be seen in  $\eta=200$  mV case. All these EIS results demonstrate that the resulting MC-GO catalysts exhibits lower

impedance and superior charge transfer ability between the catalyst and the electrolyte, and thus leading to an acceleration of electrocatalytic activities for the HER.

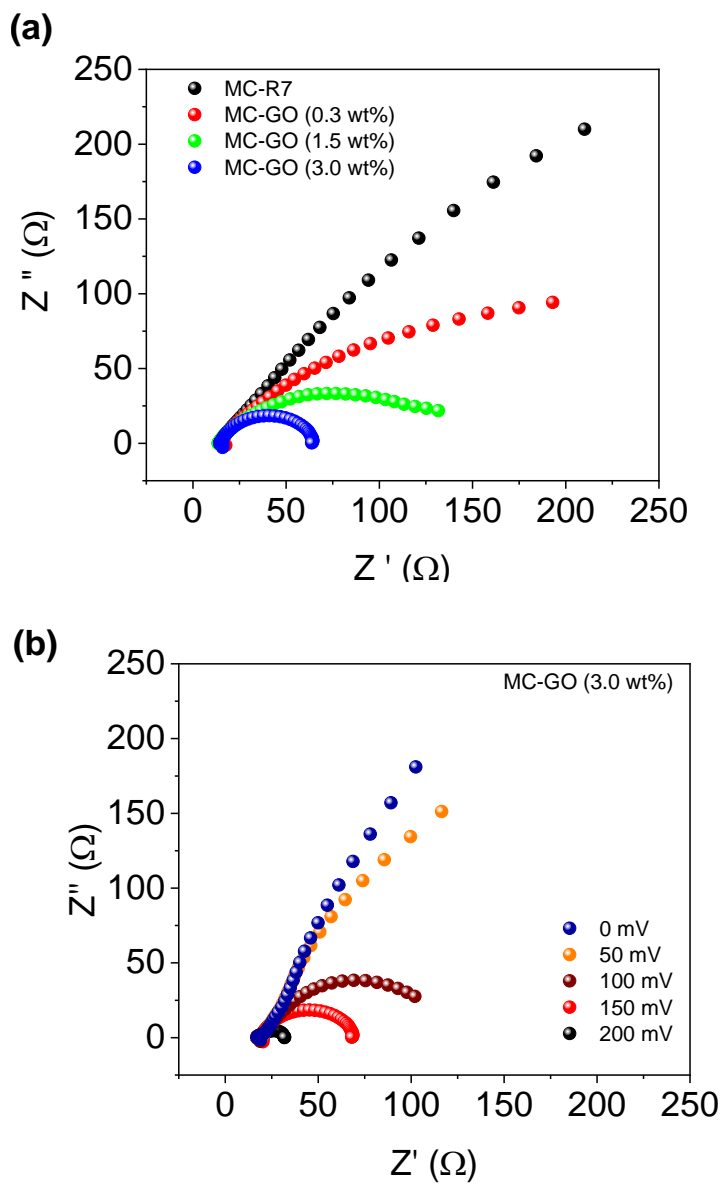


**Figure 96** EIS spectra (Nyquist Plots) of Mo<sub>2</sub>C-GO nanocomposites (a) with different GO content, and (b) with different  $\eta=0, 50\text{mV}, 100\text{mV}, 150\text{mV}, 200\text{mV}$  obtained in 0.5 M H<sub>2</sub>SO<sub>4</sub> at 25 °C in the frequency range of 100 mHz to 100 kHz.

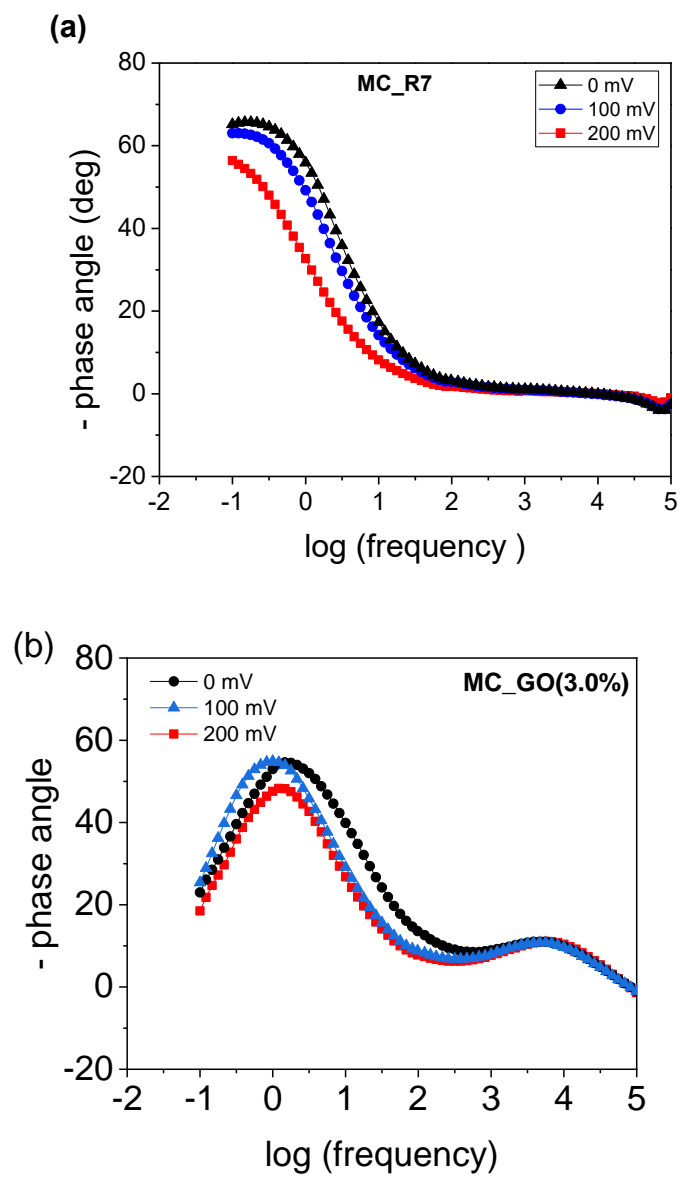


**Figure 97** EIS spectra (Bode Plots) of Mo<sub>2</sub>C and Mo<sub>2</sub>C-GO nanocomposites obtained at  $\eta=0$ , 100, 200 mV in 0.5 M H<sub>2</sub>SO<sub>4</sub> at 25 °C in the frequency range of 100 mHz to 100 kHz.

### Two-time-constant model

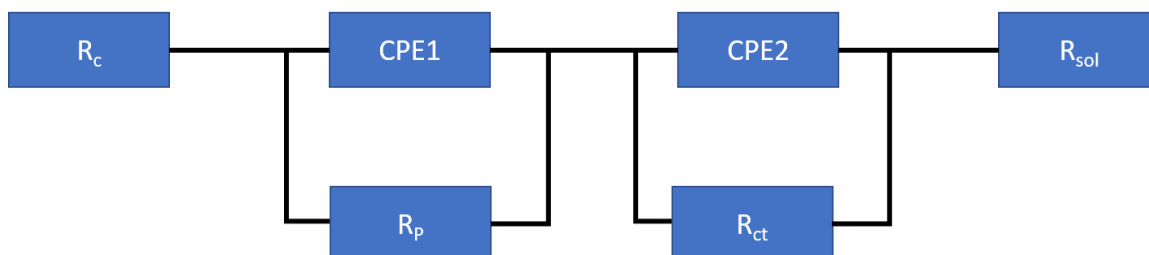


**Figure 98** Electrical Equivalent circuit models for the EIS response of: two-time constant model, including the series resistance ( $R_s$ ), the charge transfer resistance ( $R_{ct}$ ), resistivity related to the porosity of the electrode surface ( $R_p$ ) and constant phase elements CPE1 and CPE2.

Figure 99 depicts schematic representation of incorporation of GO into  $Mo_2C$  and the resultant highly active electrocatalysts for HER reaction. In terms of HER activity and durability results, the  $Mo_2C/GO$  composites not only possess superior HER activity but also provide excellent long-term stability and would be a promising electrocatalytic material for the HER. The relatively superior activity of  $Mo_2C/GO$  composites to the bare  $Mo_2C$  catalysts can be ascribed to the smaller particle size, large surface area, mesoporous structure and relatively high electronic conductivity. With the perspective of maximizing the density of activity sites, the size of  $Mo_2C$  particles should be decreased. Due to aggregation and coalescence of bare  $Mo_2C$  nanoparticles the resultant HER activity can be inferior. In this regard, especially graphene-like supports with large surface area and good conductivity, provide better dispersion of  $Mo_2C$  nanoparticles to prevent aggregation and the over-growth of small nanoparticles into bigger cluster-like particles. In addition, the functional groups (carboxy, hydroxyl) in supporting material (graphene) provides

support for size control during the nucleation and growth of Mo<sub>2</sub>C nanoparticles. Due to tight anchoring and coupling effect between Mo<sub>2</sub>C nanoparticles and graphene sheets,<sup>129</sup> Mo<sub>2</sub>C/GO composite nanostructures in this study provide better HER activities. The synergistic effect between Mo<sub>2</sub>C and graphene and graphitic carbons increase the conductivity and favors the interface contact between electrocatalyst and electrolyte.<sup>130</sup> Our results show from the sheet resistance and EIS measurements show that the conductivity and charge transfer across the interface increases for Mo<sub>2</sub>C/GO compared to Mo<sub>2</sub>C. Construction of a well-defined graphene based nanocomposite structure leads to a significantly enhanced electrochemical performance because of decrease particles size, enhanced conductivity, optimized micro porosity especially for the mass and charge transfer.

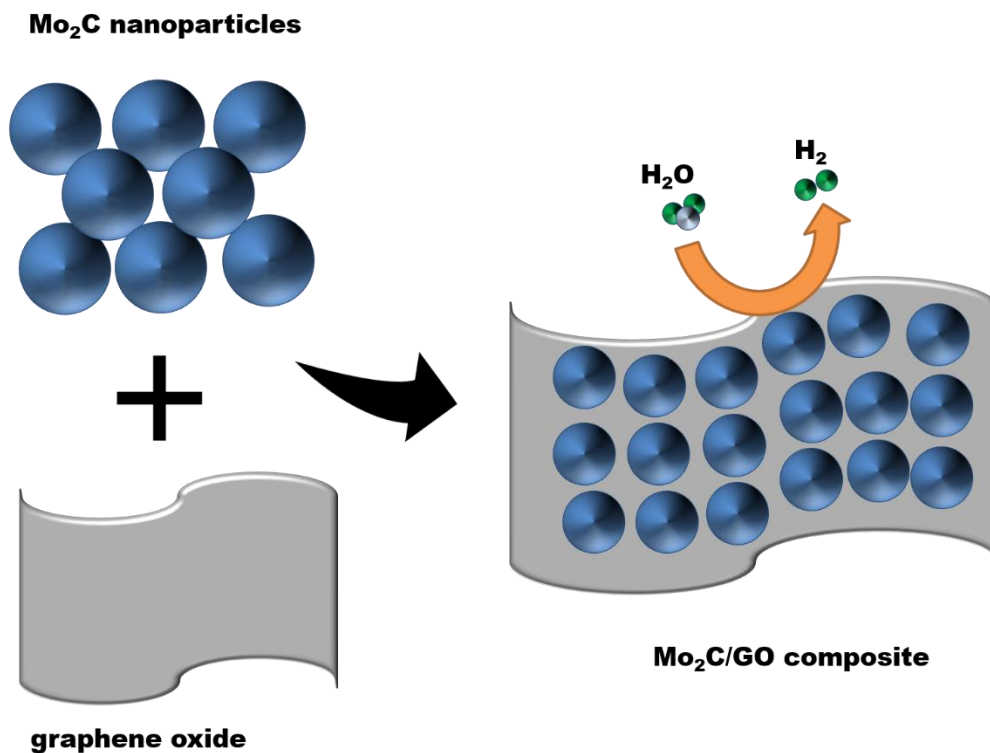


**Figure 99** Schematic representation of Mo<sub>2</sub>C-Go composites as an active electrocatalyst for HER

## **7.0 CONCLUDING REMARKS AND FUTURE WORK**

In order to secure the accessibility of sufficient energy to an increasing world population in the future, it is essential to transform the available sources of energy, aside from the present energy industry monopolized by fossil fuels. Metamorphosis into renewable energy sources from conventional fossil-based sources has become an important part of this goal. However, there is no doubt about the need to extensive research for the feasibility of sustainable energy and of course political implementation of renewable energy-based policies is urgently needed in order to achieve sustainable future energy goals.

This work has dealt with catalytic hydrogen evolution in an electrochemical cell and light induced hydrogen and photocurrent generation in a photoelectrochemical cell. Photoelectrochemical water splitting has been investigated since 1970s to find out the most favorable light absorbing materials, morphologies and catalysts capable of reaching high solar to hydrogen conversion efficiencies. Hitherto, the industrial application of self-sufficient photoelectrochemical systems has not been achieved. The evolution of hydrogen via water splitting has been appealing to researchers and industry, and to obtain hydrogen in a more environmentally friendly and more sustainable way in comparison with conventional industrial hydrogen production, proper electrocatalysts appear to be a promising way. Developing hydrogen evolution reaction (HER) catalysts that can efficiently operate under all medium is the emphasis of ongoing research.

One of the main aspirations of the presented thesis was the development and improvement of advanced nanostructured systems for solar-light -induced water splitting. The first part of the study focused attention on improvement of  $\text{BiVO}_4$  based photoelectrode systems. Employment of plasmonic particles with a well-defined structure was one of the methods to improve overall photoelectrochemical efficiency of  $\text{BiVO}_4$  photoanode. Second part of the study was concentrated on benefits of utilization of heteronanostructures of different light absorbing materials (cadmium chalcogenides) on highly conductive  $\text{SnO}_2$  nanowire arrays.

The other main objective of the demonstrated thesis work was the development of proper electrocatalysts for an efficient hydrogen evolution reaction (HER). With this anticipation,  $\text{Mo}_2\text{C}$  nanoparticles synthesized via novel microwave assisted method and nanocomposites of  $\text{Mo}_2\text{C}$  and graphene oxide was employed as an efficient electrocatalyst for HER.

Finally, the major outcomes of this research project can be summarized as follows;

#### ***A. Plasmonic Nanoparticles Decorated $\text{BiVO}_4$ for Efficient Photoelectrochemical Cells***

This study was able to optimize a facile fabrication process for coating of plasmonic nanoparticles of two kinds of core shell particles,  $\text{SiO}_2@Ag$  and  $\text{SiO}_2@Ag@SiO_2$  on surface of  $\text{BiVO}_4$  photoelectrode, increasing their photoelectrochemical efficiency.

- i. A novel and facile fabrication method has been developed to synthesize  $\text{BiVO}_4$  thin films on FTO
- ii. Optimization of the  $\text{BiVO}_4$  and plasmonics decorated  $\text{BiVO}_4$  thin films for high photoelectrochemical activity has been achieved.

- iii. Two kinds of core shell nanoparticles were successfully synthesized by a two-step and shape and size of the resultant nanoparticles can be easily controlled
- iv. Bismuth vanadate thin films were successfully fabricated via pulse laser deposition technique providing growth of BiVO<sub>4</sub> thin films with well-defined nanostructure and appropriate stoichiometry.
- v. Visible light absorption and scattering is significantly improved in BiVO<sub>4</sub> thin films decorated with the core shell or core shell-shell particles
- vi. The improvement induced by plasmonic nanoparticles can be explained by localized field intensity and enhanced scattering
- vii. Moreover, Ag nanoparticles provide catalytic effect which also contributes to overall photoelectrochemical improvement
- viii. It can be concluded that a combined effect of the near field intensity, light scattering efficiency, localized enhancement, and surface catalytic efficiency can be seen in overall photoelectrochemical enhancement

### ***B. 3-D CdS/CdSe/SnO<sub>2</sub> Cascade Heterojunction for Efficient Photoelectrochemical Cell***

We designed a novel heteronanostructured CdS and CdSe sensitized SnO<sub>2</sub> nanowires and Sb doped SnO<sub>2</sub> nanowires. Photoelectrochemical results show significant enhancement upon this novel heteronanostructure compare with conventional cascade structures or one-layer structures.

We here propose several reasons for the enhancement:

- i. The morphology of SnO<sub>2</sub> NWs keeps the advantage of the wires such as efficient charge separation and transport properties as well as superior light harvesting efficiency while the wires that exposed in the electrolyte favor more CdS and CdSe nanoparticles.
- ii. Compared with bare SnO<sub>2</sub> NWs electrode the CdS and CdSe co-sensitized electrodes have an intense absorption in the visible region, which greatly raised the utilization rate of the solar energy.
- iii. The stepwise band-edge structure would create efficient charge transfer channel and would trigger a higher resistance to transport excited electrons back to the electrolyte, resulting in a higher performance of the co-sensitized electrode.
- iv. The fine heterojunction formed between CdS and SnO<sub>2</sub> is helpful for CdS to collect excited electrons from CdSe to SnO<sub>2</sub> in the stepwise band-edge structure.
- v. A novel approach of polystyrene treatment enables us to preferred locational deposition of CdS and CdSe which enables locational light absorption and provides enhanced photovoltaic performance.
- vi. Sb doping provided increased charge carrier concentration, enhanced charge carrier mobility, and a drastic improvement of electrical conductivity with high transparency in the visible region of the spectrum; hence an improved photovoltaic performance of Sb doped photoelectrodes

***C. Mo<sub>2</sub>C and Graphene Oxide-Mo<sub>2</sub>C Nanocomposites for Efficient Hydrogen Evolution (HER) Reaction***

- i. Rational design and fabrication of nanostructured molybdenum carbide based electrocatalysts for electrocatalysis. especially for hydrogen evolution reaction.
- ii. Development of facile one-step synthesis method to prepare transition metal based electrocatalysts.
- iii. Improvement of electronic conductivity of the nanocomposite systems with sophisticated connectivity among the active material and graphene oxide matrix.
- iv. Preparation of molybdenum carbide nanoparticles and molybdenum carbide nanoparticles with graphene oxide in the form of nanocomposite, as efficient and long-lasting electrocatalysts for hydrogen evolution reaction (HER)'

## REFERENCES

1. Kamat P.V., *J. Phys. Chem. Lett.* **2013**, 4, 1727.
2. *World Energy Resources 2016 Report*, World Energy Council, **2016**.
3. *Annual Energy Outlook*, U.S. Energy Information Administration, **2016**.
4. *Renewables 2016 Global Status Report*, Renewable Energy Policy Network for the 21<sup>st</sup> Century, **2016**.
5. Barroso, M.; Mesa, C. A.; Pendlebury, S. R.; Cowan, A. J.; Hisatomi, T.; Sivula, K.; Gratzel, M.; Klug, D. R.; Durrant, J. R., *Proc. Natl. Acad. Sci. U.S.A.* **2012**, 109, 15640.
6. Wiberg, E.; Wiberg, N., *Inorganic Chemistry*, Academic Press, **2001**.
7. Sivula, K.; Le Formal, F.; Gratzel, M., *ChemSusChem* **2011**, 4, 432.
8. Walter, M. G.; Warren, E. L.; Mc Kone, J. R.; Boettcher, S. W.; Mi Q.; Santori, E. A.; Lewis, N. S., *Chem. Rev.* **2010**, 110, 6446.
9. Tamirat, A. G.; Rick J.; Dubale A. A., Sub W. N., Hwang B. J. *Nano Horiz.*, **2016**,1, 243.
10. Kumar, S.G.; Devi, L.G., *J. Phys. Chem. A* **2011**, 115, 13211.
11. Tada, H.; Fujishima, M.; Kobayashi, H., *Chem. Soc. Rev.* **2011**, 40, 4232.
12. Khan, M.A.; Woo, S.I.; Yang, O., *Int. J. Hydrog. Energy* **2008**, 33, 5345.
13. Kurian S., Seo H., Jeon H., *J. Phys. Chem. C* **2013**, 117, 16811.
14. O'Regan, B.; Gratzel, M., *Nature* **1991**, 353, 737.

15. Holmes, M.A.; Townsend, T.K.; Osterloh F.E., *Chem. Commun.* **2012**, 48, 371.
16. Hou, W.; Cronin, S.B., *Adv. Funct. Mater.* **2013**, 23, 1612.
17. Jang, J.S.; Kim, H.G.; Lee, J.S., *Catal. Today* **2012**, 185, 270.
18. Hou, Y.; Zuo, F.; Dagg, A.; Feng, P., *Nano Lett.* **2012**, 12, 6464.
19. Tian, J.; Zhang, Q.; Zhang, L.; Gao, R.; Shen, L.; Zhang, S.; Qu, X.; Cao, G., *Nanoscale* **2013**, 5, 936.
20. She, G.; Zhang, X.; Shi, W.; Fan, X.; Chang, J. C., *Electrochem. Commun.* **2007**, 9, 2784
21. Cheng, H.M.; Chiu, W.H.; Lee, C.H.; Tsai, S.Y.; Hsieh, W.F., *J. Phys. Chem. C* **2008**, 112, 16359.
22. Li, C.; Yang, L.; Xiao, J.; Wu, Y.C.; Sodergaard, M.; Luo, Y.; Li, D.; Meng, Q.; Iversen, B. B., *Phys. Chem. Chem. Phys.* **2013**, 15, 8710.
23. Chen, J.; Li, C.; Song, L.; Sun, X. W.; Lei, W.; Deng, W. Q., *Appl. Surf. Sci.* **2009**, 255, 7508.
24. Marschall, R.; Wang L., *Catal. Today* **2014**, 225, 111.
25. Walsh, A.; Yan, Y.; Huda, M. N.; Al-Jassim, M. M.; Wei, S. H., *Chem.Mater.* **2009**, 21, 547.
26. Ansari, S. A.; Cho, M. H., *Sci. Rep.* **2016**, 6, 25405.
27. Aronne, A.; Fantauzzi, M.; Imperato, C.; Atzei, D.; De Stefano, L.; D'Errico, G.; Sannino, F.; Rea, I.; Pirozzi, D.; Elsener, B.; Pernicea, P.; Rossib, A., *RSC Adv.*, **2017**, 7, 2373.
28. Hodes, G.; Kamat, P. V., *Phys. Chem. Lett.* **2015**, 6, 4090.
29. Kim, T. W.; Ping, Y.; Galli, G. A.; Choi, K. S., *Nat. Commun.* **2015**, 6, 8769
30. Park, Y.; McDonald, K. J.; Choi K.S., *Chem. Soc. Rev.*, **2013**, 42, 2321.

31. Xia, X.; Yang, P.; Sun, Y.; Wu, Y.; Mayers, B.; Gates, B.; Yin, Y.; Kim, F.; Yan, H., *Adv. Mater.* **2003**, 15, 5.
32. Parthangal, P.; Cavicchi, R.; Meier, D.; Herzing, A.; Zachariah, M., *J. Mater. Res.* **2011**, 26, 3.
33. Lupan, O.; Chow, L.; Chai, G.; Schulte, A.; Park, S.; Heinrich, H.; Sontea, V.; Trofim, V.; Railean, S., *IEEE*, **2008**.
34. Kar, A.; Stroschio, M.; Dutta, M.; Kumari, J.; Meyyappan, M., *Semicond. Sci. Technol.* **2010**, 25, 024012.
35. Ishizaki, T.; Saito, N.; Takai, O., *J. Electrochem. Soc.* **2009**, 156, 413.
36. Azam, A.F.; Ali, R. M.; Ali, K., *Mater. Lett.* **2008**, 62, 1789.
37. Choi, Y.; Hwang, I.; Park, J.; Choi, K.; Park, J.; Lee, J., *Nanotech.* **2008**, 19, 095508.
38. Qin, L.; Xu, J.; Dong, X.; Pan, Q.; Cheng, Z.; Xiang, Q.; Li, F., *Nanotech.* **2008**, 19, 185705.
39. Tischner, A.; Köck, A.; Maier, T.; Edtmaier, C.; Gspan, C.; Kothleitner, G., *Microelectron. Eng.* **2009**, 86, 1258.
40. Chandra, D.; Mukherjee, N.; Mondal, A.; Bhaumik, A., *J. Phys. Chem. C* **2008**, 112, 8668.
41. Liu, H.; Avrutin, V.; Izyumskaya, N.; Ozgur, U.; Morkoc, H., *Superlattices Microstruct.* **2010**, 48, 458.
42. Thapa A., J. Zai T., Elbohy H., Poudel P., Adhikari N., Qian X. F., Qiao Q. Q., *Nano Res.*, **2014**, 7, 1154.
43. Yu, J. G.; Wang, Y.; Xiao, W., *J. Mater. Chem. A*, **2013**, 1, 10727.
44. Cheng, C. W.; Ren, W. N.; Zhang, H. F., *Nano Energy*, **2014**, 5, 132.

45. Zhai, T.; Fang, X.; Liao, M., *Sensors* **2009**, 9, 6504.
46. Poizot, P.; Laruelle, S.; Grugeon, S.; Dupont, L.; Tarascon, J. M., *Nature* **2000**, 407, 496.
47. Asamoto, M.; Miyake, S.; Sugihara, K.; Yahiro, H., *Electrochem. Comm.* **2009**, 11,1508.
48. Snaith, H. J.; Mende, L. S., *Adv. Mater.* **2007**, 19, 3187.
49. Sun, B.; Sirringhaus, H., *Nanolett.* **2005**, 5, 2408.
50. Kim, B. J.; Ryu, Y. R.; Lee, T. S.; White, H. W., *Appl. Phys. Lett.* **2009**, 94, 103506.
51. Im, J.S.; Park, S.J.; Kim, T.; Lee, Y.S., *Int. J. Hydrogen Energy*, **2009**, 34, 3382.
52. Wan, Q.; Lin, C. L.; Yu, X. B.; Wang, T. H., *Appl. Phys. Lett.* **2004**, 84, 124.
53. Hepel, M.; Hazelton, S., *Electrochim. Acta*, **2005**, 50, 5278.
54. Quintana, M.; Ricra, E.; Rodriguez, J.; Estrada, W., *Catal. Today* **2002**, 76, 141.
55. Rout, C. S.; Hegde, M.; Govindaraj, A.; Rao, C. N. R., *Nanotech.* **2007**, 18, 205504.
56. Zhao, S.; Wei, P.; Chen S., *Sensor Actu. B* **2000**, 62, 117.
57. Li, Y.; Valle, F. D.; Simonnet, M.; Yamada, I.; Delaunay, J. J., *Nanotech.* **2009**, 20, 45501.
58. Johnson, R. W.; Hultqvist, A.; Bent, S. F., *Mater. Today* **2014**, 236.
59. Schlesinger, T. E. R.; Tacconi, N. R., *Electrodeposition of Semiconductors*; Springer, New York, **2010**.
60. Atwater, H. A.; Polman, A., *Nat. Mater.* **2010**, 9, 205.
61. Zhang, J.; Zhang, L.; Xu W., *J. Phys. D* **2012**, 45, 11.
62. Warren, S.C.; Thimsen, E., *Energy Environ. Sci.*, **2012**, 5, 5133.
63. Silva, G.; Juarez, C.; Marino, R.; Molinari, R.; Garcia, H., *J. Am. Chem. Soc.* **2010**, 133, 595.

64. Barpuzary, D.; Khan, Z.; Vinothkumar, N.; De, M.; Qureshi, M., *J. Phys. Chem. C* **2012**, 116, 150.
65. Wang, H.; Wang, T.; Wang, X.; Liu, R.; Wang, B.; Wang, H.; Xu, Y.; Zhang, J.; Duan, J., *J. Mater. Chem.* **2012**, 22, 12532.
66. Kim, H.; Seol, M.; Lee, J.; Yong, K., *J. Phys. Chem. C* **2011**, 115, 25429.
67. Cao, X.; Chen, P.; Guo, Y., *J. Phys. Chem. C* **2008**, 112, 20560.
68. Leventis, H.C.; O'Mahony, F.; Akhtar, J.; Afzaal, M.; O'Brien, P.; Haque, S.A., *J. Am. Chem. Soc.* **2010**, 132, 2743.
69. Leschkies, K.S.; Beatty, T.J.; Kang, M.S.; Norris, D.J.; Aydil, E.S., *ACS Nano* **2009**, 3, 3668.
70. Shen, Q.; Toyoda, T., *J. Appl. Phys.* **2004**, 43, 2946.
71. Emin, S.; Yanagida, M.; Peng, W.; Han, L., *Sol. Energy Mater. Sol. Cells* **2012**, 101, 5.
72. Feng, H.L.; Wu, W.Q.; Rao, H.S.; Wan, Q.; Li, L.B.; Kuang, D.B.; Su, C.Y., *ACS Appl. Mater. Interfaces* **2015**, 7, 5199.
73. Zinola, C.F.; Martins, M.E.; Tejera, E. P.; Neves, N.P., *Int. J. Electrochem.* **2012**, 12, 1.
74. Jiao, Y.; Zheng, Y.; Jaronies, M.; Qiao, S. Z., *Chem. Soc. Rev.* **2015**, 44, 2060.
75. Ruban, A.; Hammer, B.; Soltze, P.; Skriver, H. L.; Noirskov, J. K., *J. Mol. Catal. A. Chem.* **1997**, 115, 421.
76. Wang, Q.; Cha, C.S.; Lu, J.; Zhuang, L., *Phys. Chem. Chem. Phys.* **2009**, 11, 679.
77. Bligaard, T.; Norskov, J.; Dahl, S.; Matthiesen, J.; Christensen, C.; Sehested, J., *J. Catal.* **2004**, 224, 206.
78. Michalsky, R.; Zhang, Y.J.; Peterson, A.A., *ACS Catal.* **2014**, 4, 1274.

79. Wang, F.; Shifa, T. A.; Zhan, X.; Huang, Y.; Liu, K.; Cheng, Jiang Z. C.; He, J., *Nanoscale* **2015**, 7, 19764.
80. Chen, J. G., *Chem. Rev.* **1996**, 96, 1477.
81. Morales G. C.; Stern L. A.; Hu, X., *Chem. Soc. Rev.* **2014**, 43, 6555.
82. Zeng M.; Li, Y. G., *J. Mater. Chem. A* **2015**, 3, 14942.
83. Vesborg, P. C. K.; Seger, B.; Chorkendorff, I., *J. Phys. Chem. Lett.* **2015**, 6, 951.
84. Pan, L. F.; Li, Y. H.; Yang, S.; Liu, P. F.; Yu M. Q.; Yang, H. G., *Chem. Commun.* **2014**, 50, 13135.
85. Jin, Y.; Wang, H.; Li, J.; Yue, X.; Han, Y.; Shen P. K.; Cui, Y., *Adv. Mater.* **2016**, 28, 3785.
86. Kibsgaard, J.; Jaramillo, T. F., *Angew. Chem., Int. Ed.* **2014**, 53, 14433.
87. Li, H.; Tsai, C.; Koh, A. L.; Cai, L.; Contryman, A. W.; Fragapane, A. H.; Zhao, J.; Han, H. S.; Manoharan H. C.; Pedersen, F.A., *Nat. Mater.*, **2016**, 15, 48.
88. Sasaki, W. F. K.; Ma, C.; Frenkel, A. I.; Marinkovic, N.; Muckerman, J. T.; Zhu Y.; Adzic, R. R., *Angew. Chem., Int. Ed.* **2012**, 51, 6131.
89. Zheng, W.; Cotter, T. P.; Kaghazchi, P.; Jacob, T.; Frank, B.; Schlichte, K.; Zhang, W.; Su, D. S.; Schueth, F.; Schloegl, R., *J. Am. Chem. Soc.* **2013**, 135, 3458.
90. Wan, C.; Regmi, Y. N., Leonard, B. M., *Angew. Chem. Int. Ed.* **2014**, 53, 6407.
91. Ma, L.; Ting, L. R. L.; Molinari, V.; Giordano, C.; Yeo, B. S., *J. Mater. Chem. A* **2015**, 3, 8361.
92. Hugosson, H. W.; Eriksson, O.; Nordstrom, L.; Jansson, U.; Fast, L.; Delin, A.; Wills, J. M.; Johansson, B., *J. Appl. Phys.* **1999**, 86, 3758.

93. Wang, J.; Xia, H.; Peng, Z.; Lv, C.; Jin, L.; Zhao, Y.; Huang, Z.; Zhang, C., *ChemSusChem* **2016**, 9,855.
94. Hanif, A.; T. Xiao, York, A. P. E.; Sloan, J.; Malcolm L. H., *Green Chem. Mater.* **2002**, 14, 1013.
95. Giordano, C.; Erpen, C.; Yao, W.; Milke, B.; Antonietti, M., *Chem. Mater.* **2009**, 21, 5136.
96. Wang, S.; Wang, J.; Zhu, M.; Bao, X.; Xiao, B.; Su, D.; Li, H.; Wang, Y., *J. Am. Chem. Soc.* **2015**, 137, 15753.
97. Brownson, D.A.C.; Banks, C.E., *The Handbook of Graphene Electrochemistry* Springer, London, **2014**.
98. a) Biswas, C.; Lee, Y. H., *Adv. Funct. Mater.* **2011**, 21, 3806.; b) Huang, C.; Li, C., Shi, G., *Energy Environ. Sci.* **2012**, 5, 8848.; c) Kong, X. K.; Chen, C. L.; Chen, Q.W., *Chem. Soc. Rev.* **2014**, 43, 2841.
99. Li, Y.; Wang, H.; Xie, L.; Liang, Y.; Hong, G.; Dai, H., *J. Am. Chem. Soc.* **2011**, 133, 7296.
100. Lin, Z.Y.; Liu, Y.; Wong C.P., *Langmuir* **2010**, 26, 16110.
101. Bekyarova, E.; Itkis, M.E.; Ramesh, P.; Berger, C. Sprinkle, M.; Heer, W.A.D.; Haddon R.C. *J. Am. Chem. Soc.* **2009**, 131, 1336.
102. Jiao, Y.; Zheng, Y.; Jaroniec, M.; Qiao, S. Z., *J. Am. Chem. Soc.* **2014**, 136, 4394.
103. Alexander, B. D.; Kulesza, P.J.; Rutkowska, I.; Solarskac R.; Augustynski J., *J. Mater. Chem.* **2008**, 18, 2298.
104. Wang, G.; Ling, Y.; Lu, X.; Qian, F.; Tong, Y.; Zhang, J. Z.; Lordi, V.; Leao, C. R.; Li, Y., *J. Phys. Chem. C* **2013**, 117, 10957.
105. Woodhouse, M.; Parkinson, B. A., *Chem. Soc. Rev.* **2009**, 38, 197.

106. Walsh, A.; Yan, Y.; Huda, M. N.; Al-Jassim, M. M.; Wei, S.H. *Chem. Mater.* **2009**, 21, 547.
107. Rettie, A.J.E.; Lee, H.C.; Marshall, L.G.; Lin, J.F.; Capan, C.; Lindemuth, J.; McCloy, J.S.; Zhou, J.; Bard, A.J.; Mullins C.B., *J. Am. Chem. Soc.* **2013**, 135, 1389.
108. Abdi, F. F.; Firet, N.; van de Krol, R., *ChemCatChem* **2013**, 5, 490.
109. Pilli, S.K.; Furtak, T.E.; Brown L.D.; Deutsch, T.G.; Turner J.A.; Herring, A. M., *Energy Environ. Sci.* **2011**,4, 5028.
110. Galembeck, A.; Alves, O. L., *Thin Solid Films* **2000**, 365, 90.
111. Kelly, K. L.; Coronado, E.; Zhao, L. L.; Schatz, G. C., *J. Phys. Chem. B* **2002**, 107, 668.
112. Derkacs, D.; Lim, S. H.; Matheu, P.; Mar, W.; Yu, E.T., *Appl. Phys. Lett.* **2006**, 89, 093103.
113. Seabold, J. A.; Choi, K.S., *J. Am. Chem. Soc.* **2012**, 134, 2186.
114. Subramanian, V.; Wolf, E.; Kamat, P.V., *J. Phys. Chem. B* **2001** 105, 11439.
115. Chi, C. F.; Cho, H. W.; Teng, H.; Chuang, C. Y.; Chang, Y. M.; Hsu, Y. J.; Lee, Y. L., *Appl. Phys. Lett.* **2011**, 98, 12101.
116. Rao,H.S.; Wu,W.Q.; Liu,Y.; Xu, Y.F.; Chen, B.X.; Chen, H.Y.; Kuang, D.B.; Su, C.Y., *NanoEnerg.* **2014**, 8, 1.
117. Ma, B.; Wang, L.; Dong, H.; Gao, R.; Geng, Y.; Zhu, Y.; Qiu, Y., *Phys. Chem. Chem. Phys.* **2011**, 13, 2656.
118. Kudo, A.; Tsuji I.; Kato, H., *Chem. Commun*, **2002**, 1958.
119. Cheng, L.; Zhang, H.; Chng, C., *RSC Adv.* **2016**, 6, 37407.

120. Gao, C.; Zhang, Z.; Li, X.; Chen, L.; Wang, Y.; He, Y.; Teng, F.; Zhou, J.; Han, W.; Xie, E.; *Sol. Energy Mater Sol. Cells* **2015**, 141, 101.
121. Rodenas, P.; Song, T.; Sudhagar, P.; Marzari, G.; Han, H.; Bou, L. B.; Gimenez, S.; Santiago, F. F.; Sero, M. I.; Bisquert, J.; Paik, U.; Kang, Y. S. *Adv. Energy Mater.* **2013**, 3, 176.
122. Wang, P.; Zhang, Y.; Su, L.; Gao, W.; Zhang, B.; Chu, H.W.; Yiding Z.; Jun, Y.; William W., *Electrochimica Acta* **2015**, 165, 110.
123. Ellis, A. B.; Kaiser, S. W.; Bolts, J. M.; Wrighton, M. S., *J. Am. Chem. Soc.* **1977**, 99, 2839.
124. Mu, Y.; Zhang, Y.; Fang, L.; Liu, L.; Zhang, H.; Wang, Y., *Electrochimica Acta* **2016**, 215, 357.
125. Xiang, M.; Li, D.; Li, W.; Zhong B.; Sun, Y., *Catal. Commun.* **2007**, 8, 513.
126. Sheng, W. H.; Gasteiger, A.; Shao-Horn, Y., *J. Electrochem. Soc.* **2010**, 157, 1529.
127. Liu, N.; Guo, Y. L.; Yang, X. Y.; Lin, H. L.; Yang, L. C.; Shi, Z. P.; Zhong, Z. W.; Wang, S. N.; Tang, Y.; Gao, Q. S., *ACS Appl. Mater. Interfaces* **2015**, 7, 23741.
128. Geim A. K.; Novoselov, K. S., *Nat. Mater.* **2007**, 6, 183.
129. He, C.; Tao, J., *Chem. Commun.* **2015**, 51, 8323.
130. Pan, L. F.; Li, Y. H.; Yang, S.; Liu, P. F.; Yu, M. Q.; Yang, H. G., *Chem. Commun.* **2014**, 50, 13135.